MODERN HEURISTICS IN STRUCTURAL DAMAGE DETECTION USING FREQUENCY RESPONSE FUNCTIONS

A Dissertation

by

TAMÁS RÓBERT LISZKAI

Submitted to the Office of Graduate Studies of
Texas A&M University
in partial fulfillment of the requirements for the degree of

DOCTOR OF PHILOSOPHY

August 2003

Major Subject: Civil Engineering

MODERN HEURISTICS IN STRUCTURAL DAMAGE DETECTION USING FREQUENCY RESPONSE FUNCTIONS

A Dissertation

by

TAMÁS RÓBERT LISZKAI

Submitted to the Office of Graduate Studies of
Texas A&M University
in partial fulfillment of the requirements for the degree of

DOCTOR OF PHILOSOPHY

Approved as to style and content by:

Anne M. Raich (Chair of Committee)	Gary T. Fry (Member)
Harry L. Jones (Member)	Jorge V. Leon (Member)

Paul Roschke
(Head of Department)

August 2003

Major Subject: Civil Engineering

ABSTRACT

Modern Heuristics in Structural Damage Detection Using Frequency Response Functions. (August 2003)

Tamás Róbert Liszkai, M.S., University of Miskolc

Chair of Advisory Committee: Dr. Anne M. Raich

This research addresses the problem of structural damage detection using linear vibration information contained in frequency response functions. The structural damage identification method is stated as an unconstrained optimization problem, which minimizes the error between measured and analytically computed vibration signatures using minimal measurement information. Two types of genetic algorithms are implemented to solve the structured and unstructured optimization problem of damage detection. The proposed algorithms are evaluated on case study simulations for different types of structures with increasing complexity. Noisy measurements are included in the simulations to investigate their effect on damage detection accuracy. The proposed method is compared to existing damage detection algorithms using accuracy measures that are based on Euclidean geometry. Case study results show that the proposed damage identification method is robust even in noisy measurement environments.

A methodology for optimizing excitation and sensor layouts used for detecting damage in structures is presented by applying multi-objective genetic algorithms. In sensor layout optimization, the objectives are to reduce the number of sensors required while trying to increase the amount of information contained in the vibration signatures. Several case studies were investigated to determine the effect of using the optimum sensor layout designs evolved on the performance of the FRF-based damage detection method. The results show that the quality of the measurement information increased when the optimal sensor locations were used and the ability of the damage detection method to uniquely identify damaged elements was enhanced.

ACKNOWLEDGEMENTS

The author would like to express his gratitude to Dr. Anne M. Raich, who served as the Chair on the author's Committee, for her guidance, encouragement and fruitful discussions throughout the author's study at Texas A&M University. The author gratefully acknowledges the help and support provided by the other Members of the Committee, Dr. Gary T. Fry for his invaluable assistance in advising the author toward the research presented in this dissertation, Dr. Harry L. Jones for his unconditional and sincere encouragement and Dr. Jorge V. Leon for his time and support.

Special thanks to Peter Sculley and Brent Bartell for their help in generating computer simulations and evaluating the program developed during this research.

Friends from all over the world are greatly appreciated who gave the author inspiration in achieving his goals. The author is very much obliged to his and his wife's family for their understanding. All the author's gratitude and respect is devoted to his beloved wife, Szilvia, for her unreserved support and patience and for being his partner through foul and fair.

NOMENCLATURE

a, a_j, b	=	Proportionality constants for viscous damping
a	=	Vector of time independent complex amplitudes of acceleration response
A	=	Cross-sectional area
A, **A**(ω)	=	Accelerance matrix
ASAC	=	Active structural acoustic control
b	=	Vector of base two binary coded string
B	=	Base multiplier controlling frequency for writing output
c	=	Finite element damping matrix
C	=	Structural damping matrix in global coordinate system
COMAC	=	Coordinate modal assurance criterion
D	=	Diagonal inverse receptance matrix in the natural coordinate system
DLAC	=	Damage location assurance criterion
DOF	=	Degrees of freedom
dV	=	Infinitesimal volume
dS	=	Infinitesimal surface
e	=	Natural logarithmic base number, 2.7182818285
ene	=	Euclidean normalized error
E	=	Young's modulus or modulus of elasticity
f	=	Objective (error) function for optimization
$\overline{f}$	=	Average fitness of individuals in the current population
f_{max}	=	Fitness value of best individual in the current population
F	=	Vector of body forces per unit volume
$\mathbf{f}_0$	=	Vector of time independent complex amplitudes
FAAC	=	Frequency amplitude assurance criterion
FDAC	=	Frequency domain assurance criterion
FRAC	=	Frequency response assurance criterion
FRCM	=	Frequency response curvature method
FRF	=	Frequency response function

$\mathbf{g}$	=	Vector of Gray coded string
$G_{ff}(\omega)$	=	Force signal auto-spectrum function
$G_{fx}(\omega)$	=	Response signal auto-spectrum function
$G_{xx}(\omega)$	=	Force – response cross-spectrum function
GA	=	Genetic algorithm
GAC	=	Global amplitude criterion
GL	=	Gene locator
GSC	=	Global shape criterion
h	=	Iteration dependency factor for non-uniform mutation
$\mathbf{H}$, $\mathbf{H}(\omega)$	=	General FRF matrix
i	=	Imaginary unit, $i^2 = -1$, or nonnegative integer indices
I	=	Second moment of inertia
$\mathbf{I}$	=	Identity matrix
IRR	=	Implicit redundant representation
j, k	=	Nonnegative integer indices
$\mathbf{k}$	=	Finite element stiffness matrix in local coordinate system
$\mathbf{K}$	=	Structural stiffness matrix in global coordinate system
$\mathbf{k}^g$	=	Finite element stiffness matrix in global coordinate system
k_1, k_2	=	Constants between zero and one, primary and secondary crossover rates
k_3	=	Exponent controlling output frequency
k_y	=	Shear correction factor
l_g	=	Number of bits in an encoded gene instance
l_{GL}	=	Number of bits in the gene locator (GL) pattern
l_s	=	$n_{bits} - l_{GL} - 1$
L	=	Length of a finite element
LAC	=	Local amplitude criterion
LQG	=	Linear quadratic Gaussian
$\mathbf{m}$	=	Finite element mass matrix in local coordinate system
$\mathbf{M}$	=	Structural mass matrix in global coordinate system
$\mathbf{m}^g$	=	Finite element mass matrix in global coordinate system
MAC	=	Modal assurance criterion

MOGA	=	Multiobjective genetic algorithm
n	=	Number of degrees of freedom in a finite element model
n_{bit}	=	Number of bits used to encode one variable
n_{bits}	=	Number of bits in a chromosome
n_e	=	Number of finite elements
n_{meas}	=	Number of measurements (sensors)
$n_{out,i}$	=	Generation number for which output is written to the postprocessor and/or text files
n_{pop}	=	Population size
n_{sens}	=	Number of DOFs where sensors can be placed
n_{tour}	=	Tournament selection size
$n_{u,meas}$	=	Maximum number of measurements (sensors) allowed
N_{GL}	=	Probable number of gene instances found in the string
NLP	=	Nonlinear programming
NN	=	Neural networks
NSGA	=	Nondominated sorting genetic algorithm
ODS	=	Operational deflection shapes
ope	=	Orthogonal projection error
p_c	=	Probability of crossover
p_{GL}	=	Probability of occurrence of a specific gene locator (GL) pattern
p_m	=	Probability of mutation
$\mathbf{p}_j$	=	External nodal for force at finite element node j
PI	=	Performance index
$\mathbf{q}$	=	Vector of natural or modal coordinates
r	=	Uniform distributed random number between 0 and 1
$\mathbf{R}$, $\mathbf{R}(\omega)$	=	Receptance matrix
$\mathbf{s}_l$	=	Sensor location vector
$\mathbf{S}$	=	Vector of step sizes for hillclimbing algorithm
S_e	=	Surface of finite element
SA	=	Simulated annealing
SAT	=	Satisfiability problem

SDIM	=	Structural damage identification method
SGA	=	Simple genetic algorithm
t	=	Instantaneous time
$\mathbf{T}_r$	=	Rotation matrix from local coordinate system to global coordinate system
$\mathbf{T}_r^e$	=	Finite element rotation matrix
tae	=	Trigonometric angle error
tpe	=	True projection error
TS	=	Tabu search
TSP	=	Traveling salesman problem
u	=	Local axial coordinate of a one dimensional finite element
$\mathbf{u}$, $\mathbf{u}(t)$	=	Displacement field vector
$\mathbf{u}_e$	=	Vector of interpolated displacements for a finite element
$\mathbf{U}$	=	Vector of nodal displacements for a finite element
v	=	Local transverse coordinate of a one dimensional finite element
$\mathbf{v}$	=	Vector of time independent complex amplitudes of velocity response
$\mathbf{V}$, $\mathbf{V}(\omega)$	=	Mobility matrix
V_e	=	Volume of a finite element
x	=	Global Cartesian coordinate axis
$\mathbf{x}^s$	=	Vector of damage indicators
$X_k(\omega)$	=	General response in the frequency domain at node k
y	=	Global Cartesian coordinate axis
y_n	=	Noise level in measurements
$\mathbf{z}$	=	Vector of time independent complex amplitudes of displacement response
α	=	Angle of element orientation
α_j	=	Arbitrary constant
β	=	Probability of occurrence of a specific bit value
β_1, β_2	=	Step size modification factors for hillclimbing
$\gamma^2(\omega)$	=	Coherence function

$\delta\boldsymbol{\varepsilon}$	=	Vector of virtual strains
$\Delta(t,m)$	=	Non-uniform bit position generating function
$\boldsymbol{\varepsilon}$	=	Vector of strains
ζ_j	=	j^{th} modal damping ratio
λ, λ_j	=	Eigenvalue
$\boldsymbol{\Lambda}$	=	Diagonal matrix of eigenvalues
ρ	=	Mass density of material
$\boldsymbol{\sigma}$	=	Vector of stresses
φ	=	Local rotational coordinate of a one dimensional finite element
$\boldsymbol{\varphi}$	=	Eigenvector, mode shape, shape vector
ϕ_y	=	Shear slenderness factor
$\boldsymbol{\Psi}$	=	Vector of prescribed surface tractions on the element surface S_e
ω	=	Circular frequency of excitation
ω_j	=	Natural circular frequency of the system

TABLE OF CONTENTS

Page

ABSTRACT iii

ACKNOWLEDGEMENTS iv

NOMENCLATURE v

TABLE OF CONTENTS x

LIST OF FIGURES xiv

LIST OF TABLES xxiv

1 INTRODUCTION 1

1.1 Overview 1
1.2 Research Objectives 3
1.3 Scope 4
1.4 Background and Literature Review 7
1.4.1 Relevant and On-going Research in Damage Detection 7
1.4.1.1 General Concepts 7
1.4.1.2 Modal Methods 8
1.4.1.3 FRF Methods 10
1.4.1.4 Other Methods 11
1.4.2 Relevant and On-going Research in Near-optimal Sensor Placement 13
1.4.2.1 General Concepts 13
1.4.2.2 Sensor Placement for Modal Based Damage Detection 15
1.4.2.3 Other Methods 19
1.5 Overview of Modal Based Damage Index SDIMs 20
1.5.1 Damage Index A 21
1.5.2 Damage Index B 22
1.5.3 Damage Index C 22
1.6 Overview of Frequency Domain Criteria for SDIMs 24
1.7 Organization of the Dissertation 27

2 THEORY OF DAMAGE DETECTION 29

2.1 Equations of Motion for Dynamic Systems 29
2.2 Frequency Response Functions 33
2.2.1 Free Vibration of a Linear System 35
2.2.2 Modal Decomposition of FRF Matrices for Viscously Damped Systems 39

Page

2.2.3 Measuring FRF Data, Displacement, Velocity and Acceleration.....43
2.3 Damage Indicators.....47
2.4 Use of FRF Data in Damage Detection.....50
2.5 Excitation and Sensor Placement.....53
2.5.1 Information Contained in Measurements.....54
2.5.2 Optimum Excitation and Sensor Layout Design.....56

3 OPTIMIZATION ALGORITHMS.....57

3.1 Overview of Traditional Optimization Algorithms.....57
3.1.1 Classes of Optimization Problems.....57
3.1.2 Local and Global Search Techniques.....59
3.2 Introduction to Genetic Algorithms.....62
3.2.1 Genetic Operators.....63
3.2.2 A Short Tutorial on Simple Genetic Algorithms (SGA).....68
3.2.3 Advanced Genetic Operators.....72
3.3 Fixed and Implicit Redundant Representations.....78
3.3.1 Encoding for Damage Detection.....79
3.3.2 Encoding for Excitation and Sensor Layout Design.....84
3.4 Local Optimizer, Hillclimbing Algorithm.....87
3.5 Multiobjective Optimization Using Nondominated Sorting Genetic Algorithm.....90
3.5.1 The Notion of Multiobjective Optimization.....91
3.5.2 Nondominated Sorting Genetic Algorithm (NSGA).....92

4 COMPUTATIONAL PROGRAMMING.....97

4.1 Preprocessor and Utility Program.....98
4.2 Processor.....101
4.3 Postprocessor.....104

5 DESCRIPTION OF CASE STUDIES.....108

5.1 Simple Beam Type Structures.....109
5.1.1 Simple Cantilever Beam.....109
5.1.2 Two-span Continuous Beam.....111
5.2 Moment Frame Type Structures.....112
5.2.1 Two-story, Three-bay Cross-braced Moment Frame.....112
5.2.2 Three-story, Three-bay Unbraced Moment Frame.....114
5.3 Baseline Structure for Evaluation of the Proposed Damage Detection Method.....116

6 CASE STUDY RESULTS AND DISCUSSION, CANTILEVER BEAM.....120

Page

6.1 Input Parameters for Cantilever Beam Case Studies 120
6.2 Common Cantilever Beam Damage, Case Study CANT I and CANT II 121
6.2.1 Comparison of Fixed and IRR Representations 127
6.2.2 Alternative Objective Function Formulation 129
6.2.3 Verification Case Study CANT II 136
6.3 Unusual Measurement Configurations, Case Studies CANT III and IV 138
6.4 Optimum Sensor Locations, Case Study CANT OPT 141
6.4.1 Optimum Excitation and Sensor Locations 141
6.4.2 Results Using Optimal Sensor Locations 145

7 CASE STUDY RESULTS AND DISCUSSION FOR TWO-SPAN CONTINUOUS BEAMS 150

7.1 Equal Damages, Case Studies TWSP IA, IB and II 151
7.2 Unequal Damages, Case Studies TWSP IIIA and IIIB 156
7.2.1 Objective Function Based on FRF Correlation Criteria 162
7.2.2 Effect of Noise on Objective Function Formulations 168
7.3 Optimum Sensor Locations, Case Study TWSP OPT 175
7.3.1 Optimal Excitation and Sensor Locations 175
7.3.2 Damage Detection Results Using Optimal Sensor Placement 180

8 CASE STUDY RESULTS AND DISCUSSION, MOMENT FRAMES 188

8.1 Two-story, Three-bay Braced Frame 188
8.1.1 Fine Tuning, Finding a Good Set of GA Parameters 188
8.1.2 A Mixture of Bracing and Joint Damages in Beams and Columns 194
8.2 Three-story, Three-bay Unbraced Frame 199
8.2.1 Single Damage Cases for a First Floor Beam 199
8.2.2 Optimum Excitation and Sensor Locations for the Unbraced Frame 204
8.2.3 Damages Associated with Soft-story Mechanism 206
8.2.4 Damages Associated with Strong Column Weak Beam Design Concept 208

9 CASE STUDY RESULTS AND DISCUSSION, BENCHMARK STRUCTURE 216

9.1 Result Obtained for the Benchmark Case Studies 216
9.2 Accuracy Measures of SDIMs 222

10 CONCLUSIONS 236

10.1 Future Recommendations 239

REFERENCES 241

Page

APPENDIX A 251

APPENDIX B 254

APPENDIX C 265

APPENDIX D 269

VITA 317

LIST OF FIGURES

Page

Figure 2.1. Stresses, inertial and applied body forces on an infinitesimal element.....31

Figure 2.2. Cyclic history of a structural connection 52

Figure 3.1. A 14-city *symmetric* traveling salesman problem (TSP) 58

Figure 3.2. Schematic of simple genetic algorithms and genetic operators 64

Figure 3.3. Roulette wheel selection, the wheel is spun to select individuals for reproduction proportionally to their fitness values 66

Figure 3.4. Tournament selection process diagram.....67

Figure 3.5. Single point crossover.....67

Figure 3.6. Uniform mutation.....68

Figure 3.7. Parabolic function on the integer interval [0, 31] 69

Figure 3.8. Multi-point crossover.....73

Figure 3.9. Algorithms to convert binary and Gray coding.....75

Figure 3.10. Normalized contour plot of the bit position function used in non-uniform mutation as a function of the random number; The level lines indicate the relative generation age, t/T and $b = 1.5$.....77

Figure 3.11. Normalized contour plot of the bit position function used for non-uniform mutation, as a function of the relative generation age, the level lines indicated are corresponding random numbers, r, $b = 1.5$ 77

Figure 3.12. Fixed representation for damage detection 80

Figure 3.13. Implicit redundant representation (IRR) for damage detection 81

Figure 3.14. Zero damage individual using fixed representation.....83

Figure 3.15. Zero damage individual using IRR 84

Figure 3.16. Fixed representation for excitation and sensor layout design problem.....85

Page

Figure 3.17. Implicit redundant representation (IRR) for excitation and sensor layout problem 85

Figure 3.18. Comparison of fixed and IRR representations for the excitation and sensor layout design problem of simple cantilever beam 87

Figure 3.19. Flowchart of hillclimbing algorithm 89

Figure 3.20. Repair operator for fixed representation strings....95

Figure 4.1. Main menu structure of *GaDamDet* program 100

Figure 4.2. Settings menu and its corresponding toolbar of *GaDamDet* program....100

Figure 4.3. Monitor graph of an IRR GA run....104

Figure 4.4. Results menu and its submenus....105

Figure 4.5. Results toolbar corresponding to "Results" menu and its submenus....105

Figure 4.6. View menu and its corresponding view toolbar....107

Figure 5.1. Cantilever beam modeled with 10 finite elements, node numbers are regular and element numbers are in italics....110

Figure 5.2. Two-span continuous beam modeled with 20 finite elements, node numbers are regular and element numbers are in italics 110

Figure 5.3. Standard W-shape steel section and cross sectional properties 110

Figure 5.4. Two-story three-bay braced frame and dimensions 113

Figure 5.5. Standard double angles, 2L5 × 3½ × ½....113

Figure 5.6. Three-story three-bay unbraced frame and dimensions 115

Figure 5.7. Finite element models of a plate girder structure, (a) original model used by Kim and Stubbs (2002), (b) model used in this research....117

Figure 6.1. Damage detection results for case CANT I, fixed representation, seeded initial population, noise levels of 0, 5 and 10% 122

Figure 6.2. Damage detection results for case CANT I, fixed representation, seeded initial population, noise levels of 20 and 50% 123

Page

Figure 6.3. Damage detection results for case CANT I, implicit redundant representation (IRR), seeded initial population, noise levels of 0, 5 and 10%....124

Figure 6.4. Damage detection results for case CANT I, implicit redundant representation (IRR), seeded initial population, noise levels of 20 and 50% 124

Figure 6.5. Damage detection results for case CANT I, implicit redundant representation (IRR), unseeded initial population, noise levels of 0, 5 and 10%....125

Figure 6.6. Damage detection results for case CANT I, implicit redundant representation (IRR), unseeded initial population, noise levels of 20 and 50%....125

Figure 6.7. Comparison of the best individuals in the initial and final populations for the fixed representation SGA and the IRR GA 129

Figure 6.8. Undamaged and damaged accelerance FRFs and their differences for the cantilever beam case study, CANT I....131

Figure 6.9. Global Amplitude Criterion for the cantilever beam case study, CANT I....131

Figure 6.10. Damage detection results for case CANT I, fixed representation, seeded initial population, objective function is the sum of GSC and GAC squares, noise levels of 0, 5 and 10% 133

Figure 6.11. Damage detection results for case CANT I, fixed representation, seeded initial population, objective function is the sum of GSC and GAC squares, noise levels of 20 and 50% 133

Figure 6.12. Damage detection results for case CANT I, implicit redundant representation (IRR), seeded initial population, objective function is the sum of GSC and GAC squares, noise levels of 0, 5 and 10%....134

Figure 6.13. Damage detection results for case CANT I, implicit redundant representation (IRR), seeded initial population, objective function is the sum of GSC and GAC squares, noise levels of 20 and 50%....134

Figure 6.14. Damage detection results for case CANT I, implicit redundant representation (IRR), unseeded initial population, objective function is the sum of GSC and GAC squares, noise levels of 0, 5 and 10%....135

Page

Figure 6.15. Damage detection results for case CANT I, implicit redundant representation (IRR), unseeded initial population, objective function is the sum of GSC and GAC squares, noise levels of 20 and 50% 135

Figure 6.16. Damage detection results for case CANT II, fixed and implicit redundant representations (IRR), seeded and unseeded initial population, noise free measurements 137

Figure 6.17. Damage detection results for case CANT III, fixed and implicit redundant representations (IRR), seeded and unseeded initial population, noise free measurements 139

Figure 6.18. Damage detection results for case CANT IV, fixed and implicit redundant representations (IRR), seeded and unseeded initial population, noise free measurements 140

Figure 6.19. Pareto front and individuals in the final population represented in the objective space for the cantilever problem using fixed representation GA, population size is 200 144

Figure 6.20. Pareto front and individuals in the final population represented in the objective space for the cantilever problem using IRR GA, population size is 200 144

Figure 6.21. Damage detection results for case CANT OPT, fixed representation, seeded initial population, noise levels of 0, 10 and 20% 146

Figure 6.22. Damage detection results for case CANT OPT, implicit redundant representation (IRR), seeded initial population, noise levels of 0, 10 and 20%.....146

Figure 6.23. Damage detection results for case CANT OPT, implicit redundant representation (IRR), unseeded initial population, noise levels of 0, 10 and 20%.....147

Figure 6.24. Comparison of damage detection results using different measurement configurations at a noise level of 10% for the cantilever problem.....149

Figure 6.25. Comparison of damage detection results using different measurement configurations at a noise level of 20% for the cantilever problem.....149

Figure 7.1. Damage detection results for case TWSP IA, fixed and implicit redundant representations (IRR), seeded and unseeded initial population, noise free measurements 153

Page

Figure 7.2. Damage detection results for case TWSP IB, fixed and implicit redundant representations (IRR), seeded and unseeded initial population, noise free measurements 153

Figure 7.3. Convergence plot demonstrating the dynamic and adaptive ability of IRR GAs, case study TWSP IA unseeded IRR GA 154

Figure 7.4. Damage detection results for case TWSP II, fixed and implicit redundant representations (IRR), seeded and unseeded initial population, noise free measurements 155

Figure 7.5. Damage detection results for case TWSP IIIA, fixed representation, seeded initial population, noise levels of 0, 5 and 10% 157

Figure 7.6. Damage detection results for case TWSP IIIA, fixed representation, seeded initial population, noise levels of 20 and 30% 157

Figure 7.7. Damage detection results for case TWSP IIIA, implicit redundant representation (IRR), seeded initial population, noise levels of 0, 5 and 10%.....158

Figure 7.8. Damage detection results for case TWSP IIIA, implicit redundant representation (IRR), seeded initial population, noise levels of 20 and 30% 158

Figure 7.9. Damage detection results for case TWSP IIIA, implicit redundant representation (IRR), unseeded initial population, noise levels of 0, 5 and 10%.....159

Figure 7.10. Damage detection results for case TWSP IIIA, implicit redundant representation (IRR), unseeded initial population, noise levels of 20 and 30%.....159

Figure 7.11. Damage detection results for case TWSP IIIB, fixed and implicit redundant representations (IRR), seeded and unseeded initial population, noise free measurements 162

Figure 7.12. Damage detection results for case TWSP IIIB, fixed representation, seeded initial population, objective function is the sum of GSC and GAC squares, noise levels of 0, 5 and 10% 164

Figure 7.13. Damage detection results for case TWSP IIIB, fixed representation, seeded initial population, objective function is the sum of GSC and GAC squares, noise levels of 20 and 30% 164

Page

Figure 7.14. Damage detection results for case TWSP IIIB, implicit redundant representation (IRR), seeded initial population, objective function is the sum of GSC and GAC squares, noise levels of 0, 5 and 10%.....165

Figure 7.15. Damage detection results for case TWSP IIIB, implicit redundant representation (IRR), seeded initial population, objective function is the sum of GSC and GAC squares, noise levels of 20 and 30%.....165

Figure 7.16. Damage detection results for case TWSP IIIB, implicit redundant representation (IRR), unseeded initial population, objective function is the sum of GSC and GAC squares, noise levels of 0, 5 and 10%.....166

Figure 7.17. Damage detection results for case TWSP IIIB, implicit redundant representation (IRR), unseeded initial population, objective function is the sum of GSC and GAC squares, noise levels of 20 and 30%.....166

Figure 7.18. Simulated FRF measurements for case study TWSP IIIB, (a) FRF 1 – Excitation at node 18 and measurement at node 4, (b) FRF 2 – Excitation at node 18 and measurement at node 14.....169

Figure 7.19. Complex amplitudes of simulated measurement and analytical FRF differences for case study TWSP IIIB, (a) FRFs measured between nodes 18 and 4, (b) FRFs measured between nodes 18 and 14.....172

Figure 7.20. Correlation measures for case study TWSP IIIB, (a) Global Shape Criterion (GSC), (b) Global Amplitude Criterion (GAC).....173

Figure 7.21. Pareto front and individuals in the final population represented in the objective space for the two-span continuous beam problem using fixed representation GA, population size is 300.....177

Figure 7.22. Pareto front and individuals in the final population represented in the objective space for the two-span continuous beam problem using IRR GA, population size is 300.....178

Figure 7.23. Convergence plot of measurement information for the two-span continuous beam sensor layout design problem using fixed representation GA with a population size of 300.....179

Figure 7.24. Damage detection results for case TWSP OPT, fixed representation, seeded initial population, noise levels of 0, 5 and 10%.....181

Figure 7.25. Damage detection results for case TWSP OPT, fixed representation, seeded initial population, noise levels of 20 and 30%.....181

Page

Figure 7.26. Damage detection results for case TWSP OPT, implicit redundant representation (IRR), seeded initial population, noise levels of 0, 5 and 10%....182

Figure 7.27. Damage detection results for case TWSP OPT, implicit redundant representation (IRR), seeded initial population, noise levels of 20 and 30% 182

Figure 7.28. Damage detection results for case TWSP OPT, implicit redundant representation (IRR), unseeded initial population, noise levels of 0, 5 and 10%....183

Figure 7.29. Damage detection results for case TWSP OPT, implicit redundant representation (IRR), unseeded initial population, noise levels of 20 and 30%....183

Figure 7.30. Comparison of damage detection results using different measurement configurations at a noise level of 5% for the two-span continuous beam problem....185

Figure 7.31. Comparison of damage detection results using different measurement configurations at a noise level of 10% for the two-span continuous beam problem....186

Figure 7.32. Comparison of damage detection results using different measurement configurations at a noise level of 20% for the two-span continuous beam problem....186

Figure 7.33. Comparison of damage detection results using different measurement configurations at a noise level of 30% for the two-span continuous beam problem....187

Figure 8.1. Results for trial 28, noise free measurements case study BRFRM II 194

Figure 8.2. Pareto front and individuals in the final population represented in the objective space for the two-story three-bay braced moment frame problem using fixed representation GA, population size is 200 196

Figure 8.3. Results for trial 29, 30 and 31, 5% measurement noise, case study BRFRM II 198

Figure 8.4. Damage detection results for case UBFRM I, implicit redundant representation (IRR), seeded initial population, noise levels of 0, 5 and 10%....201

Page

Figure 8.5. Damage detection results for case UBFRM I, implicit redundant representation (IRR), unseeded initial population, noise levels of 0, 5 and 10%....202

Figure 8.6. Damage detection results for case UBFRM II, implicit redundant representation (IRR), seeded initial population, noise levels of 0, 5 and 10%....203

Figure 8.7. Damage detection results for case UBFRM II, implicit redundant representation (IRR), unseeded initial population, noise levels of 0, 5 and 10%....203

Figure 8.8. Pareto front and individuals in the final population represented in the objective space for the three-story three-bay unbraced moment frame problem using fixed representation GA, population size of 200 205

Figure 8.9. Damage detection results for soft-story mechanism case UBFRM III, seeded IRR GA, trials 1(a) and 1(b)....208

Figure 8.10. Damage detection results for soft-story mechanism case UBFRM III, seeded IRR GA, trials 2(a) and 2(b)....208

Figure 8.11. Damage detection results for case UBFRM IV, seeded IRR GA, trials 3, 4 and 5(a)....210

Figure 8.12. Damage detection results for case UBFRM IV, seeded IRR GA, trials 5(b) and 6 211

Figure 8.13. Damage detection results for case UBFRM IV, seeded IRR GA, trials 7 and 8 212

Figure 8.14. Damage detection results for case UBFRM IV, seeded IRR GA, trials 9 and 10 213

Figure 8.15. Damage detection results for case UBFRM IV, seeded IRR GA, trial 11 215

Figure 9.1. Normalized damage indices for case study KSTSP II, fixed representation GA after 200 generations....220

Figure 9.2. Geometrical definition of error measures 224

Figure A.1. One dimensional finite elements, (a) Bar element, (b) Beam element ...251

Page

Figure A.2. Arbitrarily oriented two-dimensional frame element with 6 DOF.....252

Figure B.1. Sample input file of a cantilever beam for the *ModalFEM* utility program 256

Figure B.2. Objective function dialog box 257

Figure B.3. Genetic algorithm property sheet in *GaDamDet* program 257

Figure B.4. Additional property pages on the genetic algorithm property sheet 258

Figure B.5. Finite element input and MATLAB measurement data file dialog.....259

Figure B.6. Preprocessor dialog box for output request control 260

Figure B.7. Dialog to monitor progress of the GA and hillclimber at run-time.....261

Figure B.8. Monitor graph of a fixed GA run 262

Figure B.9. Monitor graph of an excitation/sensor layout design problem.....262

Figure B.10. Individual plot of an IRR string 263

Figure B.11. Structure plot of a cantilever beam 263

Figure B.12. Damage indicator dialog 263

Figure B.13. Drawing properties property sheet and property page to set element display configuration.....264

Figure B.14. Property pages for legend and finite element nodes display settings.....264

Figure C.1. Finite element mesh and node numbering for braced two-story three bay moment frame.....265

Figure C.2. Finite element mesh and element numbering for braced two-story three bay moment frame.....266

Figure C.3. Finite element mesh and node numbering for unbraced three-story three-bay moment frame 267

Figure C.4. Finite element mesh and element numbering for unbraced three-story three-bay moment frame 268

Page

Figure D.1. Optimum excitation and sensor layout designs in the Pareto front for the cantilever problem.....276

Figure D.2. Optimum excitation and sensor layout designs in the Pareto front for the two-span continuous beam problem.....289

LIST OF TABLES

Page

Table 3.1. Randomly generated initial population 70

Table 3.2. First generation of individuals 71

Table 3.3. Binary and Gray codes for 4-bit strings 74

Table 5.1. Case studies for cantilever beam....111

Table 5.2. Case studies for two-span continuous beams....112

Table 5.3. Case studies for two-story three-bay cross-braced moment frame 114

Table 5.4. Case studies for three-story three-bay unbraced moment frame....116

Table 5.5. Case studies for two-span continuous beam used by Kim and Stubbs (2002) 118

Table 5.6. Results for the plate girder damage detection problems obtained by Kim and Stubbs (2002) 119

Table 6.1. GA parameters for cantilever beam trials 121

Table 6.2. Comparison of the performance of different objective functions at a 5% noise level in measurements for the cantilever beam 136

Table 6.3. Comparison of the performance of different objective functions at a 20% noise level in measurements for the cantilever beam 136

Table 6.4. GA settings for excitation and sensor layout design for the cantilever problem 141

Table 6.5. Pareto optimal excitation and sensor locations for the cantilever beam problem, CANT....142

Table 6.6. Average fitness values of initial populations using non-optimized and optimal sensor locations for the cantilever beam case studies CANT I and OPT 148

Table 7.1. GA parameters for two-span continuous beam trials....150

Table 7.2. Comparison of the performance of different objective functions at a 5% noise level in measurements for the two-span continuous beam....167

Page

Table 7.3. Comparison of the performance of different objective functions at a 20% noise level in measurements for the two-span continuous beam....167

Table 7.4. GA settings for excitation and sensor layout design for the two-span continuous beam problem 176

Table 7.5. Pareto optimal excitation and sensor locations for the two-span continuous beam problem, TWSP....177

Table 7.6. Average fitness values of initial populations using non-optimized and optimal sensor locations for the two-span continuous beam case studies TWSP IIIA and OPT....184

Table 8.1. GA input parameters for the braced frame case study, BRFRM I....189

Table 8.2. Comparison of results for the braced frame case BRFRM I....191

Table 8.3. Results for braced frame study BRFRM I using different random seeds....193

Table 8.4. Pareto optimal excitation and sensor locations for the two-story three-bay braced moment frame problem, BRFRM....195

Table 8.5. Comparison of individuals' average fitness for trials 29, 30 and 31....198

Table 8.6. GA input parameters for three-story three-bay unbraced moment frame....200

Table 8.7. Pareto optimal excitation and sensor locations for the three-story three-bay unbraced moment frame problem, UBFRM....205

Table 8.8. GA input parameters for the soft-story mechanism case study, UBFRM III....206

Table 8.9. Trials for case study UBFRM IV....209

Table 9.1. GA parameters for plate girder trials....218

Table 9.2. Damage detection result for the plate girder case studies after discordancy test for fixed representation GA and reduced hillclimbing, noise free measurements....220

Page

Table 9.3. Damage detection result for the plate girder case studies after discordancy test for seeded IRR GA and reduced hillclimbing, noise free measurements....221

Table 9.4. Damage detection result for the plate girder case studies after discordancy test for unseeded IRR GA and reduced hillclimbing, noise free measurements....222

Table 9.5. Damage detection accuracy measures for Damage Index A and B methods, noise free measurement cases....226

Table 9.6. Damage detection accuracy measures for Damage Index C method, noise free measurement cases....227

Table 9.7. Damage detection accuracy measures for fixed representation GA, noise free measurement cases....228

Table 9.8. Damage detection accuracy measures for seeded implicit redundant representation (IRR) GA, noise free measurement cases....229

Table 9.9. Damage detection accuracy measures for unseeded implicit redundant representation (IRR) GA, noise free measurement cases....230

Table 9.10. Damage detection result for the plate girder case studies after discordancy test for seeded IRR GA and reduced hillclimbing, 5% measurement noise included....231

Table 9.11. Damage detection accuracy measures for seeded implicit redundant representation (IRR) GA, 5% measurement noise included....232

Table 9.12. Comparison of accuracy measures for different types of damage detection algorithms....233

Table B.1. Cards that can be used in the text input file (*.inp) for the *ModalFEM* utility program....254

Table D.1. Damage detection results for case CANT I, fixed representation, seeded initial population, noise levels of 0, 5 and 10%....269

Table D.2. Damage detection results for case CANT I, fixed representation, seeded initial population, noise levels of 20 and 50%....269

Page

Table D.3. Damage detection results for case CANT I, implicit redundant representation (IRR), seeded initial population, noise levels of 0, 5 and 10%....270

Table D.4. Damage detection results for case CANT I, implicit redundant representation (IRR), seeded initial population, noise levels of 20 and 50%....270

Table D.5. Damage detection results for case CANT I, implicit redundant representation (IRR), unseeded initial population, noise levels of 0, 5 and 10%....270

Table D.6. Damage detection results for case CANT I, implicit redundant representation (IRR), unseeded initial population, noise levels of 20 and 50%....271

Table D.7. Damage detection results for case CANT I, fixed representation, seeded initial population, objective function is the sum of GSC and GAC squares, noise levels of 0, 5 and 10%....271

Table D.8. Damage detection results for case CANT I, fixed representation, seeded initial population, objective function is the sum of GSC and GAC squares, noise levels of 20 and 50%....271

Table D.9. Damage detection results for case CANT I, implicit redundant representation (IRR), seeded initial population, objective function is the sum of GSC and GAC squares, noise levels of 0, 5 and 10%....272

Table D.10. Damage detection results for case CANT I, implicit redundant representation (IRR), seeded initial population, objective function is the sum of GSC and GAC squares, noise levels of 20 and 50%....272

Table D.11. Damage detection results for case CANT I, implicit redundant representation (IRR), unseeded initial population, objective function is the sum of GSC and GAC squares, noise levels of 0, 5 and 10%....272

Table D.12. Damage detection results for case CANT I, implicit redundant representation (IRR), unseeded initial population, objective function is the sum of GSC and GAC squares, noise levels of 20 and 50%....273

Table D.13. Damage detection results for case CANT II, fixed and implicit redundant representations (IRR), noise free measurements....273

Page

Table D.14. Damage detection results for case CANT III, fixed and implicit redundant representations (IRR), noise free measurements.....273

Table D.15. Damage detection results for case CANT IV, fixed and implicit redundant representations (IRR), noise free measurements.....274

Table D.16. Damage detection results for case CANT OPT, fixed representation, seeded initial population, noise levels of 0, 10 and 20% 275

Table D.17. Damage detection results for case CANT OPT, implicit redundant representation (IRR), seeded initial population, noise levels of 0, 10 and 20%.....275

Table D.18. Damage detection results for case CANT OPT, implicit redundant representation (IRR), unseeded initial population, noise levels of 0, 10 and 20%.....275

Table D.19. Damage detection results for case TWSP IA, fixed and implicit redundant representations (IRR), noise free measurements.....276

Table D.20. Damage detection results for case TWSP IB, fixed and implicit redundant representations (IRR), noise free measurements.....277

Table D.21. Damage detection results for case TWSP II, fixed and implicit redundant representations (IRR), noise free measurements.....278

Table D.22. Damage detection results for case TWSP IIIA, fixed representation, seeded initial population, noise levels of 0, 5 and 10% 278

Table D.23. Damage detection results for case TWSP IIIA, fixed representation, seeded initial population, noise levels of 20 and 30% 279

Table D.24. Damage detection results for case TWSP IIIA, implicit redundant representation (IRR), seeded initial population, noise levels of 0, 5 and 10%.....280

Table D.25. Damage detection results for case TWSP IIIA, implicit redundant representation (IRR), seeded initial population, noise levels of 20 and 30% 281

Table D.26. Damage detection results for case TWSP IIIA, implicit redundant representation (IRR), unseeded initial population, noise levels of 0, 5 and 10%.....281

Page

Table D.27. Damage detection results for case TWSP IIIA, implicit redundant representation (IRR), unseeded initial population, noise levels of 20 and 30%.....281

Table D.28. Damage detection results for case TWSP IIIB, fixed and implicit redundant representations (IRR), noise free measurements.....282

Table D.29. Damage detection results for case TWSP IIIB, fixed representation, seeded initial population, objective function is the sum of GSC and GAC squares, noise levels of 0, 5 and 10% 282

Table D.30. Damage detection results for case TWSP IIIB, fixed representation, seeded initial population, objective function is the sum of GSC and GAC squares, noise levels of 20 and 30% 283

Table D.31. Damage detection results for case TWSP IIIB, implicit redundant representation (IRR), seeded initial population, objective function is the sum of GSC and GAC squares, noise levels of 0, 5 and 10%.....284

Table D.32. Damage detection results for case TWSP IIIB, implicit redundant representation (IRR), seeded initial population, objective function is the sum of GSC and GAC squares, noise levels of 20 and 30%.....285

Table D.33. Damage detection results for case TWSP IIIB, implicit redundant representation (IRR), unseeded initial population, objective function is the sum of GSC and GAC squares, noise levels of 0, 5 and 10% 285

Table D.34. Damage detection results for case TWSP IIIB, implicit redundant representation (IRR), unseeded initial population, objective function is the sum of GSC and GAC squares, noise levels of 20 and 30% 286

Table D.35. Damage detection results for case TWSP OPT, fixed representation, seeded initial population, noise levels of 0, 5 and 10% 286

Table D.36. Damage detection results for case TWSP OPT, fixed representation, seeded initial population, noise levels of 20 and 30% 287

Table D.37. Damage detection results for case TWSP OPT, implicit redundant representation (IRR), seeded initial population, noise levels of 0, 5 and 10%.....288

Table D.38. Damage detection results for case TWSP OPT, implicit redundant representation (IRR), seeded initial population, noise levels of 20 and 30% 288

Page

Table D.39. Damage detection results for case TWSP OPT, implicit redundant representation (IRR), unseeded initial population, noise levels of 0, 5 and 10%.....288

Table D.40. Damage detection results for case TWSP OPT, implicit redundant representation (IRR), unseeded initial population, noise levels of 20 and 30%.....289

Table D.41. Damage detection results of trials 1, 2, 3 and 5 for the braced frame problem BRFRM I 290

Table D.42. Damage detection results of trials 4, 7, 8 and 10 for the braced frame problem BRFRM I 290

Table D.43. Damage detection results of trials 6, 9, 11 and 12 for the braced frame problem BRFRM I 292

Table D.44. Damage detection results of trials 13, 15, 16 and 17 for the braced frame problem BRFRM I 292

Table D.45. Damage detection results of trials 14, 19, 21, 23, 24 for the braced frame problem BRFRM I 293

Table D.46. Damage detection results of trials 18, 20, 22, and 25 for the braced frame problem BRFRM I 294

Table D.47. Results of 25 initial trials arranged in trial pairs by mutation rate.....295

Table D.48. Results of 25 initial trials arranged in trial pairs by primary crossover rate.....296

Table D.49. Results of 25 preliminary trials arranged by population size.....297

Table D.50. Damage detection results of trials 28, 29, 30, and 31 for the braced frame problem BRFRM II including 5% measurement noise 298

Table D.51. Damage detection results for case UBFRM I, implicit redundant representation (IRR), seeded initial population, noise levels of 0, 5 and 10%.....299

Table D.52. Damage detection results for case UBFRM I, implicit redundant representation (IRR), unseeded initial population, noise levels of 0, 5 and 10%.....299

Page

Table D.53. Damage detection results for case UBFRM II, implicit redundant representation (IRR), seeded initial population, noise levels of 0, 5 and 10%.....300

Table D.54. Damage detection results for case UBFRM II, implicit redundant representation (IRR), unseeded initial population, noise levels of 0, 5 and 10%.....300

Table D.55. Damage detection results of trials 1(a) and 1(b) for the unbraced frame problem UBFRM III.....301

Table D.56. Damage detection results of trials 2(a) and 2(b) for the unbraced frame problem UBFRM III.....301

Table D.57. Damage detection results of trials 3, 4 and 5(a) for the unbraced frame problem UBFRM IV.....302

Table D.58. Damage detection results of trials 5(b), 6 and 7 for the unbraced frame problem UBFRM IV.....302

Table D.59. Damage detection results of trials 8, 9 and 10 for the unbraced frame problem UBFRM IV.....303

Table D.60. Damage detection results of trial 11 for the unbraced frame problem UBFRM IV.....304

Table D.61. Plate girder damage detection results for cases KSTSP I, II and III, fixed representation, seeded initial population, noise free measurements.....304

Table D.62. Plate girder damage detection results for cases KSTSP IV, V and VI, fixed representation, seeded initial population, noise free measurements.....306

Table D.63. Plate girder damage detection results for cases KSTSP VII and VIII, fixed representation, seeded initial population, noise free measurements.....307

Table D.64. Plate girder damage detection results for cases KSTSP IX and X, fixed representation, seeded initial population, noise free measurements.....309

Page

Table D.65. Plate girder damage detection results for cases KSTSP I, II and III, implicit redundant representation (IRR), seeded initial population, noise free measurements 311

Table D.66. Plate girder damage detection results for cases KSTSP IV, V and VI, implicit redundant representation (IRR), seeded initial population, noise free measurements 311

Table D.67. Plate girder damage detection results for cases KSTSP VII and VIII, implicit redundant representation (IRR), seeded initial population, noise free measurements 311

Table D.68. Plate girder damage detection results for cases KSTSP IX and X, implicit redundant representation (IRR), seeded initial population, noise free measurements 312

Table D.69. Plate girder damage detection results for cases KSTSP I, II and III, implicit redundant representation (IRR), unseeded initial population, noise free measurements 312

Table D.70. Plate girder damage detection results for cases KSTSP IV, V and VI, implicit redundant representation (IRR), unseeded initial population, noise free measurements 313

Table D.71. Plate girder damage detection results for cases KSTSP VII and VIII, implicit redundant representation (IRR), unseeded initial population, noise free measurements 313

Table D.72. Plate girder damage detection results for cases KSTSP IX and X, implicit redundant representation (IRR), unseeded initial population, noise free measurements 314

Table D.73. Plate girder damage detection results for cases KSTSP I, II and III, implicit redundant representation (IRR), seeded initial population, 5% noise in measurements 314

Table D.74. Plate girder damage detection results for cases KSTSP IV, V and VI, implicit redundant representation (IRR), seeded initial population, 5% noise in measurements 315

Table D.75. Plate girder damage detection results for cases KSTSP VII and VIII, implicit redundant representation (IRR), seeded initial population, 5% noise in measurements 315

Page

Table D.76. Plate girder damage detection results for cases KSTSP IX and X, implicit redundant representation (IRR), seeded initial population, 5% noise in measurements 316

1 INTRODUCTION

1.1 Overview

Engineering as a profession requires practicing engineers to enhance the wealth, comfort, and safety of the general public by providing solutions to challenges that have not yet been solved. These challenges of the 21st century require engineers to develop systems similar to biological organisms that are conscious about the environment and able to adapt accordingly. Technological advances in computer science, miniaturization, material science, and measurement theory enable the collection of a vast amount of information from the environment surrounding us. In biological systems, this information is processed and interpreted by a central processing unit, such as the brain that triggers responses according to the changing environment. Keeping these challenges in mind, one of the ultimate goals of engineering is to design sophisticated systems that are aware of the environment surrounding them, are able to sense changes in this environment and then are able to respond appropriately to any changes.

Diverse areas in engineering that currently are separate will, in the future, need to be intricately linked together to create a complex system that is capable of autonomous decision making. In civil engineering, for instance, distinct areas of research in structural control, system identification, damage detection, and sensor optimization currently exist. All the above-mentioned research areas, however, share some common characteristics. These procedures rely on information collected from the structure and in general may include any response caused by the changing environment (change in temperature, displacement, velocity, acceleration, strains, stresses, curvatures, etc.). Using the collected information an inverse problem is formulated for the specific task and by solving the inverse problem system parameters are obtained or system input is generated. The difficulty in solving inverse problems is that only some incomplete discrete set of data is available representing some continuous domain. Solving an inverse problem using

---

This dissertation follows the style and format of the *Journal of Structural Engineering*, ASCE.

limited information leads to uniqueness problems of that solution, i.e. several solutions can be found satisfying the inverse problem formulation. Noise in measurement data further intensifies the complexity of inverse problems. To tackle these types of problems, available data must be extended or curtailed (noise filtering) to convert the ill-posed inverse problem into well-structured domain that can be solved with some deterministic tools. Alternatively, optimization approaches can be used to avoid the contamination of measurements, which results in multiple local optima of the objective and non-uniqueness problems. Robust optimization or other pattern recognition algorithms that are able to solve inverse problems posed may be found to have algorithms development feature that are to the common areas of structural control, system identification, damage detection and sensor optimization.

In the future, smart structures will have the ability to adapt to better fit the continuously changing environment by changing system parameters (e.g. healing) based on the information collected. Accomplishing this goal requires identifying different tasks in a modular fashion, with a central processing unit linking the modules together. The modules, however, are typically interconnected, which complicates their design. In a smart structure these modules must operate together. For example, if the damage detection module signals the occurrence of damage, then the system identification module must adjust the overall system parameters, while the control unit adjusts the structural response and the sensor optimization unit identifies measurement locations that are more beneficial in the changing environment. Feedback must also be provided considering the changes made by the individual modules to the system in order to provide continuous stimuli flow similar to human neurological systems.

In particular, structural damage identification methods (SDIM) have several roles to play over the life-cycle of a structure. Serving as part of an automated continuous monitoring system for structures, SDIMs would enable the early detection of structural disintegration, and provide more accurate and efficient scheduling of regular maintenance and repair actions. SDIMs can also work to assess damage following the occurrence of natural hazards, such as earthquakes, hurricanes, and tornadoes. Using the information provided by SDIMs, more accurate assessments can be made concerning property

damage losses and the current level of safety and reliability provided by the structure. In addition, the necessary actions for rehabilitation, or in certain cases demolition, can be made. In recent years, significant research has been focused on developing reliable, yet cost effective, SDIMs that allow engineers to accurately assess the condition of structures. These SDIMs are beneficial in reducing maintenance, rehabilitation, equipment, and professional labor costs.

1.2 Research Objectives

This thesis research develops a SDIM that is robust and efficient and that requires only minimal measurement information to precisely locate and quantify the severity of damage in structures. The SDIM exploits the inherent information contained in frequency response functions (FRF) using advanced methods in engineering dynamics and soft computing methods. The SDIM methodology developed can be used to identify damage that occurs after severe events, such as earthquakes or hurricanes. The performance of SDIM is evaluated using simulated case studies that range from beam type structures having single and multiple damages to "large" plane frame structures.

The important effect of the level of noise in the measurement data on the accuracy and robustness of the proposed SDIM is also investigated. The performance of the SDIM in a noisy environment is evaluated using the same defined case study simulations, but examining different noise levels. To provide a rigorous evaluation of the performance of the SDIM, an objective comparison to existing procedures that are based on modal information is made. In addition, new accuracy measures are developed, which are based on Euclidean geometry, that are more consistent in assessing the accuracy and robustness of damage localization and severity estimation provided by different SDIMs.

To maximize the efficiency and performance of the SDIM developed, a multiobjective optimization approach is defined that optimizes the specific excitation and sensor locations that are used to collect measurement information. Case study simulations are again used to evaluate the effect of optimally placing sensors and excitations. Results obtained from the SDIM using the optimal excitation and sensor placements are compared with results obtained using randomly selected measurement locations.

By accomplishing these objectives, this research will advance the field of damage detection by providing a sophisticated heuristic SDIM that is capable of accurately predicting the location and severity of damage in structures using a minimal amount of measurement information.

1.3 Scope

The SDIM developed in this research assumes that damage affects the stiffness of structural members. Damage types that may change the stiffness properties of structural members include the loss of cross-sectional area due to corrosion or chemical degradation, material softening due to cyclic loading, loss of structural members, and loosening of bolted structural connections. The SDIM developed also requires that the global structural response remains linear after damage has occurred, since the proposed SDIM relies on a linear model of the structure. This requirement, however, does not imply that localized non-linear actions cannot be present in the structure (e.g. in joints). As with any SDIM that uses the inherent information contained in linear vibration data to detect damages, the SDIM developed only detects damages that influence the global vibration characteristics of the structure. Therefore, undetectable damages may include cracks that remain closed while vibration measurements are taken. Such cracks may occur in compression members (or in the compression fibers of beams), and even if the entire cross-section of the member is cracked, the stiffness in compression is not altered. Therefore linear vibration signatures will not be sensitive to these types of damages. Another type of damage that may not be detected by the SDIM is changes in support conditions because of their nonlinear nature. Overall any type of damages that require some non-linear actions (such as openings of cracks) to take place in order to change the global vibration characteristics of the structure may not be detected by the proposed SDIM.

FRFs are selected as the vibration signature used in this research since they are relatively easy to measure and they provide information over a frequency range instead of at single frequencies. The measured FRF data are used directly in the SDIM, and

therefore do not require any pre- or postprocessing that may result in the contamination or loss of crucial information.

For the FRF-based SDIM, it is assumed that an analytical model of the intact structure is available before the SDIM is applied. A linear finite element model of the intact structure is used as the baseline model for the SDIM. To detect damage, the stiffness parameters of the intact model are updated until the analytically computed FRFs match the corresponding measured FRFs.

The proposed SDIM defines an optimization procedure to minimize the error function between the measured FRFs and the analytically computed FRFs. The solution to the optimization problem is a set of damage indicators that uniquely identify both the location and severity of member damage. By assuming a proportionally damped linear system, the modal decomposition of FRF matrices increases the computational efficiency of performing the iterative calculations common to heuristic optimization algorithms.

Genetic algorithms (GA) are used to solve the optimization problem defined for the SDIM, in this research. Two distinct GA representations are considered. The simple genetic algorithm (SGA) optimizes a structured problem formulation domain of the SDIM. The implicit redundant representation (IRR) GA takes advantage of the true unstructured nature of damage detection and optimizes an unstructured problem formulation. Reducing the size of the search space without having to use subjective assumptions provides significant benefits to the optimization procedure and results in an effective and robust approach for relatively large problems. A good set of GA parameters is established on the basis of trial case study results. Currently the proposed SDIM is not applicable for real-time monitoring applications because of the iterative, and therefore time consuming, calculations required.

Several case studies are designed to evaluate the performance of the SDIM developed. Simulated measurement data are obtained for each case study by modifying the stiffness properties of members in the analytical model. The cases investigated become more complex as the number of elements in the finite element model increases and the number of damaged elements increases. The first set of case studies defines a simple cantilever beam with single damage cases and varying excitation and sensor

locations. The second set of case studies defines a two-span continuous beam with multiple damages at various locations. To further verify robustness of the SDIM developed, a two-story, three-bay braced frame and a three-story, three-bay unbraced plane-frame structure are also investigated. For the frame structure case studies, several single and multiple damage cases are investigated.

In order to study the effect of noise on performance, noise is introduced to the measurement data in a commonly accepted way using a Gaussian random noise generator. For all case studies, a series of measurement noise levels are introduced. All results are compared with noise-free results obtained for the same case studies. Objective comparison of the proposed SDIM results is performed using the same plate girder model used by Kim and Stubbs (2002) to test their modal-based damage index SDIMs. Error measures based on Euclidean geometry are introduced to assist in quantifying the accuracy of SDIMs. The measures defined account for both the location and severity accuracy of the predicted damage.

A multiobjective optimization methodology is developed to evolve a Pareto-optimal set of excitation and sensor layouts specifically to improve the performance of the proposed SDIM. The information measure defined for measurements is based on the FRF sensitivity with respect to the damage indicators that are the independent variables of optimization in the SDIM. The Pareto-front set of solutions enables the selection of layout alternatives based on the judgment of the designer. A multiobjective GA (MOGA) is defined that generates Pareto-optimal fronts for each of the case studies defined. Both SGA and IRR representations are evaluated to determine the effect on the performance of the MOGA. The optimal sensor configurations can then be used to collect measurement data for each case study investigated in order to evaluate the benefit that using optimal excitation and sensor placements has on the performance of the SDIM in detecting both single and multiple damages.

1.4 Background and Literature Review

1.4.1 Relevant and On-going Research in Damage Detection

1.4.1.1 General Concepts

Overloading, corrosion, material aging, or other unexpected events, are inevitable over the life-cycle of most structures. Unfortunately these acts result in the deterioration of structures with time. The goal of SDIMs performing in this environment is to assess accurately the current condition of a structure, which facilitates decision-making related to rehabilitation and maintenance of the structure. Accurate damage assessment can significantly reduce life-cycle cost, while increasing performance and possibly lengthening the service-life.

Rytter (1993) classified SDIMs into four levels.

Level 1. (DETECTION) The method gives qualitative information about the existence of damage in the structure.

Level 2. (LOCALIZATION) The method gives information about the probable damage locations.

Level 3. (ASSESSMENT) The method gives an estimate of the severity of damages.

Level 4. (PREDICTION) The method gives information about the impact of damage on the structure, e.g. estimates the remaining life.

Pioneering research in the field of damage detection started in the 1970s with the realization that mere visual inspection of fatigue prone structures was not sufficient to maintain the reliability of aircraft structures and steel bridges (Liu and Yao 1978). In early research, damage was found to change the dynamic stiffness of structures and natural frequency measurements could be used to detect damage using a finite element model of structures, (Cawley and Adams 1979). A review of early system identification methods using natural frequencies and modal information is given by Hart and Yao (1977). Chondros and Dimarogonas (1980) investigated the influence of crack depth on the natural frequency ratios obtained for welded beam structures using a one-dimensional

frequency equation for transverse vibrations. Other researches have investigated minimizing a Bayesian inference function using a modified Newton-Raphson algorithm to obtain a better correlation between the measured and analytical natural frequencies and mode shapes (Béliveau and Chater 1982). In addition to using modal data, Kabe (1985) used structural connectivity information to optimally adjust the stiffness matrices of structures. The optimization problem was developed using Lagrange multiplier constrained minimization theory. Frequency response functions (FRF) were used by Springer et al. (1988) to determine the natural frequencies of a longitudinally vibrating beam. The beam model consisted of two undamaged elements connected by a short element representing the damage. Hajela and Soeiro (1990) proposed a SDIM based on system identification, in which an error function is minimized between measured and predicted responses, including static deflections and vibration modes. A comprehensive literature review of existing model parameter updating methods is provided by Natke (1988), and Mottershead and Friswell (1993), in which the use of FRF data in parameter updating, as well as other procedures, is investigated.

1.4.1.2 Modal Methods

In the last decade, the majority of research has focused on SDIMs that use modal information. Pandey and Biswas (1994) used several lower frequency modes of vibration to estimate the flexibility matrix of structures. The changes in the flexibility matrices were used to locate damage. A two-stage SDIM was developed by Hamamoto and Kondo (1994). The damage detection problem is divided into global damage detection at the system level and local damage detection at the element level. Another two-stage SDIM that used modal information was developed by Kim and Bartkowicz (2001) to investigate a hexagonal experimental truss. On the global level, the modal properties of the structure are identified. If the global damage is determined to be significant, then the damage detection of structural elements is carried out to localize and quantify damage. Inverse sensitivity equations were used by Fritzen et al. (1998) for damage detection. These equations can be based on any vibration data, including modal information, FRFs, time series, or a combination of these. Using measured natural frequencies and mode shapes,

Abdalla et al. (1998) formulated the damage detection problem as a feasibility problem in order to find the damaged stiffness matrix of the structure. The feasibility problem was solved using an alternating projection method to best satisfy the problem constraints. Doebling et al. (1997) investigated the selection of mode shapes that maximize the accuracy of damage detection. They found that mode shapes storing the highest strain energy in the damaged structural configuration provided the most information for damage detection. These mode shapes can be selected based on modal assurance criterion (MAC). Capecchi and Vestroni (1999) proposed an algorithm that only uses the natural frequencies. Their approach also accounts for the unstructured nature of damage detection in the definition of objective function for optimization. The use of natural frequency information only, however, poses a limitation to the applicability of this method. An approach for using noisy and incomplete modal data was proposed by Law et al. (1998). Other approaches include reducing the analytical model by introducing super-elements representing a portion of a large structure (Law et al. 2001). The sub-elements can be evaluated for damage using modal information. Waldron et al. (2002) used operational deflection shapes (ODS), which are the actual vibration displacement or velocity patterns of the vibrating structure. Discontinuities of the ODSs or their derivates indicated the existence of damage, but the quantification of damage severity could not be inferred. Alvin and Park (1999) used modal information to extract substructural flexibility information from global measurements. Jones and Turcotte (2002) found that including the information contained in antiresonant frequencies, in addition to the natural frequencies, enhanced the accuracy of model updating. Palacz and Krawczuk (2002) investigated the sensitivity of different damage indicators for changes in vibration signatures caused by damage. The measures investigated were the Cawley-Adams criterion, damage location assurance criterion (DLAC), modal assurance criterion (MAC), coordinate modal assurance criterion (COMAC), and frequency response curvature method (FRCM). A family of SDIMs using modal information became known as the damage index methods. These methods were developed by Kim and Stubbs (1995), Stubbs and Kim (1996), and Kim and Stubbs (2002). Damage index methods are reviewed in greater detail in Section 1.5.

1.4.1.3 FRF Methods

In this research, a FRF-based SDIM is developed. The advantages of using FRF data instead of modal parameter data are that FRF data can be measured directly on structures without any intermediate steps and that FRF data provide information over a frequency range instead of only at specific frequencies. Several researchers have used FRF information for system identification and damage detection. A method for identifying joint properties of structures from measured FRF data was proposed by Ran and Beards (1995). A set of over-determined equations for the dynamic stiffness matrices of joints between substructures were solved in a least square sense to obtain the joint parameters. Wang et al. (1997) used measured FRF data obtained before and after damage to develop an algorithm based on nonlinear perturbation equations. To reduce the influence of errors, the perturbation equations were weighted at selected locations and frequencies. An iterative modification of the procedure was proposed to overcome difficulties associated with incomplete measurement data. An FRF-based SDIM for beam structures was introduced by Lee and Shin (2002) using the dynamic equation motion for the intact and damaged beams in the continuous domain. The damages throughout the beam were described by a damage distribution function, which was assumed to be a piecewise uniform function with non-zero values at the damage locations. A reduced domain strategy was also developed which eliminated regions of possibly undamaged areas from the solution domain using an iterative technique. Thyagarajan et al. (1998) investigated the possibility of optimization based on FRF measurements to localize damages in a finite element model of a structure. The proposed optimization problem was solved using a gradient-based optimization subroutine contained in MATLAB (1999a) optimization toolbox. This study stated that a more robust optimization algorithm is desired for noisy measurements and a technique that is able to reduce the optimization domain by eliminating possibly undamaged elements would be beneficial for larger problems. Marwala and Heyns (1998) used a combination of objective functions that used FRF and modal information to minimize an error function using the MATLAB (1999a) optimization toolbox.

1.4.1.4 Other Methods

Changes in substructural flexibilities were used in procedures proposed by Park et al. (1997) and Park and Reich (1999). Reich and Park (2000) investigated the impact of damage on the substructural transmission zeros characterizing substructural FRFs. The invariance property of transmission zeros can be used to identify damage when the system response characteristics are changed without a corresponding change in the transmission zeros. Strain and displacement measurements were used by Reich and Park (2001) for system identification of translational and rotational degrees of freedoms. Worden et al. (2000) applied statistical outlier analysis, which relies on the concept of discordancy so that the method signals deviations from normal condition. Several researchers have developed system identification techniques using different measurement information (Hoshiya and Saito 1984 used an extended Kalman filter, Ghanem and Shinozuka 1995 and Shinozuka and Ghanem 1995 used earthquake acceleration records, Kobayashi et al. 1997 used forced vibration information, Quek et al. 1999 used ambient vibrations, Takewaki and Nakamura 2000 used limited earthquake records).

In recent years, artificial intelligence and machine learning techniques have been applied to damage detection. Neural networks (NN) are learning algorithms that are capable of recognizing patterns between input and output after suitable training operations (Haykin 1999). NNs have been successfully used for damage detection in several studies. Yun and Bahng (2000) used a back-propagation NN approach to localize damages by using natural frequencies and mode shapes as input to the NN. Damage identification was carried out on a substructure to reduce the number of unknowns. In another study, Yun et al. (2001) used the same back-propagation NN and substructuring technique to identify damage of connections modeled as rotational springs. A committee of NNs was employed by Marwala (2000) to detect damages in a steel, seam-welded cylindrical shell. The committee of NNs was simply a combination of several NNs that used different input information in such a way that the overall output was a weighted average of the output of each NN. In this study, three inputs FRFs, modal data, and

wavelet transform were used. Other researchers have used fuzzy logic and obtained remarkable results even at high noise levels (Sawyer and Rao 2000).

Genetic algorithms (GA) have received significant attention in recent years and have been applied successfully to a variety of optimization problems. Pioneering research in the topic was done by Holland (1975) and Goldberg (1989). GAs mimic nature's evolutionary mechanism and Darwin's "survival of the fittest" theory (Michalewicz 1996). GAs have been applied to a variety of damage detection problems including crack detection in composite materials based on Lamb waves (Xu et al. 2002). To improve the performance of SGAs, Xu et al. (2002) employed a restarting strategy together with a hybrid approach in which the global search capabilities of GAs are combined with local search algorithms. The resulting GA was called the projection GA (pGA). A common feature of all GA-based SDIMs is that they employ an error function between the measured data and the discrete analytical model. Mares and Surace (1996) used GAs to maximize an objective function based on the residual force method, which is computed from measured natural frequencies and mode shapes. Dunn (1998) studied the performance of GAs and stochastic hillclimbing on a finite element model identification problem in which the error function between the measures and analytical FRFs was minimized. Krawczuk (2002) employed a simple genetic algorithm (SGA) to find damages using spectral beam finite elements for wave propagation. The finite element consisted of a dimensionless spring modeling a single non-propagating crack. The goal of the optimization was to find the location and extent of the crack by maximizing a correlation type objective function between the measured and analytical information. The implicit redundant representation (IRR) of genes (Raich and Ghaboussi 1997a), which allows the dynamic change or evolution of optimization variables, was applied by Chou and Ghaboussi (2001). In their approach, however, static equilibrium equations were used instead of vibration data to set up the optimization problem. Moslem and Nafaspour (2002) considered the unstructured nature inherent in damage detection problems by applying a two-stage identification procedure in which areas with possible damage are first identified and then only elements of that area are included in the optimization domain. Chiang and Lai (1999) used a simulated evolution algorithm, in which the

continuous parameters were not encoded into genes and a random Gaussian mutation operator was used without crossover. Another study that used a real coded GA was presented by Hao and Xia (2002) in which the error function was based on modal information.

1.4.2 Relevant and On-going Research in Near-optimal Sensor Placement

1.4.2.1 General Concepts

A wide variety of engineering tools developed in modern society depend heavily on measurement information, especially in terms of quantity and quality. Applications cover a broad range of engineering disciplines including aerospace, mechanical and civil engineering. Because of the diversity of applications, the information that must be captured in measurements varies significantly. In situations when the desired measurement input is vibration data, vibration transducers, such as force gauges, accelerometers and impedance heads, are the primary source of information (Ewins 2000). In most cases, however, the number of possible sensor locations is much larger than the actual number of sensors used in measurements. Therefore, it is necessary that the limited sensors are placed in a near-optimal way with respect to the application that uses the measurement information as an input.

A survey of actuator and sensor placement problems from a wide range of engineering disciplines was provided by Padula and Kincaid (1999). Although references from different areas were cited, the main focus of the survey was concerned with aerospace vibration control and noise attenuation applications. Several optimization procedures were discussed, including manual optimization techniques, intuitive recipes, and combinatorial and continuous algorithms. Among the possible combinatorial optimization techniques, several applications used simulated annealing (SA), tabu search (TS), and genetic algorithms (GA). Three aerospace application areas for sensor and actuator placement optimization were identified: active structural acoustic control (ASAC), where actuators attached to the aircraft fuselage are used to control (reduce) noise in the passenger compartment; optimum sensor placement for system identification

and control of aeroelastic structures; and smart technologies to provide three-axis control in an aircraft wing. The objective for ASAC problems was to determine the control forces and locations of the actuators, which minimizes the noise levels at each microphone.

For the placement of sensors for system identification, in most cases the optimization problem is established by assuming a finite element model of the structure. Using the finite element model, a matrix, $\mathbf{X}^a$, of the n most important vibration modes at m potential sensor locations is formed. The task is to select a subset of k sensor locations and to form the reduced mode shape matrix, $\mathbf{X}$, by selecting corresponding rows from $\mathbf{X}^a$. The best subset is identified as the one that maximizes the Fisher information matrix $\mathbf{X}^T\mathbf{X}$. This problem can be solved using any combinatorial optimization algorithm.

Gawronski (1997) targeted two types of actuator and sensor placement problems. The first one related to structural testing, in which the dynamic environment cannot be duplicated during testing. In this case in order to obtain the performance of the test configuration close to the performance of the structure in the real environment, the potential actuator and sensor locations are selected to imitate the real-world environment. In a control design problem, actuators and sensors are placed at available locations related to disturbance and performance evaluation locations, respectively. The procedure employs the controllability and observability grammians defined for a modal state space representation of a flexible structure, which are used to obtain the Hankel singular value as a geometric mean of the two grammians. Reynier and Kandil (1999) also used observability requirements for sensor optimization based on the observability grammians. In their study, the sensor locations obtained were compared with a technique that minimizes the noise effect in modal identification by finding modal parameters in a least square sense.

A study focusing on the modal identification of mechanical systems was provided by Shih and Lee (1998). The method was based on modified controllability and observability measures with physical representations on FRF plots. Several criteria based on the above measures were compared. The selection of optimal sensor locations employed a ranking procedure based on the effectiveness of sensors evaluated at different locations.

Multiobjective optimization for structural control was investigated by Brown et al. (1999). The research goal was to identify Pareto optimal solutions of control design such that the regulated outputs (control force, displacement, velocity or acceleration) were minimized while satisfying design constraints. Pareto fronts were compared to determine the preferred locations for actuators and sensors for a given loading situation. To solve the multiobjective optimization, a modified multiobjective linear quadratic Gaussian (LQG) technique was employed. Pareto optimal trade-off curves for an example shear-building model were compared to determine the minimum amount of control force while satisfying structural response requirements (floor displacement or acceleration). The benefit of using Pareto optimal solutions was that the designer could compare the potential actuator and sensor locations based on trade-off curves, which show the relation between contradicting objectives.

Other research has focused on evaluating vibration control strategies using optimal actuator and sensor locations. Bruant et al. (1999) investigated the optimum configuration of piezoelectric actuator and sensor placement on beam structures to increase control efficiency (i.e. to suppress unwanted vibrations as quickly as possible). Other researches (Hanagan et al. 2000) used different measures for vibration control to optimize the actuator and sensor locations, including expressing the dissipation energy of the system due to control action in a quadratic performance index (PI) using the output feedback.

1.4.2.2 Sensor Placement for Modal Based Damage Detection

The optimum sensor placement methodology proposed by Shi et al. (2000) focused on the ability to improve measurement information specifically defined for a SDIM that used modal information. Assumptions for structural damage detection included that only structural stiffness changes were present and the mass and damping properties were not affected by damage. It was further assumed that the stiffness changes were small enough not to disturb structural connectivity. For a small perturbation in stiffness, the eigenvalue problem for a *n*-DOF dynamic system can be written.

$$\left[\left(\mathbf{K}+\Delta\mathbf{K}\right)-\left(\lambda_i+\Delta\lambda_i\right)\mathbf{M}\right]\left(\boldsymbol{\varphi}_i+\Delta\boldsymbol{\varphi}_i\right)=0 \tag{1.1}$$

where **K** and **M** are structural stiffness and mass matrices, respectively; λ_i and $\boldsymbol{\varphi}_i$ are the i^{th} eigenvalue and mode shape, respectively; and the symbol Δ indicates small perturbations in the corresponding quantities. Assuming that the perturbation of the i^{th} mode shape, $\Delta\boldsymbol{\varphi}_i$, is a linear combination of the mode shapes and using orthogonality relationships the following expression can be obtained.

$$\Delta\boldsymbol{\varphi}_i=\sum_{\substack{r=1\\ r\neq i}}^{n}\frac{-\boldsymbol{\varphi}_r^T\Delta\mathbf{K}\boldsymbol{\varphi}_i}{\lambda_r-\lambda_i}\boldsymbol{\varphi}_r \tag{1.2}$$

Shi et al. (2000) assumed that the reduction in structural stiffness could be obtained as the summation (assembly) of each elemental stiffness matrix multiplied by a damage coefficient.

$$\Delta\mathbf{K}=\sum_{k=1}^{n_e}\alpha_k\mathbf{k}_k \qquad -1\le\alpha_k\le 0 \tag{1.3}$$

where $\mathbf{k}_k$ is the k^{th} elemental stiffness matrix, α_k is the k^{th} element damage coefficient, and n_e is the number of elements. Using the definition of the i^{th} mode shape perturbation vector and the damage coefficients, the following equation can be written.

$$\Delta\boldsymbol{\varphi}_i=\sum_{k=1}^{n_e}\alpha_k\sum_{\substack{r=1\\ r\neq i}}^{n}\frac{-\boldsymbol{\varphi}_r^T\Delta\mathbf{K}\boldsymbol{\varphi}_i}{\lambda_r-\lambda_i}\boldsymbol{\varphi}_r \tag{1.4}$$

Using the vector notation for the above equation and introducing the **F**(**K**) vector of sensitivity coefficients of the i^{th} mode shape changes and the damage vector, δ**A,** definition Eq. (1.4) can be written.

$$\Delta\boldsymbol{\varphi}_i=\mathbf{F}\left(\mathbf{K}\right)\delta\mathbf{A} \tag{1.5}$$

where

$$\mathbf{F}(\mathbf{K}) = \left(\sum_{\substack{r=1 \\ r\neq i}}^{n} \frac{-\boldsymbol{\varphi}_r^T \Delta \mathbf{k}_1 \boldsymbol{\varphi}_i}{\lambda_r - \lambda_i} \boldsymbol{\varphi}_r \quad \sum_{\substack{r=1 \\ r\neq i}}^{n} \frac{-\boldsymbol{\varphi}_r^T \Delta \mathbf{k}_2 \boldsymbol{\varphi}_i}{\lambda_r - \lambda_i} \boldsymbol{\varphi}_r \quad \cdots \quad \sum_{\substack{r=1 \\ r\neq i}}^{n} \frac{-\boldsymbol{\varphi}_r^T \Delta \mathbf{k}_{n_e} \boldsymbol{\varphi}_i}{\lambda_r - \lambda_i} \boldsymbol{\varphi}_r \right) \tag{1.6}$$

$$\delta \mathbf{A} = \begin{pmatrix} \alpha_1 & \alpha_2 & \cdots & \alpha_{n_e} \end{pmatrix}^T$$

If the mode shapes before and after damage are available than Eq. (1.5) can be solved analytically in a least square sense to give the optimal estimates of the damage coefficient vector.

$$\delta \bar{\mathbf{A}} = \left[\mathbf{F}(\mathbf{K})^T \mathbf{F}(\mathbf{K}) \right]^{-1} \mathbf{F}(\mathbf{K})^T \Delta \boldsymbol{\varphi}_i \tag{1.7}$$

The bracketed term for which the inverse is taken in the above equation is the Fisher information matrix, $\mathbf{A}_0$, which is a summation of the contribution of each DOF or sensor location to the mode shapes of the structure.

$$\mathbf{A}_0 = \mathbf{F}(\mathbf{K})^T \mathbf{F}(\mathbf{K}) \tag{1.8}$$

Each DOF contains some information in the Fisher information matrix, but each has a different contribution. The information contained in the measurements can be formulated as the rank of the following matrix.

$$\mathbf{E} = \mathbf{F}(\mathbf{K}) \left[\mathbf{F}(\mathbf{K})^T \mathbf{F}(\mathbf{K}) \right]^{-1} \mathbf{F}(\mathbf{K})^T \tag{1.9}$$

The diagonal terms of the matrix **E** represent the fractional contribution of each DOF to the rank of E. Therefore DOFs contributing the least information are redundant and can be eliminated from the candidate set of possible sensor locations. The remaining set of DOFs can be considered as the optimum set of sensor locations, which maximizes

the information contained in the Fisher matrix with respect to the specific modal-based SDIM used.

Worden and Burrows (2001) also focused on sensor optimization for damage detection. Several optimization algorithms were compared, including an iterative insertion/deletion technique, genetic algorithms (GA), and simulated annealing (SA). The base line SDIM employed a neural network (NN) with the input parameters of mode shapes and curvatures. The NN was trained for a cantilever plate problem using a 20×20 finite element mesh. The number of measurement points used for training the neural network was 20 out of the 400 available nodal points. The fitness measure used for optimization was defined as the mean square error (MSE) between the desired network responses and those estimated by the network after training. Using the fitness measures, a mixed objective function was defined based on the average and maximum MSE and also on the number of misclassifications for each trained neural network. Sensor configurations providing the lowest ranks with no misclassifications were judged best.

Cobb and Liebst (1997) proposed a method of prioritizing sensor locations for a damage detection method that used measured modal data based on a finite element representation of the structure. The goal was to determine a subset of sensor locations that could capture observable changes in natural frequencies and mode shapes. The perturbation in a partial mode shape, which is called the partial eigenvector sensitivity, was expressed based on the eigenvalue problem using the damage fraction values. Damage fraction for an element was defined as the ratio of the stiffnesses of the element after and before damage. Two properties of the partial eigenvector sensitivity matrices were investigated: detectability and colinearity. Detectability is a measure of the amount of change that occurs from changes in a design variable, whereas colinearity is a measure of the direction of change. Both sensor prioritization and damage localization problems used the same measures (detectability and colinearity) and therefore could be considered as dual problems. In solving these problems, threshold values for the two measures were used to account for uncertainties and modeling errors. This approach resulted in elements in which damage could not be detected from measured data. A subset of collinear

elements in the set of the remaining (detectable) elements is indistinguishable from each other.

1.4.2.3 Other Methods

An application having similar computational challenges to damage detection is structural parameter estimation from measured vibration data. The efficiency of parameter estimation therefore also depends on the quality of measurements information, which suggests the existence of optimal sensor locations specific to this problem. Pothisiri and Hjelmstad (2002) proposed an algorithm for the selection of a near-optimal set of possible sensor locations. Their method minimizes the sensitivity of the parameter estimates with respect to observed response. The structural parameters were estimated from modal information by minimizing a combination of weighted error functions for the measured modes. The goal was to find a subset of sensor locations that provided the least sensitive measurement information for noise. Monte Carlo simulation was also used to generate the mean and covariance estimates needed for the selection algorithm. Random staring points were used in the optimization to locate multiple local solutions to the problem. The optimum set of sensor locations are defined as the set for which the noise sensitivity cannot be significantly reduced.

A review of existing procedures for sensor optimization problems was also provided in the paper by Worden and Burrows (2001). The cited literature mainly used modal information as the base data for optimization concerning control or identification problems. The measures investigated ranged from simple information-based approach, Fisher information matrix, average driving point residue, Guyan model reduction to kinetic energy methods based on observability of modes. All above methods used mode shapes to quantify the quality of measurements based on some intuition that possibly provides the best solution for sensor placement. None of them were specifically concerned with identifying damage.

1.5 Overview of Modal Based Damage Index SDIMs

In this section three specific SDIMs that use modal information are discussed (Kim and Stubbs 1995, Stubbs and Kim 1996, Kim and Stubbs 2002). These SDIMs are widely accepted as baseline techniques in damage detection using modal information.

Assume that a discrete analytical model of the undamaged structure can be modeled with n_e element and n nodes. If the structure is linear, then the i^{th} modal stiffness is obtained from the stiffness matrix of the entire structure and the i^{th} mode shape and the contribution of the j^{th} member to the i^{th} modal stiffness is expressed by

$$\begin{aligned} K_i &= \boldsymbol{\varphi}_i^T \mathbf{K} \boldsymbol{\varphi}_i \\ K_{ij} &= \boldsymbol{\varphi}_i^T \mathbf{K}_j \boldsymbol{\varphi}_i \end{aligned} \tag{1.10}$$

where K_i is the i^{th} modal energy, $\boldsymbol{\varphi}_i$ is the i^{th} mode shape, $\mathbf{K}$ is the structural stiffness matrix, K_{ij} is the contribution of element j to the i^{th} modal energy, and $\mathbf{K}_j$ is contribution of the j^{th} element to the structural stiffness matrix. Consequently, the fraction of modal energy of the i^{th} mode with respect to the j^{th} member can be defined as

$$F_{ij} = \frac{K_{ij}}{K_i} \tag{1.11}$$

It is further assumed that the linear stiffness contribution matrix of element j can be separated into a matrix dependent on only geometrical properties and a scalar that is material specific.

$$\mathbf{K}_j = E_j \mathbf{K}_{j0} \tag{1.12}$$

where the scalar E_j is the material stiffness otherwise known as Young's modulus of the j^{th} element and $\mathbf{K}_{j0}$ is a matrix that only depends on the geometric properties of element j.

1.5.1 Damage Index A

This method was proposed by Kim and Stubbs (1995). This was the original damage index method. If the damaged structure is denoted by a *d* superscript and the assumption is made that the modal sensitivities in the i^{th} mode and j^{th} element are the same for both the undamaged and damaged structure, $F_{ij}^{d} \simeq F_{ij}$, then the following expression holds.

$$\frac{F_{ij}^{d}}{F_{ij}} = \frac{K_{ij}^{d} K_{i}}{K_{ij} K_{i}^{d}} = 1 \tag{1.13}$$

Substituting the definitions of the modal stiffness and the elemental contribution, the damage index of the j^{th} element, β_j, is defined by the expression.

$$\beta_j = \frac{E_j}{E_j^{d}} = \frac{\sum_{i=1}^{n_m} \gamma_{ij}^{d} K_i}{\sum_{i=1}^{n_m} \gamma_{ij} K_i^{d}} \tag{1.14}$$

where $\gamma_{ij} = \boldsymbol{\varphi}_i^{T} \mathbf{K}_{j0} \boldsymbol{\varphi}_i$ and $\gamma_{ij} = \left(\boldsymbol{\varphi}_i^{d}\right)^{T} \mathbf{K}_{j0} \boldsymbol{\varphi}_i^{d}$, n_m is the number of modes, and damage is indicated in element j if $\beta_j > 1$. Assuming that the relationship between the Young's modulus of the damaged and undamaged structures is described by $E_j^{d} = E_j \left(1 + \alpha_j\right)$, the severity estimator, α_j, can be written.

$$\alpha_j = \frac{1}{\beta_j} - 1, \quad \alpha_j \geq -1 \tag{1.15}$$

The severity estimator, α_j, gives the reduction in stiffness of the j^{th} member and can be used to assess damage in structures.

1.5.2 Damage Index B

There is a problem with the definition of the damage index in Eq. (1.14). The equation becomes singular when the denominator is zero, which can happen if the element size approaches zero and its location coincides with a nodal point of a mode. To remove this limitation, the reference axis for the modal sensitivities is shifted by one, $F_{ij} \rightarrow F_{ij} + 1$ and $F_{ij}^d \rightarrow F_{ij}^d + 1$. After some mathematical manipulations using this assumption, the equation for the damage index, β_j, for the j^{th} element can be obtained.

$$\beta_j = \frac{E_j}{E_j^d} = \frac{\sum_{i=1}^{n_m} \left(\gamma_{ij}^d + \sum_{k=1}^{n_e} \gamma_{ik}^d \right) K_i}{\sum_{i=1}^{n_m} \left(\gamma_{ij} + \sum_{k=1}^{n_e} \gamma_{ik} \right) K_i^d} \tag{1.16}$$

where damage is indicated for the j^{th} element if $\beta_j > 1$. The severity estimator is unaltered by the new definition of the damage index and Eq. (1.15) still holds.

The damage index B procedure was used by Worden et al. (1999) in an experimental study involving a stiffened plate. Ho and Ewins (1999) investigated the performance of damage index B algorithm in a noisy environment and in situations when only partial mode shape measurements were available.

1.5.3 Damage Index C

The details of this of this version of the damage index method can be found in Kim and Stubbs (2002). Without presenting a rigorous derivation here, the damage index for n_m vibration modes at the j^{th} location is defined by

$$\beta_j = \frac{E_j}{E_j^d} = \frac{\sum_{i=1}^{n_m} \gamma_{ij}^d}{\sum_{i=1}^{n_m} \left(\gamma_i g_i \left(\lambda, \boldsymbol{\varphi} \right) + \gamma_{ij} \right)} \tag{1.17}$$

where $g_i(\lambda, \boldsymbol{\varphi})$ is a dimensionless factor representing the systematic change in modal parameters of the i^{th} mode due to damage. Again the severity estimator, α_j, is given by Eq. (1.15).

In all of the above damage index procedures, the damage detection model is a mathematical representation of the structure in which the degrees of freedoms (DOF) correspond to actual or interpolated sensor readings. For one dimensional elements, such as Bernoulli beam elements (APPENDIX A) a third order spline, $w(x)$ can be generated from the measured mode shape of the i^{th} modal vector $\boldsymbol{\varphi}_i$. Using the spline approximation of the mode shape, the instantaneous curvature is computed at each node, $\varphi_i''(x) = w''(x)$. The values for γ_{ij}, γ_{ij}^d and γ_i used in the damage index equations are computed using the following integrals.

$$\gamma_{ij} = \int_{x_k}^{x_k+\Delta x_k} \left[\varphi_i''(x)\right]^2 dx, \quad \gamma_{ij}^d = \int_{x_k}^{x_k+\Delta x_k} \left[\varphi_i''^d(x)\right]^2 dx, \quad \gamma_i = \int_0^L \left[\varphi_i''(x)\right]^2 dx \tag{1.18}$$

where x_k and $x_k+\Delta x_k$ are corresponding nodal locations of element j and L is the length of the one dimensional structure.

The authors (Kim and Stubbs, 2002) used statistical criteria for damage localization. For any given set of modes, the damage locations are selected based on a rejection of hypotheses. In this approach, the set of damage indices, β_j (j = 1,2,…,n_e) is treated as a normally distributed random variable representing a sample space. Using statistical properties, the normalized damage indicator is obtained.

$$Z_j = \frac{\beta_j - \bar{\beta}}{\sigma_\beta} - 2 \tag{1.19}$$

where $\bar{\beta}$ and σ_β are the mean and standard deviation of the set of damage indices β_j, respectively. The members are then classified using a statistical pattern recognition that utilizes hypotheses testing. The null hypothesis, H_0, is that the j^{th} member is not

damaged and the alternate hypothesis, H_1, is that the member is damaged. The decision rule is based on the normalized damage index, Z_j, of the j^{th} member: H_0, no damage exists in member j if $Z_j < 0$, or H_1, the j^{th} elements is damaged and $Z_j \geq 0$. This classification procedure can be applied to any of the damage index algorithms. After classification, the severity estimator of the elements in the damaged group is computed, which provides the corresponding reduction in stiffness of that element.

1.6 Overview of Frequency Domain Criteria for SDIMs

When frequency response function measurements are available, correlation measures between the analytical and measured data provide useful information about the quality of a model. These correlation measures can be used to adjust the analytical model to better fit the measured data or to detect damage in structures. An overview of the most commonly used frequency domain criteria was provided by Zang et al. (2001). In addition to reviewing the commonly used correlations, the authors proposed new measures that gave information about the quality of the analytical model on a global level. In general, frequency domain criteria have several advantages over modal measures. There is no error involved due to modal analysis of the measured data. This is particularly beneficial when the modes are closely spaced or high damping exists in the structure. For some application it is necessary to find correlated mode pairs, which can be cumbersome for industrial applications.

The first such frequency domain criterion is called the frequency response assurance criterion (FRAC) (Heylen and Avitabile 1998), which is defined for the j^{th} DOF as.

$$\mathrm{FRAC}_j = \frac{\left|\mathbf{H}_X^*(\omega_i)_j \, \mathbf{H}_A(\omega_i)_j\right|^2}{\left[\mathbf{H}_X^*(\omega_i)_j \, \mathbf{H}_X(\omega_i)_j\right]\left[\mathbf{H}_A^*(\omega_i)_j \, \mathbf{H}_A(\omega_i)_j\right]} \tag{1.20}$$

where $\mathbf{H}_A(\omega_i)_j$ is the predicted or analytical FRF for the j^{th} DOF at successive frequencies ω_i, $\mathbf{H}_X(\omega_i)_j$ is the vector of corresponding FRF measurements and the

superscript, *, indicates complex conjugate transpose. This measure returns a value between zero and unity that indicates zero or perfect correlation, respectively. This measure contains information for a specific excitation and measurement point pair. In the modal domain, a similar measure is the coordinate modal assurance criterion or COMAC (Lieven and Ewins, 1988).

Using the same measurement information, a similar correlation frequency domain function, which is called the frequency amplitude assurance criterion (FAAC), can be defined as

$$\mathrm{FAAC}_j = \frac{2\left|\mathbf{H}_X^*(\omega_i)_j\,\mathbf{H}_A(\omega_i)_j\right|}{\left[\mathbf{H}_X^*(\omega_i)_j\,\mathbf{H}_X(\omega_i)_j\right]+\left[\mathbf{H}_A^*(\omega_i)_j\,\mathbf{H}_A(\omega_i)_j\right]} \tag{1.21}$$

Similar to the FRAC in Eq. (1.20), the FAAC returns a correlation value between zero and unity.

Another correlation measure, which is called the frequency domain assurance criterion (FDAC), has been defined by Pascual et al. (1997).

$$\mathrm{FDAC}(\omega_a,\omega_x) = \frac{\left|\mathbf{H}_X^*(\omega_X)\mathbf{H}_A(\omega_A)\right|^*\left|\mathbf{H}_X^*(\omega_X)\mathbf{H}_A(\omega_A)\right|}{\left[\mathbf{H}_X^*(\omega_X)\mathbf{H}_X(\omega_X)\right]\left[\mathbf{H}_A^*(\omega_A)\mathbf{H}_A(\omega_A)\right]} \tag{1.22}$$

where $\mathbf{H}_A(\omega_A)$ is a vector of predicted or analytical responses at a given frequency ω_A, $\mathbf{H}_X(\omega_X)$ is a vector of measured responses at a given frequency ω_X, and each individual element is associated with a different DOF. The FDAC also returns a correlation value between zero and one. In the modal domain, a similar measure is the modal assurance criterion (MAC), which correlates two operating shape vectors that are measured and computed at a given frequency pair. A modified version of the original FDAC was used by Heylen and Avitabile (1998). The modified measure returns a value between –1 and 1, in which the absolute magnitude of the measure corresponds to the correlation, while the sign gives the phase relation between the measured and analytical FRFs.

$$\mathrm{FDAC}_m(\omega_a,\omega_x)=\mathrm{sign}\left(\mathrm{Re}\left(\mathbf{H}_X^*(\omega_X)\mathbf{H}_A(\omega_A)\right)\right)\sqrt{FDAC(\omega_a,\omega_x)} \tag{1.23}$$

The frequency domain correlation criteria discussed so far are either amplitude based (FRAC and FAAC) or shape based (FDAC). In amplitude-based measures the correlation is defined for a DOF and in shape-based measures the correlation is a function of frequency. Zang et al. (2001) proposed new frequency correlation criteria that combined all DOFs and the amplitude and shape information as a function of frequency. The two functions defined were the global shape criterion (GSC) and the global amplitude criterion (GAC).

$$\mathrm{GSC}(\omega)=\frac{\left|\mathbf{H}_X^*(\omega)\mathbf{H}_A(\omega)\right|^2}{\left[\mathbf{H}_X^*(\omega)\mathbf{H}_X(\omega)\right]\left[\mathbf{H}_A^*(\omega)\mathbf{H}_A(\omega)\right]} \tag{1.24}$$

$$\mathrm{GAC}(\omega)=\frac{2\left|\mathbf{H}_X^*(\omega)\mathbf{H}_A(\omega)\right|}{\left[\mathbf{H}_X^*(\omega)\mathbf{H}_X(\omega)\right]+\left[\mathbf{H}_A^*(\omega)\mathbf{H}_A(\omega)\right]} \tag{1.25}$$

where $\mathbf{H}_A(\omega)$ and $\mathbf{H}_X(\omega)$ are the vectors of analytical and measured responses, respectively at a series of DOFs i, as a function of ω, while the excitation location is fixed at DOF j. From the definition of the GAC, it is easy to formulate an analogue criterion in a local sense defined for a pair of measurement and excitation DOF. The local amplitude criterion (LAC) differs from GAC only in the indexing.

$$LAC_{ij}(\omega)=\frac{2\left|\mathbf{H}_{Xij}^*(\omega)\mathbf{H}_{Aij}(\omega)\right|}{\left[\mathbf{H}_{Xij}^*(\omega)\mathbf{H}_{Xij}(\omega)\right]+\left[\mathbf{H}_{Aij}^*(\omega)\mathbf{H}_{Aij}(\omega)\right]} \tag{1.26}$$

where i and j are the response and excitation DOFs, respectively. For the GSC, an analogous local correlation also can be defined, but it would always be unity for the entire frequency range and therefore would not provide any useful information regarding damage detection. The average LAC or $\overline{LAC}$ can be obtained by averaging the LAC obtained at a series of discrete frequencies over the frequency range.

$$\overline{LAC}_{ij} = \frac{1}{N}\sum_{k=1}^{N} LAC_{ij}\left(\omega_k\right) \tag{1.27}$$

To conclude this section, it should be noted that frequency domain criteria are useful in quantifying the closeness of the analytical and measured responses. These measures can be used for model updating or damage detection to formulate a set of determined (or over determined) simultaneous equations that can be solved for the unknown quantities. They are also suitable for optimization when the goal is to obtain the best correlation between the analytical and measurement data. Zang et al. (2001) point out that the use of GSC and GAC can be particularly useful, because these criteria can quantify the overall correlation between two sets of data (analytical and measured) as a function of frequency and therefore highlighting frequency regions of good or poor correlation.

1.7 Organization of the Dissertation

The remainder of this dissertation is divided into nine sections. Section 2 presents the theory of SDIMs. The definition of FRFs is given and the modal decomposition of FRF matrices is discussed. Statistical measurement theory of FRFs is provided to demonstrate common difficulties in designing the measurement configurations. The objective function of the optimization problem is defined as an error function between the measured and analytical FRFs. In addition, an information measure is defined that allows the quantitative evaluation of the excitation and sensor placement optimization problem. The mathematical formulation of the multiobjective optimization problem for excitation and sensor placement is presented.

Section 3 discusses both traditional and heuristic optimization algorithms. An overview of traditional optimization problem classes and algorithms is provided. GAs are introduced by first discussing the simple genetic algorithm (SGA). Several advanced genetic operators are discussed which enhance the performance of GAs. Two representations are adapted for the proposed SDIM. The fixed representation implements the structured design variable formulation of the optimization problem of damage

detection while the implicit redundant representation (IRR) allows the number of variables to change during optimization. The IRR GA allows an unstructured formulation to be used. A local hillclimbing search technique is presented that fine tunes the solutions obtained by GAs. The mathematical notion of multiobjective optimization is presented and a multiobjective nondominated sorting genetic algorithm (NSGA) is adapted for the excitation and sensor layout design problem.

The implementation details of the SDIM and multiobjective optimization methodologies developed are discussed in Section 4. The hierarchical structure of the computer software is explained and the connections between the program modules are described. A description of the graphical user interface is provided.

Section 5 describes the case study problem simulations for the cantilever beam, two-span continuous beam, moment frame, and plate girder problems (Kim and Stubbs 2002) investigated in this research. The structural and geometrical parameters and finite element mesh of each case study is discussed. Unique designations for all case study trials are defined and the specific damage scenarios investigated by the case studies are summarized in tables identifying the locations and severity of inflicted damages and the excitation and sensor locations used.

Sections 6 through 9 present the SDIM results for the case study simulations. The case studies are discussed in order of increasing complexity. Result for the cantilever beam problem are presented in Section 6. Section 7 present SDIM result for the two-span continuous beam problem including multiple damage cases. Results obtained for larger frame structures are presented in 8. Section 9 provides an objective comparison of the proposed SDIM results with results obtained using the damage index SDIMs by Kim and Stubbs (2002). New accuracy measures, which assess the accuracy of SDIMs are discussed.

In Section 10, a summary of the results is provided along with the significant conclusions made within the scope of this research. In addition, future recommendations and future research extensions are identified and discussed.

2 THEORY OF DAMAGE DETECTION

This section discusses the principles of damage detection. The vibration signature used for detecting damage in this research is derived from the set of dynamic equations of motion. The analytical computation of this signature uses modal decomposition to reduce the computational expenses incurred by using the elementary definition of frequency response functions. A brief introduction into the measurement theory of frequency response functions is provided to demonstrate common difficulties in designing the measurement configuration. In the following sections, the mathematical formulation of damage detection is developed as an optimization problem. The last topic of this section presents the methodology for optimum excitation/sensor layout design, which is used for measuring frequency response functions. An information measure pertaining to the quality of measurements is defined that facilitates the optimization of the combinatorial problem.

2.1 Equations of Motion for Dynamic Systems

Although most vibrating structures cannot be represented as single degree of freedom systems (SDOF) with reasonable accuracy, SDOF systems convey the fundamental concepts of dynamics, including free and forced vibrations, natural frequency, resonance, etc. When the structure is too complex to be represented accurately as a SDOF system, then the concept of multi degree of freedom (MDOF) systems can be introduced. MDOF systems can be specified as two-, three-, or, in general, *n*-dimensional, indicating that the number of independent coordinates required to accurately describe the system is two, three, or *n*. In practice, several different types of MDOF systems are used such as shear building models, mass spring and damper systems, and theses systems use different rules to combine the stiffness and mass properties of structural members. For MDOF systems with only a few degrees of freedom (DOF), D'Alembert's principle, which includes inertia forces, can be used to formulate the equations of motion. The use of this principle, however, is impractical for large structures having more DOFs.

One particular MDOF technique for discretizing systems with infinite DOF is defining a finite element model of the system. The governing finite element equation for dynamic analysis can be derived from the principle of virtual work, which states that the work done by the internal forces equals to the work done by the external forces for any small kinematically admissible displacements. The virtual work expression for a single finite element, including inertia effects (Figure 2.1) and dissipative (damping) forces, can be written as.

$$\iiint_{V_e} \left(\delta \boldsymbol{\varepsilon}^T \boldsymbol{\sigma} + \delta \mathbf{u}_e^T \rho \ddot{\mathbf{u}}_e + \delta \mathbf{u}_e^T \kappa_d \dot{\mathbf{u}}_e \right) dV = \iiint_{V_e} \delta \mathbf{u}_e^T \mathbf{F} dV + \iint_{S_e} \delta \mathbf{u}_e^T \boldsymbol{\Psi} dS + \sum_{j=1}^{n} \delta \mathbf{u}_{e,j}^T \mathbf{p}_j \quad (2.1)$$

where $\boldsymbol{\sigma}$ is the vector of stresses, $\mathbf{u}_e$ is the vector of displacements for the element, $\delta\mathbf{u}_e$ and $\delta\boldsymbol{\varepsilon}$ are the vectors of virtual displacements and corresponding strains respectively, $\mathbf{F}$ is the vector of body forces, $\boldsymbol{\Psi}$ is the vector of prescribed surface tractions on the element surface S_e, $\mathbf{p}_j$ is the vector of concentrated nodal loads at node j, ρ is the mass density of the material, κ_d is a material damping parameter, and volume integration is carried out over the element volume V_e. Dots appearing over quantities indicate time derivatives, where $\ddot{\mathbf{u}}_e$ corresponds with acceleration and $\dot{\mathbf{u}}_e$ with velocity.

The displacement field and its time derivatives, which are a functions of both time and space coordinates are expressed in the following form.

$$\mathbf{u}_e = \mathbf{N}\mathbf{U}, \quad \dot{\mathbf{u}}_e = \mathbf{N}\dot{\mathbf{U}}, \quad \ddot{\mathbf{u}}_e = \mathbf{N}\ddot{\mathbf{U}} \quad (2.2)$$

where $\mathbf{N}$ is a vector or matrix containing the interpolation functions which are functions of space coordinates only, and $\mathbf{U}$ is a vector of nodal degrees of freedom for the element which are functions of time. Combining Eq. (2.2) with the expression of virtual work, Eq. (2.1), yields to the expression of the virtual work for any finite element.

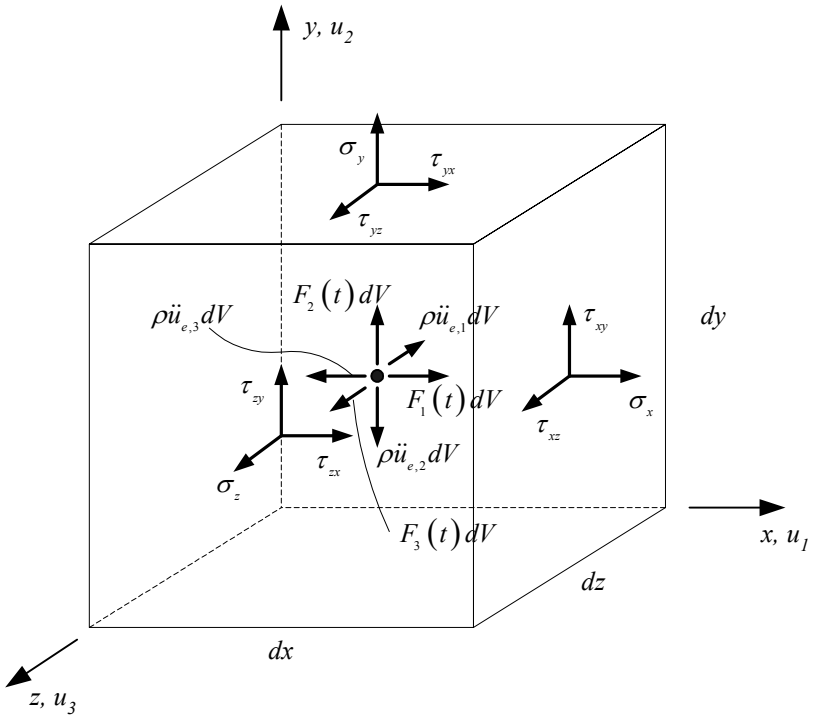

Figure 2.1. Stresses, inertial and applied body forces on an infinitesimal element

$$\delta\mathbf{U}^T\left[\iiint_{V_e}\mathbf{B}^T\boldsymbol{\sigma}dV+\iiint_{V_e}\rho\mathbf{N}^T\mathbf{N}dV\ddot{\mathbf{U}}+\iiint_{V_e}\kappa_d\mathbf{N}^T\mathbf{N}dV\dot{\mathbf{U}}\right]+$$
$$\delta\mathbf{U}^T\left[-\iiint_{V_e}\mathbf{N}^T\mathbf{F}dV-\iint_{S_e}\mathbf{N}^T\boldsymbol{\Psi}dS-\sum_{j=1}^{n}\mathbf{p}_j\right]=0 \qquad (2.3)$$

In the above equation matrix **B** is obtained from compatibility equations, which state that strains can be obtained from displacements by differentiation.

$$\boldsymbol{\varepsilon}=\partial\mathbf{u}_e\,,\qquad \boldsymbol{\varepsilon}=\mathbf{B}\mathbf{U}\,,\qquad \mathbf{B}=\partial\mathbf{N} \qquad (2.4)$$

The differential operator matrix ∂ is obtained from theory of elasticity. Since the expression of the virtual work must be valid for any arbitrary value of $\delta\mathbf{U}$, the dynamic equation of motion for a single finite element can be written as.

$$\mathbf{m}\ddot{\mathbf{U}} + \mathbf{c}\dot{\mathbf{U}} + \mathbf{r}^{\text{int}} = \mathbf{r}^{ext} \tag{2.5}$$

where the element mass and damping matrices are defined as

$$\mathbf{m} = \iiint_{V_e} \rho \mathbf{N}^T \mathbf{N} dV \tag{2.6}$$

$$\mathbf{c} = \iiint_{V_e} \kappa_d \mathbf{N}^T \mathbf{N} dV \tag{2.7}$$

The elemental internal force and external load vectors for the element are defined:

$$\mathbf{r}^{\text{int}} = \iiint_{V_e} \mathbf{B}^T \boldsymbol{\sigma} dV \tag{2.8}$$

$$\mathbf{r}^{ext} = \iiint_{V_e} \mathbf{N}^T \mathbf{F} dV + \iint_{S_e} \mathbf{N}^T \boldsymbol{\Psi} dS + \sum_{j=1}^{n} \mathbf{p}_j \tag{2.9}$$

When the element mass and damping matrices are evaluated using the same interpolation functions **N** as used for the displacement field interpolation, the resulting matrices are called consistent mass and consistent damping matrices. Assembly of these element matrices is identical to that of the element stiffness matrices. Further details may be found in any general finite element book (Cook et al. 2002, Weaver and Johnston 1984).

The internal force vector, Eq. (2.8), is valid for both linear and nonlinear materials and is a general representation of internal forces. For linear elastic materials this equation becomes.

$$\mathbf{r}^{\text{int}} = \mathbf{k}\mathbf{U}, \qquad \mathbf{k} = \iiint_{V_e} \mathbf{B}^T \mathbf{D} \mathbf{B} dV \tag{2.10}$$

where **k** is the element stiffness matrix and **D** is the matrix representing stress-strain relationship for the particular material. After assembling the element mass and

stiffness matrices, the equation of motion for a linear n DOF structure based on Eqs. (2.5) and (2.10) can be stated.

$$\mathbf{M}\ddot{\mathbf{u}} + \mathbf{C}\dot{\mathbf{u}} + \mathbf{K}\mathbf{u} = \mathbf{R}^{ext} \tag{2.11}$$

where $\mathbf{M}$ is the $n \times n$ mass matrix for the whole structure, $\mathbf{C}$ is the $n \times n$ damping matrix, $\mathbf{K}$ is the $n \times n$ stiffness matrix, and $\ddot{\mathbf{u}}$, $\dot{\mathbf{u}}$ and $\mathbf{u}$ are $n \times 1$ vectors of nodal acceleration, velocity and displacement, respectively in the global coordinate system, and $\mathbf{R}^{ext}$ is the time dependent $n \times 1$ vector of externally applied loads. Eq. (2.11) is a system of coupled, second-order ordinary differential equations in time. Dynamic analysis procedures focus on solving this set of differential equations.

In this research, the simple frame element used is obtained by combining a one-dimensional axial element and a one-dimensional Bernoulli cubic beam element. To obtain the stiffness and consistent mass matrices of the frame element for a linear elastic material, Eqs. (2.6) and (2.10) can be used. Derivation of the necessary matrices is detailed in Appendix A. Although Eq. (2.7) defines the element damping matrix, the development of such matrix usually is not done in practice. The reason is that damping is a complex phenomenon that is typically associated with the whole structure rather than individual elements. The problem with formulating a damping matrix on the element level is that damping is influenced not only by material and sectional properties of the element, but also by connection types, micro and macro cracks, plastic behavior, fatigue etc.

2.2 Frequency Response Functions

In Section 2.1 the equation of motion, Eq. (2.11), was derived for a n-DOF system consisting of linearly elastic members. At this point the assumptions about the damping forces are not necessary and a generally accepted damping model will be introduced later to increase the speed of calculations and provide a better physical representation of damping forces. Suppose that an n-DOF system that is described by Eq. (2.11) is investigated. If the system is excited by a set of sinusoidal forces with ω circular

frequency, but with different amplitudes and phases, then the right hand side of Eq. (2.11) can be rewritten (Gatti and Ferrari 1999).

$$\mathbf{M}\ddot{\mathbf{u}} + \mathbf{C}\dot{\mathbf{u}} + \mathbf{K}\mathbf{u} = \mathbf{f}_0 e^{-i\omega t} \tag{2.12}$$

where $\mathbf{f}_0$ is an $n \times 1$ vector of time independent complex amplitudes of excitation, t is the instantaneous time, and e is the natural logarithmic base number.

It is assumed that a solution exists in the from:

$$\mathbf{u} = \mathbf{z}e^{-i\omega t} \tag{2.13}$$

where $\mathbf{z}$ is an $n \times 1$ vector of time independent complex amplitudes of displacement response. Substituting Eq. (2.13) into Eq. (2.12), the formal mathematical solution is obtained:

$$\mathbf{z} = (\mathbf{K} - i\omega\mathbf{C} - \omega^2\mathbf{M})^{-1}\mathbf{f}_0 \equiv \mathbf{R}\mathbf{f}_0 \tag{2.14}$$

where the $n \times n$ receptance matrix $\mathbf{R}$ is defined as a function of ω.

$$\mathbf{R} = \mathbf{R}(\omega) \equiv \left(\mathbf{K} - i\omega\mathbf{C} - \omega^2\mathbf{M}\right)^{-1} \tag{2.15}$$

The jk^{th} member of the receptance matrix represents the displacement response of the j^{th} DOF when the excitation is applied at the k^{th} DOF. The computational expense incurred in obtaining the receptance matrix by means of Eq. (2.15) is prohibitive for iterative methods because for each frequency value, ω, in the domain of interest a large ($n \times n$) complex matrix must be inverted.

Because of the assumption made in Eq. (2.13), a matrix representing displacement responses is obtained. Each entry of this matrix is a function of ω and is also known as a frequency response function (FRF). Consequently the receptance matrix is a type of FRF matrix. In this research only receptance, mobility and accelerance matrices are of concern

but in addition to these matrices there exist several other FRF matrices (dynamic stiffness, apparent mass, mechanical impedance).

Using the assumption presented in Eq. (2.13), the velocity and acceleration responses can be obtained by differentiation.

$$\dot{\mathbf{u}} \equiv \mathbf{v}e^{-i\omega t} = -i\omega\mathbf{z}e^{-i\omega t}$$
$$\ddot{\mathbf{u}} \equiv \mathbf{a}e^{-i\omega t} = -i\omega\mathbf{v}e^{-i\omega t} = -\omega^2\mathbf{z}e^{-i\omega t} \tag{2.16}$$

where $\mathbf{v}$ is an $n \times 1$ vector of time independent complex amplitudes of velocity response, and $\mathbf{a}$ is an $n \times 1$ vector of time independent complex amplitudes of acceleration response. Using the above equation it is not difficult to prove the following relationship between the receptance, mobility, and accelerance matrices.

$$\mathbf{V}(\omega) = -i\omega\mathbf{R}(\omega)$$
$$\mathbf{A}(\omega) = -\omega^2\mathbf{R}(\omega) \tag{2.17}$$

It is widely accepted to denote FRF matrices with the notation of $\mathbf{H}(\omega)$. In this text whenever the notation of the general FRF matrix $\mathbf{H}(\omega)$ is stated the reader can substitute any FRF matrix, namely the receptance $\mathbf{R}(\omega)$, mobility $\mathbf{V}(\omega)$ and accelerance $\mathbf{A}(\omega)$ matrices. The equations derived for damage detection using the general FRF matrix are valid for any of the particular FRF matrices. After one FRF matrix is selected, however, the selection is unique. Let us suppose that the measured FRF data corresponds to acceleration response. In this case, it is natural to use the accelerance in the SDIM. If the choice of preferred FRF matrix is made then the receptance, mobility and accelerance matrices are not interchangeable.

2.2.1 Free Vibration of a Linear System

In Eq. (2.11) the system matrices **M**, **C** and **K** are generally symmetric, but not diagonal. The non-diagonal property of the system matrices results in the coupling of the equations

of motion. When the mass matrix, **M,** is not diagonal the system is said to be inertially, or dynamically coupled, and when **K** is not diagonal there is elastic, stiffness, or static coupling. In practice, the coupling due to the non-diagonal property of the damping matrix, **C,** does not have a specific name, because widely accepted damping models do not have measurable physical meanings in the same sense as **M** and **K** have. With respect to FRF matrices, the coupling effects mean that the inverse of full complex matrices must be taken, which can be extremely ineffective due to computational expense for structures with large number of DOFs.

The coupling of the set of equations of motion is not an intrinsic characteristic of the structural system, but depends on the choice of the coordinate system. The answer to this problem lies in the mathematical science of linear algebra. It is known (without rigorously stating the necessary and sufficient conditions) that for a symmetric matrix with real entries there exists a coordinate system (or basis vectors) in which the matrix is diagonal. The goal now is to find a coordinate system in which both the structural mass and stiffness matrices are diagonal, so that the set of equations of motion are uncoupled. First consider the equation motion of an *n*-DOF system in free vibration without damping.

$$\mathbf{M}\ddot{\mathbf{u}} + \mathbf{K}\mathbf{u} = \mathbf{0} \tag{2.18}$$

Further assuming that the harmonic solution of the above equation exists in the form.

$$\mathbf{u}(t) = \boldsymbol{\varphi} e^{-i\omega t} \tag{2.19}$$

where $\boldsymbol{\varphi}$ is a time independent shape vector, and $\mathbf{0}$ is an $n \times 1$ zero vector. The interpretation of the shape vector, $\boldsymbol{\varphi}$, is while the system moves synchronously its shape does not change with respect to time, but the amplitude of motion does. Substituting Eq. (2.19) into Eq. (2.18) gives

$$\left(\mathbf{K}-\omega^2\mathbf{M}\right)\boldsymbol{\varphi}=\mathbf{0} \tag{2.20}$$

or, written in the generalized form,

$$\mathbf{K}\boldsymbol{\varphi}=\omega^2\mathbf{M}\boldsymbol{\varphi}=\lambda\mathbf{M}\boldsymbol{\varphi} \tag{2.21}$$

Mathematically this equation is referred to as the generalized eigenvalue problem, where λ is an eigenvalue and the corresponding eigenvector is $\boldsymbol{\varphi}$. Eq. (2.21) will have a non-trivial solution if and only if the $\mathbf{K}-\lambda\mathbf{M}$ is singular, or, equivalently, if the determinant of the coefficients vanishes.

$$\det\left(\mathbf{K}-\lambda\mathbf{M}\right)=0 \tag{2.22}$$

where det() indicates matrix determinant. The solution of the generalized eigenvalue problem is not discussed here, but may be found in most linear algebra books. The expansion of the determinant in Eq. (2.22) leads to n algebraic equations, and solutions to these equations (counting multiplicities) represent the eigenvalues of the system. The square roots of the eigenvalues are the systems undamped natural circular frequencies. The n eigenvalues are collected in a diagonal eigenvalue matrix.

$$\boldsymbol{\Lambda}=\begin{pmatrix}\lambda_1 & & 0\\ & \ddots & \\ 0 & & \lambda_n\end{pmatrix}=\begin{pmatrix}\omega_1^2 & & 0\\ & \ddots & \\ 0 & & \omega_n^2\end{pmatrix},\qquad \omega_1\le\omega_2\le\ldots\omega_j\ldots\le\omega_n \tag{2.23}$$

where λ_j is the j^{th} eigenvalue of the system, and ω_j is the j^{th} natural circular frequency of the system. The convention for the natural frequencies is that they are arranged in increasing order, so ω_1 is the lowest and ω_n is the highest circular natural frequency. When substituting the j^{th} natural frequency (j = 1, 2,…, n) back into Eq. (2.20) the j^{th} mode shape or natural mode of vibration within a multiplicative arbitrary constant is obtained, so if $\boldsymbol{\varphi}_j$ is a solution then $\alpha_j\boldsymbol{\varphi}_j$ is also a solution where α_j is an arbitrary real

constant. The mode shapes are arranged in a mode shape matrix in which the j^{th} column corresponds to the j^{th} mode shape.

$$\mathbf{\Phi} = \begin{pmatrix} \varphi_{11} & \cdots & \varphi_{1n} \\ \vdots & \ddots & \vdots \\ \varphi_{n1} & \cdots & \varphi_{nn} \end{pmatrix} \tag{2.24}$$

To determine the arbitrary multiplicative constant for each mode shape, normalization of mode shapes can be used. There are several normalization techniques available, such as setting the largest value of each eigenvector to unity or setting the norm, or length, of each modal vector to unity. Among the available normalization techniques this research assumes that mass normalization is used in which eigenvectors are scaled such that

$$\boldsymbol{\varphi}_j \mathbf{M} \boldsymbol{\varphi}_k = \delta_{jk} \tag{2.25}$$

where $\boldsymbol{\varphi}_j$ and $\boldsymbol{\varphi}_k$ are the j^{th} and k^{th} mass normalized mode shapes, and δ_{jk} is the Kronecker symbol, which equals to unity when $j = k$ and zero when $j \neq k$. Whenever the mode shapes are used in derivations in this research it is assumed that they are mass normalized unless otherwise stated. The consequence of using mass normalized mode shapes is that the transformed mass and stiffness matrices have the simple form.

$$\mathbf{\Phi}^T \mathbf{M} \mathbf{\Phi} = \mathbf{I} \tag{2.26}$$

$$\mathbf{\Phi}^T \mathbf{K} \mathbf{\Phi} = \mathbf{\Lambda} \tag{2.27}$$

where $\mathbf{I}$ is the identity matrix. Without proof it is mentioned that any two $\boldsymbol{\varphi}_j$ and $\boldsymbol{\varphi}_k$ mode shapes are orthogonal to each other when $j \neq k$. Moreover, Eqs. (2.26) and (2.27) imply that the mode shapes are also mass-orthogonal and stiffness-orthogonal.

2.2.2 Modal Decomposition of FRF Matrices for Viscously Damped Systems

The previous section discussed that the mass and stiffness matrices of an *n*-DOF linear system become diagonal under linear transformation using the eigenvectors. In the transformed or natural coordinate system, the equations of motion are uncoupled and can be solved as a set of *n*-SDOF problem. Dissipative forces are often included in models as viscous damping forces proportional to velocity. The equation of motion for an *n*-DOF viscously and lightly damped system in free vibration can be written.

$$\mathbf{M}\ddot{\mathbf{u}} + \mathbf{C}\dot{\mathbf{u}} + \mathbf{K}\mathbf{u} = \mathbf{0} \tag{2.28}$$

Using only the real part of the assumed solution in Eq. (2.19) and substituting into the above equation and premultiplying by the transpose of the mass normalized mode shape matrix, we arrive to the following expression.

$$\mathbf{I}\ddot{\mathbf{q}} + \boldsymbol{\Phi}^T\mathbf{C}\boldsymbol{\Phi}\dot{\mathbf{q}} + \boldsymbol{\Lambda}\mathbf{q} = \mathbf{0} \tag{2.29}$$

where $\mathbf{q}$ is the vector of natural or modal coordinates. In general, the set of *n* differential equations in Eq. (2.29) are not uncoupled unless the damping matrix can be diagonalized under the transformation $\boldsymbol{\Phi}^T\mathbf{C}\boldsymbol{\Phi}$. If this is the case then the *n* uncoupled equations of motion can be written as

$$\ddot{q}_j + 2\omega_j\zeta_j\dot{q}_j + \omega_j^2 q_j = 0, \quad j = 1,2,\ldots,n \tag{2.30}$$

where ζ_j is the j^{th} modal damping ratio. The usefulness of a diagonalizable damping matrix is apparent from Eq. (2.30). Having a damping matrix that diagonalizes under linear coordinate transformation, however, is only a mathematical convenience, and usually does not have any connection to the physical dissipative properties of the real structure. As mentioned earlier, however, very little is known about damping or dissipative forces in structures, since damping is not an intrinsic property of the members (or finite elements), but depends on the structure, i.e. connection types, applied material, micro cracks etc. Probably the only case when damping is known partially is when

dampers are installed at certain structural locations to control dynamic characteristics. Therefore, the proposition that is widely accepted in practice is as follows: If we know very little about damping then why not make it at least convenient for mathematical calculations, i.e. chose it in such a way that it diagonalizes under the modal coordinate transformation.

Some common assumptions about damping matrices include the linear combination of the mass and stiffness matrices, since any linear combination of two matrices that are diagonalize under modal coordinate transformation will still be diagonalizable.

$$\begin{aligned} \mathbf{C} &= a\mathbf{M} \\ \mathbf{C} &= b\mathbf{K} \\ \mathbf{C} &= a\mathbf{M} + b\mathbf{K} \end{aligned} \tag{2.31}$$

where a and b are proportionality constants to be determined. The damping matrix formulations in Eq. (2.31) are known as proportional damping and the last one stated is often called Rayleigh damping. Only mass or stiffness proportional damping matrices are rarely used in practice, since a greater control over the modal damping ratios can be achieved using Rayleigh damping. Let's suppose that from a free vibration amplitude decay test, two of the modal damping ratios (ζ_k, ζ_m) and natural frequencies (ω_k, ω_m) were measured. Then for these two k^{th} and m^{th} frequencies the following equations can be obtained.

$$\begin{aligned} \boldsymbol{\varphi}_k^T \left(a\mathbf{M} + b\mathbf{K} \right) \boldsymbol{\varphi}_k &= a + b\omega_k^2 = 2\omega_k \zeta_k \\ \boldsymbol{\varphi}_m^T \left(a\mathbf{M} + b\mathbf{K} \right) \boldsymbol{\varphi}_m &= a + b\omega_m^2 = 2\omega_m \zeta_m \end{aligned} \tag{2.32}$$

or, in matrix form,

$$\frac{1}{2} \begin{pmatrix} 1/\omega_k & \omega_k \\ 1/\omega_m & \omega_m \end{pmatrix} \begin{pmatrix} a \\ b \end{pmatrix} = \begin{pmatrix} \zeta_k \\ \zeta_m \end{pmatrix} \tag{2.33}$$

from which the constants a and b can be obtained. The damping ratio in any j^{th} frequency can then be determined when j is different from k and m.

$$\zeta_j = \frac{a + b\omega_j^2}{2\omega_j} \tag{2.34}$$

Characteristic to Rayleigh damping, the middle frequencies have more or less the same damping ratios and the lower and higher frequencies have increasing damping ratios. The concept of Rayleigh damping can be extended to any number of r measured damping ratios by considering the orthogonality properties of mode shapes. If r damping ratios, $\zeta_1, \zeta_2, \ldots \zeta_r$, are given, then a damping matrix using the Caughey summation can be used.

$$\mathbf{C} = \sum_{j=0}^{r-1} a_j \mathbf{M}\left(\mathbf{M}^{-1}\mathbf{K}\right)^j \tag{2.35}$$

where the a_j proportionality constants can be obtained from the system of r simultaneous equations.

$$\frac{1}{2}\begin{pmatrix} 1/\omega_1 & \omega_1 & \omega_1^3 & \cdots & \omega_1^{2r-3} \\ 1/\omega_2 & \omega_2 & \omega_2^3 & & \omega_2^{2r-3} \\ 1/\omega_3 & \omega_3 & \omega_3^3 & & \omega_3^{2r-3} \\ \vdots & & & \ddots & \vdots \\ 1/\omega_r & \omega_r & \omega_r^3 & \cdots & \omega_r^{2r-3} \end{pmatrix}\begin{pmatrix} a_0 \\ a_1 \\ a_2 \\ \vdots \\ a_{r-1} \end{pmatrix} = \begin{pmatrix} \zeta_1 \\ \zeta_2 \\ \zeta_3 \\ \vdots \\ \zeta_r \end{pmatrix} \tag{2.36}$$

Another common practice in modal analysis is to directly specify the modal damping ratio, ζ_j, for the j^{th} mode. The modal damping ratios can be determined experimentally or by using common sense. Typically, lower modes will have smaller damping ratios, while higher modes are damped more. Regardless of the preferred formulation, proportional damping matrices become diagonal after modal coordinate transformation and Eq. (2.30) holds for all modes.

Recall the definition of the receptance matrix presented in Eq. (2.15) and assume that the system is proportionally damped so the damping matrix becomes diagonal under the modal coordinate transformation. The inverse of the receptance matrix, also known as the dynamic stiffness matrix, is given as

$$\left(\mathbf{K} - i\omega\mathbf{C} - \omega^2\mathbf{M}\right) = \mathbf{R}^{-1} \tag{2.37}$$

Premultiply both sides by the transpose of the mode shape matrix, $\mathbf{\Phi}^T$, and postmultiply by $\mathbf{\Phi}$ to obtain

$$\left[\mathbf{\Lambda} - i\omega\,\mathrm{diag}\left(2\zeta_j\omega_j\right) - \omega^2\mathbf{I}\right] = \mathrm{diag}\left(\omega_j^2 - 2i\omega\zeta_j\omega_j - \omega^2\right) = \mathbf{\Phi}^T\mathbf{R}^{-1}\mathbf{\Phi} \equiv \mathbf{D} \tag{2.38}$$

where diag() indicates diagonal matrix, and $\mathbf{D}$ is defined as the inverse receptance matrix in the natural coordinate system. Taking the inverse of matrix $\mathbf{D}$, which is simply the reciprocal of the diagonal elements, and pre- and postmultiplying both sides by $\mathbf{\Phi}$ and $\mathbf{\Phi}^T$, respectively, gives the receptance matrix.

$$\mathbf{R} = \mathbf{\Phi}\mathbf{D}^{-1}\mathbf{\Phi}^T = \mathbf{\Phi}\,\mathrm{diag}\left(\frac{1}{\omega_j^2 - 2i\omega\zeta_j\omega_j - \omega^2}\right)\mathbf{\Phi}^T \tag{2.39}$$

where the jk^{th} element of the receptance matrix can be written as

$$R_{jk} = \sum_{m=1}^{n}\left(\frac{1}{\omega_m^2 - 2i\omega\zeta_m\omega_m - \omega^2}\right)\varphi_{jm}\varphi_{km} \tag{2.40}$$

The computational effort associated with the calculation of the FRF matrix using Eqs. (2.39) or (2.40) is considerably less than that of using Eq. (2.15). Using Eq. (2.17), the mobility and accelerance matrices for a proportionally damped system can be written as

$$\mathbf{V} = \mathbf{\Phi}\,\mathrm{diag}\left(\frac{-i\omega}{\omega_j^2 - 2i\omega\zeta_j\omega_j - \omega^2}\right)\mathbf{\Phi}^T \tag{2.41}$$

$$V_{jk} = \sum_{m=1}^{n}\left(\frac{-i\omega}{\omega_m^2 - 2i\omega\zeta_m\omega_m - \omega^2}\right)\varphi_{jm}\varphi_{km} \tag{2.42}$$

$$\mathbf{A} = \mathbf{\Phi}\,\mathrm{diag}\left(\frac{-\omega^2}{\omega_j^2 - 2i\omega\zeta_j\omega_j - \omega^2}\right)\mathbf{\Phi}^T \tag{2.43}$$

$$A_{jk} = \sum_{m=1}^{n}\left(\frac{-\omega^2}{\omega_m^2 - 2i\omega\zeta_m\omega_m - \omega^2}\right)\varphi_{jm}\varphi_{km} \tag{2.44}$$

For a proportionally damped system, Eqs. (2.39), (2.41) and (2.43) establish the relationship between the FRF matrices in physical or global coordinates and the FRF matrices in modal coordinates. The FRF matrices in modal coordinates are diagonal since in natural (or modal) coordinates the equations of motion are uncoupled. In contrast, the FRF matrices in physical (or global) coordinates are usually full matrices and consequently, not diagonal. In considering Eqs. (2.40), (2.42) and (2.44), it can be concluded that FRF matrices are symmetrical for linear systems, i.e. $\mathbf{H} = \mathbf{H}^T$. Of course this is expected. Symmetry of the FRF matrices is just another form of the reciprocity theorem, which states that the response of the j^{th} DOF due to an excitation applied at the k^{th} DOF is equal to the response of the k^{th} DOF if the same excitation is applied at the j^{th} DOF.

2.2.3 Measuring FRF Data, Displacement, Velocity and Acceleration

As stated in Eq. (2.17), there is a unique relationship between the displacement, velocity or acceleration responses. Therefore in theory, it does not matter which one of the quantities is measured since the necessary measures can be obtained from any of the others. In practice, however, the available sensors, equipment, physical structure may impose a preferred quantity over the others. Vibration theory shows that displacement

measurements amplify low frequency components, and conversely, acceleration measurements are useful if high frequency components are important. In considering the measurement type it is important to know the expected frequency range in which the response can occur. When the frequency range to be measured is distributed with equal weight throughout a wide band then velocity response measurements are desirable because they weight equally low and high frequency components. Velocity has another important property that can be advantageous in certain applications, namely that it is directly related to kinetic energy from which conclusions about the severity of vibration can be made.

On the other hand, acceleration transducers, or in short accelerometers, are versatile and commercially available at a lower cost. Accelerometers also have small dimensions and relatively high frequency and dynamic ranges. In addition, analogue electronic integration is more accurate and reliable than electronic differentiation, which makes accelerometers more appealing in most cases. In measurement theory, the signal to noise ratio is extremely important and it is necessary to keep it as low as possible, which can significantly influence the preferred type of measurement.

The design of the data acquisition system is a rather complicated problem and requires careful consideration of many influencing factors and collaboration of experts from different fields of science. In a typical single input single output test situation, the structure is excited at exactly one point and the response is measured at exactly one point i.e. the H_{jk} entry of an FRF matrix is measured. This type of test is usually performed by using a dual channel digital analyzer. The excitation (shaker, sledgehammer, etc.) is measured in channel 1 and the response signal is fed into channel 2. By moving either the excitation or the response point while the other location remains fixed an entire row or column of the n-DOF system FRF matrix can be measured, respectively. In the frequency domain, the response at node k when the excitation is at point j can be written as.

$$X_k(\omega) = H_{jk}(\omega) F_j(\omega) \tag{2.45}$$

where $X_k(\omega)$ is the general response (displacement, velocity or acceleration) at the k^{th} DOF. The FRF can be calculated by simultaneously sampling the excitation and the response signal. The formal solution of the jk^{th} transfer function from Eq. (2.45) becomes.

$$H_{jk}(\omega) = \frac{X_k(\omega)}{F_j(\omega)} \tag{2.46}$$

The above expression for the calculation of the response functions is not practical, since in real world situations one has to deal with all types of signals (transient, periodic, random, etc.) and elimination of noise in the signals is practically impossible. In digital analyzers, the FRF functions are obtained from the so-called "trispectrum average" which can be defined for any two signals that are simultaneously sampled. The principle of the method is to take a number of repeated measurements, calculate the three spectra estimates (it is very important that we only deal with estimates) and then average them to get the FRF and coherence (measure how well the force signal is related linearly to response signal) functions (McConnell 1995). The three spectra under discussion are the force signal auto-spectrum $G_{ff}(\omega)$, the response signal auto-spectrum $G_{xx}(\omega)$, and the cross-spectrum $G_{fx}(\omega)$ between the force and response signals. Without rigorously defining the auto-spectrum and cross-spectrum functions, which can be found in any books focusing on stochastic vibrations (Lutes and Sarkani 1997), the calculation of FRF matrices can be formulated by multiplying both sides of Eq. (2.45) with $F_j^*(\omega)$, which is the complex conjugate of $F_j(\omega)$.

$$F_j^*(\omega) X(\omega) = H(\omega) F_j^*(\omega) F(\omega) \tag{2.47}$$

After averaging a theoretically infinite number of measurements the equation for the spectrum functions become.

$$G_{fx}(\omega) = H(\omega) G_{ff}(\omega) \tag{2.48}$$

or rearranging and indexing the average estimator transfer function,

$$H_1(\omega) = \frac{G_{fx}(\omega)}{G_{ff}(\omega)} \tag{2.49}$$

Another relationship between the transfer and spectra functions can be derived when multiplying both sides of Eq. (2.45) by $X_k^*(\omega)$ to obtain another expression for the average estimator transfer function.

$$H_2(\omega) = \frac{G_{xx}(\omega)}{G_{xf}(\omega)} \tag{2.50}$$

In ideal situations (noise free measurement, infinite number of measurements) Eqs. (2.49) and (2.50) give the same FRF functions. This is rarely the case, however, so a coherence function may be defined as an indicator of the linear correlation between the obtained transfer functions.

$$\gamma^2(\omega) \equiv \frac{H_1(\omega)}{H_2(\omega)} = \frac{\left|G_{fx}(\omega)\right|^2}{G_{ff}(\omega)G_{xx}(\omega)} \tag{2.51}$$

The coherence function ranges from zero (no correlation) to unity (perfect correlation) and can be thought of as a measure of the quality of the measurements.

Further assumptions on the signals, i.e. both the excitation and response signals consist of a “true” and a “noisy” part, lead to expressions for the transfer functions in terms of the auto- and cross-spectrum of the “true” and “noisy” parts of the signals. In general noises are classified as electrical or mechanical noises. Typical electrical noises are the intrinsic noise of electric circuits, fluctuation or disturbance of the power source, interference of electromagnetic or radio frequencies, ground loops, etc. Among the unwanted mechanical noises are construction activities in the vicinity of the object to be measured, operation of elevators and escalators inside a building, wind induced vibrations, etc. Based on the reasonable assumption that noise in signals are uncorrelated

with each other and the excitation and the "true" response signals, it can be shown that H_1 and H_2 are a lower and upper bound estimators for H. To conclude this section a commonly accepted expression for approximating the transfer function is introduced, in which the geometric mean of the two functions H_1 and H_2 is simply taken.

$$H(\omega) = \sqrt{H_1(\omega) H_1(\omega)} \tag{2.52}$$

The goal of the above discussion was to point out the importance of carefully designing measurements. Obtaining the necessary FRF functions with acceptable accuracy could be the subject of an entire dissertation and would require considerable knowledge in the field of probabilistic mathematics and dynamics, electronics, measurement theory, instrumentation, etc. This section only briefly discusses the problem of measuring transfer functions. In order to evaluate SDIMs and their limitations, however, it is necessary to understand that measurements do not lack of noise and contamination. In most situations, further manipulating on the raw data to obtain certain dynamic characteristics of structures can and will introduce even more errors in to the models. With this in mind, the goal is to develop an SDIM that minimizes the contamination and manipulations (data filters are not considered as sources of errors) on raw measurement data. Ultimately, the methods developed will use FRF data as they are measured on structures for damage detection with the hope that they contain the information necessary for locating and quantifying damage in members.

2.3 Damage Indicators

The definition of damage is difficult to conceptualize in a general and widely accepted manner. The sources of damages are unknown in most cases and the range of probable causes makes it difficult to generalize damage. However, it is often accepted (with certain limitations) that damage affects the behavior of structures (e.g. vibration characteristics), which is described by the structural properties of stiffness, damping and mass. In general, after damage has occurred the member stiffnesses are affected as well as the damping characteristics of the structure. Altering the mass only, in comparison, may or may not be

considered damage. Consider a parking garage in downtown Houston that is almost empty at dawn, but by 9 a.m. it is closed because the maximum capacity of the garage has been reached. In this case, the mass of the structure has changed significantly in a matter of couple of hours, but certainly it does not imply that the structure is damaged.

To avoid ambiguity such as in the example above and to simplify the SDIM it is assumed that the mass of the structure does not change between the phases of its lifetime, or if it has changed the magnitude of the change is known so the finite element model of the structure can be updated accordingly. Although it is not required by the approach used in this research, for simplicity and demonstration purposes of the proposed method it is assumed that damage only affects the stiffness of the structure, while damping and mass are not affected. For a linear finite element model, stiffness reduction can be accomplished in several ways, including alteration of section properties (cross sectional area, moment of inertia, plate thickness etc.), Young's modulus, etc. Probably the easiest but most effective way to alter member stiffness is to change the Young's modulus. By altering the Young's modulus, all DOF's stiffness properties are reduced or increased by the same proportions in the same element. As an example, consider a reinforced concrete column in compression. Also assume that in the intact structure there were no cracks in the column. After some external effect, the column cracks and the goal is to find the change in stiffness caused by these cracks. One could assume that the stiffness of the column is reduced through its Young's modulus and obtain a damage indicator. In a more realistic case one could argue that when the concrete cracks its cross sectional area (in compression) does not change but its second moment of inertia does, which requires the introduction of two damage indicators one for the cross sectional area and the other for the second moment of inertia. Using two separate damage indicators provides more information about the source and characteristics of damage, but the SDIM imposes a significantly more difficult problem to solve. For this particular problem, the change in the damping properties of the column could also be considered since cracked reinforced concrete members dissipate more energy than uncracked members. Another problem may arise if it is assumed that this column is part of a multi-story frame system on the first floor subject to certain dead loads. In this case the stiffness of the column in compression

may not be affected at all. When the column is acting mainly in compression (very small bending) then vibration data will not be affected by the change in stiffness of the column unless the amplitudes of vibration is adequately large (i.e. the crack opens). In this situation the size of the crack does not even matter because the stiffness of the column in compression is not affected by the crack. This example points out some of the limitations in using vibration data as signatures for damage detection.

To introduce damage in structures, a damage indicator is assigned to each finite element in the model. The goal of the SDIM is to obtain the vector of damage indicators, $\mathbf{x}^s$, for all finite elements in the structure. The stiffness of a damaged finite element is computed by means of its damage indicator.

$$\begin{aligned} &\mathbf{k}_j^{dam} = \left(1 - x_j^s\right)\mathbf{k}_j, \quad j = 1, 2, \ldots, n_e \\ &0 \le x_j^s \le 1 \end{aligned} \tag{2.53}$$

where $\mathbf{k}_j^{dam}$ is the stiffness matrix of the j^{th} damaged finite element, $\mathbf{k}_j$ is the stiffness matrix of the j^{th} intact finite element, x_j^s is the damage indicator of the j^{th} finite element, and n_e is the number of finite elements in the model. The limits on the damage indicators in Eq. (2.53) suggest that only reduction of the element stiffness is attainable. A zero damage indicator is related to an undamaged element, whereas a damage indicator of unity (100%) means that the element has lost all its stiffness. In some cases, an increase in stiffness may occur as certain materials can undergo hardening when stressed beyond their elastic limit (the modulus of elasticity increases). The stiffness loss assumption made in Eq. (2.53) is not strict and Eq. (2.53) can be easily modified to accommodate stiffness increases due to hardening. The use of damage indicators ensures that the location of detected damage is unique and that the damage value bears a physical meaning, namely the reduction (or increase) in stiffness. Using the damage indicators, any of the analytical FRF matrices of the structure can be obtained by Eqs. (2.15) and (2.17).

2.4 Use of FRF Data in Damage Detection

The idea behind the SDIM developed in this research is that the difference between the FRF matrices of the undamaged structure and the damaged structure captures both the location and severity of damage. In real structures, the number of DOFs is infinite. Although in a finite element representation the number of DOFs is finite, this number is still large and only certain entries of an FRF matrix can be measured in practical situations. In general, the jk^{th} member of an FRF matrix represents the response of the j^{th} DOF when the excitation is applied at the k^{th} DOF. As was mentioned in earlier sections, the particular FRF matrix that is used the SDIM, is insignificant. The same formulation is valid for receptance, mobility and accelerance matrices. Therefore to emphasize this interchangeability property of FRF matrices in the SDIM, the general notation of **H** or **H**(ω) will be used in place of any specific FRF matrices.

In order to formulate the damage detection problem as an optimization problem, an objective or error function is defined that needs to be minimized. The main idea is to minimize an error term between the measured FRF data and the analytical FRF functions computed by means of the damage indicator vector. The solution to the optimization problem will result in a damage indicator vector that correctly identifies the location and severity of damage(s) in the structure. The objective function defined in Eq. (2.54) assumes that there is only one excitation, but measurements may be taken at multiple locations.

$$\min f = \sum_{k=k_1}^{k_n} \left(\int_{\varpi_0}^{\varpi_1} \left| \bar{H}_{jk}(\omega) - H_{jk}(\omega) \right| d\omega \right)^2 \tag{2.54}$$

where j is the excitation DOF, k is the DOF where the response is measured, H_{jk} is the jk^{th} FRF function in the finite element model, $\bar{H}_{jk}$ is jk^{th} measured FRF function on the damaged structure, $k_1, k_2, \ldots k_n$ are the DOF's where measurements are taken, ϖ_0 and ϖ_1 are the lower and upper frequencies of the measured frequency range, and the symbol $|\ |$ indicates complex magnitude. If there are multiple excitation locations then another

summation on j is added to the equation and the objective function remains valid for multi-excitation, multi-measurement cases.

$$\min f = \sum_{j=j_1}^{j_r} \left(\sum_{k=k_1}^{k_n} \left(\int_{\varpi_0}^{\varpi_1} \left| \bar{H}_{jk}(\omega) - H_{jk}(\omega) \right| d\omega \right)^2 \right) \tag{2.55}$$

where $j_1, j_2, \ldots, j_r$ are DOF's where excitation is applied. The objective function formulation implies that the H_{jk} entries of the FRF matrix must be reevaluated at every iterations using the current damage indicators and that at the global optimum point the objective value is zero (perfect match of the measured and analytically computed FRF data).

The H_{jk} FRF is a function of the element stiffness matrices, and therefore, it is also a function of the damage indicators. The goal of damage detection is to find the damage indicators for each finite element; consequently the damage indicators become the unknown variables of the optimization problem. From the definition of the objective function it is also clear that the minimum value of this function is zero when the measured FRFs perfectly match the analytical FRFs. The imposed problem is an unconstrained optimization problem with n_e (number of finite elements) continuous variables in the interval of zero and unity. Later in the discussion of variable representations we will return to this point and redefine the problem to account for the unstructured nature of damage detection.

Other observations related to the SDIM include assuming that an n-DOF finite element model of the intact structure is available and that the structure can be modeled as a linear system (both material and geometrical non-linearities are insignificant), i.e. the principle of superposition holds. By using FRF functions it is implicitly implied that the structure is linear otherwise the response in frequency domain could not be obtained as a simple multiplication of the forcing term and the FRF. On the other hand, modal decomposition of linear structures is a common practice providing a faster way to compute the necessary entries of FRF matrices. The assumption of linear structure,

however, does not imply in any way that the structure did not undergo nonreversible deformations (damages) up to the point when measurements are taken.

For example, a building was hit by an (moderate) earthquake that induced plastic deformations in certain structural connections of the structure. After the overloading effect (i.e. the earthquake) ceased, the structure returned to a new equilibrium position without any significant or life threatening damages in its structural members and connections. The cyclic history of a structural connection is depicted in Figure 2.2. After a certain number of cycles the particular connection returns to a new equilibrium position, which is in the elastic zone. If the excitation of measurement does not exert significantly large forces on the structure then the connection will oscillate around its new equilibrium position in the elastic zone, therefore a linear model will suffice.

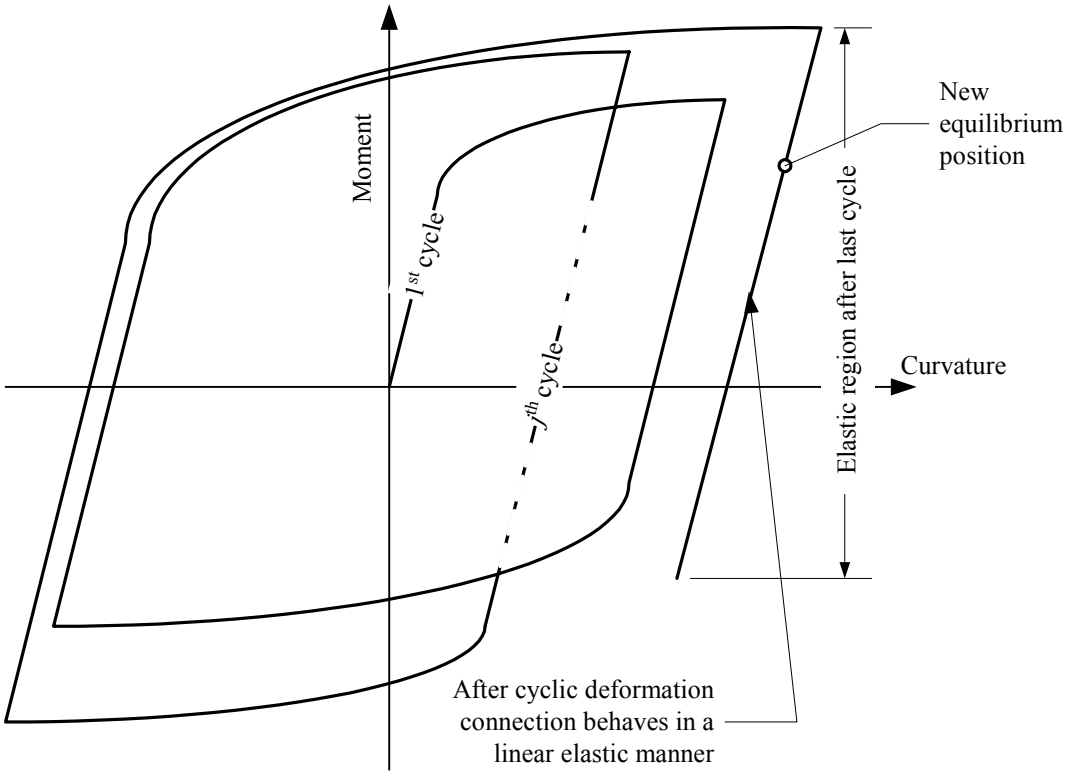

Figure 2.2. Cyclic history of a structural connection

Yielding itself, however, may not influence stiffness or the vibration signatures of the structure. Referring to Figure 2.2, the stiffness of the material did not change in the new linear equilibrium position and consequently, vibration signatures will not be able to capture damage (yielding). To be able to detect damage other structural properties must change e.g. cross sectional area or second moment of inertia. In bolted connections in steel frames, for example, it is possible that the bolts yielded and therefore the connection loosened up reducing the stiffness of the structural connection. In this situation it may be possible to detect damage(s) using vibration signatures in the elastic region. For some reinforced concrete structures subjected to cyclic loading it is possible that the stiffness of the new equilibrium position in Figure 2.2 will not be parallel to that of the original modulus and in this case damage can also be detected. Again, this has identified some the limitations of using vibration data for damage detection. Unfortunately there is not a single signature that is able capture all types of damages that can occur in structures. Currently there does not exist a universal SDIM that is preferred over any other procedures. Relying on a single SDIM in the hope that it is able to detect all type of damages is infeasible. Rather, a combination of existing methods may provide a higher level of confidence about detecting the location and severity of damages.

2.5 Excitation and Sensor Placement

Since most SDIMs operate on measured vibration data it is essential to design the excitation and sensor layout in such a way that the information contained in the vibration data with respect to the selected SDIM is maximized. Excitation and sensor layout design therefore poses an optimization problem with at least two objectives. The first objective is to maximize the information included in the vibration data to enhance the efficiency and reliability of damage detection. This objective however contradicts the practical need to minimize the number of sensors used for measurements.

In order to evaluate the quality of measurement data, the information contained in measurements has to be quantified. Today, a wide variety of sophisticated engineering tools depend heavily on measurement data. Applications include a broad range of engineering domain including aerospace, mechanical and civil engineering. Because of

the diversity of applications the information necessary to capture in measurements varies significantly. In this section, an information measure contained in the vibration data will be defined considering the SDIM presented in this dissertation. The proposed measure is based on the sensitivities of FRFs with respect to the damage indicators of the finite element model. By maximizing this information measure, an increased objective value of the damage detection problem is expected, which would indicate higher sensitivities and possibly results in more unique and stable identification of the damaged elements. The number of sensors, however, that can be used for measurement may be limited by the available equipment, labor cost or time. For instance if the digital analyzer used for measurements only has 8 input channels, then the number of measurements may be limited to 7 (one channel is reserved for the excitation) since moving the analyzer requires rewiring, calibration, testing, etc. In general, minimizing the number of sensors reduces the cost of equipment, preparation, installation and labor.

2.5.1 Information Contained in Measurements

The sensor layout design problem is developed using a finite element model of the structure. The vibration signatures carrying measurement information are the receptance, mobility and accelerance FRFs. In the damage detection process, the goal is to identify the damage indicators defined for each finite element in the model. Therefore, it is natural to define an information measure that accounts for the sensitivity of FRF data to the damage indicators. The sensitivity of an FRF matrix with respect to the damage indicator of the j^{th} finite element can be written.

$$\frac{\partial \mathbf{H}(\omega)}{\partial x_j^s} = -\mathbf{H}(\omega)\frac{\partial \mathbf{Z}(\omega)}{\partial x_j^s}\mathbf{H}(\omega) \tag{2.56}$$

where $\mathbf{H}(\omega)$ is an FRF matrix (receptance, mobility or accelerance), $\mathbf{Z}(\omega)$ is the inverse of the FRF matrix under investigation (for receptance matrices the inverse is the dynamic stiffness matrix, or more precisely the receptance matrix is the inverse of the dynamic stiffness matrix, Gatti and Ferrari 1999). Eq. (2.56) is computationally

prohibitive for large structures, and in those cases, a numerical differentiation of the FRFs is used to obtain the sensitivities.

$$\frac{\partial H_{km}(\omega)}{\partial x_j^s} \approx \frac{H_{km}(\omega)\big|_{x_j^s=0} - H_{km}(\omega)\big|_{x_j^s=\Delta x_j^s}}{\Delta x_j^s} \tag{2.57}$$

where $H_{km}(\omega)$ is an FRF (km^{th} element of $\mathbf{H}(\omega)$) for which the excitation is located at the k^{th} DOF and the measurement is taken at the m^{th} DOF, and Δx_j^s is a small perturbation at element j (usually between 0.1% and 1%). The information function is defined for a pair of excitation, k^{th}, and measurement, m^{th}, DOFs using the FRF sensitivities with respect to the damage indicator vector $\mathbf{x}^s$.

$$\iota_{km} = \sum_{j=1}^{n_e} \left(\int_{\varpi_0}^{\varpi_1} \left| \frac{\partial H_{km}(\omega)}{\partial x_j^s} \right| d\omega \right)^2 \tag{2.58}$$

where ι_{km} is the information contained in the H_{km} FRF, ϖ_0 and ϖ_1 are the lowest and highest measured frequencies respectively, n_e is the number of finite elements in the model. The information function is defined with respect to all finite elements in the model, consequently this function gives an overall quality measure of the information contained in the measurement data. The total information, I, contained in n_{meas} measurements (number of sensors) assuming only one excitation DOF is defined as.

$$\mathrm{I} = \sum_{m \in J}^{n_{meas}} \left(\iota_{km} \right)^2 \tag{2.59}$$

where J is the set of unrestrained measured DOFs. The information measure defined above is formulated by considering the objective function for damage detection and therefore provides a function, which gives the most information about the quality of the measurements with respect to the proposed SDIM.

2.5.2 Optimum Excitation and Sensor Layout Design

The optimization problem for the excitation and sensor layout design can be stated as follows. Minimize the number of sensors used, and maximize the total information contained in the measurement such that the number of sensors used is at least one, but not more than a specified number, $n_{u,meas}$.

$$\begin{aligned} &\min f_1(\mathbf{x}) = n_{meas} \\ &\max f_2(\mathbf{x}) = \mathrm{I} \end{aligned} \tag{2.60}$$

subject to:

$$0 < n_{meas} \le n_{u,meas} \tag{2.61}$$

The decision variables for the sensors are logical variables such that each variable acts as an "On/Off" switch related to an unrestrained DOF in the finite element model where sensor(s) can be placed. Besides, there is an additional discrete decision variable, x_0, related to the excitation DOF.

$$\begin{aligned} &\mathbf{x} = \left[x_1, \;\; x_2, \;\; \ldots, \;\; x_{n_{sens}} \right]^T \qquad x_i = \{0,1\} \qquad i = 1,2,\ldots,n_{sens} \\ &n_{meas} = \sum_{i=1}^{n_{sens}} x_i \end{aligned} \tag{2.62}$$

The above problem falls into the area of multiobjective optimization. Details about the solution of such problems will be given in the next section.

3 OPTIMIZATION ALGORITHMS

In Section 2 the optimization problems for damage detection and excitation/sensor layout design were developed. To solve these problems algorithms including traditional and evolutionary optimization are considered. A brief overview of standard optimization problems and traditional optimization techniques is given in the first two subsections of this section. Then genetic algorithms are reviewed and demonstrated through a simple example. Advanced operators for the fine-tuning of genetic algorithms are reviewed and developed for binary representations. Adaptation of genetic algorithms to the damage detection and excitation/sensor layout design problems is developed using different representations of the problem domains. The advantages and drawbacks of the traditional fixed and a new implicit redundant binary representation are compared. A hybrid optimization approach for the damage detection problem is developed by combining genetic algorithms with a local hillclimbing search algorithm. In the last subsection of this section we revisit the multiobjective optimization problem proposed for the excitation and sensor layout design. The notion of Pareto optimum solutions are introduced and the nondominated sorting genetic algorithm capable of solving multiobjective optimization problems is presented. To tackle the constraints associated with the excitation and sensor layout design problem, specialized repair, re-initialization and penalty operators are developed.

3.1 Overview of Traditional Optimization Algorithms

3.1.1 Classes of Optimization Problems

In traditional optimization, there are three elementary problems for which solution algorithms are sought (Michalewicz and Fogel, 2000). Of course, there are other optimization problem domains but all practical problems, in some ways, resemble one of the elementary problems. One of these elementary problems is the satisfiability problem

(SAT) in which a statement, $F(\mathbf{x})$, of Boolean variables has to be TRUE. An example of the SAT problem of n logical variables is shown in Eq. (3.1).

$$F(\mathbf{x}) = \left(x_1 \cup x_2 \cup \tilde{x}_3\right) \cap \left(x_4 \cup \tilde{x}_5\right) \cap \ldots \cap \left(\tilde{x}_{n-2} \cup \tilde{x}_{n-1} \cup x_n\right) \tag{3.1}$$

where $\cup$ is the logical AND statement, $\cap$ is the logical OR statement and $\tilde{x}_i$ is negation of the logical variable x_i. The task in this problem is to find the logical (TRUE or FALSE) state for each x_i variable, $i = 1 \ldots n$, such that $F(\mathbf{x})$ = TRUE. The search space of the problem is 2^n because there are n variables and each variable has two different states (0, 1).

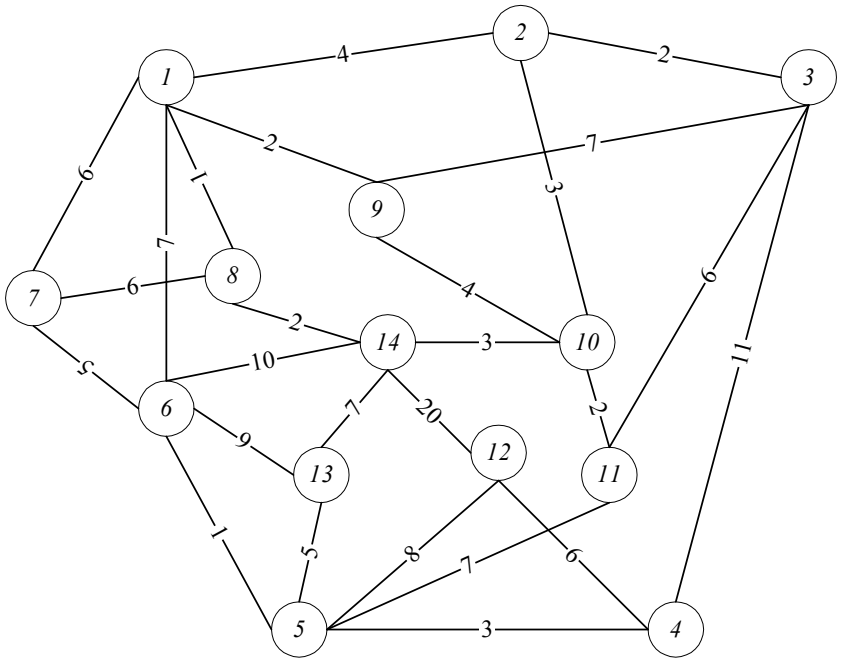

Figure 3.1. A 14-city *symmetric* traveling salesman problem (TSP)

Another classical optimization problem is the traveling salesman problem (TSP) in which a salesman has to visit every city on the map exactly once and then return to the starting city. This task is to be accomplished in such a way that the salesman travels the minimum total distance. A fourteen-city symmetric TSP is illustrated in Figure 3.1. A

symmetric tour occurs when distances between each pair of cities are the same regardless the direction of travel. The size of the search space for the TSP is always larger than that of the SAT problem if the number of variables is greater than 6. The size of the search space for a TSP with n cities is $|\mathcal{S}| = n!/(2n) = (n\text{-}1)!/2$. For most TSP problems, the exact solution is not known due to the large number of possible solutions, e.g. a 50-city TSP has approximately 10^{62} possible solutions. Unsymmetric TSPs pose additional search difficulties.

Another class of optimization problems are nonlinear programming problems (NLP). Most NLP problems find the vector of n-real variables that optimizes a given objective subject to different design constraints.

$$\begin{aligned} &\min f(\mathbf{x}), \quad x = (x_1, \ldots, x_n) \in \mathbb{R}^n \\ &s.t. \quad h_j(\mathbf{x}) = 0, \quad j = q+1, \ldots, m \\ &\qquad \mathrm{g}_j(\mathbf{x}) \le 0, \quad j = 1, \ldots, q \\ &\qquad l_i \le x_i \le u_i, \quad i = 1, \ldots, n \end{aligned} \tag{3.2}$$

where $\mathbf{x} \in \mathcal{F} \subseteq \mathcal{S}$, the objective function is defined on the search space $\mathcal{S} \subseteq \mathbb{R}^n$, the feasible region $\mathcal{F} \subseteq \mathcal{S}$ is defined by a set of m equality and inequality constraints, and the variables are restricted by their lower, l_i, and upper, u_i, bounds.

The damage detection task discussed in Section 2 can be classified as an unconstrained NLP with simple bounds on the variables. In comparison, the excitation/sensor layout design problem is classified as a constrained combinatorial problem, similar to the TSP.

3.1.2 Local and Global Search Techniques

A large number of traditional optimization algorithms have been developed to solve one or more of the above classes of problems. The main shortcoming of traditional algorithms is their robustness. A traditional algorithm that works well for one problem may give poor results for another. If the optimization domain changes, then the algorithm

changes too. When used appropriately (for a specific problem for which they were designed), traditional methods can be very effective. Michalewicz and Fogel (2000) divided the set of traditional algorithms into two main groups: Algorithms that evaluate complete solutions and algorithms that evaluate partial or approximate solutions. The importance of making this distinction is that solutions obtained using complete solutions can be always used even if the algorithm was terminated before convergence. Partial solutions, however, may be difficult to use if the algorithm was terminated before a complete solution was obtained.

Conceptually, the simplest algorithm is an exhaustive search that systematically checks every possible solution systematically in the search domain in order to find the global optimum solution. Exhaustive search, however, is extremely time consuming and is therefore not used for practical problems. Random walk is a method similar to exhaustive search. Instead of systematically evaluating solutions in the search space, a random walk selects possible solutions to evaluate randomly. In the worst case, performing a random walk is even more time consuming than an exhaustive search.

Local search techniques can be summarized based on their characteristics rather than the details. A popular local search technique, hillclimbing can be applied to optimize problems in any of the optimization problem classes discussed in Section 3.1.1. Hillclimbing is easy to implement and only uses the information contained in the objective function to improve the current solution iteratively. This technique uses a single point for the search. At each iteration, new points are selected from the neighborhood of the current (best) solution. If the best among the newly selected points is better than the current point, then that solution becomes the current point and a new iteration starts. If there was no better point found in the new solutions, then another neighborhood is selected and tested. The process terminates if no further improvements are possible or another termination condition is satisfied. In Section 3.4, the implementation details of the hillclimbing procedure used in this research to improve results obtained by genetic algorithms will be discussed.

There are local search algorithms, GSAT and 2-opt, or its extension *k*-opt, that are developed specifically for SAT and TSP problems, respectively. Both algorithms are

similar to hillclimbing in the sense that in a predefined neighborhood the possible solution is selected as the current solution.

Most of the traditional methods available for NLP are local search strategies. Some algorithms only use the information provided by the objective function, such as bracketing or its improved faster converging modification called Regula Falsi. In addition, there is a family of the Newton's methods that use gradient information and/or second order derivates (Hessian matrix). These procedures are designed to find the minimum of a quadratic bowl in only one step. Calculating the Hessian using Gaussian elimination provides the process called Newton-Gauss, while others often refer to as quasi-Newton methods. These procedures are very effective if derivative information about the objective is available. In most real world situations, however, this is not the case, and getting the inverse of the Hessian can be cumbersome. For problems involving linear objective and constraint functions, the exact optimum solution can be found using the simplex algorithm and its variations. Heuristic algorithms use some kind of heuristics, or rules of thumb, about the best possible move in attaining a solution. Some of the most well known heuristic procedures are greedy algorithms (at a step the values of each decision variables are assigned one by one such that it makes the "best" available decision) and dynamic programming (a recursive procedure that utilizes the decomposition of the problem). Branch and bound techniques rely on the idea of successive partitioning of the search domain by eliminating parts of the search space that are areas where optimum solution cannot be found.

Most of the traditional methods discussed in this section do not guarantee finding the global solution to the problem. Only exhaustive search provides this guarantee but at a prohibitive computational cost. Indeed, practical experience shows that local search techniques tend to get stuck in local optima, and therefore multiple runs from different starting points are required to get a better solution. The solution found is still not guaranteed to be the global optimum of the problem. Two methods have been developed to circumvent the possibility of getting stuck in a local optimum: simulated annealing and tabu search. Simulated annealing is based on the iterated hillclimber with an additional parameter (temperature) that controls the probability of accepting a new point as the

current point even if its fitness value is worse. Alternatively, tabu search uses the memory concept to store information about previous solutions in the view of finding the optimum. Regardless of the concepts adapted by these algorithms, the goal is to facilitate exploration of the search space at the early stages of the optimization process, while performing a more localized search at later stages (exploitation).

3.2 Introduction to Genetic Algorithms

In Section 3.1, a brief overview of the traditional optimization methods was provided. Some methods use deterministic rules to improve the current solution (e.g. hillclimber) and always return the same result for the same initial starting point. Other methods use probabilistic rules, such as simulated annealing, that can return different solutions for the same problem even using the same starting point. Most of the procedures are local search techniques guaranteed to return only a local optimum, although simulated annealing and tabu search can escape from local optima by using probabilistic transition rules or a memory concept. All of the above techniques, however, share a common characteristic. They rely on a single solution (the current solution) to explore the search space and find a local or global optimum.

Now, let us consider an idea that is based on nature's evolutionary mechanism and Darwin's "survival of the fittest" theory. The method that became known as the genetic algorithm (GA) was developed by Holland (1975) who gave encouragement to his former student Goldberg (1983) majoring in Civil Engineering to perfect the method. As a result of this fruitful collaboration Goldberg (1989) wrote a book, which is still one of the best introductory texts on genetic algorithms available today.

The main driving force in developing genetic algorithms was that traditional procedures lack robustness. The idea of a tool that works well on a large variety of optimization problems is appealing and contributes largely to the increasing popularity of GAs. Furthermore, theoretical and empirical studies proved that GAs provide a robust search tool in complex domains. Beside its robustness, GAs are computationally simple and easy to implement requiring only basic mathematical knowledge. Rigorous

assumptions about the search space are not necessary (continuity, existence of derivatives etc.) and therefore their applicability is not restricted.

GAs cannot be classified in one of traditional optimization tool categories. There are clear differences between GAs and traditional methods. Goldberg (1989) identified four significant dissimilarities regarding simple genetic algorithms (SGA).

- Parameters (variables) are coded into strings and GAs operate on these strings instead of the parameters,
- GAs use a population (set) of points instead of a single point,
- The only information used is provided by the fitness (objective function) of an individual (string), no auxiliary information (derivatives etc.) is used,
- GAs use probabilistic transition rules to explore the search space.

The above-identified differences make GAs a unique search technique and help contribute to their robustness.

3.2.1 Genetic Operators

Nature has designed a mechanism that drives evolution into directions that have never been explored before. SGAs adapt this biological marvel in a surprisingly simple way. Just as humans live in populations (villages, cities, etc.), the SGA works with a set of individuals (strings) called the population. In this population, there are several individuals carrying different "genetic information" in their string or coding. In biological systems, the information carrying units are called chromosomes, which uniquely define the individual. When the time comes, biological systems reproduce passing the genetic information to the next generation of individuals. Reproduction of species involves competition, usually among male members, to gain privilege for mating. The fitter the individual is, the more likely that he is the lucky one who can pass his genes to the next generation in the mating process. Children of the next generation are like their parents, but yet different. They carry most of the characteristics of their parents, both in appearance and behavior, but may be worse than or better than their parents in certain aspects. In rare situations, the children's genetic information may change due to an unexpected event called mutation. The outcome of the mutation can be either beneficial

or harmful, and helps nature to experiment with new genetic solutions to solve the problem of survival.

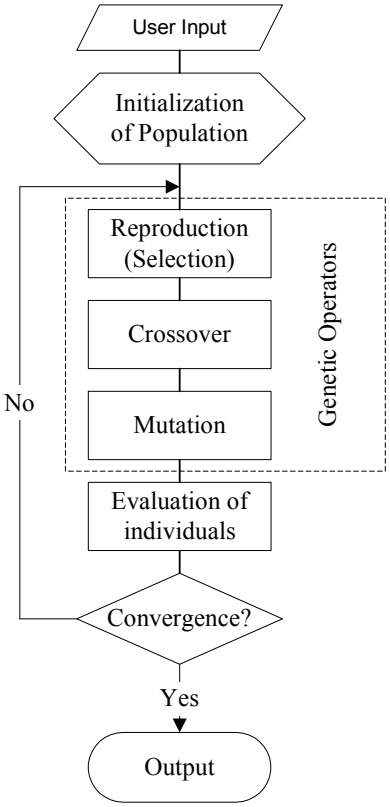

Figure 3.2. Schematic of simple genetic algorithms and genetic operators

Based on biological systems, the first task in a SGA is to code the parameters into strings (chromosomes). In most SGAs, binary stings are used to code the parameters. A binary string is a sequence of zeros and ones and each position is called a bit. The binary strings then can be interpreted in many different ways to decode the variables (base 2 numbers mapped to decimal numbers, on/off switches 0-off and 1-off, true and false states, etc.). In Figure 3.2, the flowchart of a SGA is depicted. The coding process can be identified as part of the population initialization in which the problem domain is translated into binary digits. The user input, preceding initialization, consists of crucial data that have not been identified yet, including population size, crossover and mutation

rate, tournament size, number of crossover sites, etc. In SGAs, three genetic operators are defined that are used for generating successive populations (generations). The names imply their roles in the mating process.

Reproduction (selection) is a process in which strings of individuals are copied according to some selection criteria based on their fitness value. In GAs the fitness may be the objective value but not necessarily. In some situations the fitness can include other properties other than the objective of the optimization. In the SGA proposed by Goldberg (1989), a roulette wheel reproduction procedure was used to copy individuals according to their fitness values. In this selection method, individuals with higher fitness have a higher probability of contributing one or more offspring in the next generation. Roulette wheel selection is illustrated in Figure 3.3. On the roulette wheel, each individual of the current population is assigned a slot that is proportional to its fitness (e.g. if the total sum of each individual's fitness value is 1000 and the fitness value of the first individual is 10 then this individual is assigned a slot on the roulette wheel which is a 1% slice of the whole circle). After spinning the roulette wheel, individuals with larger slots (higher fitness values) have a higher chance of being selected. Each time an individual is required, the roulette wheel is spun yielding the candidate for reproduction. In SGAs, the population size, n_{pop} (the number of individuals in the current population), is fixed at each generations and individuals in the current population are always replaced with new strings in the next generation. This reproduction technique, however, has several drawbacks. It assumes that fitness values are nonnegative, which often requires mapping the objective (fitness) function. A more important characteristic of this selection process is that in most cases regulation of the number of copies of an individual is necessary. In early generations of the SGA, especially for GAs with small population size, it is common to have a few extraordinary, highly fit individuals in the population. These individuals can quickly take over a significant portion of the population, which in turn can result in premature convergence. To remedy this undesirable property of the roulette wheel selection, Goldberg (1989) suggested the use of fitness scaling.

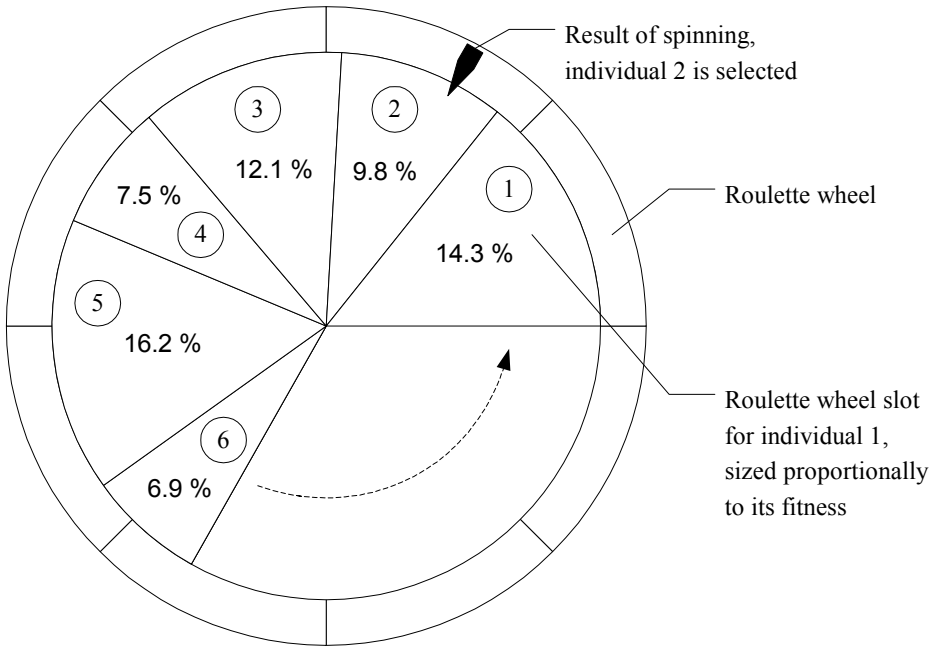

Figure 3.3. Roulette wheel selection, the wheel is spun to select individuals for reproduction proportionally to their fitness values

As an alternative to the roulette wheel, or proportional, selection tournament selection may be used to pick the individuals for reproduction (Goldberg 1991). Conceptually, tournament selection is even simpler than roulette wheel selection and can overcome the difficulties associated with the later one. The process diagram of the tournament selection is illustrated in Figure 3.4. In a single operation, the method selects n_{tour} ($n_{tour} \leq n_{pop}$) number of individuals and picks the best one from this set to take into the next generation. This process is repeated until the population size, n_{pop}, is reached. It is clear that larger tournament sizes, n_{tour}, result in increased selection pressure, and therefore fitter individuals have higher probability for mating. A typical tournament size can vary anywhere between 2 to 10 depending on the population size and the selection pressure necessary to obtain good convergence. In this research, tournament selection was used because of its simplicity and effectiveness, which are characteristics of a good reproduction tool.

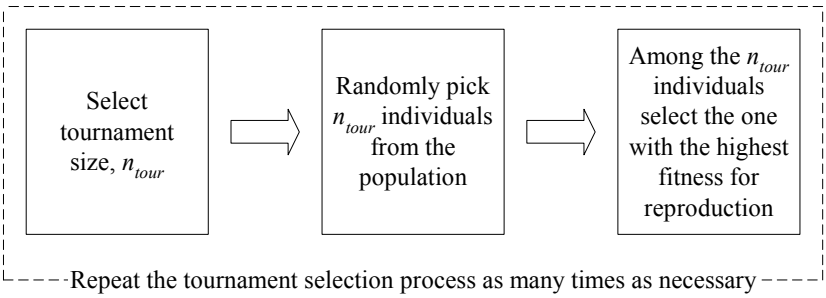

Figure 3.4. Tournament selection process diagram

The next genetic operator appearing in Figure 3.2 is the crossover. After selecting the individuals for reproduction using one of the selection operators, information is exchanged between the selected individuals. Crossover is one of the recombination operators that is used for information exchange between any two individuals. Crossover combines the features of two parents' genetic information (strings) to create two similar offspring by swapping segments of their parents' chromosomes (strings). A single point crossover operator is depicted in Figure 3.5. In single point crossover operator, the crossover site is selected randomly and the bits are simply swapped between two selected strings. As mentioned earlier, SGAs use a set of input parameters. One of these parameters is the probability of crossover, p_c, which gives the expected number, $p_c \cdot n_{pop}$, of strings undergoing recombination. In other words, for each crossover operation a random number, r, between zero and one is generated and if the probability of crossover is larger than this number, $r < p_c$, then the information exchange between the selected two individuals is performed.

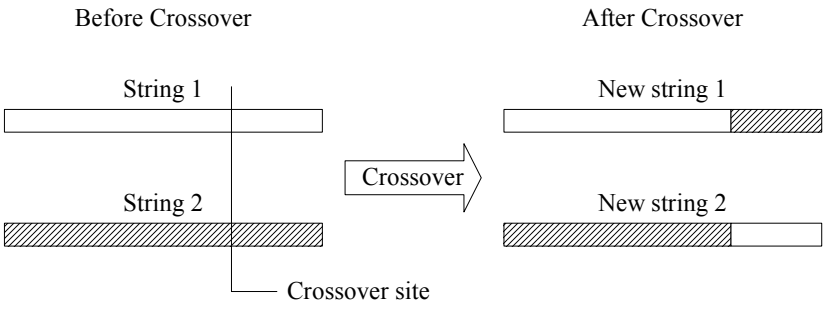

Figure 3.5. Single point crossover

Our next genetic operator is mutation (Figure 3.2). The intuition behind mutation is the introduction of new genetic information to facilitate exploration of the search space. Since GAs usually work with a finite population, there are features that are not included in the chromosomes. A simple mutation operator is depicted in Figure 3.6. Mutation arbitrarily switches one or more bits of a chromosome randomly with a probability equal to the mutation rate, p_m. The expected number of mutated bits in the entire population equals $p_m \cdot n_{bits} \cdot n_{pop}$, where n_{bits} is the number of bits in a chromosome. Every bit has the same chance to undergo mutation. For each individual in the current population and for each bit within the chromosomes, a random number, r, is generated and if $r < p_m$ the bit is mutated.

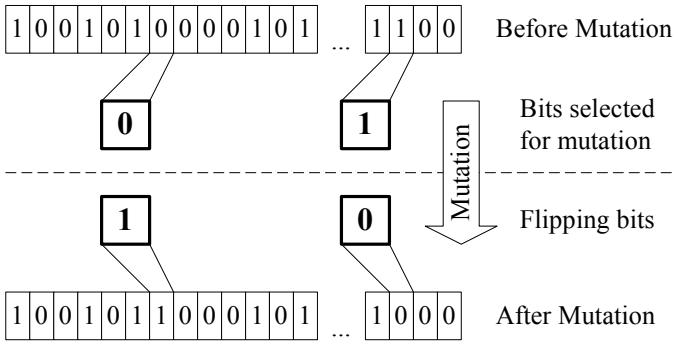

Figure 3.6. Uniform mutation

After the genetic operators are applied to the entire population, each individual is evaluated based on some objective (Figure 3.2). The role of the evaluation (fitness, objective) function is to rank individuals in terms of their fitness. At the end of each generation, convergence, which is the maximum number of generation has been reached, no improvement in certain number of generations etc., is checked. If it is satisfied, then the algorithm terminates (Figure 3.2).

3.2.2 A Short Tutorial on Simple Genetic Algorithms (SGA)

To demonstrate how SGAs work to the novice reader, an optimization example similar to the one that was used by Goldberg (1989) in his book is presented. In this example,

genetic operators are applied to a randomly generated initial population of 6 to demonstrate a single generation of the SGA. The optimization problem is a very simple maximization of the parabolic function with one independent variable on the integer interval [0, 31], Eq. (3.3). A plot of this function is depicted in Figure 3.7.

$$\begin{aligned} &\max f\left(x\right) = x^2 \\ &x = \left\{ x \in \mathbb{N}_0 \,\middle|\, 0 \le x \le 31 \right\} \end{aligned} \tag{3.3}$$

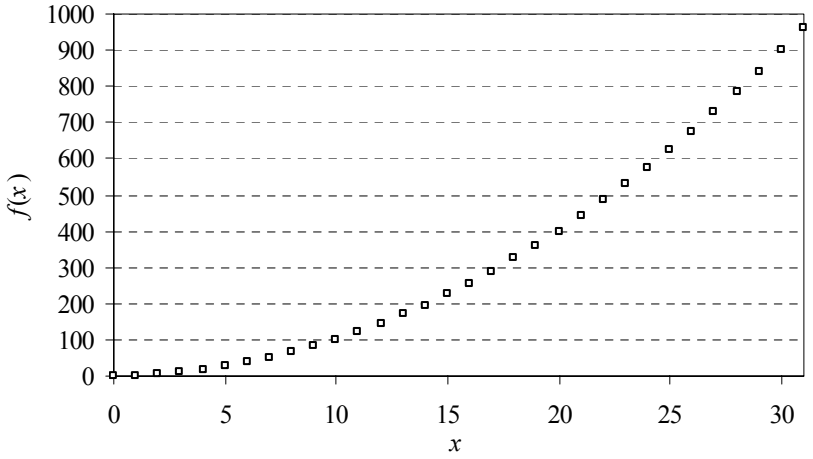

Figure 3.7. Parabolic function on the integer interval [0, 31]

To start solving the problem using a genetic algorithm, the representation or coding of the decision variable x using a finite string must be defined. The most obvious representation of the unknown variable is a binary unsigned integer with a length of 5 bits. Base 2 arithmetic is used to decode the strings into decimal numbers. An example for a binary string (00101) is shown by Eq. (3.4).

$$0 \cdot 2^4 + 0 \cdot 2^3 + 1 \cdot 2^2 + 0 \cdot 2^1 + 1 \cdot 2^0 = 4 + 1 = 5 \tag{3.4}$$

Using the binary representation, integer numbers between 0 (00000) and 31 (11111) can be obtained. In general, in base 2 binary strings with a length of n_{bit} integers

from zero to $2^{n_{bit}}-1$ can be encoded. These integers can be mapped to any decimal interval representing the search space defined by the variables of the NLP problem using Eq. (3.5).

$$x_i = l_i + \frac{x_{bin}}{2^{n_{bit}}-1}\left(u_i - l_i\right) \tag{3.5}$$

where x_{bin} is the nonnegative integer decoded from the base 2 binary representation. From the equation it is obvious that the precision provided by the binary coding is $\left(u_i - l_i\right)\Big/\left(2^{n_{bit}}-1\right)$. As a consequence, if the decimal precision is given then the number of bits required to obtain that precision can be calculated. For the parabolic function problem stated by Eq. (3.3), if a precision of at least one hundredth (0.01) is desired the number of necessary bits would be determined as follows.

$$n_{bit} = 12 \geq \frac{\ln\left(\frac{31-0}{0.01}+1\right)}{\ln 2} = 11.59 \tag{3.6}$$

For a precision of at least one hundredth, 12 bits are required in the binary coding and the actual precision obtained would be 0.00757.

Table 3.1. Randomly generated initial population

Individual	String	x - Value	$f(x) = x^2$
1	0 0 1 0 1	5	25
2	1 1 1 0 0	28	784
3	0 1 0 1 1	11	121
4	0 1 0 0 1	9	81
5	1 0 1 1 0	22	484
6	0 1 1 0 1	13	169
Average			**277.3**
Max			**784**

The optimization domain is now defined. Now we are ready to randomly generate the initial population of size 6. The initial population was created by tossing an unbiased coin 30 times (heads = 1, tails = 0). Table 3.1 lists the individuals of the initial population together with their decoded x values and fitness values.

The average fitness value of the initial population was 277.3 and the best individual has a fitness of 784, which is quite close to the optimum value of 961. In this example, tournament selection is used with a tournament size of 2, along with single point crossover with a crossover rate of 1 or 100% and uniform mutation with a mutation rate of 0.005 or 0.5%.

Table 3.2. First generation of individuals

Individual	Tournament Selection with Size 2		Single Point Crossover		x - Value	$f(x) = x^2$
	Competing individuals from initial population	Winner of tournament selection	Strings of parents (crossover site indicated)	Strings in the new population		
1	4, 2	2	1 1 | 1 0 0	1 1 1 1 0	30	900
2	5, 6	5	1 0 | 1 1 0	1 0 1 0 0	20	400
3	3, 1	3	0 1 | 0 1 1	0 1 1 1 0	14	196
4	6, 5	5	1 0 | 1 1 0	1 0 0 1 1	19	361
5	1, 6	6	0 1 1 | 0 1	0 1 1 1 1	15	225
6	4, 3	3	0 1 0 | 1 1	0 1 0 0 1	9	81
Average						**360.5**
Max						**900**

In Table 3.2, the results of a single generation are summarized. According to Figure 3.2, the first operator applied is selection. In Table 3.2, the corresponding identification numbers (Table 3.1) of the randomly picked individuals are shown. From the selected set of individuals, the one with the higher fitness value is picked for reproduction. After selection of the individuals, the single point crossover operator is

applied to a pair of individuals and is shown in Table 3.2 (the symbol, |, is used to identify the location of the randomly picked crossover site). There are no results listed for the mutation operator because the expected number of mutated bits in the entire population is $p_m \cdot n_{bits} \cdot n_{pop} = 0.15$. In this example, therefore, none of the bits underwent mutation. After the application of the genetic operators, the binary strings were decoded into the parameter values and the individuals' fitness were evaluated. Overall, the new generation shows better fitness characteristics than the initial population. The average fitness increased by 83.2 and the best individual's fitness increased by 116, which is only one away from the global optimum.

3.2.3 Advanced Genetic Operators

To enhance the performance of GAs, several researchers have focused on improving the basic operators of GAs or on inventing new ones. As an example, tournament selection was introduced to overcome the difficulties associated with premature convergence using the standard roulette wheel selection.

The first improvement considered in this research is related to the crossover operator. Using the single point crossover (Figure 3.5) certain combination of features encoded in the chromosomes cannot be obtained. Other arguments against the single point crossover include the asymmetry between mutation and crossover. The number of mutations in a chromosome ($p_m \cdot n_{bits}$) depends on the string length, while single point crossover does not. To remedy this discrepancy, researchers have experimented with other crossover operators (Eshelman et al. 1989). A natural extension of the single point crossover is the two-point crossover, or in general the multi-point crossover which is shown in Figure 3.8. Multi-point crossover works in a similar manner as single-point crossover. The chromosomes are sliced into segments that are then swapped between the two parents in an alternating fashion.

There exist more generalized versions of multi-point crossover that are particularly useful for one type of problem and quite poor for others. There is an enormous number of recommendations for the improvement of the crossover operator. Srinivas and Patnaik (1994b) experimented with adaptive probabilities of mutation and

crossover. The motivation was to maintain the diversity of the population and to extend convergence capacity of GAs.

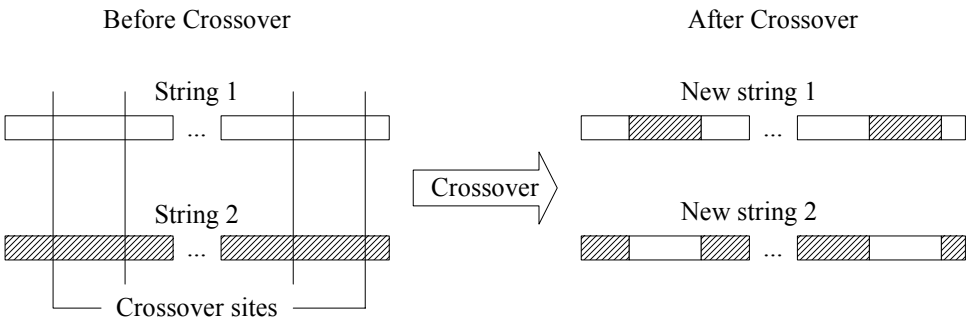

Figure 3.8. Multi-point crossover

In this approach, the probability of crossover is dependent on the fitness values of the individuals. Individuals with higher fitness are protected (undergo crossover with less probability), while poorer individuals are unprotected (more likely to undergo crossover). The crossover rate in an adaptive formulation in a maximization problem is defined by.

$$p_c = \begin{cases} k_1 \dfrac{(f_{max} - f')}{(f_{max} - \bar{f})} & \text{if } f' \geq \bar{f} \\ k_2 & \text{otherwise} \end{cases} \tag{3.7}$$

where k_1 and k_2 are positive constants (primary and secondary crossover rates, respectively) between zero and one, f_{max} and $\bar{f}$ denote the maximum and the average fitness values of the current population, and f' is the larger fitness of the two individuals selected for crossover. According to Eq. (3.7), individuals with below average fitness have a crossover rate of $p_c = k_2$. If one of the individuals selected for crossover is the best in the entire population, then the probability of crossover is zero. Individuals between the average and maximum fitness have a crossover rate that is linearly interpolated between zero and k_1.

Table 3.3. Binary and Gray codes for 4-bit strings

Decimal	Binary	Gray
0	0 0 0 0	0 0 0 0
1	0 0 0 1	0 0 0 1
2	0 0 1 0	0 0 1 1
3	0 0 1 1	0 0 1 0
4	0 1 0 0	0 1 1 0
5	0 1 0 1	0 1 1 1
6	0 1 1 0	0 1 0 1
7	0 1 1 1	0 1 0 0
8	1 0 0 0	1 1 0 0
9	1 0 0 1	1 1 0 1
10	1 0 1 0	1 1 1 1
11	1 0 1 1	1 1 1 0
12	1 1 0 0	1 0 1 0
13	1 1 0 1	1 0 1 1
14	1 1 1 0	1 0 0 1
15	1 1 1 1	1 0 0 0

In base 2 coded binary strings, slow convergence may result from the presence of Hamming cliffs. In base 2 binary representations it is possible that two points close to each other in the problem space may represent two points that are far apart in the representation space. An example is shown in Table 3.3. If the problem search space included integer numbers from 0 to 15 then a 4 bit binary string would be suitable for the representation. In this search space the integers 7 and 8 are consecutive, but in the representation space, these numbers differ in 3 bits or their Hamming distance is 3. If the optimum is located at the variable value of 8 but our current best individual in the population encodes the value 7, then three bits in the representation must be changed to obtain the optimum.

To remedy the problems associated with Hamming cliffs, Gray coding may be used. Gray coding has the property that two points close to each other in the search space

are also close to each other in the representation space. As shown in Table 3.3, Gray coding has the property that any two points next to each other in the search space differ by one bit only. Gray codes also form a closed loop in the sense that getting from one end of the search space to the other is only one bit apart (0 and 15 in Table 3.3).

Gray codes can be generated in several ways, including recursively or using linear transformation matrix. The algorithm for converting a binary number $\mathbf{b} = [b_1,\ldots,b_m]$ into a Gray code number $\mathbf{g} = [g_1,\ldots,g_m]$ and vice versa is given in Figure 3.9.

```
procedure Binary to Gray
begin
   g1 = b1
   for k = 2 to m do
      gk = bk-1 XOR bk
end

procedure Gray to Binary
begin
   value = g1
   b1 = value
   for k = 2 to m do
   begin
      if gk = 1 then value = NOT value
      bk = value
   end
end
```

Figure 3.9. Algorithms to convert binary and Gray coding

In SGAs, the exploration and exploitation of the search space is balanced fairly equally throughout the optimization process. In later generations it may be more beneficial to put the emphasis on exploitation while in early generations the exploration of the search is desired. By shifting the balance between exploration and exploitation of the search space fine-tuning of the results can be accomplished. Non-uniform mutation is one possibility for fine-tuning the system. The non-uniform mutation operator suggested by Michalewicz (1996) is defined for floating point variables. Therefore, a modified version of the original operator is presented that is valid for binary strings.

Consider a base 2 binary string in which the k^{th} variable is coded with m bits, $\mathbf{b}_k = [b_j,\ldots,b_{j+m}]$. In this string, bits that are located at the end of the string have lower

cardinality than the ones at the beginning. If the goal is to search a close neighborhood of the current solution one should flip the low cardinality bits to attain this task. Using non-uniform mutation, the probability that bits with lower cardinality can undergo mutation increases as the population ages. Let t and T denote the number of the current generation and the maximum number of generations allowed by the user, respectively. A function that gives the position of the bit that is mutated (flipped) as a function of the current generation, t, and string length, m can be defined.

$$\Delta(t, m) = j + \text{round}\left(mr^{\left(1-\frac{t}{T}\right)^h}\right) \tag{3.8}$$

where h is the iteration dependency factor (a usual value is 1.5), r is a random number between 0 and 1, and round() is rounding function to the nearest integer. The normalized contour plots of the bit position function can be seen in Figure 3.10 and Figure 3.11. Figure 3.10 shows the relative position of the bit (0 correspond to the beginning of the string while 1 corresponds to the end) subjected to mutation as the population ages (t/T increases). From the figure it is clear that mutation is more likely to occur for bits with low cardinality as the population ages. When the current generation number, t, is 10% of the maximum generations, T, then bits are more or less equally likely to undergo mutation regardless of their position. For population with high relative age (90%), the string is most likely to be mutated in its end segment. Figure 3.11 reaches a similar conclusion (with aging population mutation is likely to occur in the end portions of the string regardless the random number).

Michalewicz (1996) reported that GAs using the non-uniform mutation outperformed GAs not using non-uniform mutation with respect to the accuracy of the found optimal solution. In addition, GAs using non-uniform mutation converged faster to the optimum. For Gray coded strings, the cardinality of end bits are not as low as that of the base 2 binary coding, and therefore, the performance increase for GAs using non-uniform mutation may not be as pronounced.

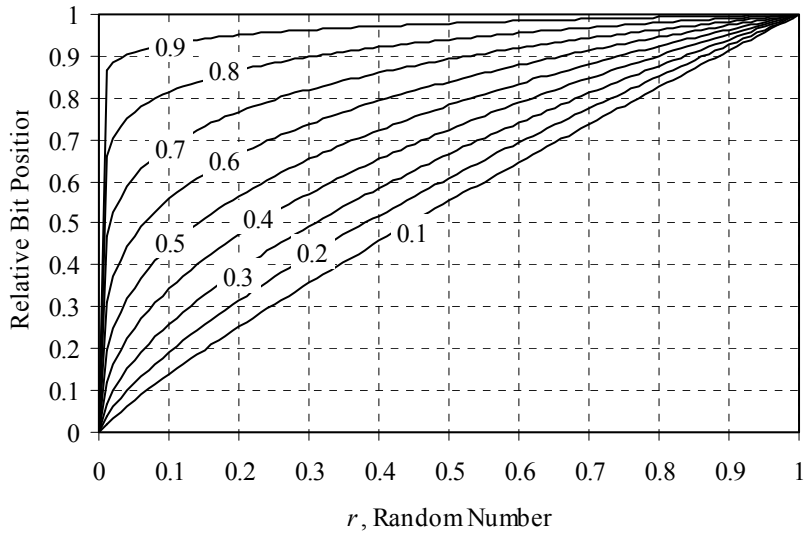

Figure 3.10. Normalized contour plot of the bit position function used in non-uniform mutation as a function of the random number; The level lines indicate the relative generation age, t/T and $b = 1.5$

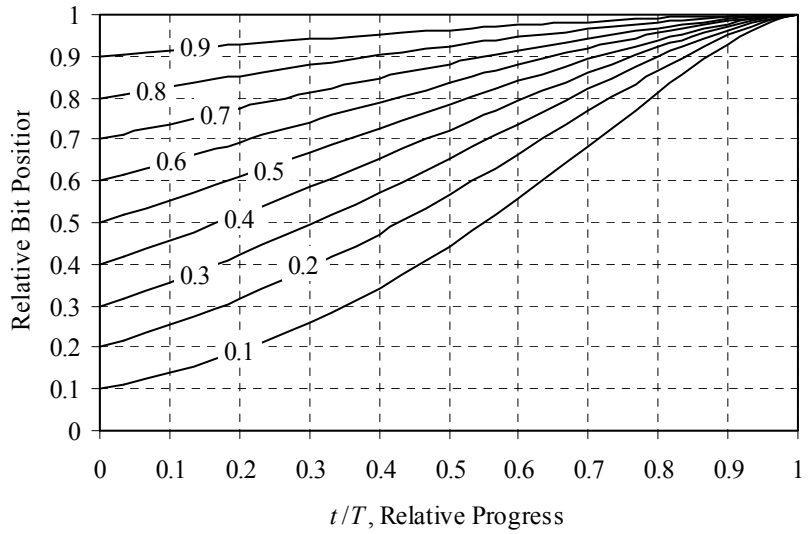

Figure 3.11. Normalized contour plot of the bit position function used for non-uniform mutation, as a function of the relative generation age, the level lines indicated are corresponding random numbers, r, $b = 1.5$

The last performance boosting strategy presented here is called elitism (De Jong 1975). The argument behind the elitist model is that the best individual found so far should be protected and retained to ensure that the fitness of the best individual never decreases between consecutive generations. The model is very simple. In an external string, the structure of the best individual is stored. If the best individual in the next generation is worse then the best individual found so far, then the worst individual in the population is replaced by the external string storing the best individual up to this point. Otherwise the best individual in the current population is copied to the external individual and retained. De Jong (1975) found that the elitist strategy significantly increased performance for unimodal functions, although on multi-modal functions it actually degraded performance. His conclusion was that elitism improves local search at the expense of global perspective.

3.3 Fixed and Implicit Redundant Representations

In the previous section, only a small number of advanced operators for the performance improvement of SGAs were considered. In addition, research has focused on improving the basic operations of SGAs by considering advanced biological phenomena. All SGAs share one common element: particular genes are represented in fixed format. One of the characteristics of the fixed representation typical to SGAs is that the optimization domain must be known beforehand. Each individual in the population represents one complete solution of the problem. The fixed SGA representation is a genotype representation of the whole problem domain and therefore can become very large. As a consequence, SGAs may perform poorly for problems having a large number of design variables (Michalewicz 1996). For example, a problem with 100 independent variables that are coded with 20 bits each results in a chromosome size of $100 \cdot 20 = 2000$. This number is quite large and explains the poor performance of SGAs for complex optimization domains.

3.3.1 Encoding for Damage Detection

In order to model a structure with reasonable accuracy, hundreds or thousands of finite elements may be required. Remember that in Section 2 the optimization problem for damage detection used in this research was formulated, Eq. (2.55) in which each finite element in the structural model was assigned a unique damage indicator. The primary goal of damage detection is to find the damage indicators for all finite elements. As a result, the number of independent variables in the damage detection optimization problem is equal to the number of finite elements in the model. The optimization problem search domain defined by the fixed SGA representation can be very large for these problems.

For the damage detection problem, however, even when the number of finite elements in the model becomes very large, the number of actual damaged elements is only a fraction of the total number of finite elements in the model. The difficulty presented for damage detection is that neither the number of actual damaged elements, nor their locations or severity are known beforehand. The assumption that only a small number of elements are damaged, is crucial in damage detection problems. In this case, the damage detection problem can be thought of as an inverse problem, in which the goal is to find system properties using a limited source of measured responses due to some external effect. The available information may not be sufficient to uniquely identify damaged elements when the number of damaged elements is relatively large. Therefore, obtaining a unique solution for multi-damage cases is often difficult or impossible. This special situation defines an unstructured optimization problem in which the number of independent variables is unknown, although bounded between zero and the number of finite elements in the model.

The fixed SGA representation for the defined damage detection optimization problem is quite straightforward. To use the fixed representation, each finite element in the model has a unique damage indicator, or in optimization terms, is an independent unknown variable. Therefore, the optimization domain is defined by the number of finite elements in the model. In Figure 3.12, each damage indicator is encoded as a binary string. The length is determined by the required precision of the encoded continuous

floating-point variables. The binary damage indicators are simply concatenated to form a string or chromosome. The total length of the string is equal to the number of finite elements times the number of bits required to encode a damage indicator, $n_e \cdot n_{bit}$. In other words, the length of the string is directly proportional to the number of finite elements. For complex problems, this means that the SGA has to tackle a search space defined by a large number of variables, which results in poor convergence or failure of the search.

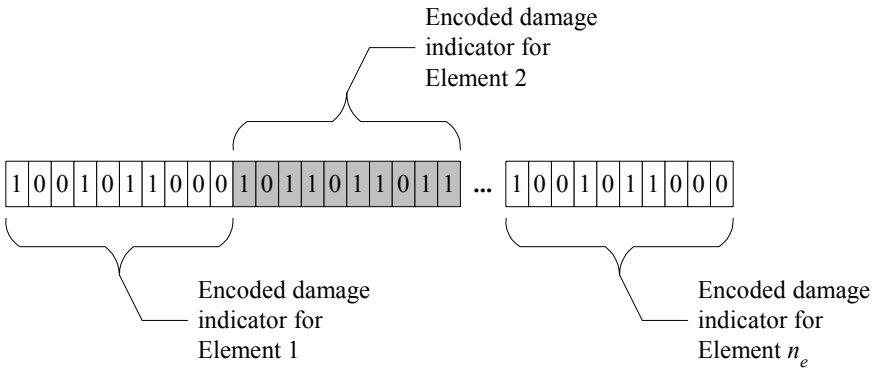

Figure 3.12. Fixed representation for damage detection

The implicit redundant representation proposed by Raich and Ghaboussi (1997a) can overcome the difficulties associated with the unstructured damage detection problem identified above. The implicit redundant representation (IRR) introduces redundant segments into the string, which allows the number of variables to dynamically change during the course of optimization. This property is appealing for damage detection problems in which neither the number of damaged elements nor their locations are known beforehand.

A typical IRR string for the damage detection problem is depicted in Figure 3.13. In this representation, three parts of the string can be identified: a predefined gene locator (GL) pattern; a gene instance, which is the useful part of the string; and redundant segments. Each gene instance consists of two parts, a segment encoding the finite element number (location of damage) and a segment encoding the damage indicator for that finite element (magnitude of damage). Between any two consecutive gene instances, one may

find a redundant segment that does not currently provide any information regarding a damaged element. The redundant segment may become a useful gene instance in later generations through the actions of genetic operations. Gene instances encode the parameter values using binary encodings (base 2 or Gray coding) similar to other GAs. To decode a damage indicator, the IRR string is parsed until a GL pattern is found that identifies the beginning of a gene instance. Then the finite element number identifying the damage location is decoded along with the corresponding damage indicator value. If more than one gene instance identifies the same finite element then the average of the damage indicators is taken and used to quantify the severity of damage. The IRR does not require the number of parameter values to be pre-specified, since the number of gene instances can be changed dynamically to reach a better solution implicitly implied in the objective function.

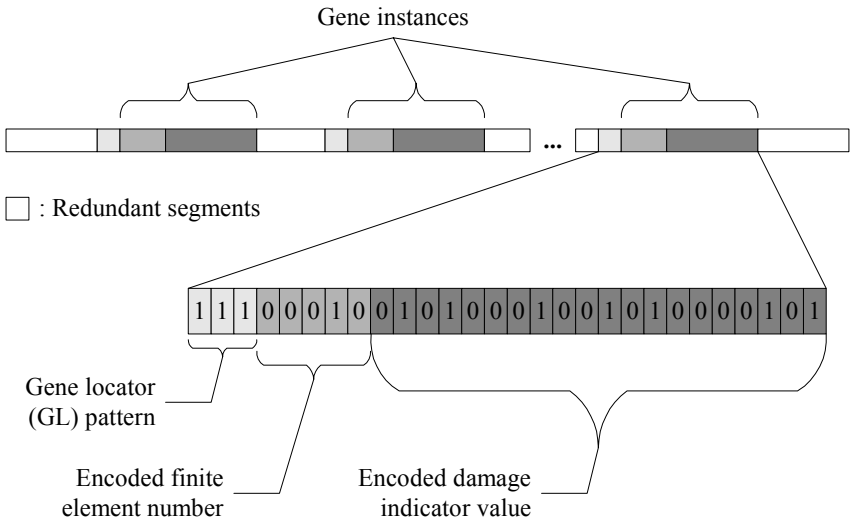

Figure 3.13. Implicit redundant representation (IRR) for damage detection

The structure of the GL pattern has an arbitrary meaning since there is not one preferred combination of binary digits that is superior over any other. The most influencing property of a GL pattern is its length. In Figure 3.13, the selected GL pattern has a length of three digits and the pattern consists of only binary ones, [1 1 1]. The

probability of finding a GL pattern in a binary string decreases as the length of the GL pattern increases. The probability of occurrence of a GL pattern consisting of l_{GL} bits is defined by the equation (Raich and Ghaboussi 1997b).

$$p_{GL} = \beta^{l_{GL}} \left(\frac{1-\beta}{1-\beta^{l_{GL}}} \right)^2 \sum_{j=0}^{l_{GL}-1} \beta_j \tag{3.9}$$

where p_{GL} is the probability of occurrence of a specific GL pattern, β is the probability of occurrence of a specific bit value (it is either 0 or 1, so $\beta = 0.5$), and l_{GL} is the number of bits in the GL pattern. For example, the probability for the [1 1 1] GL pattern is $p_{GL} = 0.07143$. The probable number of non-overlapping unique GL patterns that can be found in a string taking into account the length, l_g, of the encoded gene value determines the number of gene instances for an individual (Raich and Ghaboussi 1997b).

$$N_{GL} = \frac{\left(l_s - l_g + 1\right) p}{1 + l_g p} \tag{3.10}$$

where N_{GL} is the probable number of gene instances found in the string, l_s is the number of bits in the string, n_{bits}, minus (m-1) bits to account for the end of the string and l_g is the number of bits in an encoded gene instance, which equals to the sum of the number of digits used to encode the finite element number and the corresponding damage indicator value. The string length using IRR is allocated in accordance with the expected number of damaged elements (gene instances), which is specified by the designer. Using the expected number of damaged elements and the number of bits in an encoded gene instance, the chromosome length can be determined.

$$n_{bits} = \frac{N_{GL}\left(1 + l_g p_{GL}\right)}{p_{GL}} + l_g + l_{GL} - 2 \tag{3.11}$$

For the IRR GA, each individual in the population also represents one complete solution, but the solution is defined only by the damage indicators for a small subset of

the finite elements in the model, instead of maintaining a representation of all damage indicators. The dynamic redundancy of the IRR provides additional benefits such as less disruption of crossover and mutation due to the presence of redundant segments, dynamic enlargement and reduction of the search space, and exploration of fit members through the activation of redundant material into gene instances. The self-organizing capability of the IRR provides a beneficial representation for unstructured problem domains such as the one posed by damage detection investigated in this research.

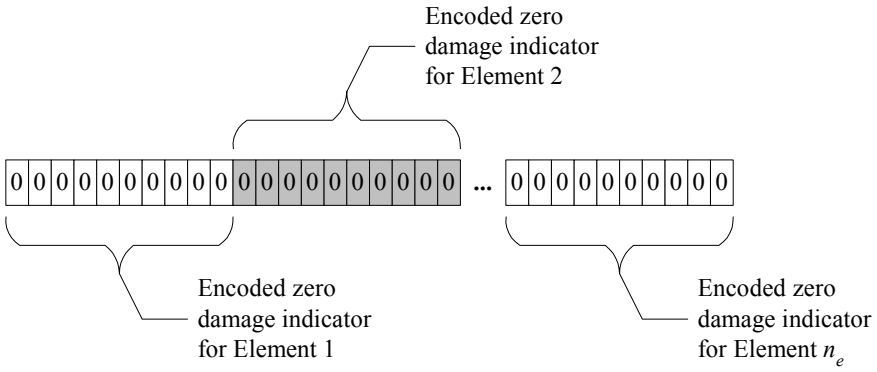

Figure 3.14. Zero damage individual using fixed representation

In damage detection problems it is often assumed that the number of damaged elements are small and the severities of these damages are also small then a zero damage individual can be used to seed the initial population of the GA. A zero damage individual encodes all finite elements with zero damage indicators. The underlying idea behind the use of a zero damage individual in the initial population is that this solution may actually be the best one in the initial population and can carry beneficial genetic information that enables the GA to find the optimum solution faster. A zero damage individual using the fixed representation is depicted in Figure 3.14. It is simply a string in which all bits are zero and therefore all damage indicators decode to zero. A zero damage individual using IRR is shown in Figure 3.15. In this representation the number of gene instances in the string is equal to the expected number of damaged elements. The GL patterns and gene instances are concatenated without any redundant segments between them. In each gene

instance the finite element number is randomly initialized while the damage indicator segment has all zero bits encoding a zero damage indicator.

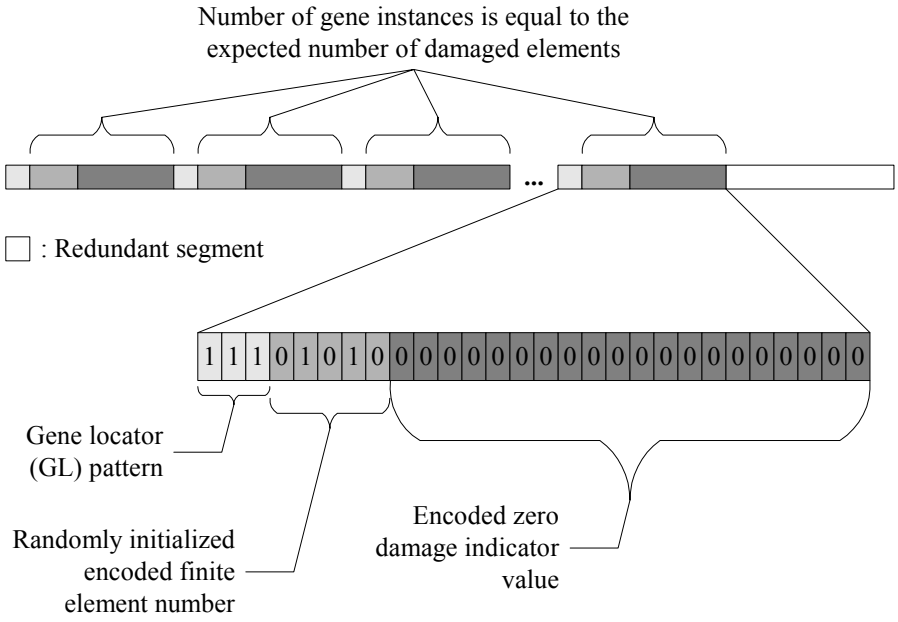

Figure 3.15. Zero damage individual using IRR

3.3.2 Encoding for Excitation and Sensor Layout Design

Similar to the studies performed on the damage detection problem, both types of gene representations (fixed and IRR) are adapted for the excitation and sensor layout design problem outlined in Section 2. In this problem, there is a set of DOFs where the excitation and/or sensors can be placed. These DOFs are collected in a vector at the beginning of each run, which is a one-dimensional array called the sensor location vector, $\mathbf{s}_l$. For example in a two dimensional frame type structure using Bernoulli frame elements (Appendix A), the excitation and sensors can be placed at any unrestrained DOFs in the horizontal or vertical direction. In most cases, however, the rotational DOFs are not available because of the difficulties associated with obtaining rotational DOF measurements.

The fixed representation gene for the excitation/sensor layout design problem is depicted in Figure 3.16. The first part of the chromosome encodes the excitation DOF. More precisely this is an index (a discrete number between 1 and the sensor location vector size, n_{sens}) of the senor location vector, which in turn identifies the excitation DOF. The second part of the gene consists of n_{sens} number of binary digits or "On/Off" switches identifying the DOFs where sensors are placed.

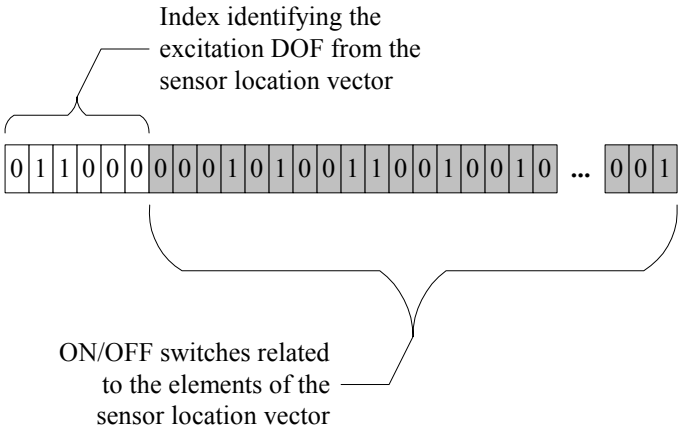

Figure 3.16. Fixed representation for excitation and sensor layout design problem

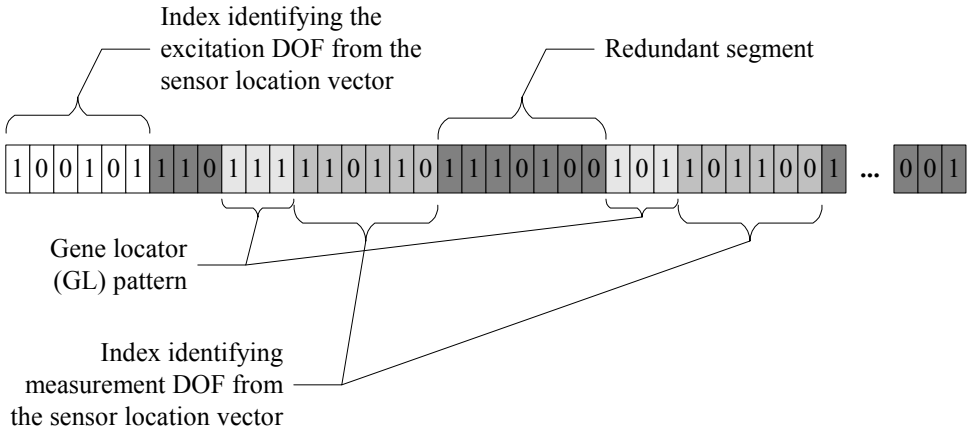

Figure 3.17. Implicit redundant representation (IRR) for excitation and sensor layout problem

The typical IRR gene representation for the excitation/sensor location problem is shown in Figure 3.17. The first part of the chromosome encodes the excitation DOF, which is identical to the chromosome defined for the fixed representation. In the second part of the IRR string, three different segments can be identified: the GL pattern identifying the beginning of a gene instance; the encoded sensor location vector index identifying a measurement DOF; and the redundant segments.

To identify the primary differences between the fixed and IRR representations, consider a simple cantilever beam problem consisting of 10 finite elements and 11 nodes as depicted in Figure 3.18. In this figure, node numbers are shown in regular text and the DOFs are labeled using italic numbers. The DOFs are numbered consecutively in the order of horizontal, vertical, and rotational DOFs, for each node starting from node 1. In this problem, sensors are placed only in the direction of the vertical DOFs and only the labels of the unrestrained vertical DOFs are defined in the sensor location vector. In total there are 10 locations where the excitation and sensors can be placed along the beam, which means that indices from 1 to 10 are encoded in the binary string. To encode 10 integer numbers, a 4-bit binary number (values from 0 to 15) is mapped to the integers ranging from 1 to 10. Consequently, the length of the fixed representation is 14, which is defined as four digits to encode the excitation DOF and 10 digits to encode the 1-bit "On/Off" switches.

Decoding the fixed representation GA string depicted in Figure 3.18 defines the following placements: the excitation is located at node 6 and four sensors are placed at nodes 3, 7, 8 and 11. In comparison, the IRR GA string shown in Figure 3.18 encodes three sensor locations and the excitation is the same as it was for the fixed representation. The first gene instance encodes the value 5, which map to DOF 17 at node 6. The other two gene instances identify sensor locations at node 10 and 3.

For this problem, the fixed representation works with a fully defined solution on the problem domain while the IRR represents a complete solution using only a smaller subset of the variables defined in the problem domain. For this simpler sensor optimization, the fixed representation may be more compact than the IRR because the coding of "On/Off" switches requires only one bit per sensor. As the structural model

becomes more complex, however, the IRR could be more efficient in finding solutions in the larger problem search spaces that must be defined.

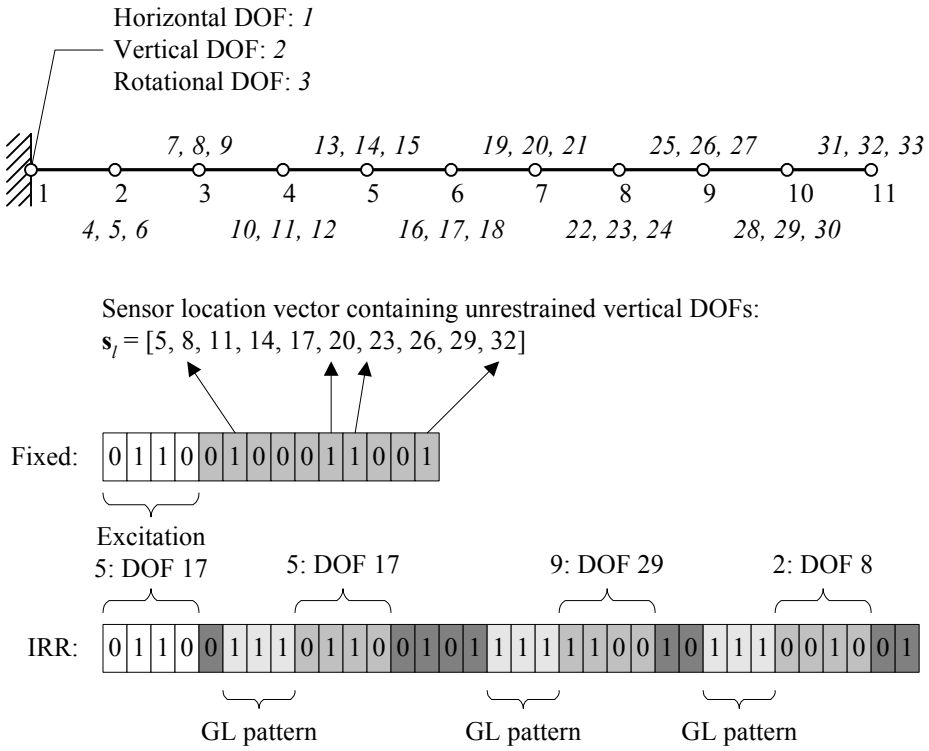

Figure 3.18. Comparison of fixed and IRR representations for the excitation and sensor layout design problem of simple cantilever beam

3.4 Local Optimizer, Hillclimbing Algorithm

In certain situations, GAs will have a slower convergence rate near the global optimum. To overcome this phenomenon, a local hillclimbing search technique is implemented to allow fine-tuning of the results obtained by the GA for the damage detection problem. Hillclimbing methods, like most local search algorithms, are iterative processes that use a single solution in the search space. The basic principle of all hillclimbing procedures is that if a point in the neighborhood of the current solution provides a better value in terms of the evaluation function then the new point becomes the current point. Otherwise, some other neighborhood is selected and tried out until no further improvements are obtained

or some other convergence criterion is satisfied. The main limitation is that hillclimbing procedures can only find local optima that are dependent on the starting point. Provided that GAs can find a solution in the region of the global optimum, hillclimbing can improve that solution locally with greater efficiency.

Hillclimbing algorithms differ in the way a new solution is selected in the neighborhood of the current solution. A version of an iterated hillclimbing algorithm is given in Figure 3.19. The first step in this implementation is to initialize the hillclimber (current point $\mathbf{x}_c$) with the best solution obtained by the GA. The local optimum of the problem is also stored in $\mathbf{x}_{local}$ initialized with the GA solution.

Next all possible neighbors of the current point are tested and compared with the current solution. If any of the neighboring points, $\mathbf{x}_n$, is better then the local solution, $\mathbf{x}_{local}$, then it becomes the local point. The neighbors of the current point are obtained using the step sizes, S_i, of each variable. The algorithm loops through each variable and modifies the current solution by first adding and then subtracting the corresponding step size to the current variable (damage indicator). Initially, the step sizes are equal to the decimal precision represented within the binary coding. Throughout the hillclimbing procedure, however, the individual step sizes are altered independently based on the failure or success of the new point. If there was an improvement in the new solution then the step size of the corresponding variable is multiplied by $\beta_1 = 1.5$. Otherwise it is multiplied by $\beta_2 = 0.5$. After testing all the neighbors of the current solution (looping through all variables), the current solution is replaced with $\mathbf{x}_{local}$ if it is better than the current point and a new iteration starts. If the there is no improvement in any of the variables, and all step sizes are smaller or equal to the decimal precision, then a local optimum is obtained and the procedure terminates. Otherwise, a new iteration starts until there is no improvement and all the step sizes are below the precision.

The success of finding the global optimum using hillclimbing depends on the initial starting point provided. Using the solution provided by the GA, hillclimbing techniques exploit this solution for possible improvements without further exploring the search space globally. Combining robust search procedures, such as GAs, with local

search techniques can result in increasing the overall effectiveness of the optimization procedure used.

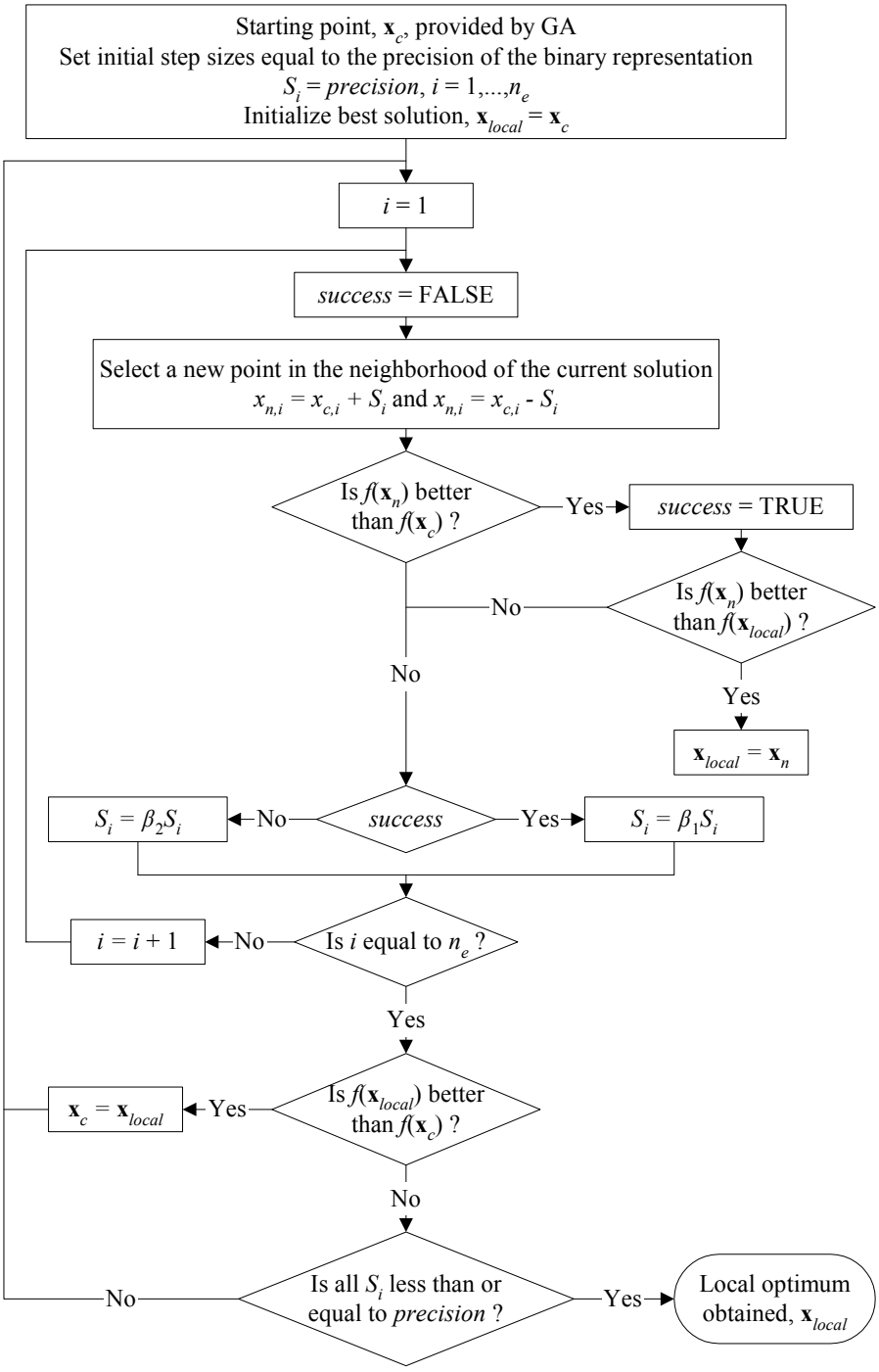

Figure 3.19. Flowchart of hillclimbing algorithm

3.5 Multiobjective Optimization Using Nondominated Sorting Genetic Algorithm

In many real-world optimization problems it is often difficult to come up with a single evaluation function that gives objective information about the quality of one solution over another. In addition, the objectives of an engineering design problem often contradict each other and an improvement in one objective may cause some other objectives to become less favorable. In single objective optimization, the aim usually is to find the best possible solution to a problem representing some local or global optimum. The notion of optimum, however, is redefined in the context of multiple objectives. The goal becomes finding a set of "best" solutions and allowing the designer to select the one that is the most favorable for the given environment. In these situations instead of trying to find a single "best" solution, an evaluation of the compromises or "trade-offs" associated with contradicting objectives may be desirable.

An intuitive approach to multiobjective (MO) optimization is the linear combination of objectives into a single scalar objective function using weights. For example, for k objectives the scalar objective is obtained.

$$\begin{aligned} &\text{opt} \sum_{j=1}^{k} w_i f_i(\mathbf{x}) \\ &\sum_{i=1}^{k} w_i = 1 \end{aligned} \tag{3.12}$$

where w_i is a nonnegative weighting coefficient representing the relative importance of the i^{th} objective. The difficulty with applying this approach is that very little is known about how to chose the weighting coefficients and that the results vary significantly depending on the importance (weighting) factors used. The benefit of this approach is that the algorithms developed for single objective optimization can still be used. The designer is required to run trials using several different sets of weighting coefficients on order to be able select the "best" solution for the given problem.

3.5.1 The Notion of Multiobjective Optimization

The excitation and sensor placement optimization problem considered in this research (Section 2) has two objectives: minimize the number of sensors used for measurements and maximize the information contained in the measurements. These two objectives contradict each other, since reducing the number of sensors usually decreases the information contained in the measurements, and vice versa. In cases where there is more than one objective function to optimize, a multiobjective optimization approach can be defined (Coello 2001), which involves optimizing the vector function consisting of k objective functions.

$$\mathbf{f}(\mathbf{x}) = \left[f_1(\mathbf{x}),\ \ f_2(\mathbf{x}),\ \ \ldots,\ \ f_k(\mathbf{x}) \right]^T \tag{3.13}$$

where $\mathbf{x} = \left[x_1,\ \ x_2,\ \ \ldots,\ \ x_n \right]^T$ is the vector of decision variables. The solution vector, $\mathbf{x}^* = \left[x_1^*,\ \ x_2^*,\ \ \ldots,\ \ x_n^* \right]^T$, must also satisfy the p equality constraints

$$h_i(\mathbf{x}) = 0 \qquad i = 1, 2, \ldots, p \tag{3.14}$$

and the q inequality constraints

$$g_i(\mathbf{x}) \geq 0 \qquad i = 1, 2, \ldots, q \tag{3.15}$$

In general, a single set of decision variables, $x_1^*, x_2^*, \ldots, x_n^*$, will not be obtained since it is rare to find a single solution that simultaneously optimizes all objective functions. Instead due to tradeoffs, multiple solutions to the problem will exist and the optimum set is defined as a collection of "trade-off" solutions.

This set of solutions, termed the Pareto optimal set was defined originally by Pareto (1896). A vector of decision variables $x^* \in \mathcal{F}$, where $\mathcal{F}$ is the set of feasible solutions, is Pareto optimal if there does not exist any $\mathbf{x} \in \mathcal{F}$ such that $f_i(\mathbf{x}) \leq f_i\left(\mathbf{x}^*\right)$ for

all $i = 1,2,\ldots,k$ and $f_j(\mathbf{x}) < f_j(\mathbf{x}^*)$ for at least one j assuming that all objectives are to be minimized. If the above conditions are satisfied for a vector of decision variables, $\mathbf{x}^*$, then it is said to be nondominated. The set of nondominated solutions is also called the Pareto front.

3.5.2 Nondominated Sorting Genetic Algorithm (NSGA)

To aid in the explanation of nondominated sorting genetic algorithms (NSGA), which are used in this research, the MO optimization problem for the excitation and sensor layout design, discussed in Section 2 is restated in Eqs. (3.16) and (3.17). The MO optimization problem concerns minimizing the number of sensors used and maximizing the total information contained in the measurements. The number of sensors used is at least one, but not more than a specified number, $n_{u,meas}$.

$$\begin{aligned} &\min f_1(\mathbf{x}) = n_{meas} \\ &\max f_2(\mathbf{x}) = \mathrm{I} \end{aligned} \tag{3.16}$$

subject to:

$$0 < n_{meas} \le n_{u,meas} \tag{3.17}$$

The decision variables for the sensors are logical variables. Each variable acts as an "On/Off" switch related to an unrestrained DOF in the finite element model where sensor(s) can be placed. In addition, a discrete decision variable, x_0, related to the excitation DOF is defined.

$$\begin{aligned} &\mathbf{x} = \left[x_1, \;\; x_2, \;\; \ldots, \;\; x_{n_{sens}} \right]^T \qquad x_i = \{0,1\} \qquad i = 1,2,\ldots,n_{sens} \\ &n_{meas} = \sum_{i=1}^{n_{sens}} x_i \end{aligned} \tag{3.18}$$

In MO optimization, the goal is to find a set of solutions that are members of the Pareto front. This is distinct from the goal of a single objective optimization problem of

finding the “best” solution. One benefit of GAs is that since GAs work with a population of solutions they have the potential to evolve several Pareto optimal solutions within a single run. Having a set of solutions allows the designer to select the “best” alternative in a given environment by evaluating the possible Pareto optimal solutions. A valuable overview of GAs in MO optimization is given by Coello (2001).

The nondominated sorting genetic algorithm (NSGA) used to evolve the Pareto front for the MO sensor optimization problem was proposed by Srinivas and Deb (1994a). The NSGA differs from a simple GA (SGA) only in the way the selection operator works, while the crossover and mutation operators remain the same. Before selection is performed, the population is ranked based on its individuals’ domination using a Pareto ranking. First, individuals that are nondominated are identified from the population and constitute the first nondominated or Pareto front. Individuals in the nondominated front are assigned the same dummy fitness value, which is used in the selection process. The dummy fitness value provides the same reproductive potential to the nondominated individuals in the same front. To maintain diversity of the population on order to maintain solutions over the Pareto front, the nondominated individuals are shared using their dummy fitness values. Then the nondominated individuals are removed from the population and the ranking procedure is repeated for the remaining individuals. The fitness value in the current rank is worse then the fitness value in the previous rank after sharing is performed. The ranking process continues until all individuals in the population are ranked.

In traditional fitness sharing (Goldberg 1989), the fitness degradation is performed if the phenotypic distance between two individuals in the current front is less than the maximum phenotypic distance allowed between any two individuals in the current front. The reason for performing fitness sharing is to avoid biasing individuals toward some Pareto optimal solutions. With fitness sharing a good distribution of individuals on the Pareto front can be maintained. In the sensor optimization problem considered in this research, one of the objective functions is discrete. Therefore, the definition of distance between two individuals becomes unnecessary. During ranking in this research, individuals in the first rank are assigned a fitness value of zero. In each

subsequent rank, the fitness value assigned is increased by one. Fitness sharing is performed if two individuals have the same number of sensors and carry the same level of measurement information. These individuals are ranked in the same level and are also possibly identical.

$$fit_i = \begin{cases} fit_i + \dfrac{1}{n_{pop}}, & \text{if } \left(f_1\right)_i = \left(f_1\right)_j \text{ and } \left(f_2\right)_i = \left(f_2\right)_j \\ fit_i, & \text{otherwise} \end{cases} \tag{3.19}$$

where *fit* is the fitness value of individuals, and *i* and *j* represent any two individuals in the population.

The only constraint defined for the excitation and sensor layout MO design problem is the limit on the number of sensors used to collect measurements. Depending on the gene representation, two constraint handling strategies were employed: repair of an individual and fitness penalizing (Michalewicz 1996).

For the fixed representation, an individual was repaired if the number of sensors was zero or exceeded the upper limit fixed by the user. The repair operator was implemented so that during early generations the individual was more likely to be repaired while in later generations it was more likely to be reinitialized. Re-initialization facilitated the exploration of the search space. The repair operator (Figure 3.20)defined selected the individual to be repaired and randomly turned off (changed the bit from one to zero) sensor locations until the number of sensors turned on equaled to a randomly selected number of sensors between the fixed limits. The re-initialization operator replaced the selected individual with a new individual that has a randomly selected number of sensors at randomly selected locations.

For the IRR representation, the gene length was calculated based on the maximum number of sensors allowed using the average number of gene instances that can be present within the string length. While the selected string length itself gives a limit on the maximum number of sensors that can appear in the gene, it still is possible that the encoded number of sensors exceeds the upper fixed limit. In situations where the number of sensors encoded was above or below the maximum or minimum number of sensors,

respectively, the fitness (or rank) of the corresponding individual was degraded. Degrading the fitness of an individual reduces its chances to reproduce or survive.

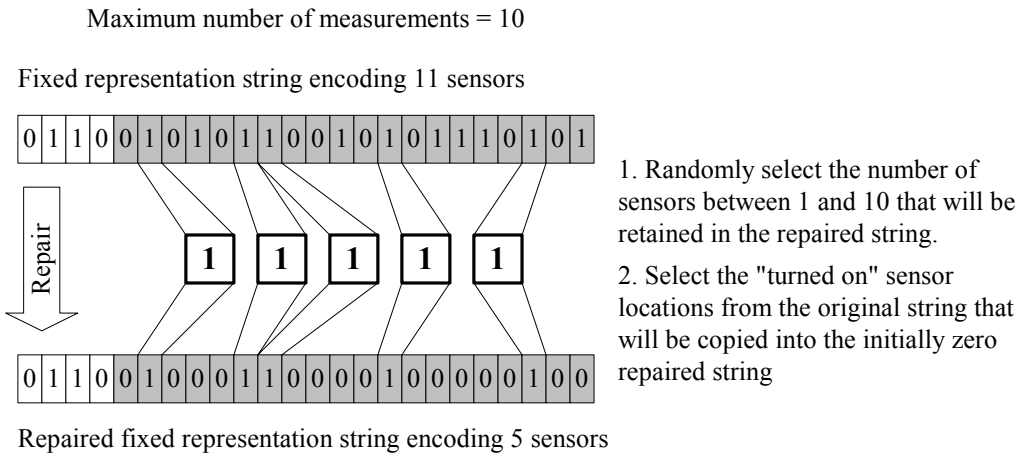

Figure 3.20. Repair operator for fixed representation strings

Because in an NSGA there is not a single individual that is superior to all the others, some of the advanced genetic operators have to be reconsidered. For example in adaptive crossover, the average fitness value of individuals and the fitness of the individual selected for crossover were used to compute the crossover rate. In the NSGA, individuals are evaluated according to their rank and not to their fitness value. Moreover, taking the average fitness of all individuals would not result in an objective measure because there is no connection between the ranks of individuals that represent one or ten sensor locations. The adaptive crossover for the MO sensor layout problem was modified, which used the primary crossover rate for individuals in the Pareto front and the secondary crossover rate for all other individuals.

Elitism also needs to be reconsidered. The difficulty again is that there are several individuals in the Pareto front that are equally superior to any other individuals in the population. Instead of having a single external individual, an external population of the Pareto front was stored. If the best individual's information measure for a given number of sensors was worse than the information measure of the corresponding individual in the

elite external set, then the worst individual was replaced with the corresponding string in the elite external population. Difficulties arose when there were no individuals representing a given number of sensors. In these situations, individuals representing most highly populated sensor numbers were selected to be replaced in the elitism process, which required additional bookkeeping of the distribution of individuals with respect to the number of sensors.

4 COMPUTATIONAL PROGRAMMING

The implementations of the SDIM and the excitation/sensor layout design problems required considerable computational programming. In a computational sense, there were two major parts of the implementation: a finite element procedure to evaluate the objectives and an optimization module, which included the genetic algorithm and the local hillclimbing method, to search for optimal solutions for both types of optimization problems. The damage detection and excitation/sensor layout programs were coded in C++ (Deitel and Deitel 2001) using Microsoft Visual C++ and the Microsoft Foundation Classes MFC (MSDN Library 1998, Bates and Tompkins 1998). To facilitate and hasten the development of the algorithms, the Maltab C/C++ Math Library 2.1. was used for matrix calculations (i.e. assembly of stiffness and mass matrices, eigenvalue and eigenvector extraction, etc.) in the finite element model (MATLAB 1999b).

The complete program consisted of three major modules: 1. preprocessor and a utility program, 2. processor including the finite element, GA and hillclimbing implementations, and a 3. postprocessor including an easy to use graphical user interface. These three units were combined into a single program. Only the utility program, which was used to generate simulated measurement data, remained separate. The overall software developed is extensive. The code consisted of about 15,000 lines, which is approximately equivalent to 320 legal-size printed pages using Times New Roman 12 point fonts and single spacing. Installation of the program was automated using InstallShield for Microsoft Visual C++ 6 (InstallShield 1997).

Extensive verification of the finite element and the genetic algorithm modules was performed on a range of test cases. The finite element module was tested by comparing vibration response results to those provided by the ABAQUS general finite element software (ABAQUS/Standard 2001). The genetic algorithm was also verified using standard optimization test functions for which the optimum solutions were known, including De Jong's Function 1 (F1), Rosenbrock's Banana function (F2), Rastrigin's function (F6), and Schwefel's deceptive function (F7).

4.1 Preprocessor and Utility Program

In this research, the measurement data were simulated using a utility program called *ModalFEM*. This program generates FRF input files for different finite element models using Bernoulli type frame elements (APPENDIX A). The user provides an input text file (*.inp) containing the finite element model of the structure. Using the input file, the utility program generates a binary MATLAB data file (*.mat) that contains simulated measurement data for specific excitation and measurement locations. Since this is a MATLAB data file it can be read into MATLAB and processed or verified by the user as necessary.

The input text file for the utility program works with cards and each card processes a different type of information. The cards used in the input files resemble those used in ABAQUS input files (ABAQUS/Standard, 2001). A list of the cards and their roles in the input file can be seen in Table B.1 of APPENDIX B. A sample input file for a cantilever problem is shown in Figure B.1 of APPENDIX B. Although these input files are very similar to ABAQUS input files, they are not compatible. It the graphical user interface of ABAQUS is used to generate the input file, it still must be manually edited to match the syntax of the *ModalFEM* program. Lines in the input file are commented out by using the standard C++ comment symbol "//" and lines starting with comment symbols are simply skipped. A typical input file contains the node locations and elements that span those nodes, in addition to cross-sectional area and moment of inertia information. When generating an input file representing the damaged structure for which simulated data are needed, the damaged members are grouped together and are assigned a material property having a modified (reduced) modulus of elasticity. This modified value corresponds to the severity of damage imposed in those members. Several of these groups can be defined to simulate different levels of damages in the same structure.

The program developed for solving the damage detection and excitation/sensor layout design problems is called *GaDamDet*. This program was built in the Windows environment and consists of the preprocessor, processor and postprocessor modules. The main menu bar of the program is depicted in Figure 4.1. The preprocessor and processor

functions can be accessed through the “Settings” menu or toolbar (Figure 4.2). The first four items in the settings menu correspond to preprocessor functions. The first item “Objective Function” enables the user to select the objective function and type of optimization (damage detection or excitation/sensor layout) through a dialog box (Figure B.2 of APPENDIX B).

By clicking on the “Genetic Algorithm” submenu item (Figure 4.2) a property sheet comes up with six tab items on it (Figure B.3 of APPENDIX B). The first property page, “population”, contains input items pertaining to the population or its initialization, such as population size, number of significant digits, random seed number, tournament size, and a checkbox for seeding the initial population with a zero damage individual. The next five property pages are shown in Figure B.4 of APPENDIX B. The “Convergence” property page takes the input for the maximum number of generations allowed and another convergence parameter “stop if no improvement”, which terminates the algorithm if there was no improvement within a certain number of generations. On the “Crossover” property page, the user can select the number of crossover sites. By choosing adaptive crossover, both the primary and secondary crossover rates must be input. Equal probability crossover requires only the primary crossover rate to be input. The mutation type (uniform or non-uniform) is selected through the “Mutation” property page and the rate of mutation is also entered. Non-uniform mutation is only implemented for the fixed representation GA, and in this case the iteration dependency factor is also an input parameter. The next property page in Figure B.4 of APPENDIX B is the “Variables” dialog enabling the selection of the fixed or IRR representations. When selecting an IRR, in addition to the number of variables, the user also has to input the expected number of damaged elements (gene instances, only if damage detection is to be performed) and the length of the GL pattern. The last property page of the “Settings - Genetic Algorithm” menu is the “Switches” dialog. On this panel, the user can turn on elitism and/or hillclimbing and also select between base 2 binary or Gray coding. A reduced version of the hillclimbing algorithm is also available in which hillclimbing is only carried out for variables carrying a damage indicator value greater than zero. In this case, when a

damage indicator becomes zero during hillclimbing it is removed from the set of variables being optimized.

Figure 4.1. Main menu structure of *GaDamDet* program

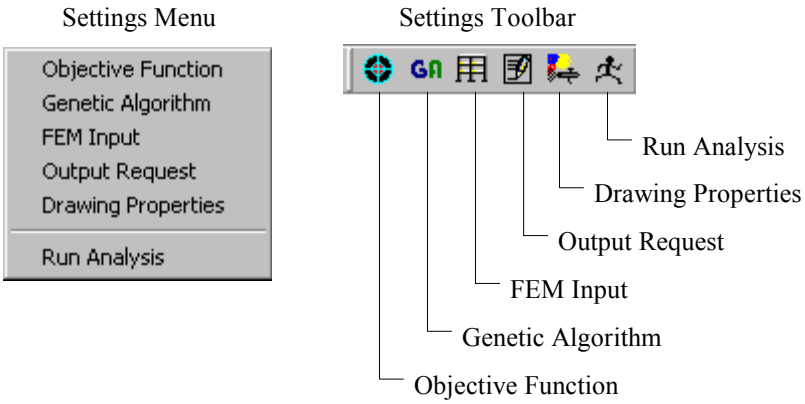

Figure 4.2. Settings menu and its corresponding toolbar of *GaDamDet* program

The next preprocessor module is associated with the finite element and measurement data input. By clicking the "FEM Input" submenu of the "Settings" main menu or its corresponding toolbar icon (Figure 4.2) a dialog box opens, in which the finite element input file and the MATLAB data file including measurement data can be selected (Figure B.5 of APPENDIX B). The finite element input file (*.inp) has the same structure as the input files used by the utility program *ModalFEM*. The only difference is that this input file contains information about the undamaged or baseline structure. This baseline structure is used to adjust the damage indicators of the finite elements to match the FRFs with the measurement data. On the "Finite Element" dialog (Figure B.5 of APPENDIX B) the finite element input file is read into a scrollable edit box to enable the user to check the syntax and verify that the correct input file is used in the analysis. In addition the finite element input file is used to identify the excitation and measurement

location in the MATLAB data file (*.mat), which can be selected by clicking the "Open Matlab File" button.

The last preprocessor module is the "Output Request" dialog box, which is shown in Figure B.6 of APPENDIX B. This function is accessed by pointing to the "Setting" main menu and then clicking on the "Output Request" submenu (Figure 4.2). On this panel, the user can control the frequency of information written to the output files and the amount of data that is output during each run. Output information can be written into text files (*.txt) and/or postprocessor binary files (*.gdd), which are only readable by the postprocessor interface of the program *GaDamDet*. By checking the "Auto Save" option, the postprocessor output is saved every time information is written to it so that information will not be lost if the system crashes or another disruption occurs. Restart of an analysis is not provided in this version of the program. The frequency of output is controlled by the recursive equation in Eq . (4.1).

$$n_{out,i} = n_{out,i-1} + B\left(i-1\right)^{k_3} \tag{4.1}$$

where $n_{out,i}$ is the i^{th} output generation number, B is the base multiplier, and k_3 is the output controlling exponent. As an example if $n_{out,1} = 0$, $B = 1$, and $k_3 = 0$ then information for all generation are output. However, if $n_{out,1} = 0$, $B = 5$, and $k_3 = 2$ then the sequence of generation numbers for output is 0, 5, 25, 70, 150, etc.

Although input error checking is done in the program, the program does not guarantee that false input parameters cannot be entered. This is especially true for the finite element input files for which syntax error checking is performed but the validity of input parameters is not checked. Careful inspection of the finite element input files is required to avoid fallacious results of damage detection and excitation/sensor layout design.

4.2 Processor

The processor is the main computational unit of the program and is mostly hidden from the user. Therefore, to the user it acts as a black box. The processor can be accessed

through the “Settings” main menu by clicking on the “Run Analysis” submenu or the corresponding toolbar (Figure 4.2). Before executing an analysis, input parameters and files are checked one more time for consistency. If any errors are found the user is notified to correct those mistakes. The processor uses the MATLAB C/C++ Math Library 2.1. (MATLAB 1999b) to store structural stiffness, mass and damping matrices and to perform the eigenvalue decomposition of FRF matrices. The eigenvalue decomposition has to be done each time the fitness value of an individual is required. The eigenvalue solver uses an iterative algorithm for the extraction of modes. Therefore, only a limited number of the modes in the low frequency range are included in the analysis, which is defined in the finite element input file. Usually the number of modes included in the modal decomposition should cover a frequency range that is at least twice as large as the highest measured frequency in the FRFs (Gatti and Ferrari 1999). Although the evaluation of FRFs typically takes less than a second, the total processing time due to the iterative computations in a GA can be very large. Assuming the fitness (FRF) evaluation takes one second, the approximate total computational time for a population size of 200 and 200 generations is $1 \cdot 200 \cdot 200 = 40{,}000$ seconds which is equivalent to 11.11 hours.

Monitoring the results during the analysis is beneficial in order to make decisions about the progress of the GA. If there is no progress then the user is able to terminate the program, while preserving the information collected up to the point of termination. Since the program is multitasking, the processor can run independently from the graphical user interface. Another desirable program feature would be restarting a terminated trial (e.g. with different settings), but this is not implemented in the current program.

The user is able to monitor the progress of the algorithm in three ways. The first way of monitoring progress is through the “Monitor” dialog (Figure B.7 of APPENDIX B). On this panel, the elapsed time, current generation number, and individual information, as well as the progress bars of the convergence criteria, can be found. The second progress monitoring capability is a child window of the “Monitor” dialog called the “Monitor Graph” dialog, which can be displayed by clicking on the “Hide/Show Graph” button. A typical “Monitor Graph” plot obtained for an IRR GA damage detection case study trial, generated by the “Monitor Graph” window, is shown

in Figure 4.3. On this graph, four separate measures are monitored and updated continuously. The best individual's fitness and the average fitness of the population are plotted in the upper graph, while the number of gene instances in the best individual and the average number of gene instances are plotted in the bottom graph. All figures can be zoomed dynamically by grabbing the handles located at the left and bottom corners of the plot. There is also a vertical cursor line (located at generation 93 in Figure 4.3) that can be grabbed and moved along the iteration axis, which in return dynamically updates the generation information displayed in the graphs. The different measures can be turned on and off to examine them independently. In certain situations, a semi-log plot of the fitness values versus the iteration number will show convergence better than linear plots. The user can switch between linear and semi-log plots to evaluate convergence. A "Monitor Graph" plot for a fixed representation GA is shown in Figure B.8 of APPENDIX B, which only plots the two progress measures but is essentially the same as the one discussed for IRR GA. In a typical plot (Figure B.9 of APPENDIX B) for an excitation and sensor location optimization problem, the individuals are plotted in the objective space. This plot shows the progress of the Pareto front, as well as the distribution of dominated individuals along the number of sensors axis.

Another monitoring technique uses the features provided by the postprocessor to plot the actual structure (cantilever beam, unbraced frame) or the corresponding string elements. This allows the damage indicator values of elements, or in case of sensor optimization the location of excitation and sensors, to be continuously monitored. The genotype of a subset of individuals can also be monitored, which provides the user with valuable information concerning the diversity of the population. These features are all part of the postprocessor and further details are discussed in details in Section 4.3. All of the monitoring capabilities assist the user in determining the real-time performance of the GA with the given parameters and the power to subsequently terminate trials with poor input parameters or prematurely abort a run if the current results meet the designer's standards.

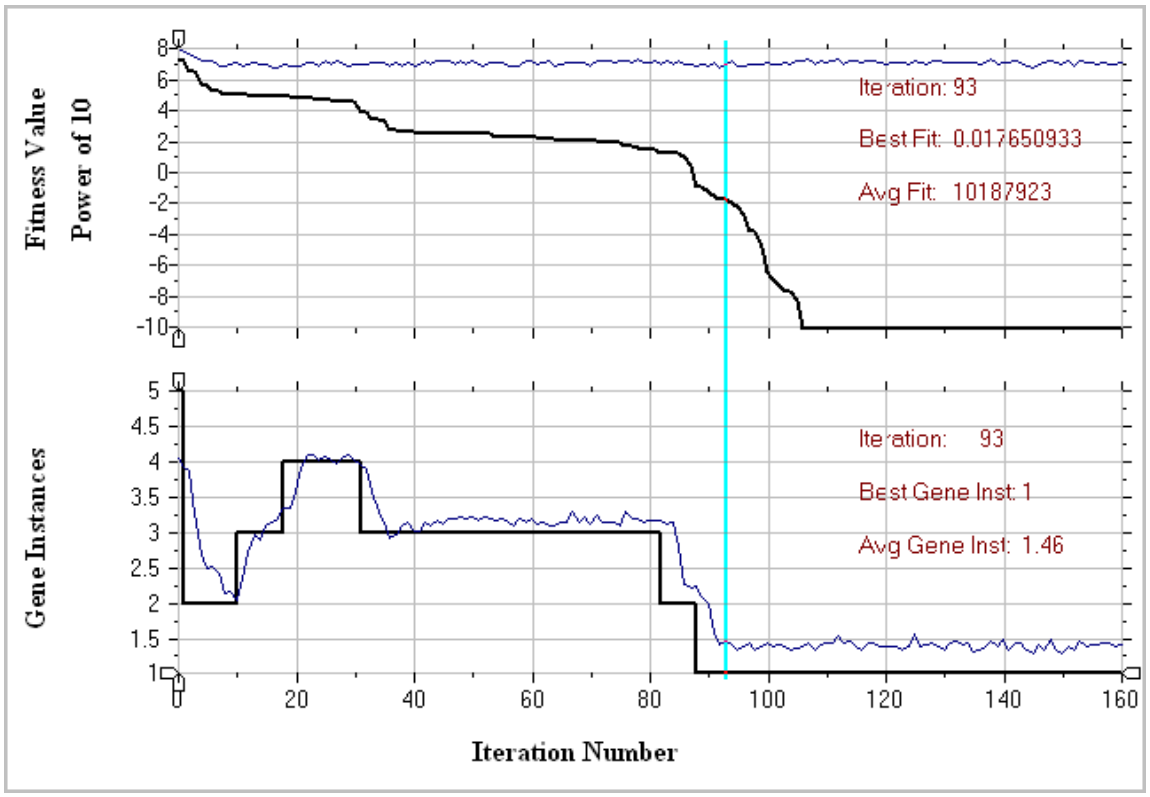

Figure 4.3. Monitor graph of an IRR GA run

4.3 Postprocessor

The postprocessor of the program *GaDamDet* enables the user to efficiently evaluate the results obtained in a graphical environment with easy to use navigational capabilities. Most of the postprocessor functions are available through the "Results" main menu (Figure 4.1). The "Results" menu and its submenus are depicted in Figure 4.4 and the corresponding toolbars in Figure 4.5. The navigation functions ("Navigate Generation" and "Navigate Individual") provide tools to quickly find a specific individual in a certain generation. In the "Results" toolbar (Figure 4.5), there are additional combo boxes with dropdown menus listing all the available generations and individuals for postprocessing. By simply selecting a candidate from the dropdown menu, the user can directly navigate to a specific location in the output file. The "Plot Convergence" menu brings up the "Monitor" (Figure B.7 of APPENDIX B) and "Monitor Graph" (Figure 4.3) dialogs

containing the final convergence plots. The “Export to Text” function outputs results into a text file defined by the user.

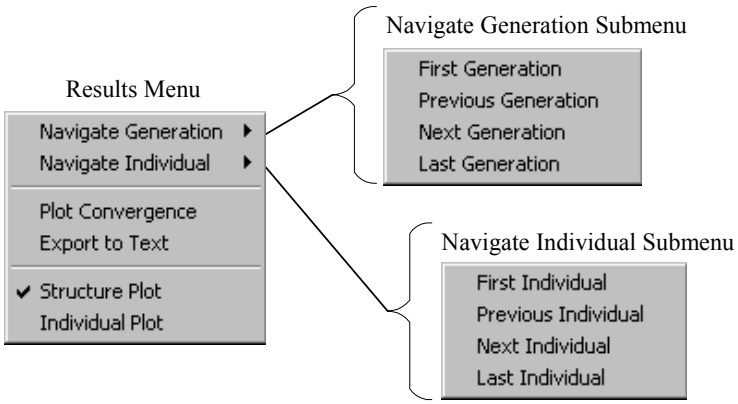

Figure 4.4. Results menu and its submenus

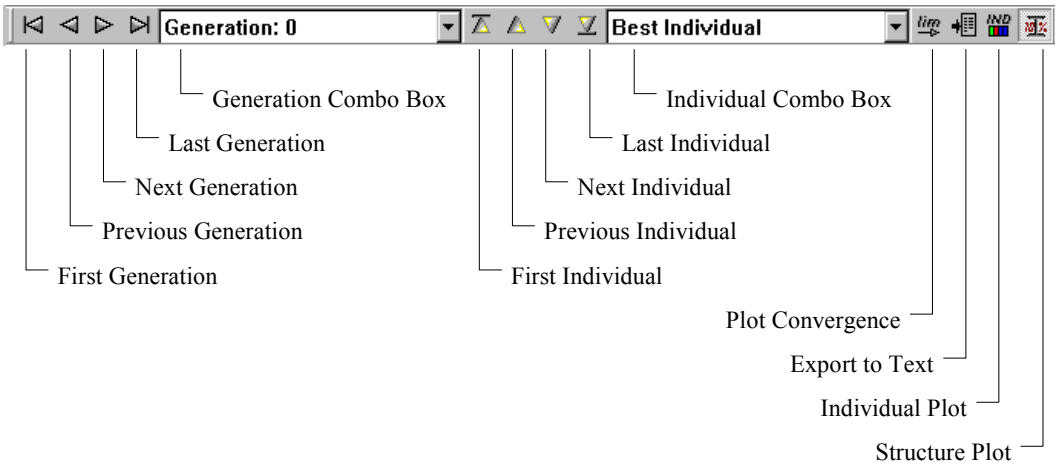

Figure 4.5. Results toolbar corresponding to “Results” menu and its submenus

There are two mutually exclusive visualization functions provided in the “Structure Plot” and the “Individual Plot” submenus. The later draws the current individual’s chromosome on the graphical output window. An example of this output can be seen in Figure B.10 of APPENDIX B. The “Individual Plot” therefore, contains crucial information about the string such as fitness value, representation type, generation number,

and number of gene instances. Using the “Individual Plot” facilitates the comparison of individuals in the same generation, which aids in providing essential information about the diversity of the current population.

By selecting the “Structure Plot” menu, the two-dimensional structure consisting of frame elements is drawn in the graphical output window. An example for a cantilever beam is shown in Figure B.11 of APPENDIX B. This view is suitable to reveal the results of damage detection or excitation/sensor layout design. There are additional functions associated with this view that can be found under the “View” menu (Figure 4.6). The first five tools appearing in the “View” menu are all mutually exclusive, in that only one can be selected at a time. The first tool in this set is the “Selection Tool”. If this tool is selected and the user moves the cursor over an element then that finite element is highlighted and a tool tip (small rectangular window used to identify the task of a toolbar) appears showing the percent damage indicator for the highlighted element. When the user double clicks on an element, a dialog box opens identifying the element number and the corresponding damage indicator value (Figure B.12 of APPENDIX B). The “FullView” function brings the entire structure into the drawing area. The other zooming and view tools are the “Box Zoom”, “Zoom In/Out”, and “Pan View” that are common in every CAD software and the names are self-explanatory.

By selecting the “Drawing Properties” function (Figure 4.2) from the “Settings” menu, the appearance and the level of details of the drawing area can be changed when “Structure Plot” is selected. This menu option brings up a property sheet with three tabs on it related to “Elements” (Figure B.13 of APPENDIX B), “Legend” and “Nodes” (Figure B.14 of APPENDIX B) properties. The different panels provide options to turn on and off certain features such as a color code legend box for damage detection, excitation and/or sensor locations (excitation symbols are a sine wave and sensor symbols are a circular gauge with a needle pointing in the direction of measurement, Figure B.11 of APPENDIX B), element and node numbering, and changing font styles.

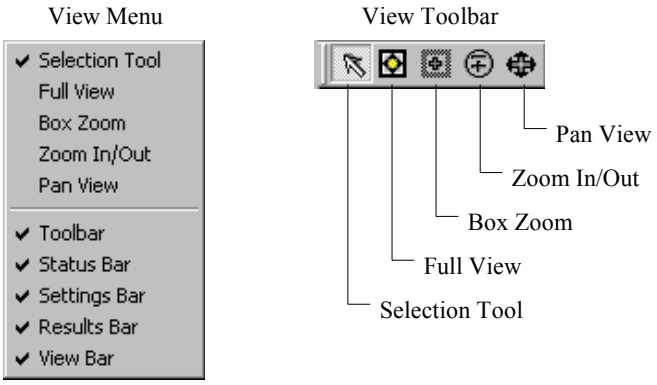

Figure 4.6. View menu and its corresponding view toolbar

5 DESCRIPTION OF CASE STUDIES

A series of case studies were investigated to evaluate the effectiveness of the proposed damage detection and excitation/sensor layout design procedures. In this research, trials were performed using both the fixed SGA representation and the IRR GA representation to compare their performance on both types of problems. Simulated measurement FRF data were generated for all test cases using the *ModalFEM* program discussed in Section 4. The case studies can be divided into three different groups: 1. Simple beam structures, including a cantilever and a two-span continuous beam modeled with a relatively small number of finite elements; 2. Moment frame structures, including a three-story, three-bay unbraced frame with 81 finite elements and a two-story, three-bay cross braced frame with 46 finite elements; and 3. Two-span continuous beam structure modeled with 50 finite elements, which were previously investigated by Kim and Stubbs (2002). The case studies defined in the first set are designed to model single damage situations and the effect of excitation/measurement location as well as to simulate multi-damages and to account for the number of measurement locations. The frame structure case studies defined have single and multiple damages imposed that represent beam, bracing or joint deterioration both in the columns and beams. The frame case studies are intended to verify the adequacy of FRF's as a sensitive vibration signature for damage detection and the robustness of the procedure. The last set of case studies (two-span continuous beam with 50 elements) provides a comparison of results obtained in this research directly with test cases from literature that used SDIMs based on modal information (Kim and Stubbs 2002). The performance of the SDIM developed in this research is compared with the modal-based SDIMs to assist in identifying strengths and weaknesses.

In addition, the effect of noise on the accuracy of SDIM results obtained was studied for all test case studies. In order to introduce noise into the measurements, normally distributed random noise was added to the simulated FRF data with zero mean

and a variance of unity. The accelerance FRF including noise can be obtained from the FRF without noise using the following equation.

$$\bar{A}_{jk} = A_{jk}\left(1 + y_n \,\text{randn}()\right) \tag{5.1}$$

where $\bar{A}_{jk}$ is jk^{th} measured FRF including noise, A_{jk} is the jk^{th} measured FRF without noise, y_n is the noise level (e.g. 0.05 relates to a 5% noise level) and randn() is the random noise generator function in MATLAB (MATLAB 1999b).

To evaluate the benefit and significance of the excitation and sensor layout design, an optimized layout is obtained using the MO methodology developed in this research and applied to all case studies. The damage detection results obtained using the optimal layouts are compared with the SDIM results that do not use optimum sensor layouts.

5.1 Simple Beam Type Structures

5.1.1 Simple Cantilever Beam

The first set of case studies focused on two beam type structures: cantilever beam and two-span continuous beam. The finite element mesh of the cantilever beam is shown in Figure 5.1, in which regular numbers indicate node numbers and element numbers are in italics. The finite element mesh of the two-span continuous beam is depicted in Figure 5.2. Both the cantilever and the two-span continuous beams are constructed of W12 × 65 standard steel sections with the cross-sectional properties listed in Figure 5.3. The Young's modulus of steel, E, is 207 GPa (30,000 ksi), Poisson's ratio, ν, is 0.3, and the mass density, ρ, is 7780 kg/m^3 (0.000728 lb-s^2/in^4) for all cases in this set.

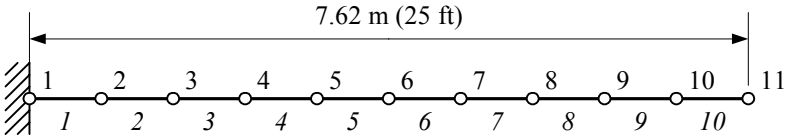

Figure 5.1. Cantilever beam modeled with 10 finite elements, node numbers are regular and element numbers are in italics

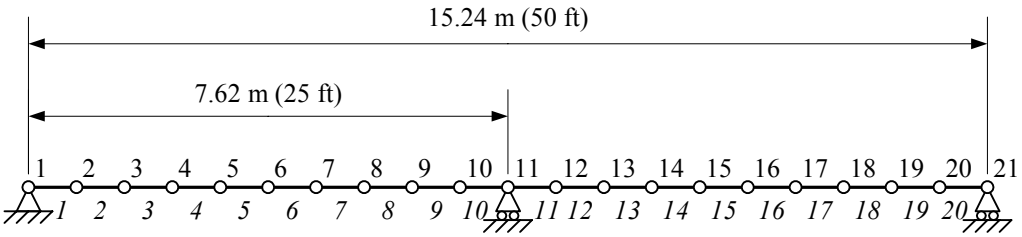

Figure 5.2. Two-span continuous beam modeled with 20 finite elements, node numbers are regular and element numbers are in italics

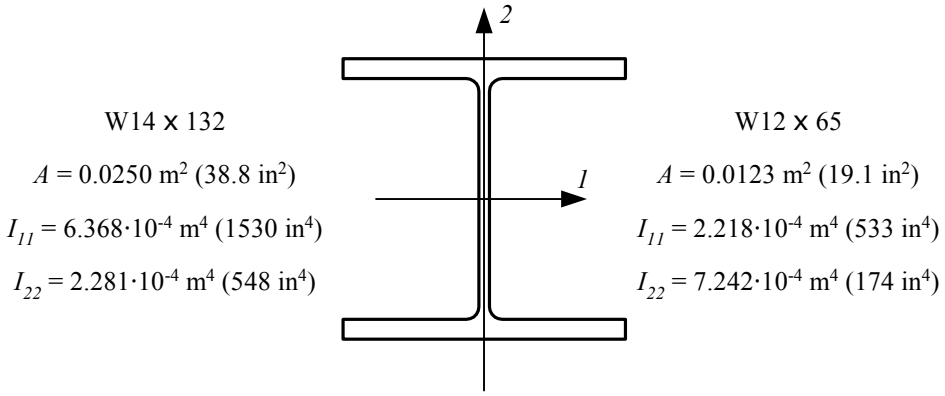

Figure 5.3. Standard W-shape steel section and cross sectional properties

Damage test cases evaluated for the cantilever beam problem are summarized in Table 5.1. To distinguish the cantilever beam problems from other cases, the designation of CANT and a capital roman number for the subcases are used. The first case, CANT I, simulates a damage close to the fixed support of the beam with a severity of 10% reduction in the stiffness matrix of element 2. For this case, the single excitation is located at the free end while a single measurement is taken almost at mid-span. The next case, CANT II, is similar to CANT I, except that the locations of the excitation and

measurement are interchanged. Case study CANT III is intended to simulate a 10% damage located at mid-span. The transfer function, however, is measured right at two nodes on either side of the damaged element, which represents an unusual measurement configuration. The fourth case, CANT IV, simulates an awkward configuration of the measurement layout. Although the excitation is placed close to the free end (node 9) of the beam, the single measurement is taken at a location close to the fixed end (node 2) where the response is not very large due to the boundary conditions in the vicinity of this location. The last case, CANT OPT, is the same as cases CANT I and II with respect to the damage configuration, but the excitation and senor placement is the optimal placement obtained from the solution to the MO excitation and sensor layout design optimization problem posed in this research. In all cases, the excitation and the measured DOFs are in the vertical or transverse direction.

Table 5.1. Case studies for cantilever beam

Test Case	Imposed Damage		Excitation	Measurement
	Element	Percent		
CANT I	2	10%	11	7
CANT II	2	10%	7	11
CANT III	6	10%	7	6
CANT IV	6	10%	9	2
CANT OPT	2	10%	Optimum*	Optimum

* Results from excitation and sensor layout design

5.1.2 Two-span Continuous Beam

The case studies investigated for the two-span continuous beam are listed in Table 5.2. To distinguish these problems from the rest of the trials, problems belonging to this set are designated with TWSP and a roman capital number, which may be followed by a capital letter relating to a sub-case. All the TWSP cases simulate two damaged elements with either equal or varying severity. The first two trials, TWSP IA and IB, both have damaged elements on one side of the two-span continuous beam at mid-span and at the

mid-support. The difference between the two trials is in the number of measurement locations. The second test case, TWSP II, is intended to simulate a somewhat unusual configuration of excitation and measurement placement when the damaged elements are located at the mid-spans of the right and left segments between the supports. Cases TWSP IIIA and IIIB are the same as the first two cases (TWSP IA and IB) except that the severity of damages is changed, 5% at mid-span and 10% at the mid-support. The last case, TWSP OPT, is the same as cases TWSP IIIA and IIIB with respect to the damage configuration, but the optimal excitation and senor placement has not been obtained from the solution to the MO excitation and sensor layout design optimization problem posed in this research. In all cases, the excitation and the measured DOFs are in the vertical or transverse direction.

Table 5.2. Case studies for two-span continuous beams

Test Case	Imposed Damage		Excitation	Measurement
	Element	Percent		
TWSP IA	6, 10	10% all	18	14
TWSP IB	6, 10	10% all	18	4, 14
TWSP II	6, 15	10% all	4	10
TWSP IIIA	6, 10	5, 10%	18	14
TWSP IIIB	6, 10	5, 10%	18	4, 14
TWSP OPT	6, 10	5, 10%	Optimum*	Optimum

* Results from excitation and sensor layout design

5.2 Moment Frame Type Structures

5.2.1 Two-story, Three-bay Cross-braced Moment Frame

The first of the two frame test structures is a two-story, three-bay cross-braced moment frame (Figure 5.4). All columns and beams are W14 × 132 and W12 × 65 (Figure 5.3) standard steel sections, respectively. Cross bracing is located within the center bay on both floors and consists of 2L5 × 3½ × ½ double angles (Figure 5.5). The Young's

modulus of steel, E, is 207 GPa (30,000 ksi), Poisson's ratio, ν, is 0.3, and the mass density, ρ, is 7780 kg/m^3 (0.000728 lb-s^2/in^4) for all cases in this set.

In order to model the beam to column connection, each beam and column was divided into three Bernoulli frame elements (APPENDIX A). Each connection was therefore surrounded by short elements one foot in length on all sides. The cross braces were modeled as a single element with zero moment of inertia to represent a hinge type connection. The node numbering of the finite element mesh can be seen in Figure C.1 of APPENDIX C and the element number are depicted in Figure C.2 of APPENDIX C. There are a total of 46 elements and 40 nodes in the model. In real-world situations, the mesh density of this model would not be fine enough, but the goal of this study is first to find a set of good GA parameters that maximize performance and then verify the performance of the SDIM developed on larger structural systems.

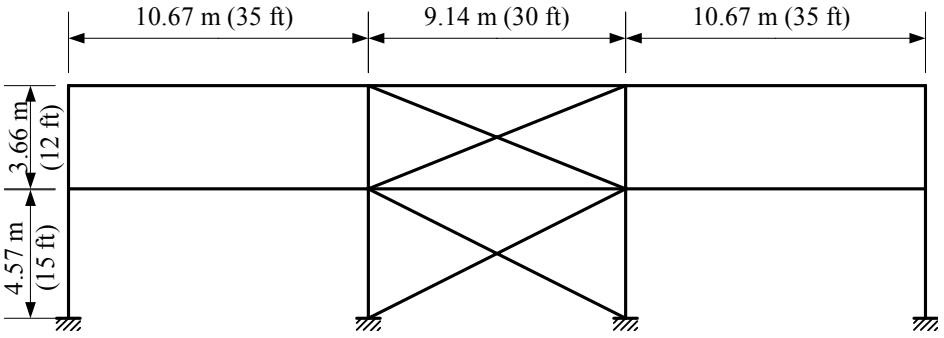

Figure 5.4. Two-story three-bay braced frame and dimensions

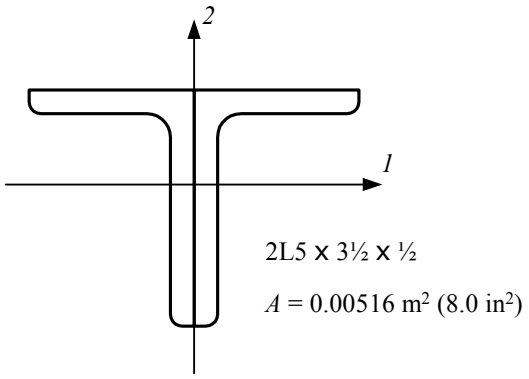

Figure 5.5. Standard double angles, 2L5 × 3½ × ½

The first test case BRFRM I is defined with one damaged element (Table 5.3). In this trial, the damaged element is a cross brace on the first story that has a damage severity of 50%. The excitation is in the horizontal direction at node 31 on the second floor perimeter beam and two sensors are used to measure FRFs in the horizontal direction at nodes 19 and 20 on the first and second floor beams of the middle bay. This first test case is used to establish a good set of GA parameters, which over a broad range of trials results in superior performance.

Having established a good set of GA parameters, the second case study BRFRM II (Table 5.3) is used to test the robustness of GA in situations when multiple damage locations exist having varying severity. Also, the optimum excitation and sensor locations obtained from the sensor layout design optimization will be used to evaluate the significance of measurement quality on the SDIM results obtained.

Table 5.3. Case studies for two-story three-bay cross-braced moment frame

Test Case	Imposed Damage		Excitation	Measurement
	Element	Percent		
BRFRM I	43	50%	31	19, 20
BRFRM II	43, 35, 37, 39	50, 10, 20, 20%	31 or Optimum*	19, 20 or Optimum

* Results from excitation and sensor layout design

5.2.2 Three-story, Three-bay Unbraced Moment Frame

The next case study concerns a three-story, three-bay unbraced moment frame structure (Figure 5.6). Similar to the previous frame case studies, all columns and beams are W14 × 132 and W12 × 65 (Figure 5.3) standard steel sections, respectively. The same material properties are also used as for the braced frame. Each column is modeled with three Bernoulli type frame elements (APPENDIX A) and each beam is divided into five finite elements. Joints are again represented using short 0.3048 m (1 ft) elements. The finite element mesh and node numbering of the frame is shown in Figure C.3 of

APPENDIX C and the element numbering in Figure C.4 of APPENDIX C. There are a total of 81 elements and 76 nodes in the model.

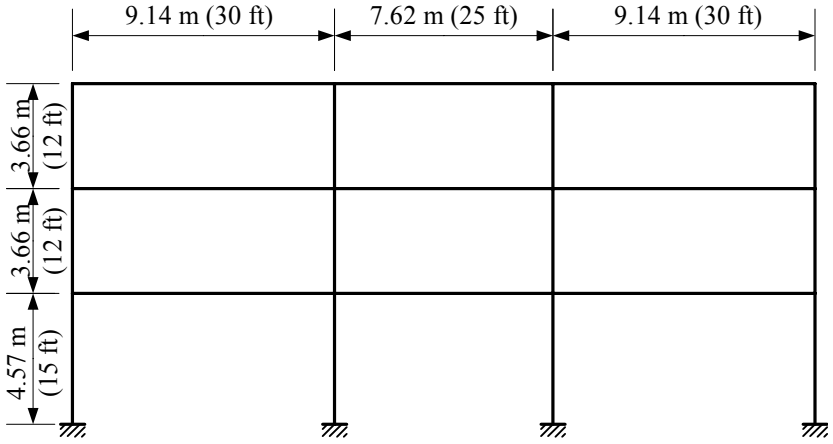

Figure 5.6. Three-story three-bay unbraced frame and dimensions

The different test cases investigated for the unbraced frame problem are listed in Table 5.4. The designation for this set of problems is UBFRM, which stands for unbraced frame. The first problem, UBFRM I, relates to a 10% damage in the first floor perimeter beam at mid-span on the left side of the frame. Case UBFRM II introduces 10% damage in the same beam as for case UBFRM I but in this case the damage is located at the perimeter joint of the beam. Essentially, this case considers joint damage in the frame. Case UBFRM III inflicts damages at four locations in the first story columns at joints with the beams. In this case, the severities of damages are different: 10% for the perimeter columns and 5% for the interior columns. Also the layout of the excitation and measurement locations are investigated to evaluate the effectiveness of using optimum sensor placement. The last case, UBFRM IV, has six damaged elements all located in the first floor beams at the joints. The severity of damage at the exterior beam joints is 20% and the interior beam joints have a damage of 10% on either side of the interior joints. For this case, the excitation and measurement configuration will be obtained from the sensor location optimization for the unbraced frame. The FRFs are measured for horizontal DOFs at the nodes specified in Table 5.4, except for the cases using the

optimal sensor locations, in which DOFs can be measured in the horizontal or vertical directions.

Table 5.4. Case studies for three-story three-bay unbraced moment frame

Test Case	Imposed Damage		Excitation	Measurement
	Element	Percent		
UBFRM I	21	10%	71	59, 67, 69
UBFRM II	28	10%	71	59, 67, 69
UBFRM III	49, 27, 3, 34	10, 5, 5, 10%	71 or Optimum*	59, 67, 69 or Optimum
UBFRM IV	28, 16, 11, 4, 10, 18	20, 10, 10, 10, 10, 20%	Optimum	Optimum

* Results from excitation and sensor layout design

5.3 Baseline Structure for Evaluation of the Proposed Damage Detection Method

In their paper Kim and Stubbs (2002) used a theoretical finite element model of a plate girder structure to evaluate three SDIMs using modal information. The procedures that were used in their research are outlined in Section 1 and are called Damage Index A, Damage Index B, and Damage Index C procedures. The original model used in their research consisted of 50 finite elements and three linear springs modeling the supports (Figure 5.7(a)). In the current implementation of the *GaDamDet* program used in this research, the only finite element type supported is the Bernoulli frame element (APPENDIX A). Therefore in this research, the linear springs are substituted with simple roller and hinge supports (Figure 5.7(b)). Changing the support conditions does not significantly alter the complexity of damage detection posed by the original problem. The geometric properties of the finite elements are an area, $A = 1.05 \cdot 10^{-3}$ m^2 (1.6275 in^2) and second moment of inertia, $I = 7.23 \cdot 10^{-7}$ m^4 (1.737 in^4). The material properties are Young's modulus, $E = 70$ GPa (10,152 ksi), Poisson's ratio, $\nu = 0.33$, and mass density, $\rho = 2710$ kg/m^3 (0.0002536 lb-s^2/in^4).

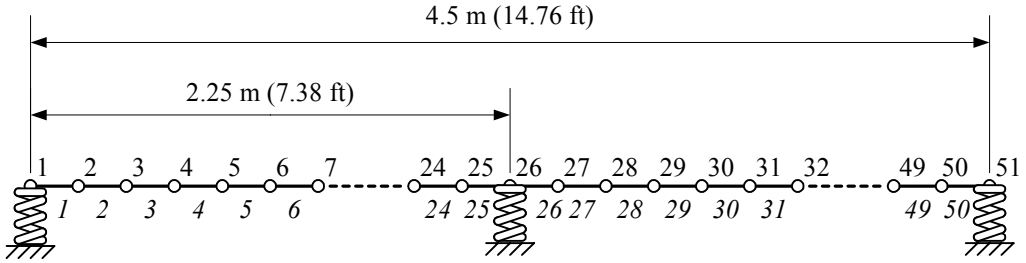

(a) Original finite element model

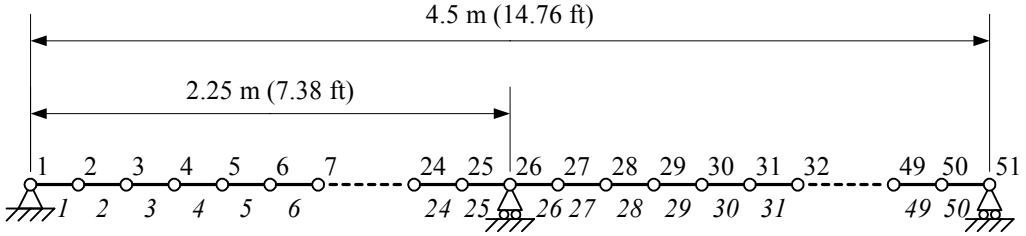

(b) Finite element model used in this research

Figure 5.7. Finite element models of a plate girder structure, (a) original model used by Kim and Stubbs (2002), (b) model used in this research

The damage scenarios investigated by Kim and Stubbs (2002) are summarized in Table 5.5. In their studies, all 51 transverse DOFs of the mode shape vector were used to generate the mode shapes as a third order spline function. This assumes that a large number of sensors are used for measurements. In the research presented in this dissertation, only two sensors are used to measure the FRFs between the excitation and the measurement locations. The first eight damage cases, KSTSP I-VIII, given in Table 5.5 represent single damage situations and the damage element is shifted from left to right as the case number increases. For scenarios, KSTSP VI-VIII, different damage levels are simulated for the same element. The last two cases involve two damaged elements at different locations, but having equal magnitudes.

Table 5.5. Case studies for two-span continuous beam used by Kim and Stubbs (2002)

Test Case	Imposed Damage		Excitation	Measurement
	Element	Percent		
KSTSP I	4	10%	14	19, 39
KSTSP II	9	10%	14	19, 39
KSTSP III	14	10%	14	19, 39
KSTSP IV	19	10%	14	19, 39
KSTSP V	24	10%	14	19, 39
KSTSP VI	39	1%	14	19, 39
KSTSP VII	39	10%	14	19, 39
KSTSP VIII	39	50%	14	19, 39
KSTSP IX	9, 34	10% all	14	19, 39
KSTSP X	14, 39	10% all	14	19, 39

Results obtained for the damage cases outlined in Table 5.5 by Kim and Stubbs (2002) are summarized in Table 5.6. From the table, it is clear that the Damage Index A method is the least accurate. The method often falsely identified elements as damaged with significant damage severity and the damage severity for the true damaged element(s) was always overestimated. In case KSTSP VI, the damaged element was not found at all. The next method, Damage Index B, correctly identified the location of the damaged elements, but the severity of damage was always underestimated. In case KSTSP VI for instance, the found damage severity was underestimated by an order of magnitude. The most accurate procedure was the Damage Index C, which was able to correctly locate the damaged elements in all cases and was able to estimate the severity of damage within 20% of the inflicted damage. All of the damage index methods presented, however used a statistical criterion to localize damage by eliminating elements that were not likely to be damaged.

Table 5.6. Results for the plate girder damage detection problems obtained by Kim and Stubbs (2002)

Test Case	Damage Index A		Damage Index B		Damage Index C	
	Location	Severity	Location	Severity	Location	Severity
KSTSP I	1, 4, 25, 26	12.8, 18.9, 8.6, 23.5%	4	3.8%	4	11.9%
KSTSP II	1, 9, 26	11.6, 18.7, 20.9%	9	1.3%	9	10.7%
KSTSP III	14, 26	18.3, 31.4%	14	1.4%	14	9.4%
KSTSP IV	19, 26	18.1, 16.8%	19	0.8%	19	9.5%
KSTSP V	24, 25, 26	15.7, 18.7, 7.6%	24	0.5%	24	9.3%
KSTSP VI	25, 26, 49	11.1, 7.3, 5.2%	39	0.1%	39	1.0%
KSTSP VII	25, 39	29.0, 18.5%	39	1.5%	39	9.6%
KSTSP VIII	25, 39	6.72, 72.7%	39	14.8%	39	46.4%
KSTSP IX	9, 34, 50	18.3, 17.5, 7.7%	9, 34	1.3, 1.1%	9, 34	11.1, 8.0%
KSTSP X	14, 26, 39	17.4, 11.3, 17.7%	14, 39	1.4, 1.4%	14, 39	10.3, 10.9%

6 CASE STUDY RESULTS AND DISCUSSION, CANTILEVER BEAM

In Sections 6, 7, 8, and 9 the results obtained for the case studies discussed in Section 5 are presented. These sections provide an objective evaluation of the damage detection and excitation and sensor layout design procedures developed in this research. Damage detection trials were performed first for ideal noise free measurements and then noisy measurements were investigated, to simulate real-world measurement situations. Case studies defining structures with increasing complexity are used to objectively assess the robustness of damage detection and to reveal its limitations and strengths. The presented SDIM is compared with existing modal-based SDIMs through an example benchmarked in the literature. New accuracy measures were defined to facilitate the objective comparison of SDIM developed with the three others that use modal information, Damage Index A, B and C (Kim and Stubbs, 2002).

Results for the trials are presented both in tabular format and in figures. In most cases, these representative aids contain the same information. Therefore, most of the tables have been placed in APPENDIX D. To save space and to make data more readable whenever possible, results for damage indicators that carry zeros are omitted from the graphs and tables and only elements with non-zero damage indicators are shown. This convention is followed throughout Sections 6, 7, 8, and 9 unless otherwise stated.

6.1 Input Parameters for Cantilever Beam Case Studies

The set of GA parameters used in the cantilever beam case study trials are summarized in Table 6.1. These parameters were selected based on the results of initial trials performed using different GA parameters. The trials are grouped into three sets of trials: fixed, IRR seeded and IRR unseeded. This classification is made to enable the effective comparison of the different representations investigated by this research effort. The number of significant digits used for the cantilever beam damage indicators was 8, which required 27 bits to represent a damage indicator with a precision of about $7.38 \cdot 10^{-9}$ or $7.38 \cdot 10^{-7}$%.

Table 6.1. GA parameters for cantilever beam trials

	Fixed Representation	IRR, Seeded*	IRR, Unseeded
Population Size	100	100	100
Tournament Size	4	8	8
Initial Seed	Yes	Yes	No
Maximum Generations	200	200	200
Stop if no Improvement	30	30	30
Crossover Type	Adaptive	Adaptive	Adaptive
Crossover Sites	8	10	10
Crossover Rates	Primary: 0.9, Secondary: 1.0	Primary: 0.9, Secondary: 1.0	Primary: 0.9, Secondary: 1.0
Mutation Type	Non-uniform	Uniform	Uniform
Mutation Rate	0.01	0.01	0.01
Elitism	Yes	Yes	Yes
Hillclimbing	Yes, Reduced	Yes, Reduced	Yes, Reduced
Coding	Gray	Gray	Gray

* For the IRR the number of gene instances (expected number of damaged elements) was 5 and the gene locator (GL) length is 3

6.2 Common Cantilever Beam Damage, Case Study CANT I and CANT II

Results for the first cantilever case study, CANT I (Table 5.1), in which the damaged element is located close to the fixed end of the beam and has a severity of 10%, are summarized in Table D.1 through Table D.6 of APPENDIX D. The same results are depicted in Figure 6.1 through Figure 6.6. Using the GA parameters defined in Table 6.1, trials were performed that considered different measurement noise levels: noise free or 0%, 5%, 10%, 20% and 50%. Fifteen trials were performed for the CANT I case study that all used the "sum of square differences" objective function defined in Eq. (2.54). For the ideal situation, in which no noise is present in the measurements, the global optimum was found for all trials either during the GA evolution process or after hillclimbing.

Using the fixed GA representation, 9 out of the 10 elements maintained a damage indicator larger than zero in the best individual after 200 GA generations (Figure 6.1, Table D.1 of APPENDIX D). Strictly speaking this means that 8 elements were falsely

identified as damaged. A closer look at the results, however, reveals that the damage indicator values for all the falsely identified elements were significantly smaller and ranged from 0.31% to $1.18 \cdot 10^{-5}$% with an average of 0.09%. The damage indicator for element 2 was 9.47%. After hillclimbing, the results indicated the damage in element 2, which was the imposed 10% and there were only two falsely identified elements with damage indicator less than $2.0 \cdot 10^{-5}$%, which were essentially zero. These small residual damage indicators may only be numerical errors due to the fact that both GA and hillclimbing use a certain precision (obtained from the number of bits used in the binary representation) to represent the continuous domain. The results presented for the fixed representation were obtained by seeding the initial population with the zero damage individual. If the initial population was not seeded for the fixed representation GA, then accurate results resembling to the original damage scenario were not obtained. The rest of the discussions of the results in the section assume that when a fixed representation is under investigation, the initial population was always seeded with the zero damage individual.

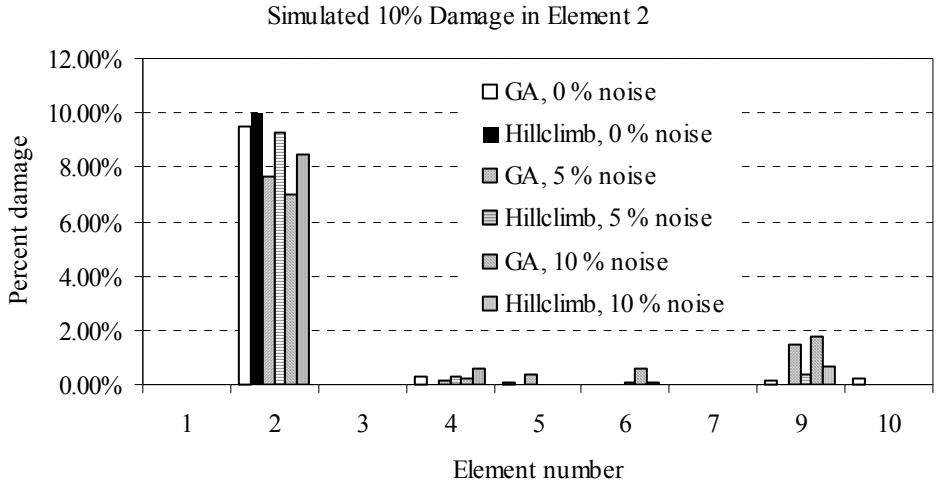

Figure 6.1. Damage detection results for case CANT I, fixed representation, seeded initial population, noise levels of 0, 5 and 10%

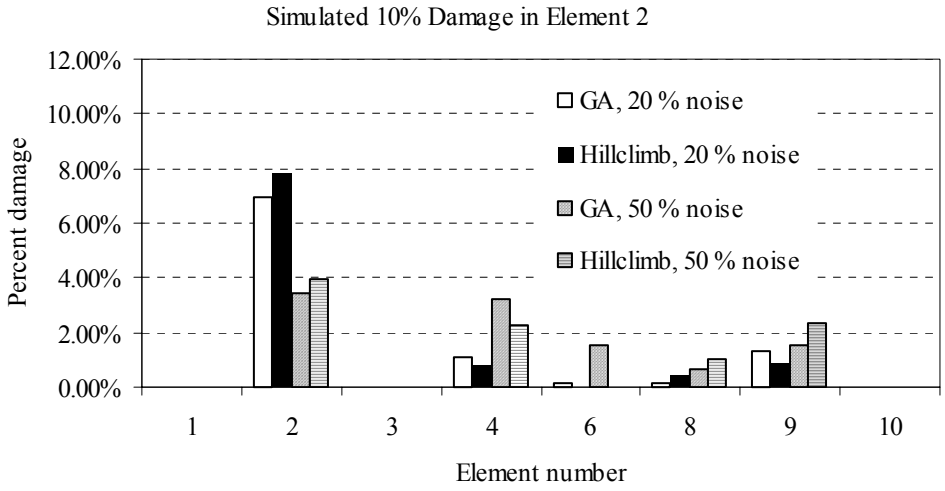

Figure 6.2. Damage detection results for case CANT I, fixed representation, seeded initial population, noise levels of 20 and 50%

Using the IRR GA, both with and without seeding the initial population with the zero damage individual, a better convergence to the imposed damage case was obtained. Results for the IRR GA trials with an initial seed are shown in Figure 6.3 and summarized in Table D.3 of APPENDIX D. After 200 GA generations, element 2 was identified with a damage of essentially 10.0% and elements 3 and 4 had damage indicators less than $7.44 \cdot 10^{-4}$%. In the initial population, the best string was the zero damage individual, which had 5 gene instances (damaged elements) but all had a zero damage indicator value. In the final population, the best individual had 3 unique gene instances, one identifying element 2 with 10% damage and two others identifying elements 3 and 4 with practically zero damage indicators. Hillclimbing improved the results by adjusting the precision of the best individual in the final population (from 9.99907% to 9.99993% for element 2, $7.44 \cdot 10^{-4}$% to $5.53 \cdot 10^{-5}$% for element 3, and $4.5 \cdot 10^{-4}$% to $4.06 \cdot 10^{-5}$% for element 4).

The IRR GA trial without seeding the initial population, performed better in locating and quantifying the damaged element (Figure 6.5 and Table D.5 of APPENDIX D). The global optimum was obtained after 130 GA generations and

therefore hillclimbing was not needed to improve the solution obtained by the GA. In the best individual of the final population, the only unique gene instance identified element 2 as damaged with a severity of 10%.

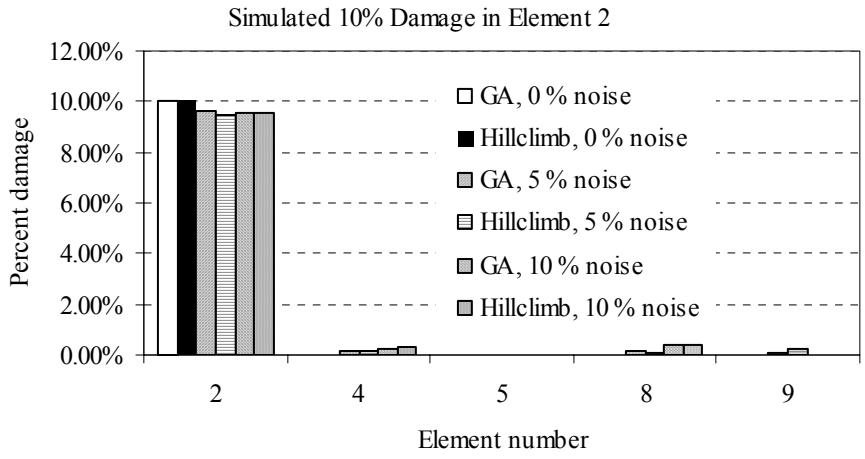

Figure 6.3. Damage detection results for case CANT I, implicit redundant representation (IRR), seeded initial population, noise levels of 0, 5 and 10%

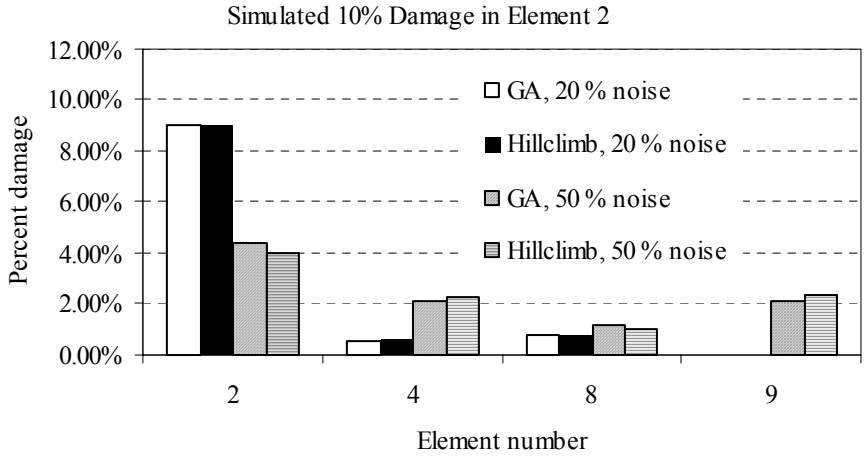

Figure 6.4. Damage detection results for case CANT I, implicit redundant representation (IRR), seeded initial population, noise levels of 20 and 50%

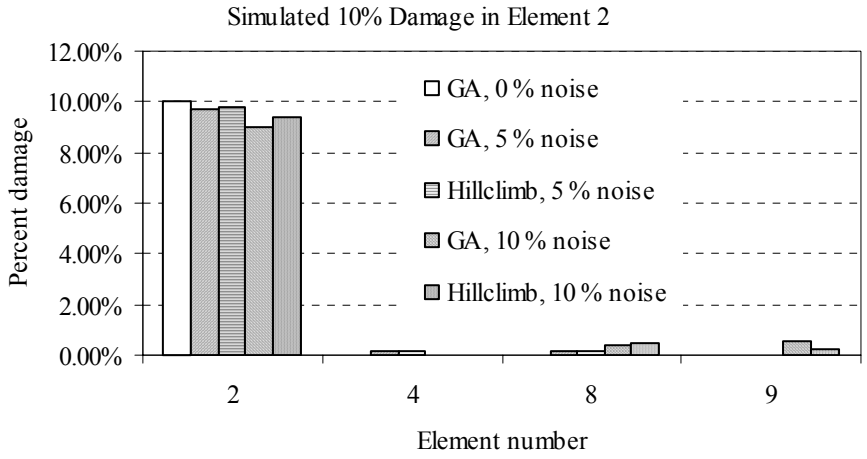

Figure 6.5. Damage detection results for case CANT I, implicit redundant representation (IRR), unseeded initial population, noise levels of 0, 5 and 10%

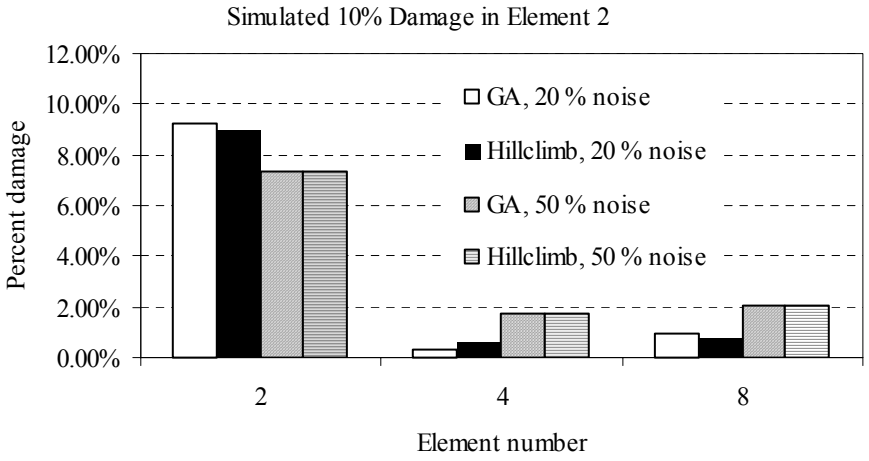

Figure 6.6. Damage detection results for case CANT I, implicit redundant representation (IRR), unseeded initial population, noise levels of 20 and 50%

To investigate the effect of measurement noise on the accuracy of damage detection four different noise levels (5, 10, 20, 50%) were used for the cantilever problem CANT I beside the noise free measurement case. Results for these situations can be seen in Figure 6.1 through Figure 6.6 and summarized in Table D.1 through Table D.6 of APPENDIX D. The accuracy of damage detection degrades with increasing noise levels

in the measurements regardless of the representation used, as is typical for any SDIM. The figures show, however, that both IRR GA methods (seeded and not seeded) better approximate the original damage case then the fixed representation for any given noise level. Using the fixed representation, the number of elements identified as damaged after 200 GA generations were 7, 5, 4 and 7 out of 10 elements for noise levels of 5, 10, 20 and 50%, respectively. It is quite interesting that with increasing noise levels, the number of falsely identified damaged elements actually decreases up to a noise level of 20% and after that increases again. After hillclimbing, the number of falsely identified elements was 3 in all CANT I trials. Even if the number of falsely identified elements decreased with increasing noise levels, the accuracy of the predicted damages degraded. The damage indicators for element 2 were 7.64/9.24%, 6.96/8.46%, 6.96/7.84% and 3.46/3.99% instead of the inflicted 10% for the 5, 10, 20 and 50% noise levels after 200 GA generations and hillclimbing. Also the damage severity of the falsely identified elements typically increased with increasing noise levels. At a noise level of 20%, element 2 was still identified with a much larger damage indicator, 6.96/7.84%, than the falsely identified element 9 with the largest damage indicator of 1.31-0.85% after 200 GA generations and hillclimbing, respectively. At a noise level of 50%, the damage location becomes ambiguous since the damage indicator values of the correctly and falsely identified elements are similar in magnitude, 3.46-3.99% and 3.23-2.24%.

For trial including noise and using the IRR GA with an initial seed, the number of falsely identified elements was 3 or 2 and for the IRR GA without initial seed this number was always two. Regardless of the noise level both sets of trials picked the same falsely damaged elements consistently. The predicted damage indicators for element 2 using the seeded IRR were 9.66/9.49%, 9.55/9.52%, 9.06/9.01% and 4.37/3.99% instead of the imposed 10% for the 5, 10, 20 and 50% noise levels after 200 GA generations and hillclimbing, respectively. The damage indicators for the falsely identified elements were less than 0.17/0.21%, 0.42/0.40%, 0.83/0.80% and 2.14/2.34% for the 5, 10, 20 and 50% noise levels, respectively.

These results were much better than the results obtained using the fixed SGA. Up to a 20% noise level, the predicted damage for element 2 was always larger than 9%,

which in turn was at least an order of magnitude larger than the maximum damage indicator of the falsely identified elements. At a noise level of 50%, the obtained result is essentially identical to that of the fixed representation. Therefore, at this noise level the SDIM breaks down. The results for the IRR GA with initial seed were very similar to those of the IRR GA without seed except at the noise level of 50%. In this case, the solution found still predicted a damage of 7.33% at element 2 and the damages at element 4 and 8 were 1.72 and 2.03%, respectively. This difference in damage severities implies that element 2 is critical in terms of damage localization.

In addition, improvements of the results obtained using the fixed representation were noticeable after hillclimbing, while these improvements were negligible for the IRR GA. Another important observation is that seeding the initial population was not necessary to find a good solution for the damage detection problem when using the IRR GA. Conversely, the fixed representation GA did not find any viable solution without seeding the initial population with the zero damage individual.

6.2.1 Comparison of Fixed and IRR Representations

From the trials for the first cantilever case study, CANT I, it is apparent that the IRR GA outperforms the traditional SGA with fixed representation even when advanced genetic operators are employed to improve the performance of SGA. The possible answer to this fact may be found in the optimization domain and the way the different representations work. To demonstrate the differences between the fixed and IRR representations, the best individuals from the initial (for the fixed GA the best individual in the initial population was the zero damage individual so in this case the second best individual is shown) and final populations are compared in Figure 6.7 for the noise free measurement case. The unstructured nature of the damage detection problem for this case requires finding one damaged element (element 2), but the total number of unknown variables is 10. In the initial population, neither of the best individuals really resembles the imposed damage scenario. Indeed, the damage indicators for the fixed representation are randomly generated and values from 0.39 to 88.4% can be found. For the IRR GA, the best individual in the initial population encodes five unique gene instances each identifying

different elements with different damage indicators. Actually, this individual looks a lot better than the fixed representation string since element 2 is already included in the damaged element set with a quite good, 16.4%, damage indicator value. As generations proceed, the fixed representation GA has to deal with all 10 variables simultaneously and therefore inefficiently tries to adjust the damage indicator values for each individual element, although only one particular member damage needs to be found. As a result, in the final population the best individual for the fixed GA identifies the damage at element 2, but still represents all of the unknown variables with some nonnegative damage indicator values.

In the best string of the final population for the IRR GA, in comparison, there are only two gene instances defined that encoded the same damaged element. Although technically there are two gene instances in this configuration, the number of unique gene instances is one. In situations when more than one gene instance encodes the same element, the average of the damage indicator values were taken (Figure 6.7). As Figure 6.7 shows the IRR GA was able to evolve the necessary number of variables to solve the problem during the optimization process and therefore significantly reduced the exploration of search space. The important key with the IRR GA representation is that the redundant segments may become useful gene instances in later generations and vice versa. In damage detection problems it is usually the case that the expected number of damaged elements (in the present example it was 5) is still larger than the number of actually damaged elements. Therefore the average amount of redundant segments usually increases with increasing number of generations (Figure 6.7). The redundant segments also help to protect good solutions when the crossover or mutation takes place in the redundant segments.

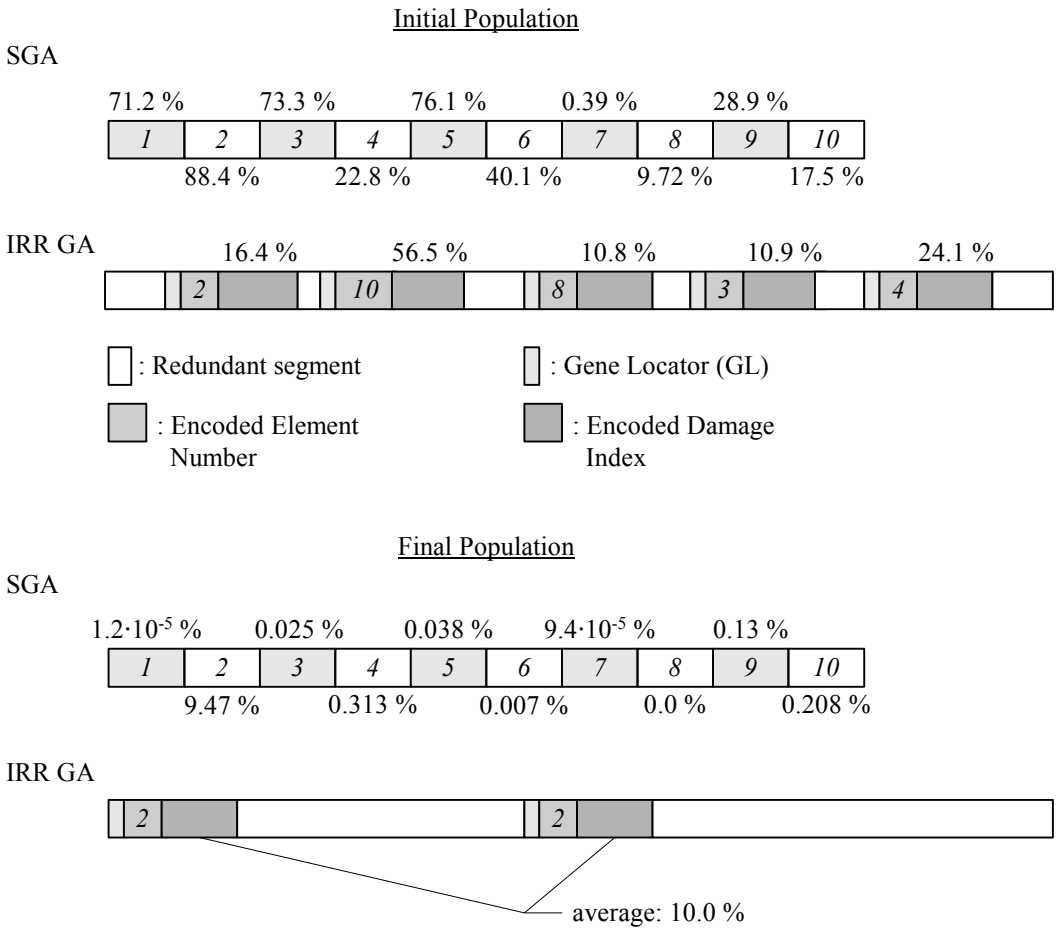

Figure 6.7. Comparison of the best individuals in the initial and final populations for the fixed representation SGA and the IRR GA

6.2.2 Alternative Objective Function Formulation

The last set of trials performed for case study CANT I was intended to compare the adequacy of different vibration signatures in damage detection. The results presented so far were obtained using the "sum of square differences" objective function, which was defined for FRFs and was given in Eq. (2.54). In Section 1, several correlation criteria were introduced that can be used as measures in quantifying the closeness of the analytical and measured responses. Although any of the criteria could be used to formulate objective functions for optimization based on the conclusions drawn by Zhang et al. (2001) the global shape criterion (GSC), Eq. (1.24) and global amplitude criterion

(GAC), Eq. (1.25) appear to hold the most benefit. Both measures are a function of frequency and are bounded between the values of zero and one. When these functions are unity over the entire frequency range then the correlation between the measured and analytical FRFs is perfect. To use the GSC and GAC for optimization, a scalar objective function was defined in which each individual term had a maximum value of one (perfect correlation).

$$\max f = \left(\frac{\int_{\varpi_0}^{\varpi_1} GSC(\omega)\, d\omega}{\varpi_1 - \varpi_0} \right)^2 + \left(\frac{\int_{\varpi_0}^{\varpi_1} GAC(\omega)\, d\omega}{\varpi_1 - \varpi_0} \right)^2 \tag{6.1}$$

where the objective function f is maximized and ϖ_0 and ϖ_1 are the lower and upper frequencies of the measured frequency range. When both terms in the objective function represent perfect correlation between the measured and analytical FRFs, the value of the objective function is two, which indicates that the global optimum was found.

A comparison between the objective function defined and used in this research and the GAC and GSC defined objective function is made using the cantilever beam case study CANT I. In Figure 6.8, the accelerance FRFs are plotted for the undamaged and the damaged cantilever beam structure measured between nodes 7 and 11. According to the objective function defined in Eq. (2.54) the difference between the corresponding FRFs are taken as a function of frequency and the area under the curve shown in Figure 6.8 is calculated. After calculating the areas under the difference function of each measured and corresponding FRFs, the squares of these areas are summed. The objective function used in this research is therefore called the “sum of square differences”.

For the CANT I problem, in comparison the GSC is unity over the entire frequency range because there is only one measured accelerance FRF. The plot of the GAC function is shown in Figure 6.9 over the measured frequency range. The objective function defined in Eq. (6.1) takes the normalized area under the GSC and GAC functions and sums the squares of these areas. For the CANT I problem, the first term of the

objective function is always unity and only the second term changes. This function is termed the “sum of GSC and GAC squares” objective function.

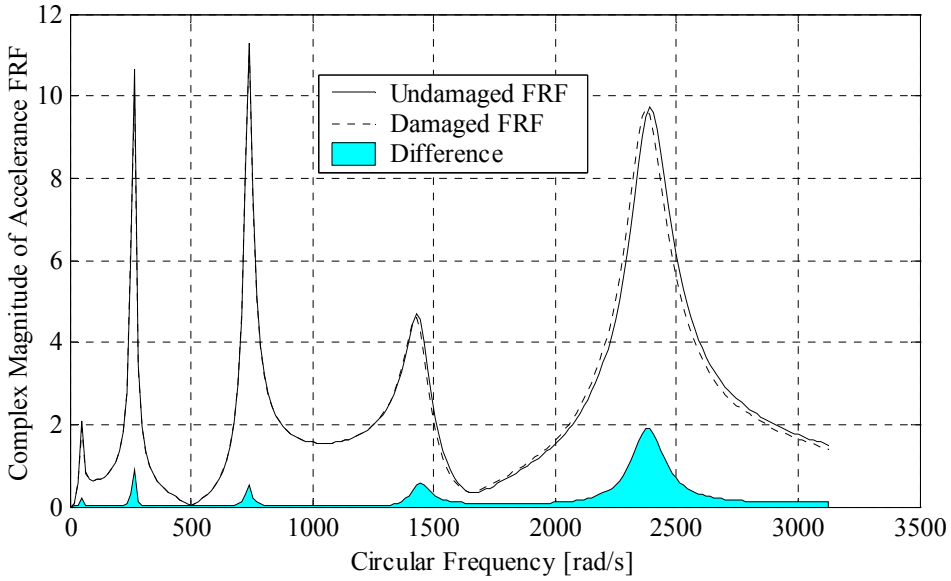

Figure 6.8. Undamaged and damaged accelerance FRFs and their differences for the cantilever beam case study, CANT I

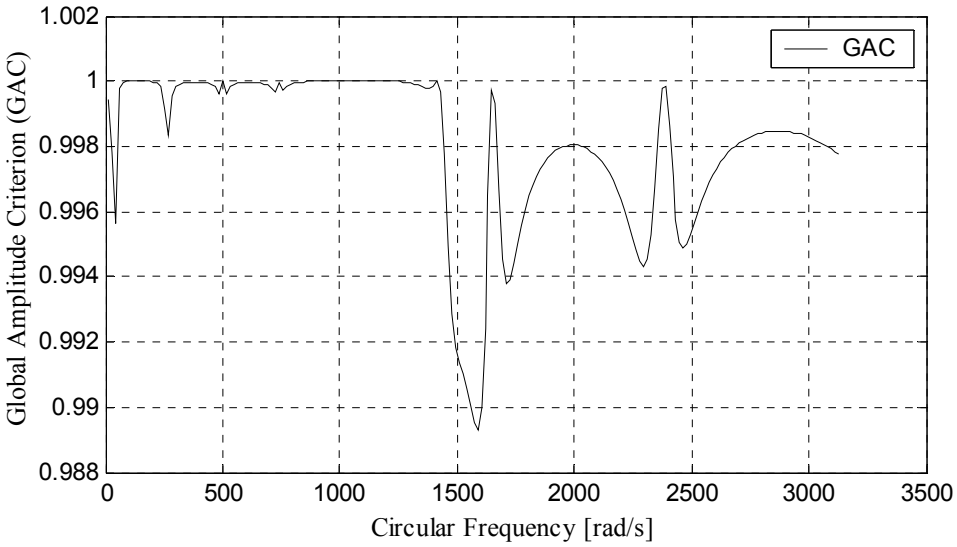

Figure 6.9. Global Amplitude Criterion for the cantilever beam case study, CANT I

Results obtained for case study CANT I using the sum of GSC and GAC squares objective function are depicted in Figure 6.10 through Figure 6.15 and summarized in Table D.7 through Table D.12 of APPENDIX D. In case of noise free measurement the fixed representation GA after 200 generations found a near-optimum solution with 9.88% damage predicted in element 2 and only very small residual damages, $2.7 \cdot 10^{-5}$ - 0.026%, in the other 8 beam elements. The local hillclimbing search was performed and the global optimum was found. Both seeded and unseeded IRR GA trials were able to find the global optimum with 10% damage at elements 2 and zero damages elsewhere after 115 and 170 generations, respectively. Local hillclimbing search did not improve the solution since the GA found the global optimum. Therefore, the performance of the two objective functions are comparable for the noise free measurement case and neither one is superior.

With increasing measurement noise, the accuracy of damage detection quickly degrades for all trials. Table 6.2 and Table 6.3 present results for both objective functions (sum of GSC and GAC squares, Eq. (6.1), as well as the sum of square differences, Eq. (2.54)) considering noise levels of 5 and 20%. From these results it is clear that the objective function originally proposed in Section 2 is less sensitive to noise than the objective function based on the GAC and GSC correlation measures. When comparing the two results it can be concluded that the performance of damage detection using the correlation measure objective function at a 5% noise level is slightly worse than that of the FRF differences objective function at 20% noise level. Also, a similar performance lag was seen between the two objective functions (correlation and FRF difference) at noise levels of 20 and 50%. The damage identification process breaks down at a noise level of 20% for the correlation objective function, since the falsely identified elements have a damage indicator value that approximately the same as the value of the correct damaged element 2 (Table 6.3). Results for the 50% noise level only contain falsely identified elements (element 6 at 5.5% and element 8 at 12.3%) while the correct damage location at element 2 has zero damage (Figure 6.11, Figure 6.13 and Figure 6.15). In general, the sum of square differences objective function outperformed the correlation objective function in every aspect and provided a better signature for damage detection even in noisy measurement environments.

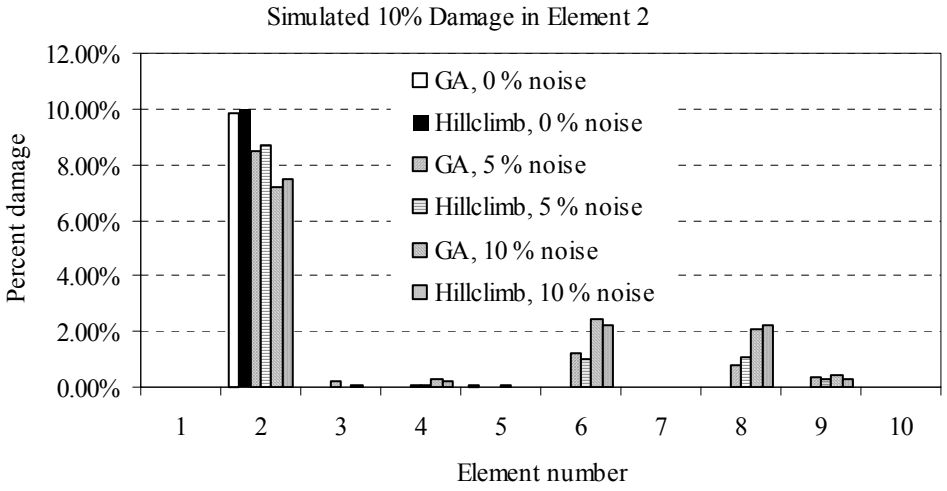

Figure 6.10. Damage detection results for case CANT I, fixed representation, seeded initial population, objective function is the sum of GSC and GAC squares, noise levels of 0, 5 and 10%

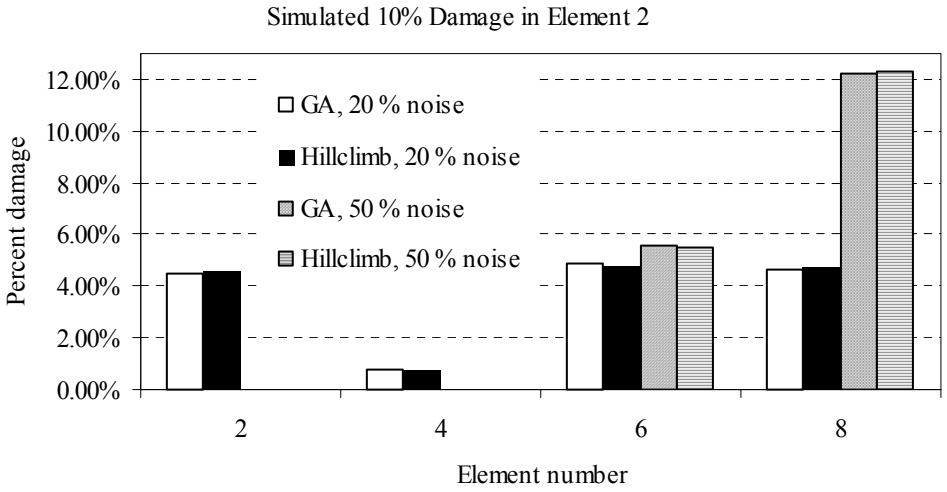

Figure 6.11. Damage detection results for case CANT I, fixed representation, seeded initial population, objective function is the sum of GSC and GAC squares, noise levels of 20 and 50%

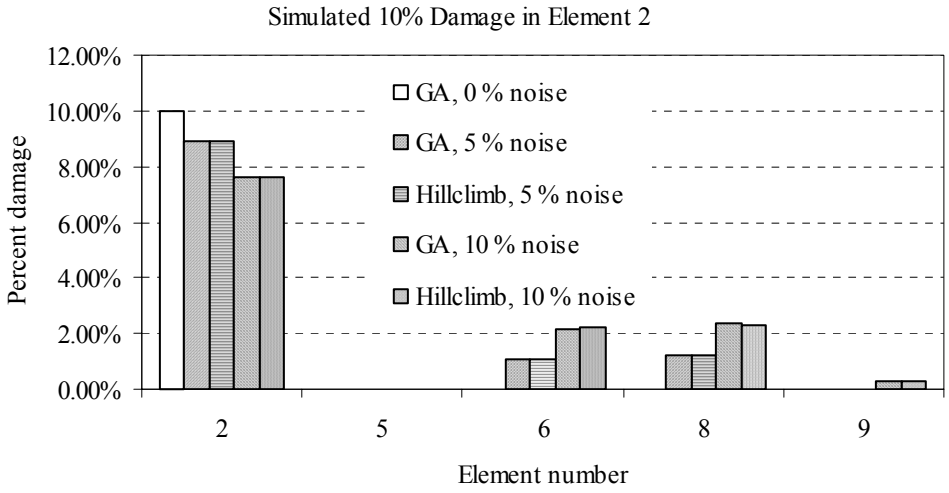

Figure 6.12. Damage detection results for case CANT I, implicit redundant representation (IRR), seeded initial population, objective function is the sum of GSC and GAC squares, noise levels of 0, 5 and 10%

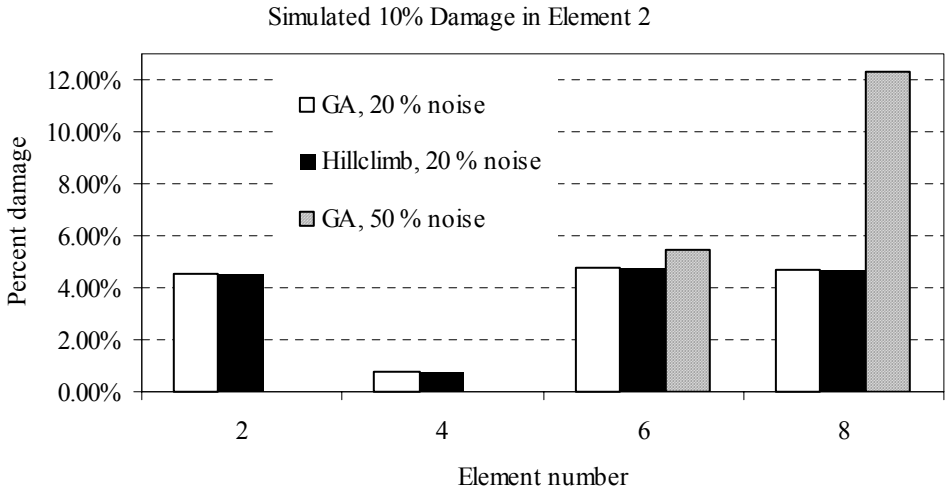

Figure 6.13. Damage detection results for case CANT I, implicit redundant representation (IRR), seeded initial population, objective function is the sum of GSC and GAC squares, noise levels of 20 and 50%

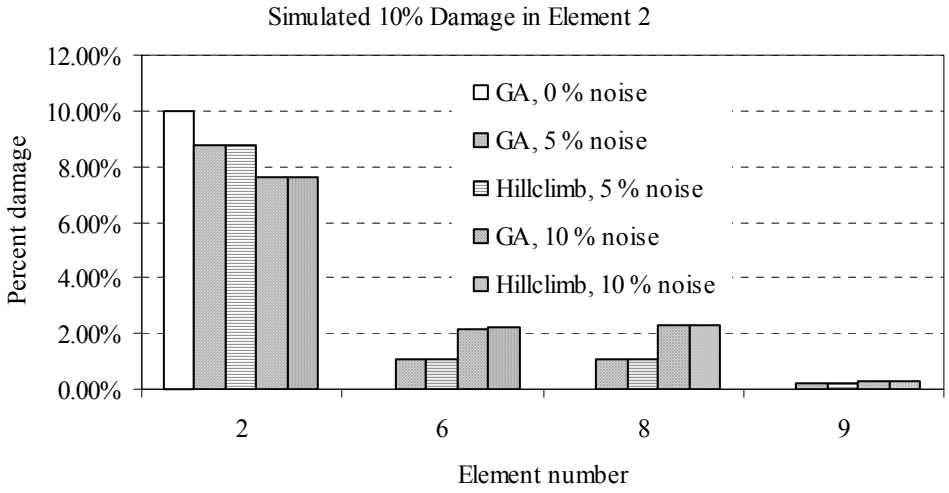

Figure 6.14. Damage detection results for case CANT I, implicit redundant representation (IRR), unseeded initial population, objective function is the sum of GSC and GAC squares, noise levels of 0, 5 and 10%

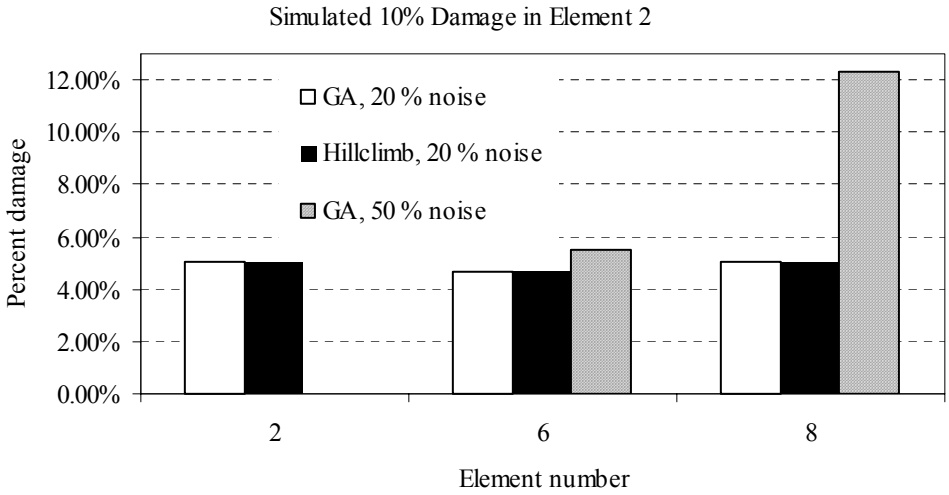

Figure 6.15. Damage detection results for case CANT I, implicit redundant representation (IRR), unseeded initial population, objective function is the sum of GSC and GAC squares, noise levels of 20 and 50%

Table 6.2. Comparison of the performance of different objective functions at a 5% noise level in measurements for the cantilever beam

	5% noise					
	Sum of GSC and GAC Squares			Sum of Square Differences		
	Fixed	IRR seeded	IRR unseeded	Fixed	IRR seeded	IRR unseeded
Damage at element 2	8.67%	8.88%	8.78%	9.24%	9.49%	9.76%
Number of false predictions	5	2	3	3	3	2
Maximum false damage	1.04%	1.20%	1.10%	0.35%	0.20%	0.20%

Table 6.3. Comparison of the performance of different objective functions at a 20% noise level in measurements for the cantilever beam

	20% noise					
	Sum of GSC and GAC Squares			Sum of Square Differences		
	Fixed	IRR seeded	IRR unseeded	Fixed	IRR seeded	IRR unseeded
Damage at element 2	4.55%	4.55%	5.03%	7.84%	9.01%	9.01%
Number of false predictions	3	3	2	3	2	2
Maximum false damage	4.78%	4.78%	5.01%	0.86%	0.80%	0.80%

6.2.3 Verification Case Study CANT II

In case study, CANT II (Table 5.1), element 2 is damaged, which is located close to the fixed support. The difference between CANT II and CANT I is that the excitation and measurement DOFs are switched and the sensor is located a node 11 and the excitation is placed at node 7. A second objective of this case study was to verify the finite element and optimization modules. The measured FRFs in the two case studies CANT I and II are identical because for linear structures the FRF matrices are symmetric. If the modules are

programmed correctly, then the results obtained for either case should be very similar. In comparing the results, consideration of the probabilistic nature of GAs is also required. Results obtained for case CANT II are shown in Figure 6.16 and tabulated in Table D.13 of APPENDIX D. In this specific trial, only noise free measurements were considered. The results obtained for case CANT II are almost identical to those for case study CANT I (only minor differences exit in the damage indicators). The fixed representation found a good solution of 9.47% damage at element 2 with some small residual damage indicator values remaining for other elements after 200 GA generations. Starting with this solution, hillclimbing found the global optimum by identifying element 2 with 10% damage. The IRR GA trial without initial seed essentially found the global optimal solution after 200 generations, hillclimbing only improved this solution by the precision provided by the binary representation. The unseeded IRR GA trial converged to the global optimum after 130 GA generations, which was the same result obtained in the CANT I trial. Switching the measurement configuration practically had no effect on the solutions when comparing this case to CANT I. The information contained in the measurements collected was sufficient to both locate and quantify damage accurately.

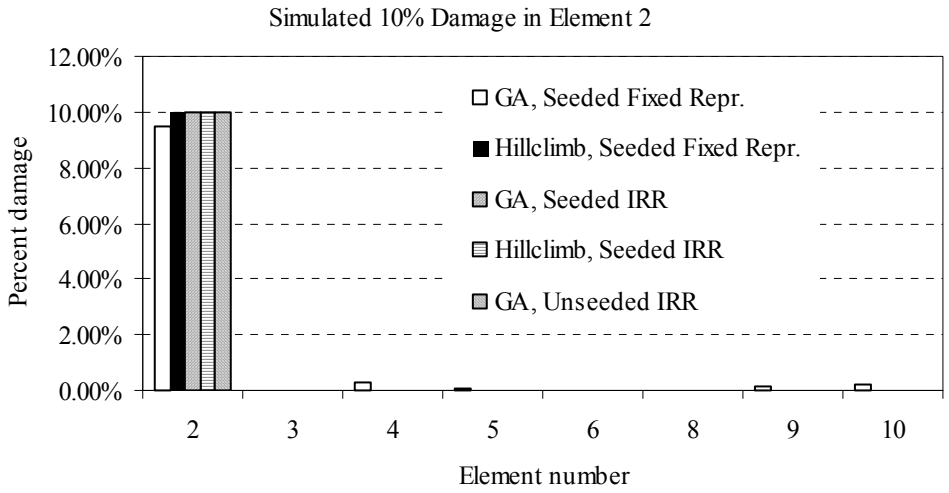

Figure 6.16. Damage detection results for case CANT II, fixed and implicit redundant representations (IRR), seeded and unseeded initial population, noise free measurements

6.3 Unusual Measurement Configurations, Case Studies CANT III and IV

The cantilever beam case study, CANT III (Table 5.1), represents a configuration in which the damaged element (element 6) is located about mid-span and the excitation and measurement are placed at the two nodes of the damaged element. To avoid premature convergence for the IRR GA, the tournament size (Table 6.1) was reduced from 8 to 4, which resulted in a lower selection pressure and promoted the exploration of the search space. The number of crossover sites was also reduced from 10 to 6 for the IRR GA to decrease the effect of disruption caused by the crossover operator.

Results for case CANT III and noise free measurements are depicted in Figure 6.17 and summarized in Table D.14. The fixed GA found a solution in which element 6 was identified with 9.06% damage and all other elements were predicted as damaged with damage indicator values ranging from 0.002 to 0.72%. The performance of the fixed GA degraded when compared to the first two cases, CANT I and II, studied due to the unusual damage and measurement configuration. After 2459 hillclimbing iterations, the global optimum was found with some small (less than $3.1 \cdot 10^{-5}$%) residual damage indicator values for elements 4, 7 and 9, but with 10% damage in element 6.

The seeded IRR GA converged to the global optimum after 129 generations and required no additional hillclimbing iterations. Since the global optimum was found, the number of gene instances in the best individual of the final population was one, which corresponded to element 6 with 10% damage. The solution provided by the unseeded IRR GA after 200 generations included element 6 with 9.85% damage but still contained three other gene instances identifying elements 3, 4 and 7 with 0.11%, 0.095% and 0.20% damage magnitudes, respectively. Hillclimbing improved the solution results up to the precision allowed by the representation. The results obtained suggest that seeding the initial population with the zero damage individual may help in locating damage elements when the measurement information does not contain a sufficient amount of information due to poor placements of sensors or excitations.

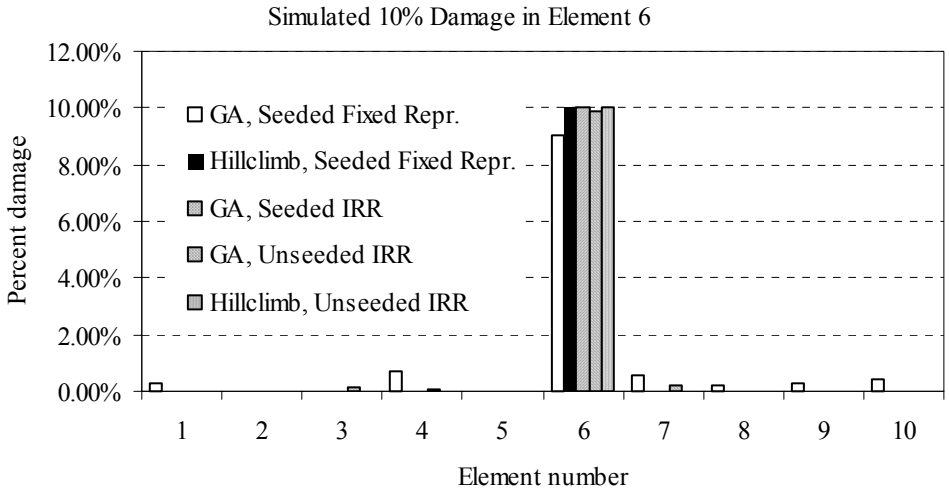

Figure 6.17. Damage detection results for case CANT III, fixed and implicit redundant representations (IRR), seeded and unseeded initial population, noise free measurements

The last set of trials performed for the cantilever problem case study corresponds to case CANT IV (Table 5.1). In this configuration, the damaged element (element 6) is located around mid-span and measurement is taken close to the fixed end at node 2 while the excitation is placed at node 9 close to the free end. This measurement layout is somewhat unusual since the response close to the free end is much smaller than anywhere else along the beam. Results for case CANT IV are provided in Figure 6.18 and summarized in Table D.15 of APPENDIX D.

The fixed representation GA with initial seed found a good solution after 200 generations in which element 6 was assigned a damage indicator of 9.67% instead of the inflicted 10%. Although all other elements had damage indicator values greater than zero the maximum of these severities did not exceed 0.26% and smallest was only $5.9 \cdot 10^{-6}$%. Using the GA result, the convergence of hillclimbing was very slow indicating that the objective function did not provide enough information about the global optimum. After 23,700 hillclimbing iterations the run was terminated because of the slow convergence. The final damage indicator of element 6 was 9.95% and three other elements were identified as damaged elements with small severity values less than 0.044%.

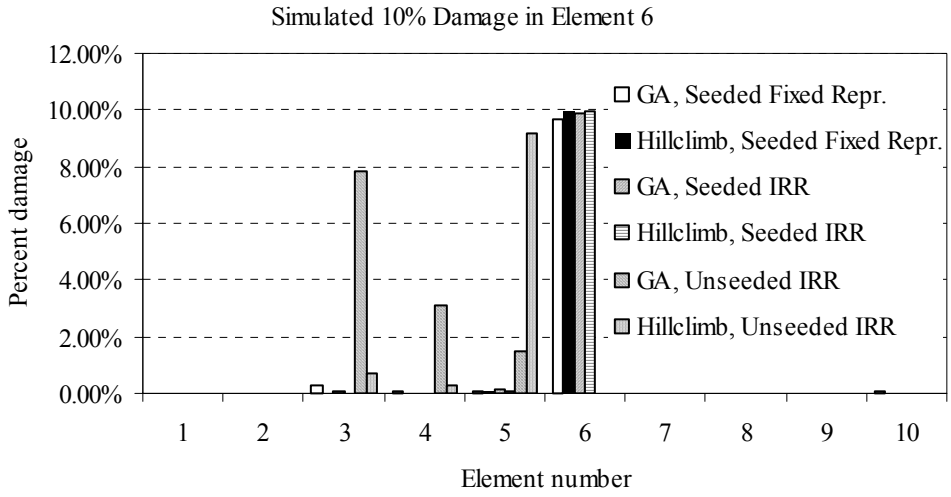

Figure 6.18. Damage detection results for case CANT IV, fixed and implicit redundant representations (IRR), seeded and unseeded initial population, noise free measurements

After 200 generations, the solution found by the IRR GA with initial seed had four gene instances, one encoding element 6 with 9.86% and three others encoding elements 3, 5 and 9 with damage indicators less than 0.12%. Again this solution was only improved very slowly by hillclimbing and the trial was terminated after 20,000 hillclimbing iterations. The solution at this point included element 6 with 9.96% damage and elements 3 and 5 with damage indicators of 0.011% and 0.042%, respectively. The IRR GA without initial seed could not locate the correct damaged element after 200 generations and falsely identified three elements (elements 3-7.85%, 4-3.11% and 5-1.5%) as damaged. Since reduced hillclimbing was used, the correct damaged element could not be located and the same three elements, 3, 4 and 5 were identified as damaged with damage values of 0.72, 0.3 and 9.19%, respectively. Although the correct location and severity of the damaged element was not obtained it is clear that the region of damage still is identified since element 5 is the immediate neighbor of element 6. The failure of the process for these trials is attributed to the unusual configuration of the measurement setup. As stated for the previous case study, it can be concluded that seeding the initial population with the zero damage individual in situations when the

measurement configuration is poorly selected can assist localizing damage. This case study highlights the effect of the excitation and sensor layout design on the results obtained and the need for optimizing the excitation and sensor layouts.

Table 6.4. GA settings for excitation and sensor layout design for the cantilever problem

Population Size	100, 200
Tournament Size	2, 3
Maximum Generations	1000
Stop if no Improvement	50
Crossover Type	Equal Probability
Crossover Sites	1
Crossover Rates	0.8
Mutation Type	Uniform
Mutation Rate	0.005
Elitism	Yes
Coding	Binary Base 2

6.4 Optimum Sensor Locations, Case Study CANT OPT

6.4.1 Optimum Excitation and Sensor Locations

The optimum locations for the excitation and sensors have to be determined before the last case study (CANT OPT, Table 5.1) of the cantilever problem can be discussed. Several trials using the GA settings defined in Table 6.4 were performed to determine the optimal measurement configurations. In these trials, both the fixed and IRR representations were investigated.

Excitation and sensor location results for the cantilever problem are summarized in Table 6.5. The graphical representation of the optimal excitation and sensor locations defined in the Pareto set, which were obtained using the program *GaDamDet*, are depicted in Figure D.1 of APPENDIX D. The maximum number of sensors for the trials was set to 10 and both horizontal and vertical DOFs were included for optimization. In all

cases, the same results were obtained from separate trials regardless of the GA parameters used. In general trials with the fixed representation converged faster than trials with the IRR representation.

From Table 6.5, it can be concluded that for a cantilever beam the best place for the excitation location is at the free end (node 11) of the beam in the vertical direction regardless of the number of sensors used for measurement. It is not surprising that the optimum location of the excitation is found at the free end of the beam since this configuration requires the least input energy to generate a certain level of response. Using 10 sensors instead of one sensor, only increases the measurement information by about 45%, which is not very significant, compared to the fact that by not placing the excitation and the first sensor on the free end, the measurement information decreases by several magnitudes. In other words, using one sensor should be sufficient for damage detection measurements for this particular case if the excitation is placed at the free end.

Table 6.5. Pareto optimal excitation and sensor locations for the cantilever beam problem, CANT

Number of sensors	Excitation at Node*	Sensor(s) at Node	Measurement Information	
			Value	Percent
1	11	11	$2.4232 \cdot 10^{18}$	100.0%
2	11	3, 11	$2.7479 \cdot 10^{18}$	113.4%
3	11	3, 5, 11	$2.9435 \cdot 10^{18}$	121.5%
4	11	3, 5, 7, 11	$3.1304 \cdot 10^{18}$	129.2%
5	11	3, 5, 7, 9, 11	$3.3009 \cdot 10^{18}$	136.2%
6	11	3, 4, 5, 7, 9, 11	$3.3826 \cdot 10^{18}$	139.6%
7	11	3, 4, 5, 7, 8, 9, 11	$3.4401 \cdot 10^{18}$	142.0%
8	11	2, 3, 4, 5, 7, 8, 9, 11	$3.4860 \cdot 10^{18}$	143.9%
9	11	2, 3, 4, 5, 6, 7, 8, 9, 11	$3.5098 \cdot 10^{18}$	144.8%
10	11	2, 3, 4, 5, 6, 7, 8, 9, 10, 11	$3.5187 \cdot 10^{18}$	145.2%

* Excitation and measurements are in the vertical direction

For the cantilever problem the Pareto optimal solutions of interest are those that find the best location for one sensor and excitation, which will be used for measurement.

Only vertical DOFs are selected for the excitation and measurement locations since the frequency range for which the optimization was performed only contains the first six natural frequencies of the cantilever beam. Only one of these natural frequencies is associated with axial vibration at a higher frequency.

In Figure D.1 of APPENDIX D a pattern is observed for the sensors placement for the cantilever problem studied in this research. If enough representative sensor optimization results for different types of structures are available, patterns of sensor placement can be identified and then used to develop expert systems to facilitate the sensor layout design for measurement. Alternatively, neural networks could be trained using the representative results to extend the solutions to structures on a larger scale or with different boundary conditions without performing a costly sensor layout optimization for every possible configuration.

In multiobjective optimization problems it is common to plot the results obtained in the objective space. If the number of objective functions is two then the plot is two-dimensional and the axes represent the objective function. Typical plots of the final population for the cantilever problem using the fixed and IRR representations in objective space are shown in Figure 6.19 and Figure 6.20, respectively. In Figure 6.19 for the fixed representation after only 48 generations, 70.5% of the converged population (there was no improvement after 50 generations) is in the Pareto front. The number of individuals present at a particular number of sensors is labeled next to each Pareto optimal solution. Figure 6.19 shows that the individuals are well distributed along the number of sensors and the high percentage of individuals in the Pareto front (on average it was 67.5%) indicates that a good solution is obtained.

The individuals in the Pareto front for the IRR GA in Figure 6.20 are not as well distributed as the individuals for the fixed representation GA. In general, the IRR GA had difficulties distributing individuals on the extremes around one sensor and the maximum number of sensors locations (10 for this case) in certain trials. Also, the percentage of individuals in the Pareto front for the IRR GA was 47.0% and on average it was 49%. The number of generations required for convergence was also somewhat higher at 66 for the IRR GA. In both figures, however, the Pareto front obtained is identical and the

hypothetical curve connecting the points in the Pareto front have a decreasing slope with increasing number of sensors. The decreasing slope can be interpreted such that the relative amount of information gained by using more sensors also decreases gradually as the number of sensors increases.

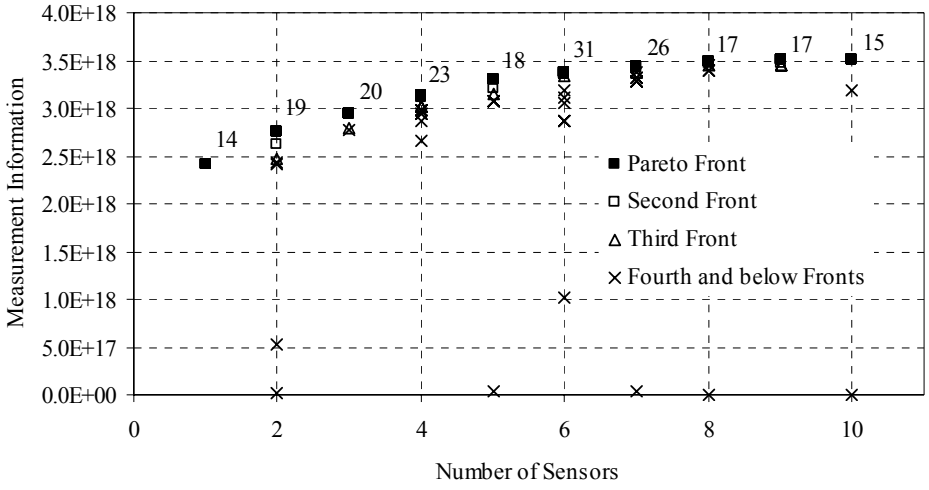

Figure 6.19. Pareto front and individuals in the final population represented in the objective space for the cantilever problem using fixed representation GA, population size is 200

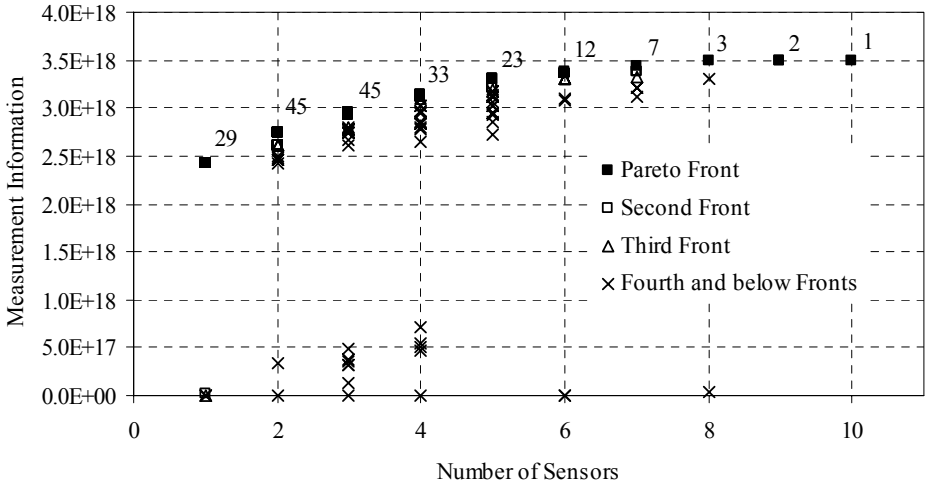

Figure 6.20. Pareto front and individuals in the final population represented in the objective space for the cantilever problem using IRR GA, population size is 200

6.4.2 Results Using Optimal Sensor Locations

Using the optimal excitation and sensor locations (excitation at the free end of the cantilever beam at node 11 and one sensor also placed at is also node 11) the damage detection trials for the CANT I case were repeated using same GA settings. In case CANT I the severity of damage imposed was 10% at element 2. Three different noise levels were investigated for the CANT OPT case: noise free, 10%, and 20% noise. Results are presented in Figure 6.21 through Figure 6.23 and summarized in Table D.16 through Table D.18 of APPENDIX D. Figure 6.21 corresponds to results obtained using the fixed representation GA. For the noise free case, the results after 200 generations were poor compared to other solutions obtained in earlier trials. The poor performance is attributed to premature convergence caused by the high selection pressure imposed by the tournament size of 8. Essentially the results did not change significantly after 23 generations, which clearly suggests premature convergence to an initial fit individual. Nevertheless hillclimbing was able to improve the solution and found the global optimum.

The IRR GA in each trial converged to a solution that was a global optimum in a sense that hillclimbing could not improve the results. In the noise free situation, element 2 with a severity of 10% was found after 101 generations. For the 10 and 20% noise cases, an optimum was found after 170 and 91 generations and there was only one falsely identified element in each trial (element 8) with damage indicators of 0.56 and 1.13%, respectively. The IRR GA without initial seed always found a near global or global optimum solution and only a couple of hillclimbing iterations were performed for the noise free and 10% noise cases. The final results (global optimums) were identical for each trial with element 2 at 10, 9.59 and 9.17% damage for the noise free, 10 and 20% noise cases, respectively. Also the falsely identified element 8 was the same in each trial with damage indicators of 0.56 and 1.13% for the 10 and 20% noisy measurements, respectively.

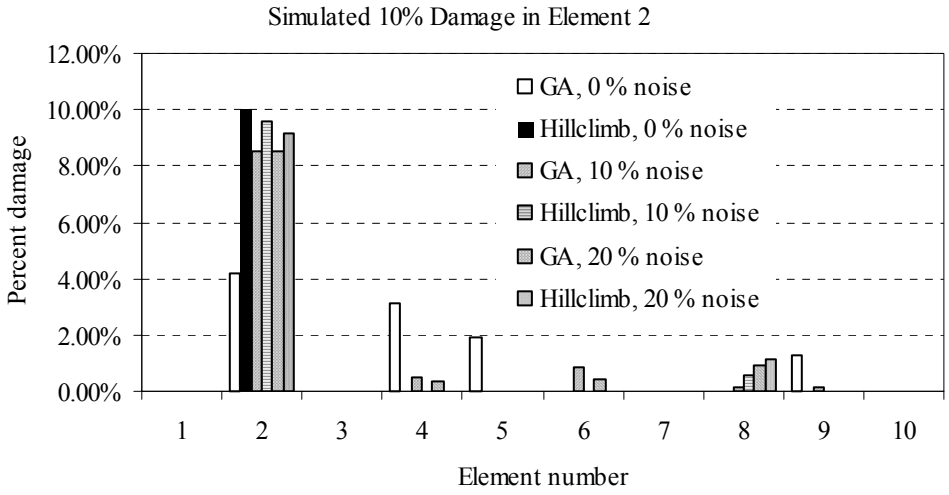

Figure 6.21. Damage detection results for case CANT OPT, fixed representation, seeded initial population, noise levels of 0, 10 and 20%

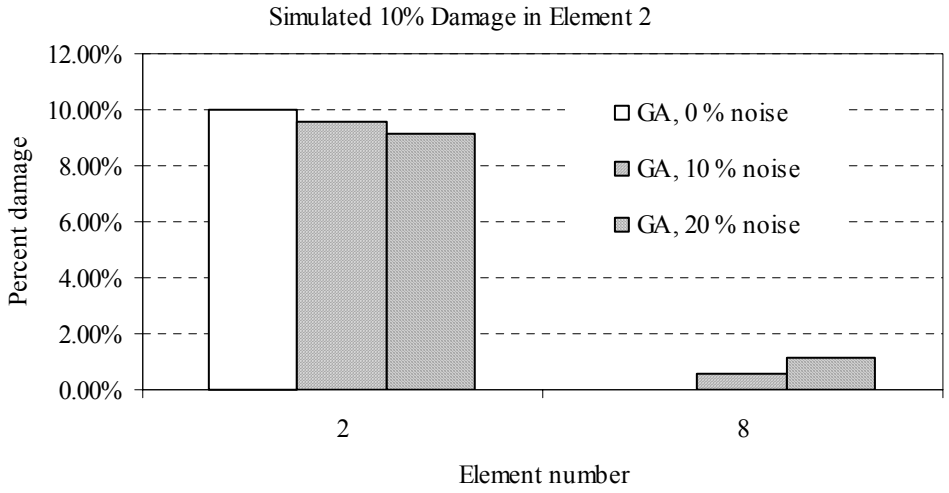

Figure 6.22. Damage detection results for case CANT OPT, implicit redundant representation (IRR), seeded initial population, noise levels of 0, 10 and 20%

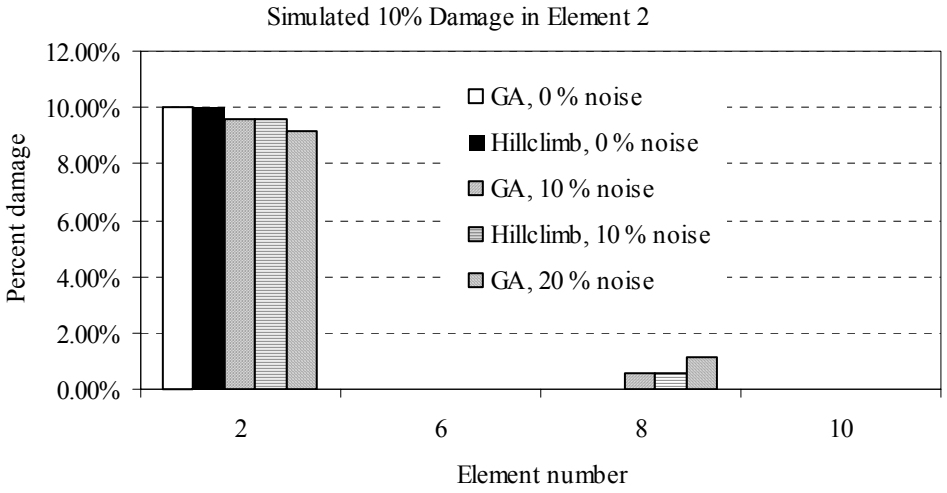

Figure 6.23. Damage detection results for case CANT OPT, implicit redundant representation (IRR), unseeded initial population, noise levels of 0, 10 and 20%

The results obtained using the optimal excitation and sensor locations are compared with those obtained without considering optimal placement for the CANT I case study. In some specific trials using the optimum sensor layout design resulted in faster convergence, but in general this was not the case and can be attributed to the probabilistic characteristics of GAs. An increase in the objective function values, however, was observed, which indicates higher sensitivities for damage detection. Table 6.6 compares the average fitness values of the initial populations for the original (CANT I) and optimal (CANT OPT) sensor layout designs. The average fitness of the initial population increased by an average factor of 3.77 times, or 277%, using the optimal sensor location. The actual objective function value increased by an average of 3.77 times with respect to the same damage. The increase in objective function is not very large. This can be explained by the fact that the excitation location is the same (optimal) in both configurations. In Figure 6.24, final results (including hillclimbing) for the damage detection problem using optimal and non-optimal sensor locations are compared at noise level of 10%. A similar plot for the 20% noise level is depicted in Figure 6.25 using the final results obtained for damage detection when optimal and non-optimal sensor locations were applied. Using the optimal sensor layout, the final results obtained

were consistently the same regardless of the GA parameters and noise levels. Therefore only these final results are plotted in Figure 6.24 and Figure 6.25 for the optimal sensor location case. From the figures, it is apparent that the damaged element was correctly identified in all cases but the damage indicator values using non-optimal sensor location are somewhat worse than those predicted using the optimal sensor layout. The optimal sensor layout results are closest to the imposed 10% damage at element 2. In the non-optimal sensor cases, three (fixed representation) or two (IRR) other finite elements were falsely identified as damaged while using the optimal sensor arrangement only one element was predicted as falsely damaged. By using the optimal sensor layout design, the damage identification is more unique and the predicted damage indicators better approximate the actual damage state.

Table 6.6. Average fitness values of initial populations using non-optimized and optimal sensor locations for the cantilever beam case studies CANT I and OPT

Representation	Noise	Average Fitness of Initial Population		Average Increase [%]
		CANT I	CANT OPT	
Fixed	0%	129,589,540	442,001,920	241.1%
Fixed	10%	128,215,170	438,705,070	242.2%
Fixed	20%	127,732,190	438,336,140	243.2%
IRR Seeded	0%	91,974,469	354,103,060	285.0%
IRR Seeded	10%	90,819,113	347,492,410	282.6%
IRR Seeded	20%	90,187,649	382,906,480	324.6%
IRR Unseeded	0%	94,274,654	368,389,990	290.8%
IRR Unseeded	10%	93,086,681	361,502,460	288.4%
IRR Unseeded	20%	92,397,953	368,609,770	298.9%
			Average:	277.4%

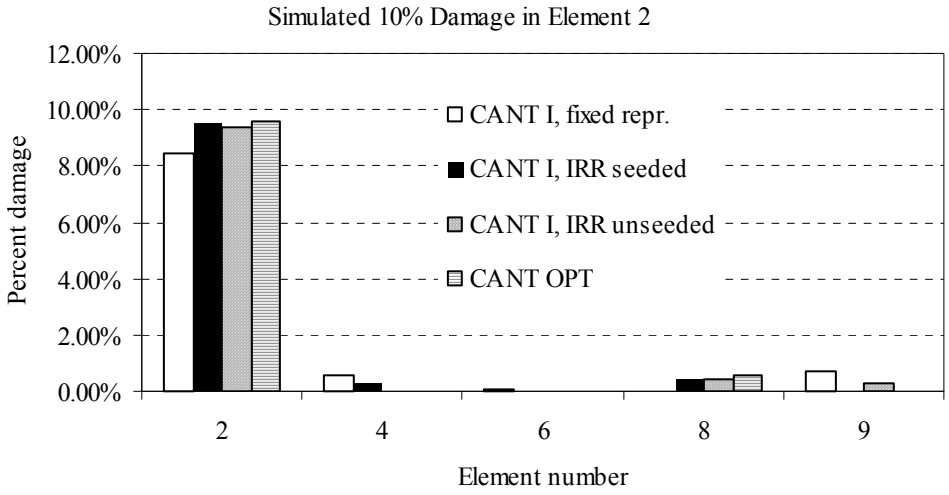

Figure 6.24. Comparison of damage detection results using different measurement configurations at a noise level of 10% for the cantilever problem

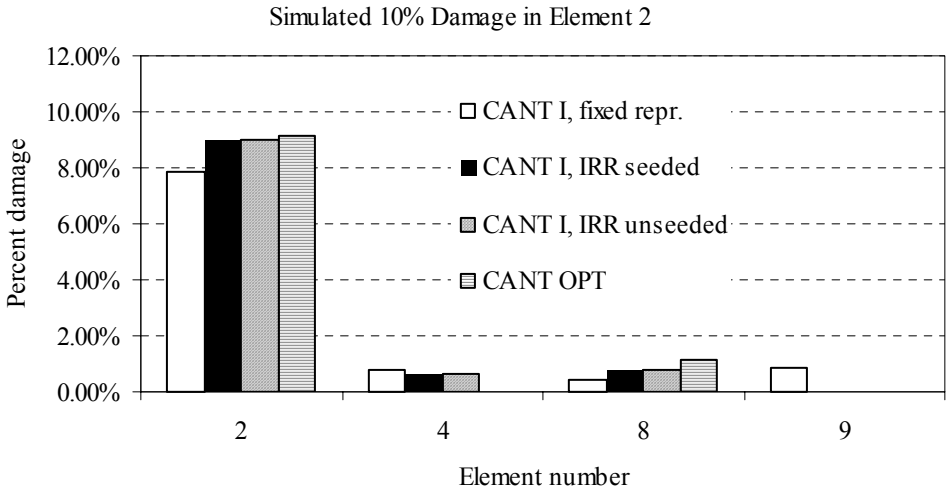

Figure 6.25. Comparison of damage detection results using different measurement configurations at a noise level of 20% for the cantilever problem

7 CASE STUDY RESULTS AND DISCUSSION FOR TWO-SPAN CONTINUOUS BEAMS

The set of GA parameters used in the two-span continuous beam trials are summarized in Table 7.1. These parameters were selected on the basis of initial trials using different GA parameters and on the experience gained during the cantilever beam trials. The selection pressure is reduced (tournament size) for the IRR GA when compared to the selection pressure used in the cantilever beam trials to enable increased exploration of the search space. Also the number of crossover sites and the mutation rate is reduced to decrease the effect of disruptions caused by crossover and mutation.

Table 7.1. GA parameters for two-span continuous beam trials

	Fixed Representation	IRR, Seeded*	IRR, Unseeded
Population Size	200	200	200
Tournament Size	4	6	6, 8
Initial Seed	Yes	Yes	No
Maximum Generations	200	200	200
Stop if no Improvement	20	20	20
Crossover Type	Adaptive	Adaptive	Adaptive
Crossover Sites	6, 8	6	6
Crossover Rates	Primary: 0.9, Secondary: 1.0	Primary: 0.9, Secondary: 1.0	Primary: 0.9, Secondary: 1.0
Mutation Type	Non-uniform	Uniform	Uniform
Mutation Rate	0.005 - 0.0075	0.005	0.005
Elitism	Yes	Yes	Yes
Hillclimbing	Yes, Reduced	Yes, Reduced	Yes, Reduced
Coding	Gray	Gray	Gray

* For the IRR the number of gene instances (expected number of damaged elements) was 10 and the gene locator (GL) length is 3

The trials are grouped into three sets fixed: IRR seeded and IRR unseeded trials. This classification is done to enable the effective comparison of the different

representations. The number of significant digits for the two-span continuous beam trials was 6, which required 20 bits to represent a damage indicator with a precision of about $9.44 \cdot 10^{-7}$ or $9.44 \cdot 10^{-5}$%.

7.1 Equal Damages, Case Studies TWSP IA, IB and II

Test cases TWSP IA and IB (Table 5.2) represent a damage scenario in which 10% stiffness reductions exist in two of the elements. The first element is located about the middle of the left span and the second element is located on the left side of the mid-support (Figure 5.2). The difference in the two sub-cases TWSP IA and IB is in the number of sensors used for measurements. TWSP IA uses one sensor location while TWSP IB uses two sensors. Only the noise free measurement situation was considered for these case studies.

Results for the two case studies are depicted in Figure 7.1 and Figure 7.2 and summarized in Table D.19 and Table D.20 of APPENDIX D. The figures show that the fixed representation GA performed reasonably well for the TWSP IA case and predicted the two damaged elements 6 and 10 with 7.54 and 9.46% instead of the imposed 10% values after 200 generations, respectively. In addition, two other elements (5 and 11) that are adjacent to the damaged elements were falsely identified as damaged with damage indicators of about 1.6%. The other 7 elements had small residual damages that do not even plot on a linear scale (Figure 7.1). Hillclimbing corrected the false readings and the global optimum was obtained for the provided precision.

For the two-sensor case TWSP IB, the fixed GA identified element 6 with 6.93% and falsely identified element 11, which is adjacent to the correct damaged element 10, with 9.87% damage after 200 GA generations. From Figure 7.2 it is clear that other elements were falsely identified with relatively small damages and the number of total false identifications was 10. After hillclimbing, the global optimum was obtained within the given precision. The false identification of element 11 instead of element 10 may be attributed to the protective nature of adaptive crossover and high selection pressure that together can cause premature convergence when a highly fit individual is present in the initial population. Recall that in adaptive crossover the best individual, if it is selected,

will not undergo crossover. In the initial population, the best individual in all cases was the zero damage individual (often more superior than any other individuals), which is therefore highly protected by adaptive crossover and elitism. It is often selected for crossover because of its superiority over other individuals and the relatively high selection pressure. This essentially means that the only way to change the zero damage individual is through mutation. The mutation rate, however, was reduced for the two-span continuous trial from 1% (cantilever problems) to 0.5%. Combining the effects of the above factors it is suspected that premature convergence occurred. This conclusion is supported by the fact that the solution in the final population (200 generations) was only slightly different from the solution at generation 23.

The IRR GA with initial seed performed quite well for both cases TWSP IA and IB. The correct damaged elements were identified with good accuracy, element 6 with 9.91/10.0% and element 10 with 9.93/9.99% for the two cases after 200 generations, respectively. The number of falsely identified elements was 3 in both cases with a maximum of 0.11/0.009% in case TWSP IA and IB, respectively. After hillclimbing, the global optimum was found in both cases within the available precision provided by the binary representation. The IRR GA without initial seed had a similar performance level as the seeded IRR GA. Both damaged elements were identified with high accuracy and hillclimbing only slightly improved the results obtained after 200 generations (Figure 7.1 and Figure 7.2). The convergence in general was not improved by including two measurement locations instead of one. This, however, does not imply that it may not be beneficial to include more measurement information in the damage identification process. This conclusion simply emphasizes that for these cases measurements pertaining to one sensor location is sufficient to accurately locate damage.

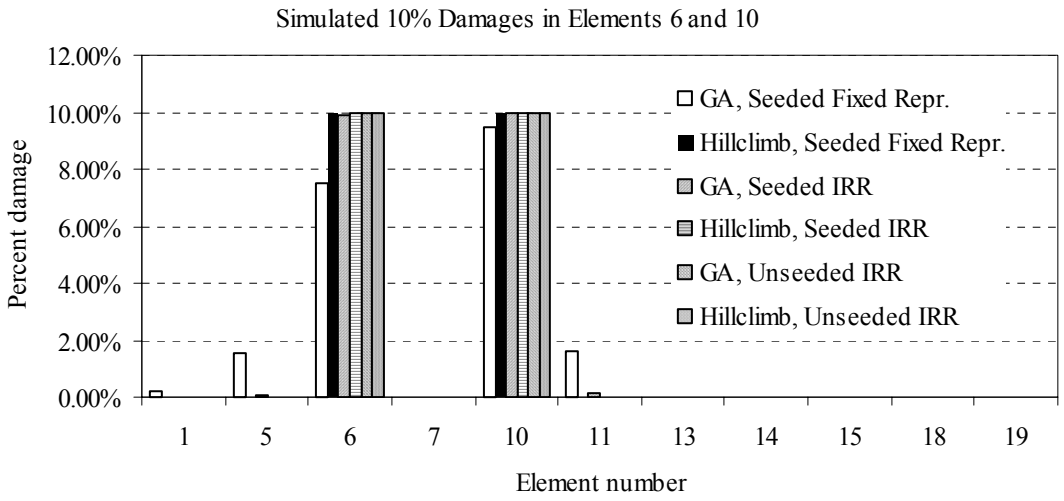

Figure 7.1. Damage detection results for case TWSP IA, fixed and implicit redundant representations (IRR), seeded and unseeded initial population, noise free measurements

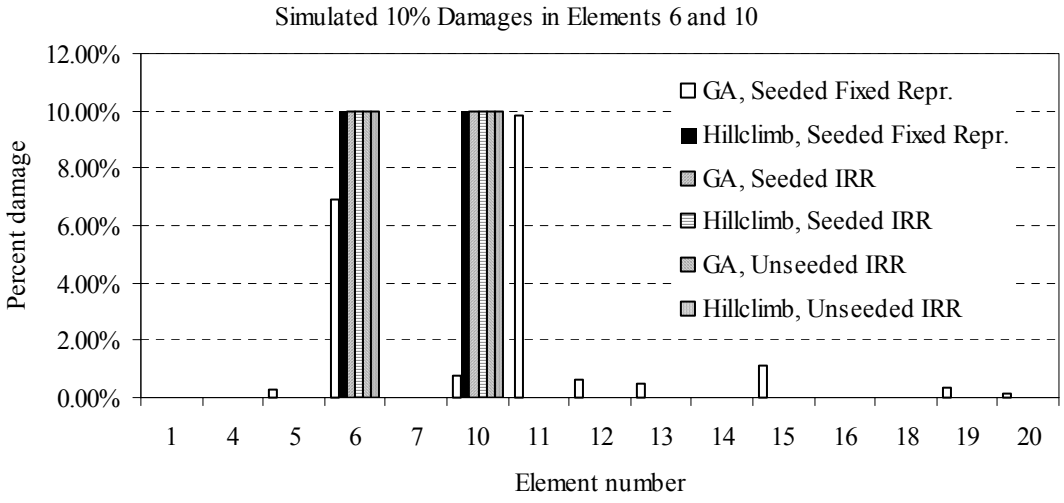

Figure 7.2. Damage detection results for case TWSP IB, fixed and implicit redundant representations (IRR), seeded and unseeded initial population, noise free measurements

In Figure 7.3, the number of gene instances in the best IRR GA individual and the average number of gene instances of the population are plotted as functions of the generation number for the unseeded IRR GA in case study TWSP IA. On a secondary

logarithmic axis, the fitness of the best individual and the average fitness of the population are also plotted in the same figure. This figure demonstrates the ability of IRR GAs to dynamically change the number of variables (gene instances) implicitly included in the objective function. IRR GAs simultaneously alter the number of variables and minimize the objective function as seen in Figure 7.3. The number of gene instances or damaged elements in the best individual of the initial population was seven, but was reduced to three after 200 generations. There were two damaged elements in this case study and the falsely identified element had a negligible damage indicator of 0.0033%. The average number of gene instances of the population shows a similar tendency and its value gradually decreased as the population aged. Since the value of the objective function at the global optimum is zero, a semi-logarithmic plot better shows the convergence. After two hundred generations, the objective value was $4.1 \cdot 10^{-5}$, which was small enough to be accepted as zero by most engineers. While the fitness of the best individual quickly approached zero, the average fitness of the population shows that diversity of the population was maintained throughout the generations.

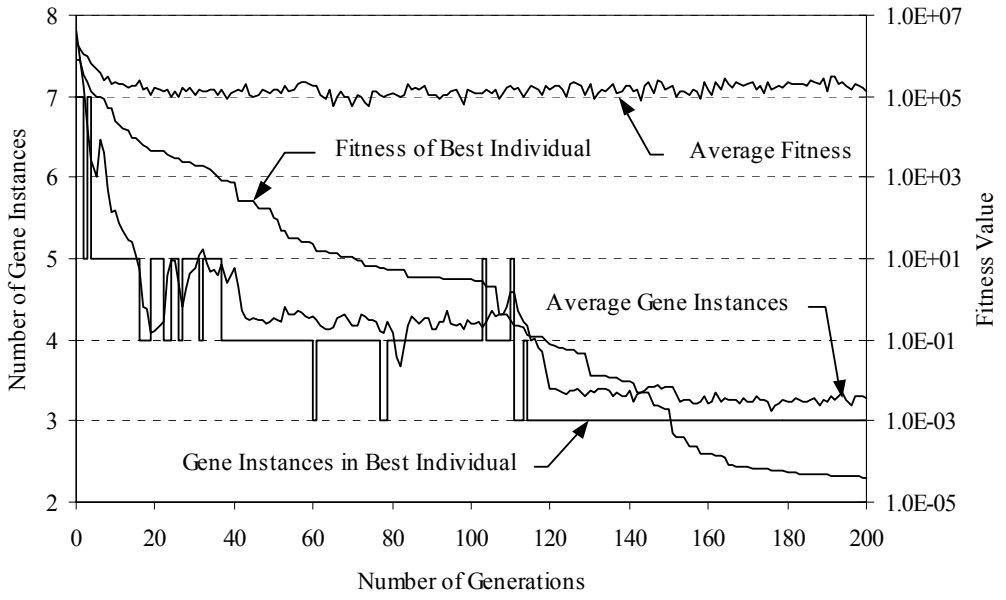

Figure 7.3. Convergence plot demonstrating the dynamic and adaptive ability of IRR GAs, case study TWSP IA unseeded IRR GA

The two damaged elements for the TWSP II (Table 5.2) case study are located approximately at the middle of the both spans of the two-span continuous beam (Figure 5.2) with damage severities of 10%. The excitation and measurement locations were also altered to investigate the effect of sensor location. Results for case TWSP II are depicted in Figure 7.4 and summarized in Table D.21 of APPENDIX D. Similar conclusions can be drawn about the performances of the different GA representations used as were concluded for cases TWSP IA and IB. The fixed representation GA found a good solution after 200 generations, which identified the two damaged elements with 10.05 and 8.16% damages and the other damage indicators were small or insignificant (Figure 7.4). Both the seeded and unseeded IRR GAs outperformed the fixed representation GA and found solutions very close to the global optimum after 200 generations. The number of falsely identified elements was greatly reduced to 2 and 3 compared to the 18 falsely identified elements found by the fixed GA and the severity of the false damages had a maximum value of 0.28%. Hillclimbing always obtained the global optimum within the available precision regardless of the representation. The change in the location of the damaged elements and the measurement configuration did not have an observable effect on the performance of SDIM developed in this research.

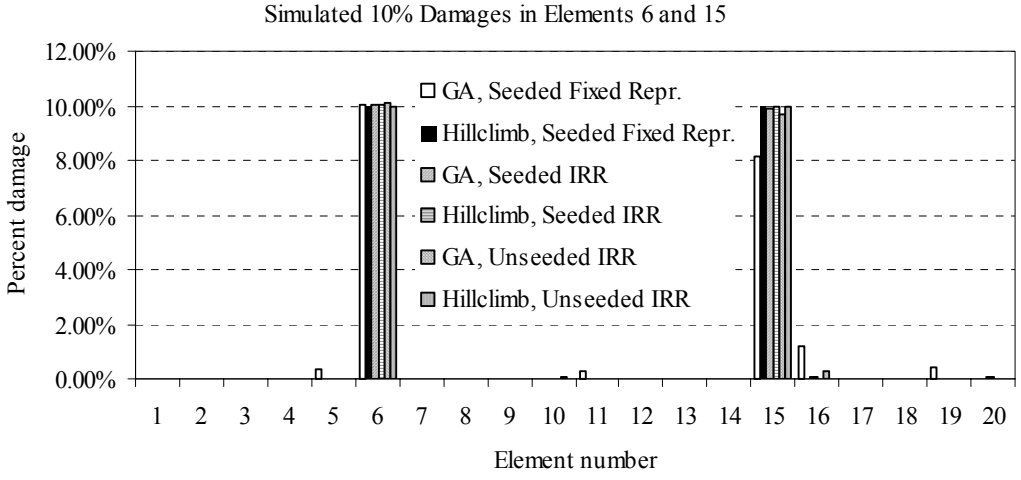

Figure 7.4. Damage detection results for case TWSP II, fixed and implicit redundant representations (IRR), seeded and unseeded initial population, noise free measurements

7.2 Unequal Damages, Case Studies TWSP IIIA and IIIB

The case studies in this section, TWSP IIIA and IIIB (Table 5.2), have two damage locations with unequal damages. The damage in the middle of the left span at element 6 is 5% and element 10 on the left side of the mid-support has 10% damage (Figure 5.2). The only difference between the two sub-cases is in the number of measurement locations. The former sun-case uses one while the later sub-case uses two FRF measurements.

Results for the TWSP IIIA case are depicted in Figure 7.5 through Figure 7.10 and summarized in Table D.22 through Table D.27. The sub-case TWSP IIIA investigated the effect of noisy measurements by including five different noise levels in the simulated measurement data: noise free, 5, 10, 20 and 30% Gaussian noise.

A similar observation concerning the noise free trials was made as for the first two TWSP IA, IB and II case studies presented. The fixed representation GA, which works with a complete solution of the problem, was not able to found the global optimum after 200 generations. Instead the fixed representation GA obtained a solution in which the correct damaged elements were identified with higher damage indicator values (4.19 and 8.82%) than any other elements. The largest false prediction was 1.48% that occurred at element 11, which is adjacent to element 10 which had the inflicted damage of 10%. The sum of damages for the two elements identified is 10.3%, which is almost equivalent to the imposed damage in element 10. All other elements had damage indicator values larger than zero, but again the values were negligible compared to the damage magnitude of the correct elements (Figure 7.5). Hillclimbing easily found the global optimum, due to the precision used in the binary representation.

As with all other cases studied so far, the IRR GAs found a near global optimum of the problem with only a few number of false predictions (3 for the seeded and 2 for the unseeded IRR GA) after 200 generations. Since the found solutions were close to the global optimum, only a few hillclimbing iterations were required to find the actual global optimum within the precision provided in the encodings (Figure 7.7 and Figure 7.9).

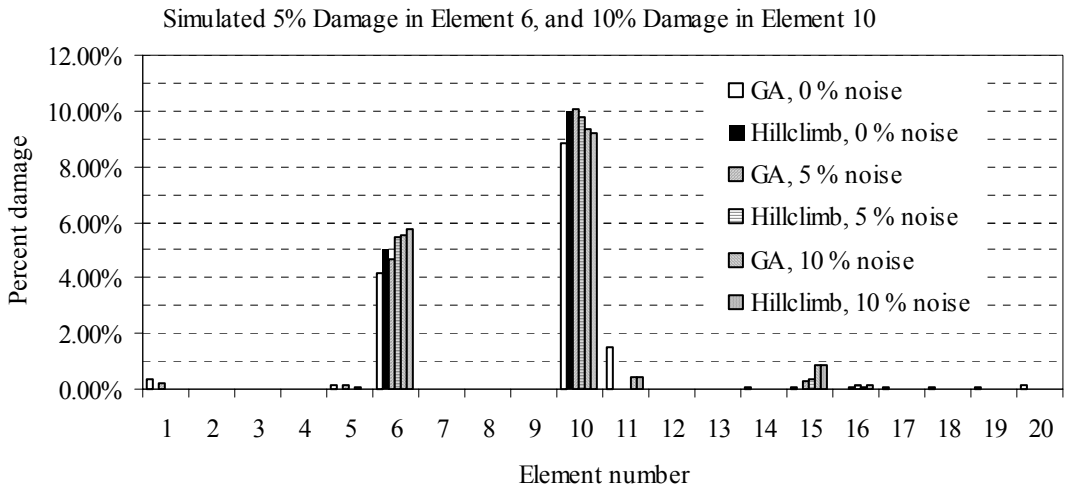

Figure 7.5. Damage detection results for case TWSP IIIA, fixed representation, seeded initial population, noise levels of 0, 5 and 10%

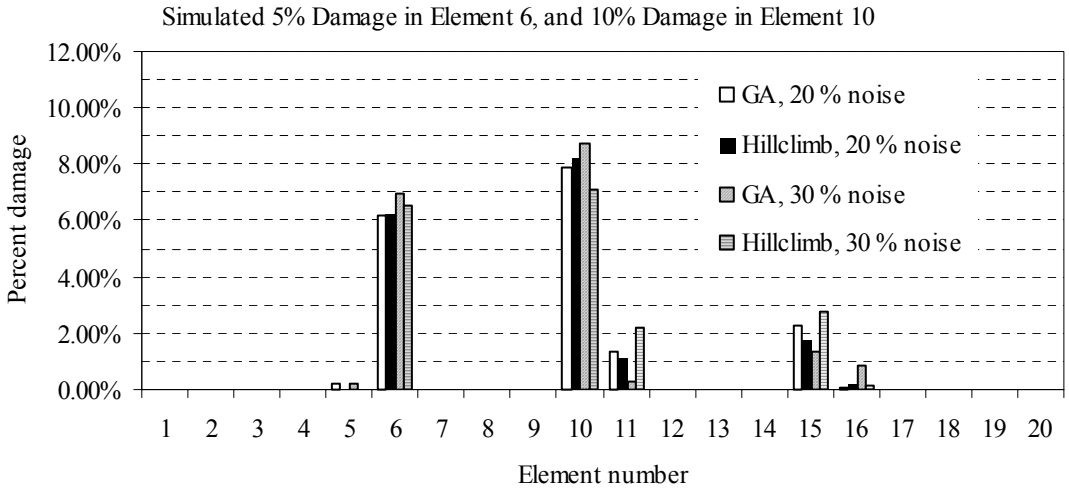

Figure 7.6. Damage detection results for case TWSP IIIA, fixed representation, seeded initial population, noise levels of 20 and 30%

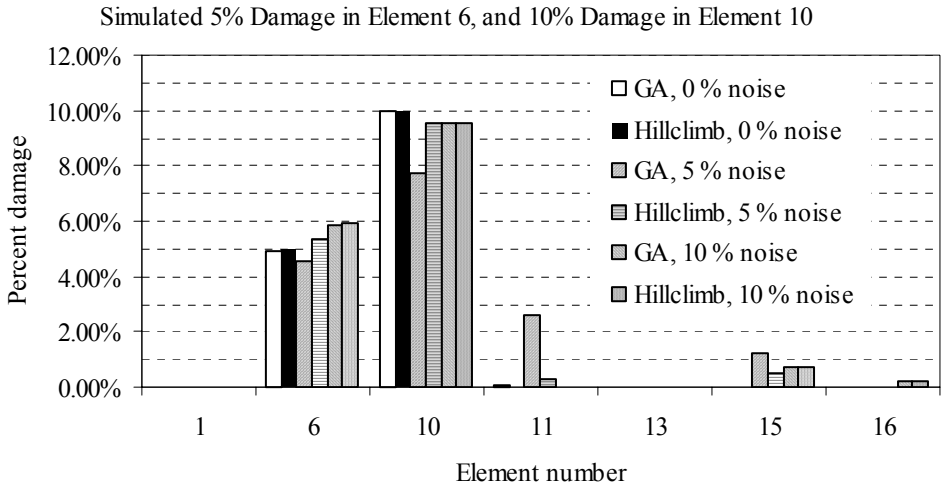

Figure 7.7. Damage detection results for case TWSP IIIA, implicit redundant representation (IRR), seeded initial population, noise levels of 0, 5 and 10%

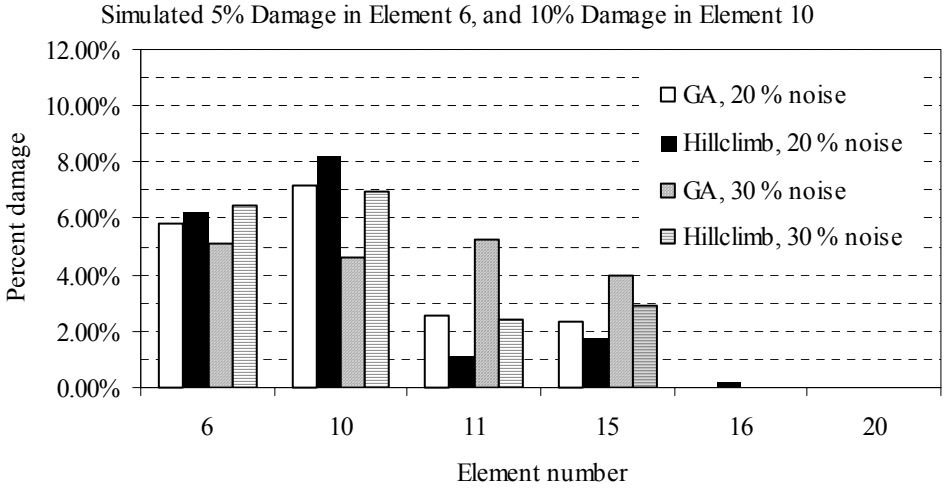

Figure 7.8. Damage detection results for case TWSP IIIA, implicit redundant representation (IRR), seeded initial population, noise levels of 20 and 30%

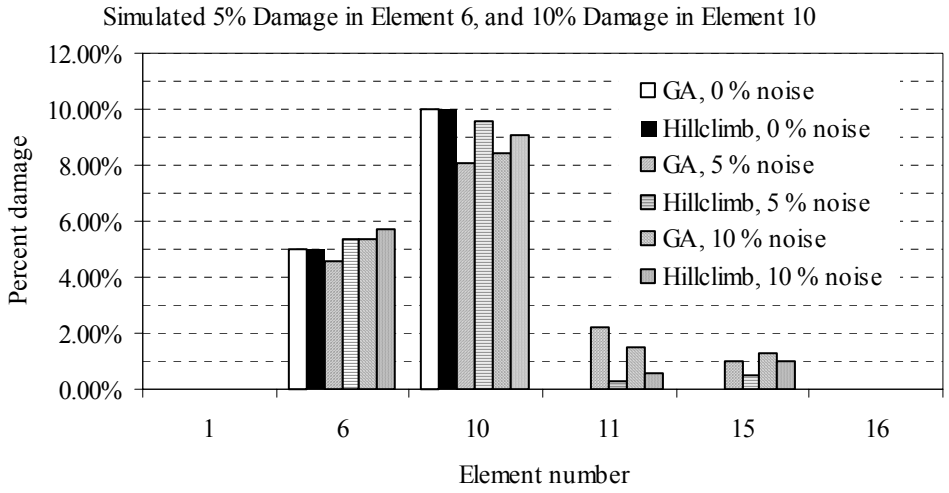

Figure 7.9. Damage detection results for case TWSP IIIA, implicit redundant representation (IRR), unseeded initial population, noise levels of 0, 5 and 10%

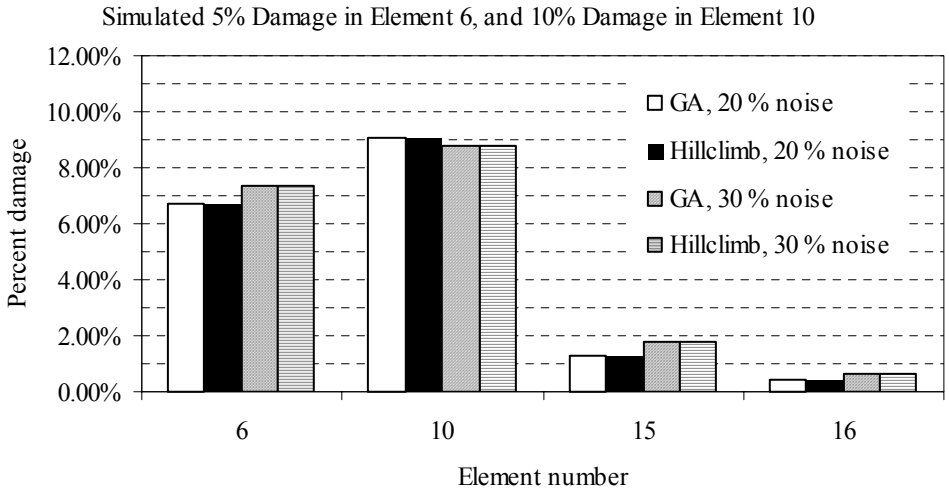

Figure 7.10. Damage detection results for case TWSP IIIA, implicit redundant representation (IRR), unseeded initial population, noise levels of 20 and 30%

In addition to the noise free measurement case, four different noise levels (5, 10, 20, 30%) were used to investigate the effect of measurement noise on the accuracy of damage detection for the TWSP IIIA (Table 5.2) case study. Results obtained for the

noisy measurement cases can be seen in Figure 7.5 through Figure 7.10 and summarized in Table D.22 through Table D.27 of APPENDIX D. As it was expected with increasing noise levels, the accuracy of damage detection degrades regardless of the representation used. Another observation that is valid for all representations, was that predictions tended to overestimate the damage in element 6, which was the element with the smaller 5% damage, and tended to underestimate the damage in element 10, which was the element at the mid-support with the larger 10% damage. This suggests that noise has the effect of equalizing damage levels in the predictions when this SDIM developed in this research was used.

Even with a noise level of 5%, all trials resulted in good solutions. The damage in the final solution after hillclimbing was between 5.38-5.91% for element 6 instead of the imposed 5% and it was between 9.10-9.74% for element 10 instead of the imposed 10% in all trials. The maximum false prediction was 0.5% for the 5% noise case and it occurred in solutions obtained for the IRR GA trials. The largest false reading for the 10% noise case was found in the solution obtained by the unseeded IRR GA trial. The fixed GA performed surprisingly well for these trials, although the number of false predictions (most of them were negligibly small) after 200 generations was considerably larger than those for the IRR GAs. The final solutions found with the fixed GA were at least as good as those found by the IRR GA (Figure 7.5, Figure 7.7 and Figure 7.9). For larger noise levels (20 and 30%), the fixed representation and seeded IRR GA had a similar overall performance on damage detection. The predicted damage for element 6 was 6.22% and 8.27% for element 10 and the same elements were falsely identified with the same severity for the 20% noise case. In both trials element 11 (adjacent to element 10) was assigned a 1.16% damage that adds up to 9.43% damage in the element at the mid-support. At the 30% noise level, similar conclusions can be made for the fixed and seeded IRR GAs (Figure 7.6 and Figure 7.8). For both noise levels (20 and 30%), the IRR GA without initial seed performed the best in the sense that the falsely identified damages were less severe and the predicted damages, 9.10 and 8.77%, for element 10 were closer to the inflicted value (10%). However, the predicted damages, 6.68 and 7.33%, for element 6 were somewhat larger than those predicted by the fixed or seeded

IRR GAs. Figure 7.10 shows that even though falsely identified elements were present, the correct damaged elements appear with more pronounced severity than the falsely identified elements.

In case study TWSP IIIB an additional measurement location was added at node 4 (Figure 5.2). The goal of this case study was to investigate the effect of including additional measurement information in to the damage detection problem. The results for this case are depicted in Figure 7.11 and summarized in Table D.28 of APPENDIX D. Trials were performed only for the noise free measurement cases. From Figure 7.11 it is clear that global optimum solutions were found in each case after hillclimbing, or in case of the unseeded IRR GA, after 180 generations. Again the solution obtained by the fixed representation GA contained several false readings with negligible damage indicator values, but the correct damaged elements were identified with damage severities close to the target values after 200 GA generations. The IRR GA with initial seed converged to a solution in which 3 elements were falsely identified as damaged with damage indicators less than 0.9%. Also, premature convergence can be observed due to the overprotection of the best individual (zero damage individual) in the initial population. In case of the unseeded IRR GA, however, premature convergence did not occur since there was not an extraordinarily fit individual in the initial population and the diversity of the population was maintained throughout the entire optimization. Significant improvements in the performance of damage detection, however, could not be confirmed for the two-measurement case over the single FRF measurement case. In both cases, the global optimums were found and the process required approximately the same amount of computational effort. These results do not provide conclusive information about the superiority of one trial over another due to the probabilistic nature of GAs.

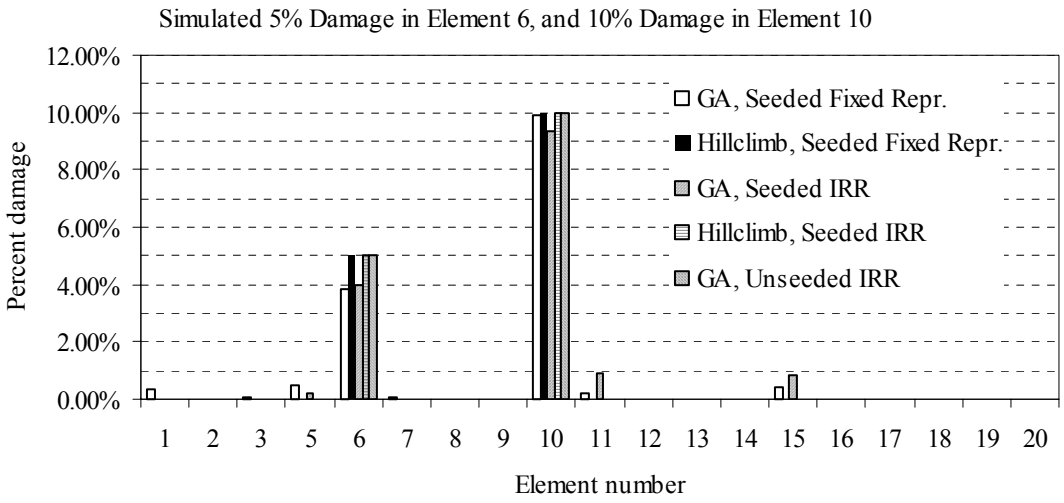

Figure 7.11. Damage detection results for case TWSP IIIB, fixed and implicit redundant representations (IRR), seeded and unseeded initial population, noise free measurements

7.2.1 Objective Function Based on FRF Correlation Criteria

The objective function defined in Eq. (6.1) for the global shape criterion (GSC) and global amplitude criterion (GAC) correlations were used in trials to compare results obtained by using different objective functions for the SDIM. The trials included cases with 0, 5, 10, 20 and 30% measurement noise. The damage and measurement configuration was the same as investigated in case study TWSP IIIB (Table 5.2). The results obtained for the correlation objective function are compared with the results obtained for case study TWSP IIIA. Again the only difference between case studies TWSP IIIA and IIIB is in the number of measured FRFs. The former case includes, one while the later two measurements.

The "sum of GSC and GAC squares" objective function case study, in which the number of measurements is two (TWSP IIIB), was chosen so that the GSC was not unity over the entire frequency range. The GSC contributes to the objective function with possibly useful information about damages. Results for case study TWSP IIIB using the sum of GSC and GAC squares objective function are depicted in Figure 7.12 through Figure 7.17 and summarized in Table D.29 through Table D.34 of APPENDIX D. For the

noise free measurements, the unseeded IRR GA nearly found the global optimum (only 3 hillclimbing iterations were performed) after 200 generations without false predictions. The solution found by the fixed and seeded IRR GAs after 200 generations were able to identify the two damaged elements (6 and 10) but the predicted severities were quite far from the imposed values. Both trials picked element 11 as damaged, so the sum of the damages in element 10 and 11 were 10.8% and 10.5% for the fixed and seeded IRR GA, respectively. Local hillclimbing required several iterations, but adjusted the results for both trials. The optimum found was near global (there were small residual damages in certain elements). Although the global optimum was found using either objective function, the performance of the sum of square differences objective function was superior in the sense that solutions after 200 generations better approximated the inflicted damage scenario and less hillclimbing iterations were required to adjust the results. Also, the number of measurements investigated would be favorable for the correlation objective function, although no actual performance advantage was found.

With increasing measurement noise, the accuracy of damage detection quickly degrades for all trials. In Table 7.2 and Table 7.3 results for both the sum of GSC and GAC squares, Eq. (6.1), as well as the sum of square differences, Eq. (2.54), objective functions are compared for noise levels of 5 and 20%, respectively. From these tables it is clear that the objective function proposed in Section 2 of this dissertation is less sensitive to noise than the objective function based on correlation measures. When comparing the values listed in the two tables it can be concluded that the FRF differences objective function outperforms the correlation measure objective function in every aspect. The damage indicator values found are closer to the original damage case when the FRF differences objective function is used. The number and severity of false predictions is also improved. The damage identification process breaks down at a noise level of 20% for the correlation objective function since the falsely identified elements have a damage indicator that is about the same (~5%) as that of the correct, damaged element 6 (Table 7.3). The GA using the correlation based objective function therefore breaks down at a 20% noise level and becomes severely ambiguous at a noise level of 30%. As an example

element 6 was not identified for the unseeded IRR GA for a 30% noise level (Figure 7.13, Figure 7.15 and Figure 7.17).

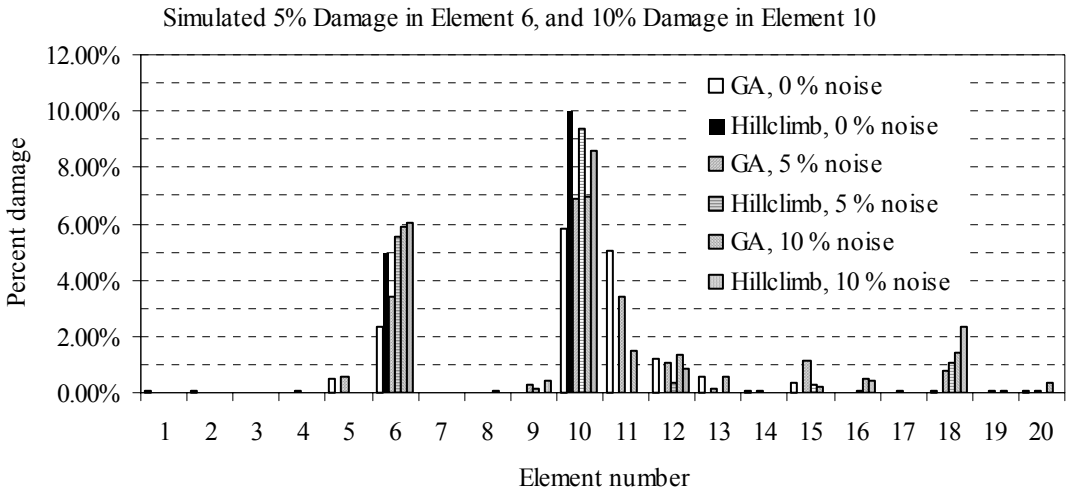

Figure 7.12. Damage detection results for case TWSP IIIB, fixed representation, seeded initial population, objective function is the sum of GSC and GAC squares, noise levels of 0, 5 and 10%

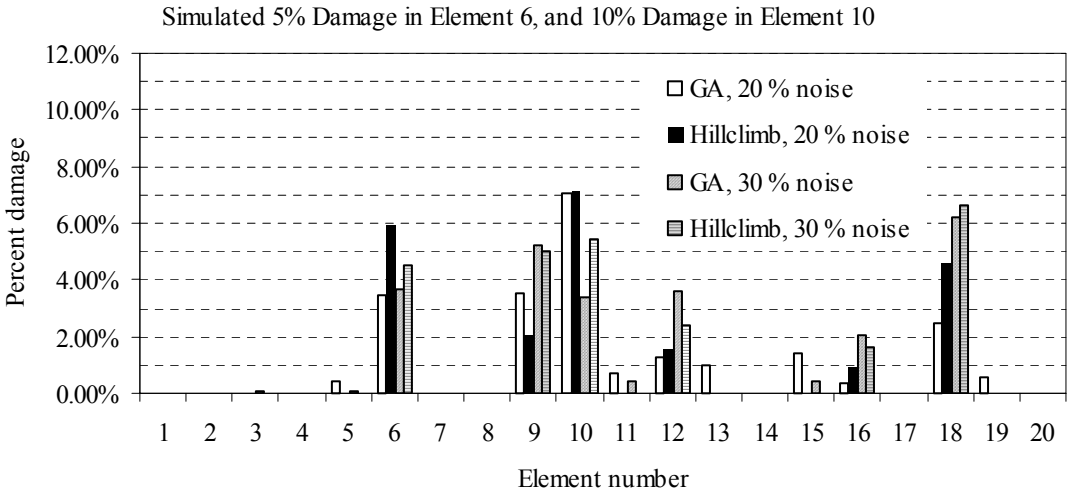

Figure 7.13. Damage detection results for case TWSP IIIB, fixed representation, seeded initial population, objective function is the sum of GSC and GAC squares, noise levels of 20 and 30%

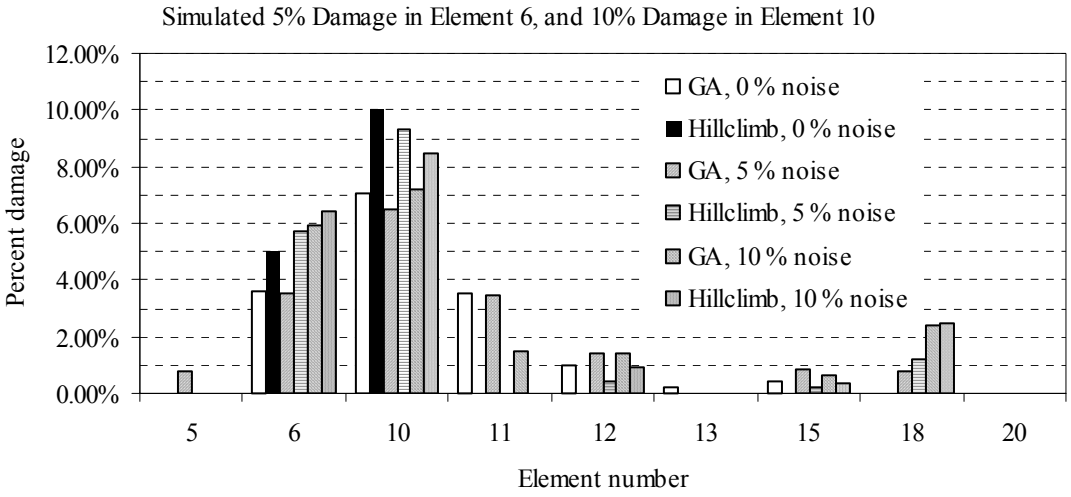

Figure 7.14. Damage detection results for case TWSP IIIB, implicit redundant representation (IRR), seeded initial population, objective function is the sum of GSC and GAC squares, noise levels of 0, 5 and 10%

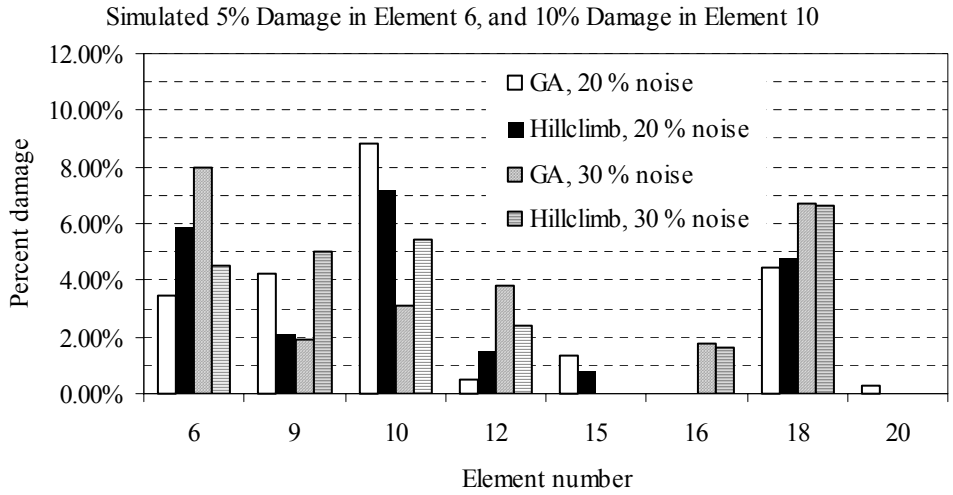

Figure 7.15. Damage detection results for case TWSP IIIB, implicit redundant representation (IRR), seeded initial population, objective function is the sum of GSC and GAC squares, noise levels of 20 and 30%

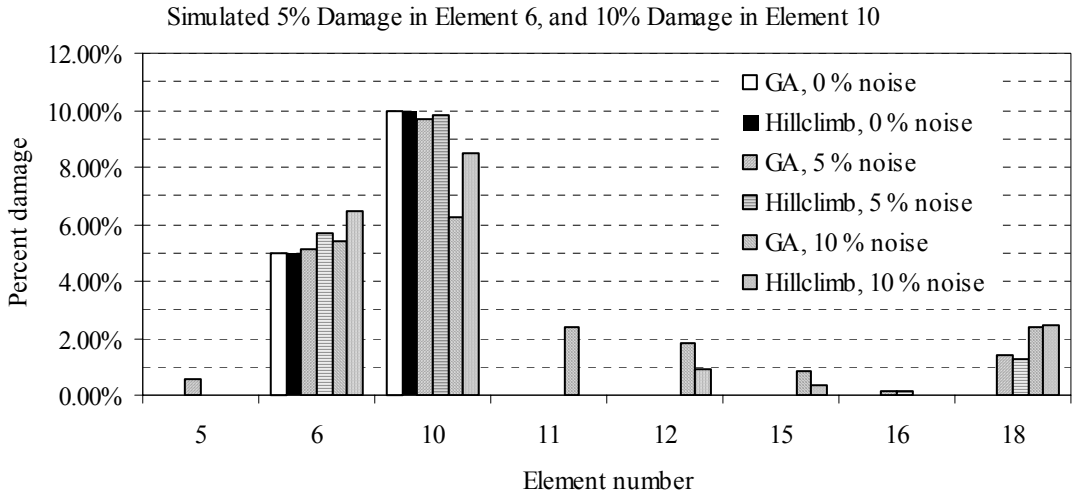

Figure 7.16. Damage detection results for case TWSP IIIB, implicit redundant representation (IRR), unseeded initial population, objective function is the sum of GSC and GAC squares, noise levels of 0, 5 and 10%

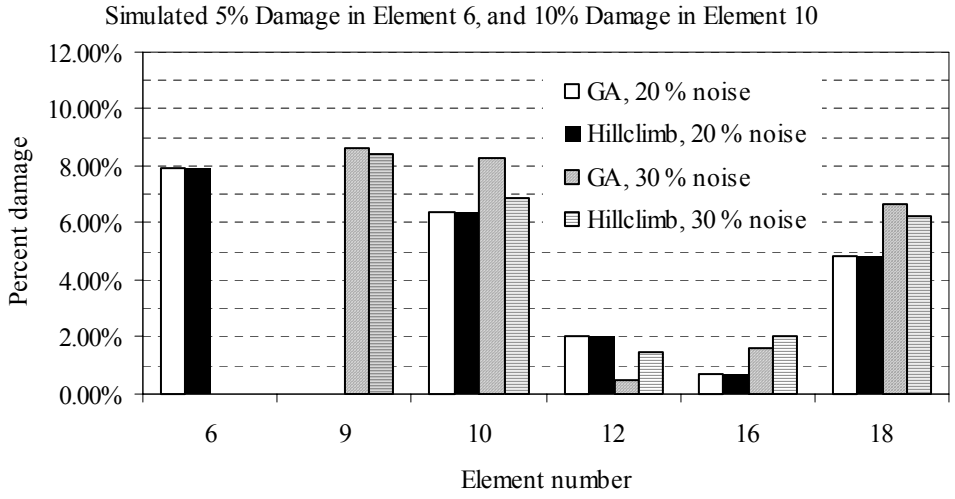

Figure 7.17. Damage detection results for case TWSP IIIB, implicit redundant representation (IRR), unseeded initial population, objective function is the sum of GSC and GAC squares, noise levels of 20 and 30%

Table 7.2. Comparison of the performance of different objective functions at a 5% noise level in measurements for the two-span continuous beam

	5% noise					
	Sum of GSC and GAC Squares			Sum of Square Differences		
	Fixed	IRR seeded	IRR unseeded	Fixed	IRR seeded	IRR unseeded
Damage at element 6 and 10	5.57, 9.37%	5.72, 9.29%	5.70, 9.84%	5.47, 9.74%	5.38, 9.56%	5.38, 9.56%
Number of false predictions	6	3	2	2	2	2
Maximum false damage	1.06%	1.19%	1.26%	0.36%	0.51%	0.51%

Table 7.3. Comparison of the performance of different objective functions at a 20% noise level in measurements for the two-span continuous beam

	20% noise					
	Sum of GSC and GAC Squares			Sum of Square Differences		
	Fixed	IRR seeded	IRR unseeded	Fixed	IRR seeded	IRR unseeded
Damage at element 6 and 10	5.93, 7.14%	5.85, 7.19%	7.94, 6.39%	6.22, 8.27%	6.22, 8.27%	6.68, 9.10%
Number of false predictions	5	4	3	3	3	2
Maximum false damage	4.62%	4.82%	4.82%	1.79%	1.79%	1.28%

7.2.2 Effect of Noise on Objective Function Formulations

Based on the results obtained for the cantilever and two-span continuous beam problems it can be concluded that both objective functions work well in localizing damages in a noise free environment. When noise is introduced into the measurements, however, (in practice noise is always present and cannot be eliminated) the information contained in the objective function based on correlation criteria is not adequate to detect damages with high confidence.

To understand the causes behind the failure of the correlation function at higher noise levels, the measured FRFs for case study TWSP IIIB are investigated in further detail. In this case study there were two measured FRFs on the damaged structure. The first one, designated as FRF 1 and measured between node 18 and 4 (Figure 5.2), is depicted in Figure 7.18 (a) for the noise free as well as the 10 and 20% added Gaussian noise cases. The second simulated accelerance (between nodes 18 and 14) for this case study is designated as FRF 2 and can be seen in Figure 7.18 (b) for 0, 10 and 20% noise levels. Figure 7.18 shows that the random Gaussian noise is simply superimposed on the noise free FRF data simulated for the damaged structure.

In both objective functions considered the areas under defined curves are taken and the sum of squares of these areas form the complete objective function. The sum of squares is used frequently in objective functions because if the squared terms were the variables, then the objective function would be a quadratic multidimensional bowl or sphere. Usually this function is easy to optimize with any kind of method. So for the purposes of the present investigation, the areas whose square is taken in the objective functions should be closely examined.

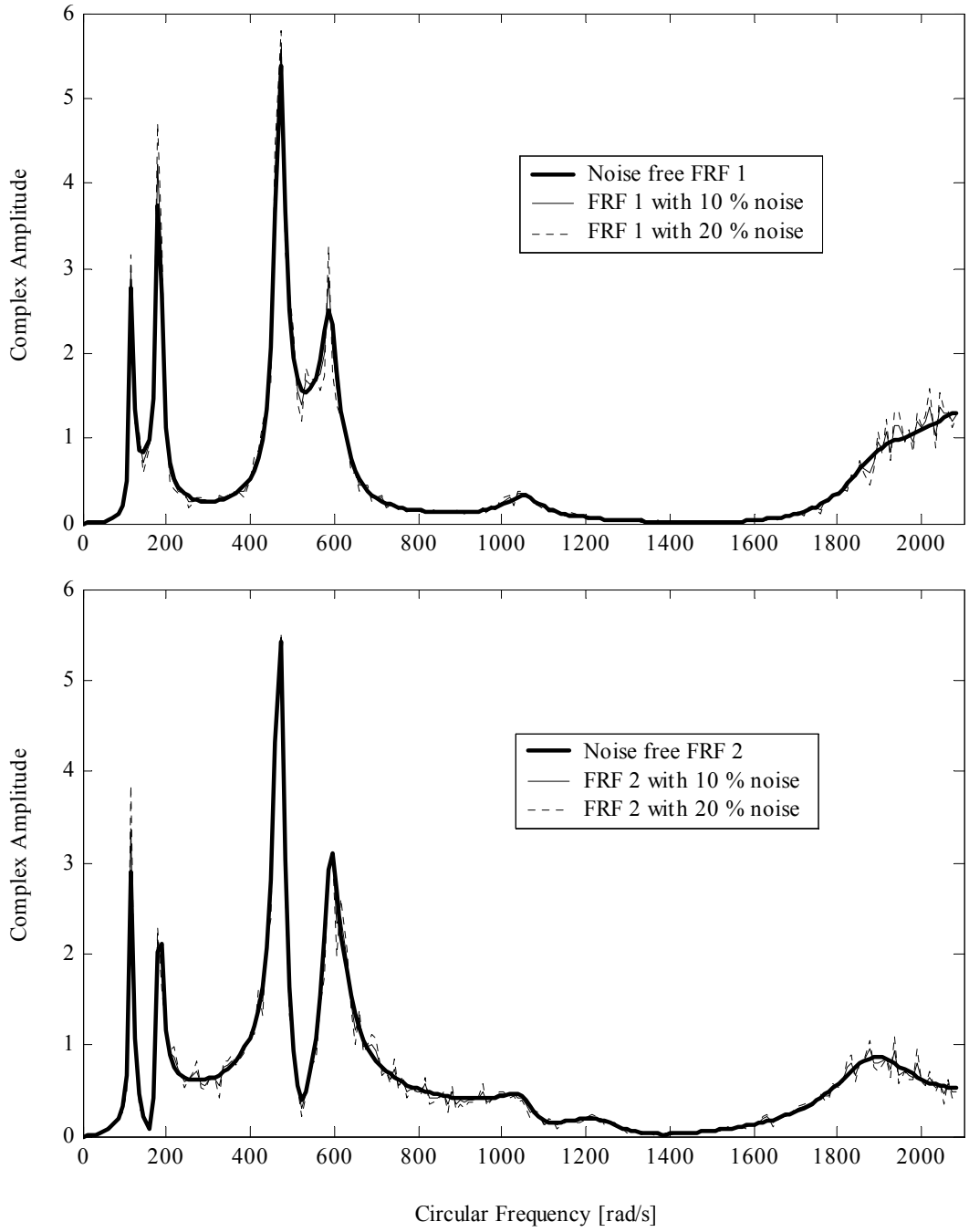

Figure 7.18. Simulated FRF measurements for case study TWSP IIIB, (a) FRF 1 – Excitation at node 18 and measurement at node 4, (b) FRF 2 – Excitation at node 18 and measurement at node 14

For the objective function proposed in Eq. (2.54) the integrand (the function used to calculate the area under) is the complex magnitude of the difference between the analytically obtained and measured FRFs. The integrand function is determined for each measured FRF between any two DOFs. For this objective function using the FRF (accelerance) measurements in case study TWSP IIIB, the integrand functions are obtained as the difference between the undamaged and damaged structure. The integrand functions for the noise free, 10 and 20% noise levels are plotted in Figure 7.19. The differences between the first nine natural frequencies of the two span continuous beam for the undamaged and damaged case are very small and the frequencies are approximately located at 117, 182, 470, 530, 592, 1055, 1238, 1595 and 1880 rad/s These frequencies show up as peaks in Figure 7.18. In Figure 7.19, the peaks of the integrand functions for the two measurements still appear at the natural frequencies of the structure, which are the main contributors to the total area under these curves. When noise is introduced into the measurements, the peaks of the integrand functions still appear at the natural frequencies and are magnified so that they are the largest contributors to the area under the curve. In frequency regions where the integrand functions were almost zero, noise appears with considerably smaller amplitudes than those of the peaks at the natural frequencies. This is especially true for the first measured FRF in Figure 7.19 (a), which in turn implies that this is a better measurement (less sensitive to noise) than the FRF measurement in Figure 7.19 (b).

For the objective function based on the correlation measures stated in Eq. (6.1), the integrands are the Global Shape Criterion (GSC) and Global Amplitude Criterion (GAC) functions. These functions combine the measured FRFs into a single function (GSC or GAC) and therefore they have the word global in their designation.

Using the FRFs for the undamaged and damaged structures, the GSC and GAC functions are plotted in Figure 7.20 for the 0, 10 and 20% noise level cases. The valleys of these functions for noise free measurements do not necessarily occur at the natural frequencies of the structure. For instance, for both correlation measures the deepest valley is found at a frequency of about 1400 rad/s, which is not a natural frequency of the two-span continuous beam. However, both functions show deviations between the undamaged and damaged structure at similar frequencies or frequency ranges. For the GSC shown in Figure 7.20 (a), there is little difference between the undamaged and damaged structure in the frequency range between zero and 1000 rad/s, which is indicated by regions with unit magnitude or perfect correlation. The variation for the GAC in this frequency range is somewhat higher, but there are large portions of the curve where the correlation between the undamaged and damaged structure is unity. These indicate regions where the information provided by the correlation measures would not be useful for damage detection. When noise is present in measurements, the different regions of the GSC and GAC do not amplified in a consistent manner. The deepest valleys for the 0 and 10% noise level cases are located around the same frequency regions although the regions that were not useful in the noise free case are amplified significantly. At a 20% noise level, the valleys are distributed randomly in the entire frequency region and the minimum valley found at a frequency that original had an almost perfect correlation value. The random distribution of valleys and the large amplification of insignificant frequency regions imply that the correlation functions are very sensitive to noise.

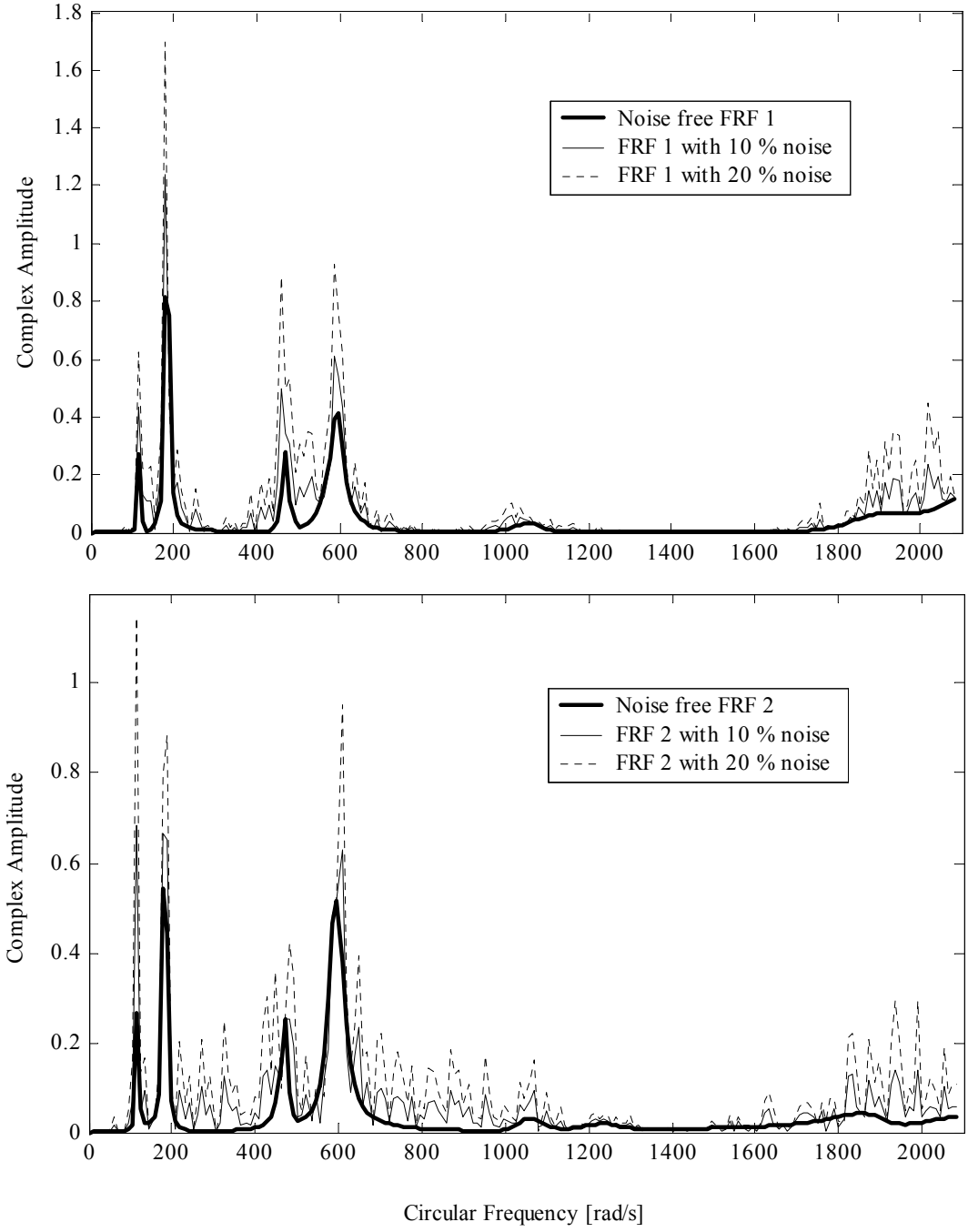

Figure 7.19. Complex amplitudes of simulated measurement and analytical FRF differences for case study TWSP IIIB, (a) FRFs measured between nodes 18 and 4, (b) FRFs measured between nodes 18 and 14

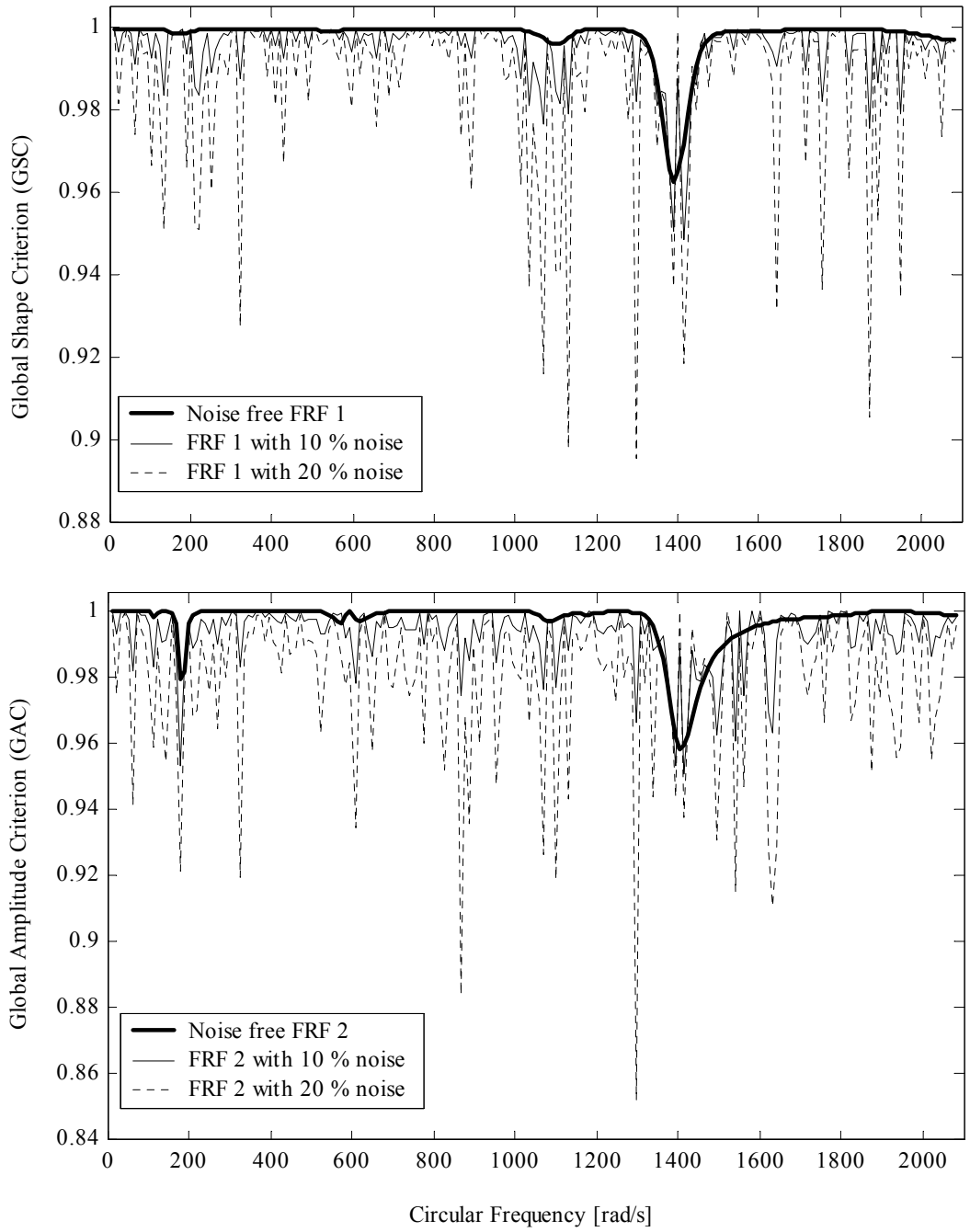

Figure 7.20. Correlation measures for case study TWSP IIIB, (a) Global Shape Criterion (GSC), (b) Global Amplitude Criterion (GAC)

If the FRF vector of the undamaged structure is stored in vector **u** and the corresponding measured FRF in vector **v**, then the integrand of the sum of square differences objective function in the noise free case is simply $\mathbf{u} - \mathbf{v}$. When there is a disturbance in the measured FRF it can be written simply as $\mathbf{v} + \Delta\mathbf{v}$. Therefore, the difference between the noise free and noisy integrands is $(\mathbf{u} - \mathbf{v}) - (\mathbf{u} - (\mathbf{v} + \Delta\mathbf{v})) = \Delta\mathbf{v}$. In other words, noise enters the integrand as a linear additive term for the sum of square differences objective function. As long as the responses at the natural frequencies have significantly larger amplitudes than that of the noise, the characteristic features of the integrand will not change (Figure 7.19) and noise remains a linear additive term.

To investigate the effect of noise on the correlation measures the definition of GSC and GAC at a single frequency value ω_x is used. The vector obtained from the combination of different FRFs at the ω_x frequency for the undamaged structure is denoted by **u** and the corresponding vector combining information at the same frequency from measured FRFs is denoted by **v**. Then for the frequency ω_x, the definition of GSC can be rewritten using the notation of vector spaces.

$$\mathrm{GSC} = \frac{\langle \mathbf{u}, \mathbf{v} \rangle^2}{\langle \mathbf{u}, \mathbf{u} \rangle \langle \mathbf{v}, \mathbf{v} \rangle} = \frac{\|\mathbf{u}\|^2 \|\mathbf{v}\|^2 \cos^2\theta}{\|\mathbf{u}\|^2 \|\mathbf{v}\|^2} = \cos^2\theta \tag{7.1}$$

where $\langle\rangle$ is an inner product on the vector space, $\| \ \|$ is the length or norm of vectors, and θ is the angle between vectors **u** and **v**. The angle between the analytical and measured data is θ and can be denoted as $\theta = \angle(\mathbf{u},\mathbf{v})$. When noise is introduced in the measured FRFs the angle will be $\theta + \Delta\theta = \angle(\mathbf{u},\mathbf{v}) + \angle(\mathbf{u},\Delta\mathbf{v})$. Therefore, noise changes the angle between the analytical and measured vectors in a linear manner, which depends on the orientation of $\Delta\mathbf{v}$. Therefore, the noise enters the GSC expression in a cosine squared manner. If there is perfect correlation between the undamaged and damaged structure at a single frequency (GSC = 1) then the error introduced by noise will be $\cos^2\Delta\theta$. This relationship results in a larger amplification of noise, and therefore, introduces larger errors than introduced using linear relationship. Another drawback is

that portions of the correlation integrand where its value is approximately unity (no useful information regarding damage detection) will be almost always contaminated by noise, while useful parts of the function may or may not be amplified. After performing some mathematical manipulations, similar conclusions can be made for the GAC measure.

Considering the significant differences between the objective functions and the results obtained for damage detection in the cantilever and two-span continuous case studies, the objective function based on correlation measures will not be investigated further. In later case studies, the focus is placed on finding good input parameters for damage detection and on identifying the limitations of the proposed SDIM.

7.3 Optimum Sensor Locations, Case Study TWSP OPT

7.3.1 Optimal Excitation and Sensor Locations

Discussion of the two-span continuous beam case study, TWSP OPT, requires the knowledge of the optimum locations for placing the excitation and sensors. Several trials using the GA settings in Table 7.4 were performed to find optimal measurement configurations. In these trials both the fixed and IRR representations were used.

Excitation and sensor location results for the two-span continuous beam problem are summarized in Table 7.5. The graphical representation of the optimal excitation and sensor locations in the Pareto set, provided by the program *GaDamDet*, are depicted in Figure D.2 of APPENDIX D. The maximum number of sensors for the trials was set to 10 and both horizontal and vertical DOFs were included in the optimization resulting in 38 possible locations for sensor placements. In all trials, the same results were obtained regardless of the GA parameters used. Overall, trials with the fixed representation converged faster than trials with the IRR representation. Table 7.5 states that for the two-span continuous beam the best place for the excitation location is at the right span (node 13) of the beam at distance of one fifth of the span length from the mid support. The same excitation locations were obtained in the vertical direction regardless of the number of sensors used for measurement. Using 10 sensors instead of one sensor increases the measurement information obtained by about 400%, which appears to be

significant. However, not placing the excitation and the first sensor at the same optimum location results in the reduction of the measurement information by several orders of magnitudes. In other words, using one sensor should be sufficient for damage detection measurements for this particular case. This conclusion is also supported by case studies TWSP IB and IIIB.

Table 7.4. GA settings for excitation and sensor layout design for the two-span continuous beam problem

Population Size	150, 200, 300
Tournament Size	2, 3
Maximum Generations	10000
Stop if no Improvement	100, 200
Crossover Type	Adaptive, Equal Probability
Crossover Sites	1, 2
Crossover Rates	Primary: 0.7, 0.8, 0.9 Secondary: 1.0
Mutation Type	Uniform
Mutation Rate	0.002, 0.005, 0.0075
Elitism	Yes
Coding	Binary Base 2, Gray

Only vertical DOFs were selected for the optimal excitation and measurement locations since the frequency range under investigation only contains a few axial vibration modes, which are associated with higher frequencies that require more energy input to obtain the same response level as with transverse vibrations. In Figure D.2 of APPENDIX D, a pattern is observable for the sensors placement that is symmetrical up to six sensors. After six sensors, the remaining four sensors are placed on the same span where the excitation is located. The lack of symmetry in the sensor placement above six measurement locations may be an indication of the optimum number of sensors required to obtain the most information to be able to identify damage at any element location.

Table 7.5. Pareto optimal excitation and sensor locations for the two-span continuous beam problem, TWSP

Number of sensors	Excitation at Node*	Sensor(s) at Node	Measurement Information	
			Value	Percent
1	13	13	$5.3574 \cdot 10^{14}$	100.0%
2	13	13, 19	$8.9212 \cdot 10^{14}$	166.5%
3	13	9, 13, 19	$1.2077 \cdot 10^{15}$	225.4%
4	13	3, 9, 13, 19	$1.4877 \cdot 10^{15}$	277.7%
5	13	3, 9, 13, 19, 20	$1.7648 \cdot 10^{15}$	329.4%
6	13	2, 3, 9, 13, 19, 20	$1.9772 \cdot 10^{15}$	369.1%
7	13	2, 3, 9, 13, 17, 19, 20	$2.1658 \cdot 10^{15}$	404.3%
8	13	2, 3, 9, 13, 15, 17, 19, 20	$2.3366 \cdot 10^{15}$	436.1%
9	13	2, 3, 9, 12, 13, 15, 17, 19, 20	$2.5027 \cdot 10^{15}$	467.1%
10	13	2, 3, 9, 12, 13, 14, 15, 17, 19, 20	$2.6658 \cdot 10^{15}$	497.6%

* Excitation and measurements are in the vertical direction

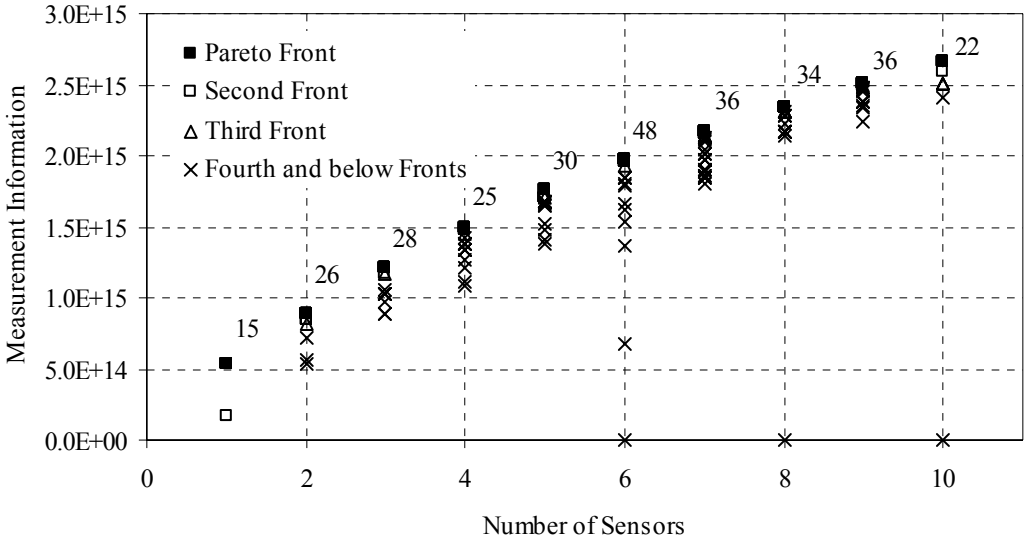

Figure 7.21. Pareto front and individuals in the final population represented in the objective space for the two-span continuous beam problem using fixed representation GA, population size is 300

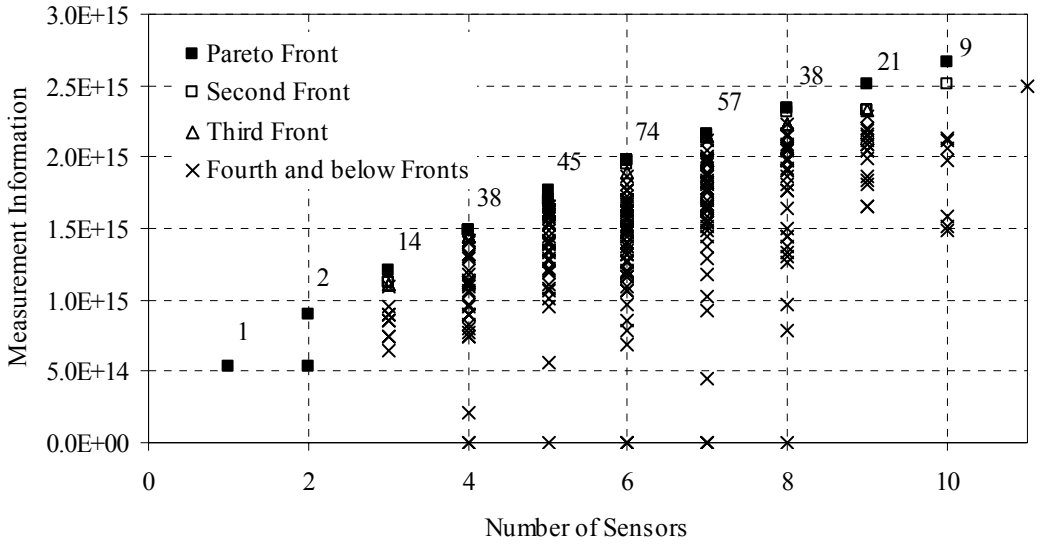

Figure 7.22. Pareto front and individuals in the final population represented in the objective space for the two-span continuous beam problem using IRR GA, population size is 300

Typical plots of the final population in the objective space are shown in Figure 7.21 and Figure 7.22 for the two-span continuous beam problem using the fixed and IRR representations, respectively. In Figure 7.21 for the fixed representation after only 34 generations, 60.3% of the converged population (there was no improvement in 100 generations) is in the Pareto front. The number of individuals present at a particular number of sensors is labeled next to each Pareto optimal solution. The figure shows that the individuals are well distributed along the number of sensors and the high percentage of individuals in the Pareto front (on average it was 56.5%) indicates that a good solution is obtained. The individuals in the Pareto front for the IRR GA results shown in Figure 7.22 are not as well distributed as individuals for the fixed representation GA. The IRR GA had difficulties with keeping individuals on the extremes around the one sensor and maximum number of sensors locations. Therefore, more generations were required to obtain convergence for the trial in Figure 7.22 and the population converged after 191 generations. The percentage of individuals in the Pareto front for the IRR GA plot was 7.33% and on average it was 20.8%. Comparing Figure 7.21 and Figure 7.22, the

individuals for the IRR GA are more scattered in the objective space indicating that only a smaller fraction of the population occupies Pareto front locations. In both figures, however, the Pareto front is identical and the hypothetical curve connecting the points in the Pareto front has a decreasing slope with increasing number of sensors. The decreasing slope can be interpreted such that the relative information gained by using more sensors also decreases gradually.

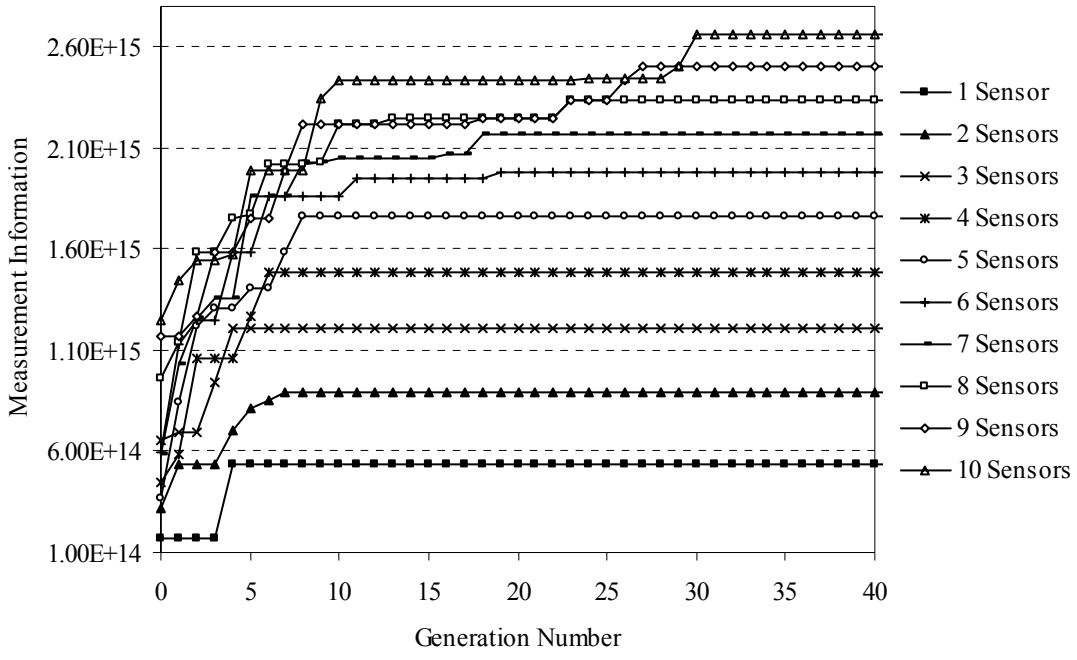

Figure 7.23. Convergence plot of measurement information for the two-span continuous beam sensor layout design problem using fixed representation GA with a population size of 300

Figure 7.23 shows the convergence plot of the measurement information as a function number of generations for 1 to 10 sensor locations. The plot is obtained using the fixed representation GA with a population size of 300. The figure shows the GAs ability to advance the Pareto front in parallel. Sensor locations are explored simultaneously for each number of sensors between 1 and 10. Fitness sharing combined with the repair operator also enables the information exchange between the optimum solutions for a

specific number of sensors, which facilitates fast convergence. For this particular plot, the entire population converged in only 34 generations and the trial was terminated after 50 unsuccessful attempts to improve (no improvement convergence criterion) the solutions currently in the Pareto front.

7.3.2 Damage Detection Results Using Optimal Sensor Placement

Using the optimal excitation location and one sensor, which are both placed at node 13 of the two-span continuous beam (Figure 5.2), the damage detection problem for the TWSP IIIA case was repeated using the same GA settings. The severity of damage imposed was 5% at element 6 and 10% at element 10. Five different noise levels were used for the TWSP OPT case: 0, 5, 10, 20 and 30% noise. The damage detection results obtained are presented in Figure 7.24 through Figure 7.29 and summarized in Table D.35 through Table D.40 of APPENDIX D. For the noise free case, the best solution was obtained by the unseeded IRR GA, but all trials somewhat underestimated the actual damage magnitudes in elements 6 and 10 after 200 generations. This is particularly true for the IRR GA with initial seed. Again, this result can be attributed to premature convergence caused by high selection pressure and overprotection of the best individual. Nevertheless, hillclimbing was able to improve the solutions and found the global optimum for all trials involving noise free FRF data.

Results obtained for noisy measurement data show that the final predicted damages in element 6 and 10 are slightly underestimated with gradually increasing magnitudes as the noise in the FRF data increases. The IRR GA without initial seed performed the best and found a solution 3 times out of 4 that was a global optimum (in the sense that hillclimbing could not improve on it). The IRR GA with initial seed outperformed the fixed representation GA for the noisy cases, but at a noise level of 20% premature convergence was experienced. Overall, the final results were very close to the inflicted damages for all trials even at a noise level of 30%. A typical solution (seeded IRR GA) was 4.67% damage for element 6 and 9.60% for element 10 and there was only one falsely identified element 17 with 0.68% damage.

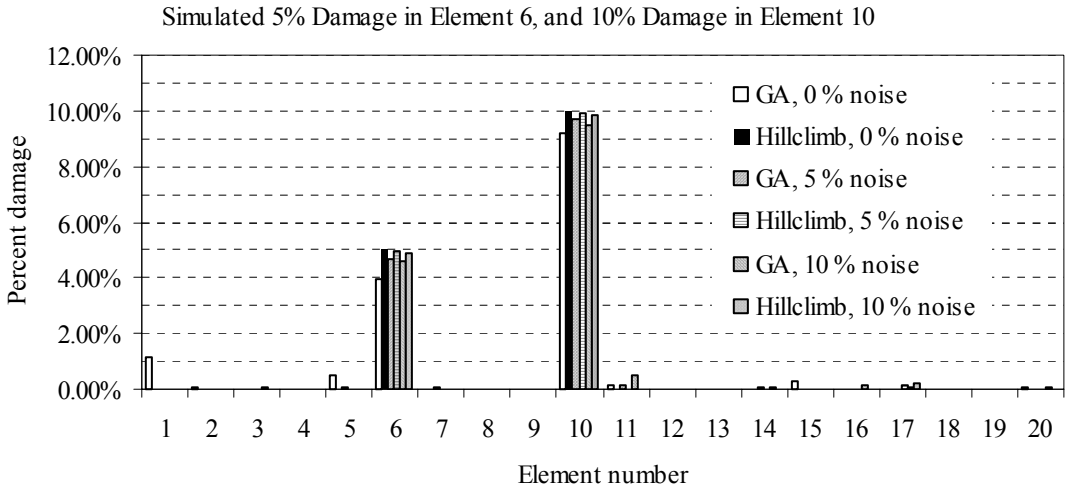

Figure 7.24. Damage detection results for case TWSP OPT, fixed representation, seeded initial population, noise levels of 0, 5 and 10%

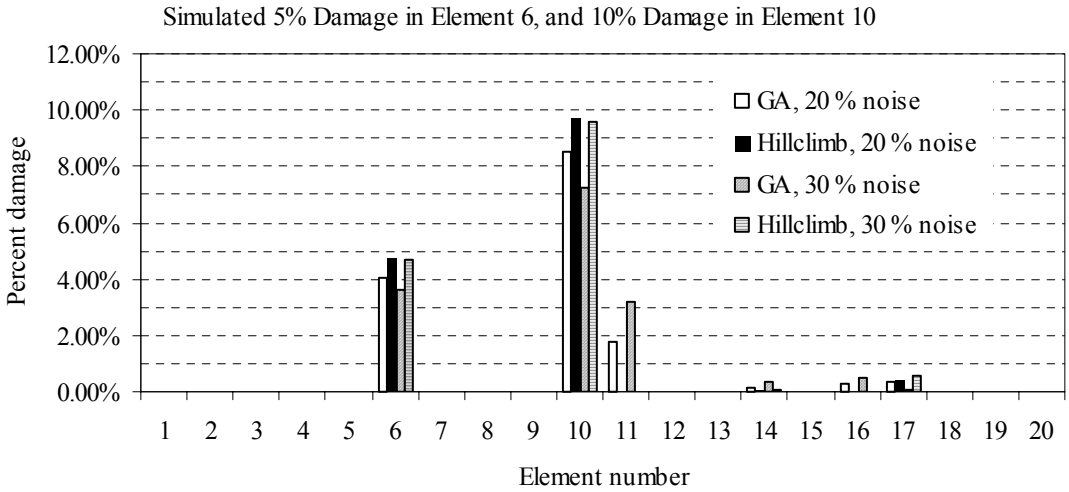

Figure 7.25. Damage detection results for case TWSP OPT, fixed representation, seeded initial population, noise levels of 20 and 30%

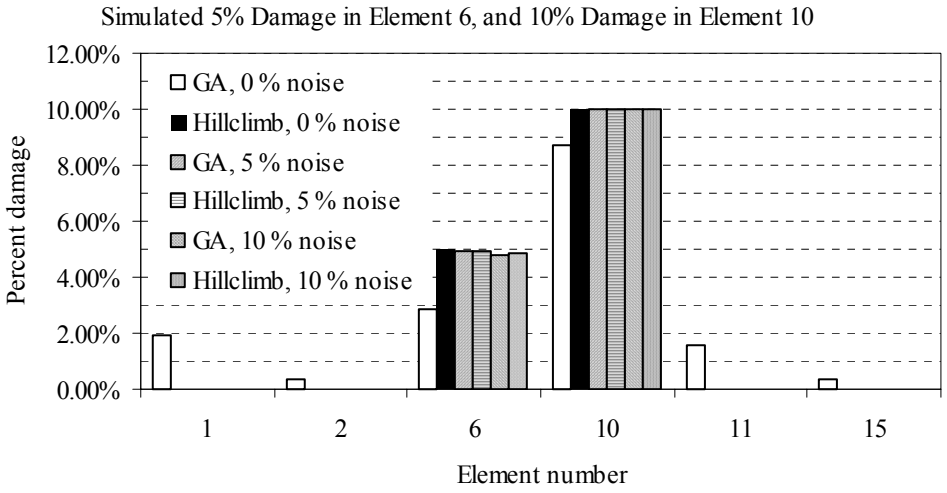

Figure 7.26. Damage detection results for case TWSP OPT, implicit redundant representation (IRR), seeded initial population, noise levels of 0, 5 and 10%

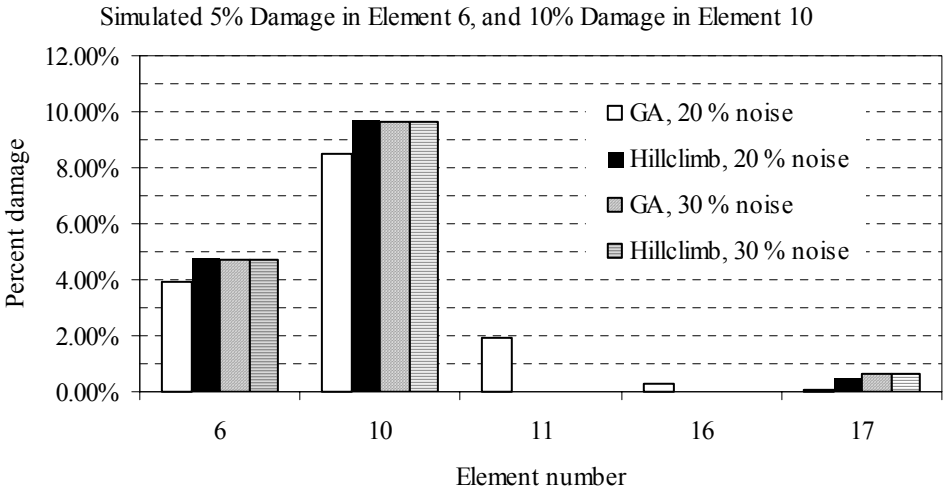

Figure 7.27. Damage detection results for case TWSP OPT, implicit redundant representation (IRR), seeded initial population, noise levels of 20 and 30%

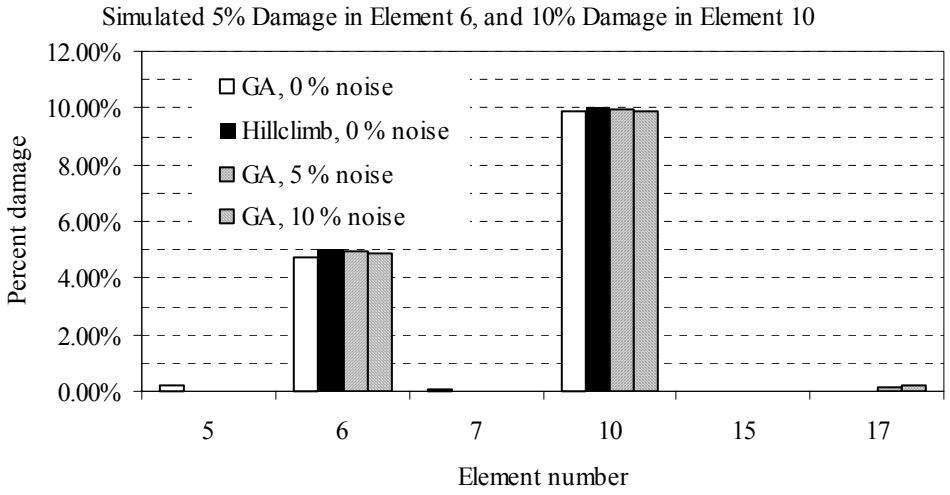

Figure 7.28. Damage detection results for case TWSP OPT, implicit redundant representation (IRR), unseeded initial population, noise levels of 0, 5 and 10%

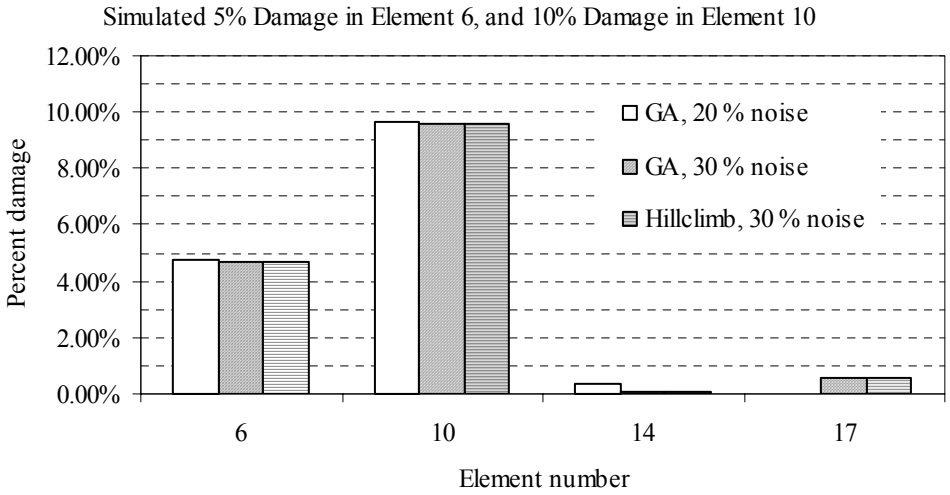

Figure 7.29. Damage detection results for case TWSP OPT, implicit redundant representation (IRR), unseeded initial population, noise levels of 20 and 30%

The results obtained using the optimal sensor location were compared with those for the TWSP IIIA case study. In most cases, the optimum sensor layout design resulted in faster convergence requiring considerably less hillclimbing iterations to find the global

solution. In Table 7.6, the average fitness values of the initial populations are compared for the original (TWSP IIIA) and optimal (TWSP OPT) sensor layout designs. The average fitness of the initial population increased by an average factor of 2.86 times and 3.9 for the fixed and IRR GA respectively using the optimal sensor location. The overall increase was 3.53 or 253%. The increase in objective function values is an indication of higher sensitivities for damage in the vibration signature. In Figure 7.30, final results (including hillclimbing) for the damage detection problem using optimal and non-optimal sensor locations are compared at a noise level of 5%. Similar plots for the 10, 20 and 30% noise levels are depicted in Figure 7.31 through Figure 7.33. All figures show significant improvements in damage detection at any noise level using the optimal excitation and sensor placements.

Table 7.6. Average fitness values of initial populations using non-optimized and optimal sensor locations for the two-span continuous beam case studies TWSP IIIA and OPT

Representation	Noise	Average Fitness of Initial Population		Average Increase [%]
		TWSP IIIA	TWSP OPT	
Fixed	0%	3,175,198	9,151,185	188.2%
Fixed	5%	3,172,925	9,114,538	187.3%
Fixed	10%	3,173,100	9,098,026	186.7%
Fixed	20%	3,181,620	9,128,257	186.9%
Fixed	30%	3,202,043	9,249,699	188.9%
IRR Seeded	0%	2,310,740	9,033,528	290.9%
IRR Seeded	5%	2,312,329	8,933,392	286.3%
IRR Seeded	10%	2,318,418	8,913,561	284.5%
IRR Seeded	20%	2,344,598	8,928,812	280.8%
IRR Seeded	30%	2,390,361	9,027,853	277.7%
IRR Unseeded	0%	2,356,495	9,135,627	287.7%
IRR Unseeded	5%	2,357,469	9,266,820	293.1%
IRR Unseeded	10%	2,363,005	9,246,730	291.3%
IRR Unseeded	20%	2,388,297	9,262,944	287.8%
IRR Unseeded	30%	2,433,628	9,366,433	284.9%
			Average:	253.5%

There are at least three distinguishable benefits of using optimum measurement layouts in damage detection. First, the damage-balancing phenomenon (i.e. predicted damage indicators of unequal damages tend to approach to a value in between the inflicted damage severities) that is observed for the non-optimal sensor location cases is not apparent in the optimum sensor location cases. The number and severity of falsely identified elements is also very much reduced. In addition, the consistency of the results is maintained at all damage levels and the accuracy of damage detection is less sensitive for noise in the measurements.

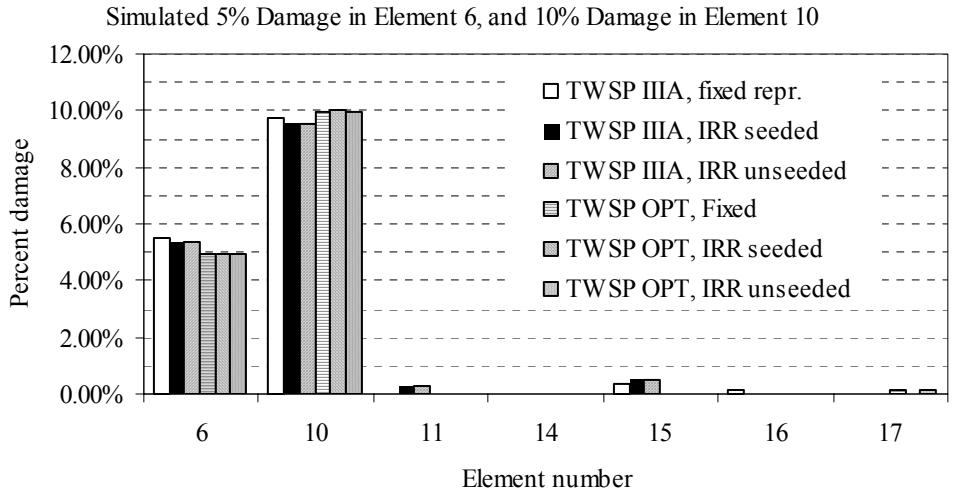

Figure 7.30. Comparison of damage detection results using different measurement configurations at a noise level of 5% for the two-span continuous beam problem

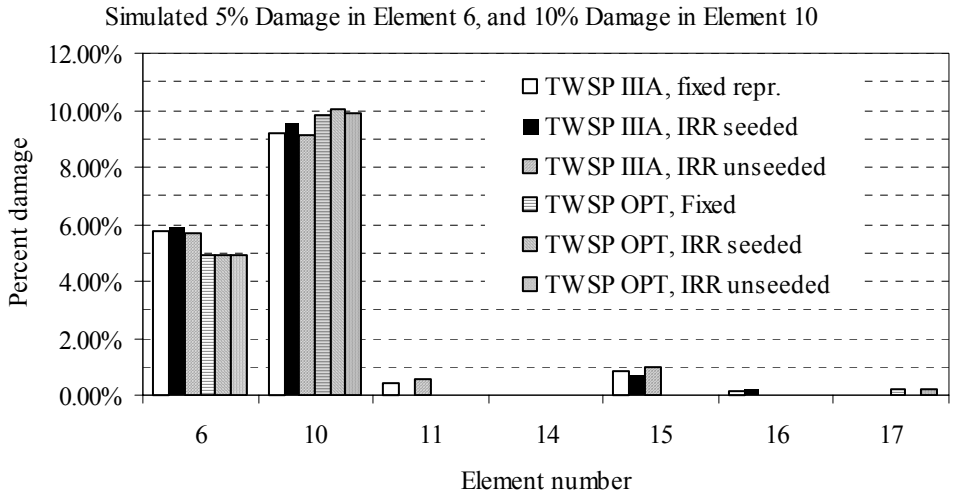

Figure 7.31. Comparison of damage detection results using different measurement configurations at a noise level of 10% for the two-span continuous beam problem

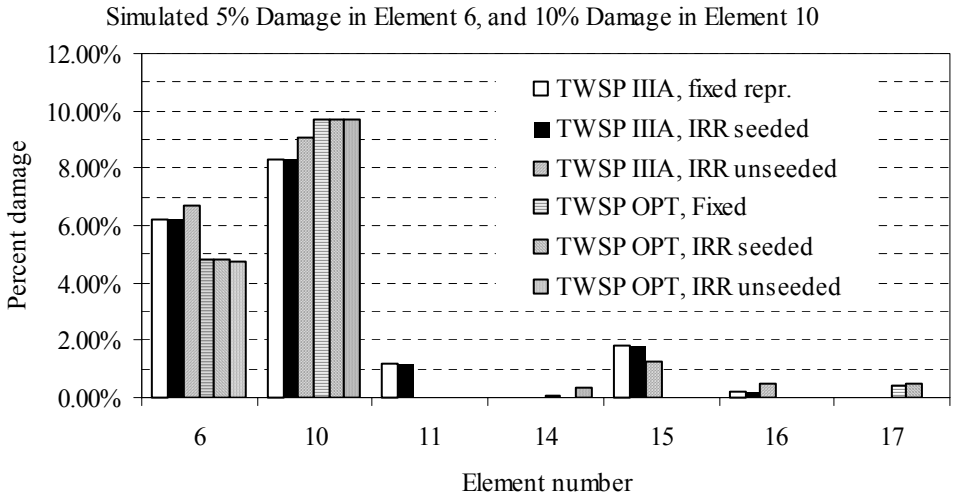

Figure 7.32. Comparison of damage detection results using different measurement configurations at a noise level of 20% for the two-span continuous beam problem

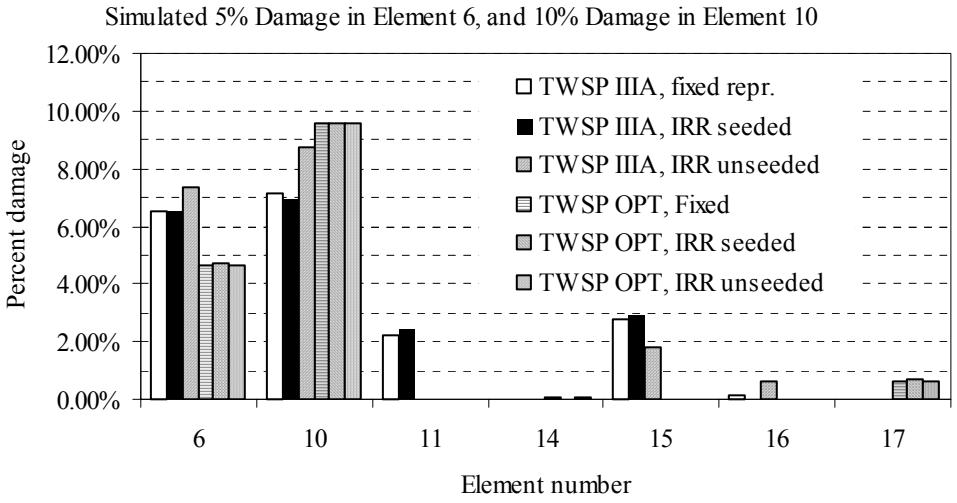

Figure 7.33. Comparison of damage detection results using different measurement configurations at a noise level of 30% for the two-span continuous beam problem

8 CASE STUDY RESULTS AND DISCUSSION, MOMENT FRAMES

8.1 Two-story, Three-bay Braced Frame

Cases studies involving the two-story, three-bay braced moment frame (thereafter referred to as braced frame) are intended to fine tune different GA parameters for further studies. A sensitivity analysis of the GA will be performed by varying six parameters: population size, primary crossover rate, mutation rate, random seed, seeding of the initial population and whether or not a fixed representation or an IRR is used. From the sensitivity analysis, a good set of GA parameters is identified. This set of GA parameters will be used in the trials investigating the repeatability of results by running trials having different random initial seeds. Random number generators are usually seeded with an arbitrary number and if this number is the same for each run then the random numbers generated will also be the same for each trial. By varying the initial random seed the repeatability of result using the same GA parameters can be tested. Repeatability of results is important in order to ensure that the solutions are not dependent on the random seed used.

Having obtained a set of "good" GA parameters, trials involving a scenario with four damaged elements will be used to evaluate the robustness of the proposed SDIM. In this set, each of the trials will build upon the previous trial. Experience obtained throughout the trials will be employed in the considerably harder problems of the three-story three-bay unbraced moment frame structure, which is the topic of the next section.

8.1.1 Fine Tuning, Finding a Good Set of GA Parameters

Using the case study, BRFRM I (Table 5.3), six of the GA parameters were altered to fine tune the optimization algorithm and to enhance performance. In this case study, one of the cross braces on the first floor is damaged by introducing a 50% reduction in the member stiffness. Altogether 25 trials were performed to determine the set of parameters that evolves results that most accurately represents the damaged model in case study

BRFRM I. A summary of the 25 trials is provided in Table 8.1. The maximum number of generations was 200, the "stop if no improvement" convergence criterion was set to 20, adaptive crossover was turned on, and measurements with zero noise were used. The random seed number was set to 7 and was the same for all trials.

Table 8.1. GA input parameters for the braced frame case study, BRFRM I

Trial	Population Size	Primary Crossover Rate	Mutation Rate	Fixed or IRR*	Initial Seed
1	100	0.7	0.005	IRR	No
2	300	0.7	0.005	IRR	No
3	300	0.7	0.01	IRR	No
4	100	0.7	0.005	Fixed	Yes
5	300	0.9	0.01	IRR	No
6	200	0.7	0.01	IRR	No
7	100	0.7	0.01	Fixed	Yes
8	200	0.7	0.005	Fixed	Yes
9	100	0.7	0.01	IRR	No
10	100	0.9	0.005	Fixed	Yes
11	100	0.9	0.005	IRR	Yes
12	300	0.9	0.005	IRR	Yes
13	300	0.9	0.01	Fixed	Yes
14	300	0.9	0.01	IRR	Yes
15	100	0.9	0.01	Fixed	No
16	300	0.7	0.01	Fixed	Yes
17	300	0.9	0.005	Fixed	Yes
18	300	0.7	0.005	Fixed	Yes
19	200	0.9	0.01	IRR	Yes
20	200	0.9	0.01	Fixed	Yes
21	200	0.9	0.005	IRR	Yes
22	200	0.7	0.01	Fixed	Yes
23	100	0.9	0.01	IRR	Yes
24	200	0.7	0.005	IRR	No
25	200	0.9	0.005	Fixed	No

* The number of gene instances for the IRR GA was 10 and the gene locator length was 3

Results for the first 25 trials are compared in Table 8.2 and the damage indicator results are summarized in Table D.41 through Table D.46 of APPENDIX D. Using the fixed representation without seeding, the initial population with the zero damage individual (trials 15 and 25) resulted in the failure of the SDIM and the correct damaged element was not identified. The GA in these cases was not able to find the solution due to the unstructured nature of the problem, since the number of variables for the fixed representation was quite large (40 finite elements in the model). Seeding the initial population provides the fixed representation GA with a solution that is "close" to the imposed damage scenario and using this information the GA was able to find solutions identifying the correct damaged element. Although most seeded fixed representation trials found a reasonable solution, the number of falsely identified elements was high and a large number of hillclimbing iterations were needed to obtain a better solution that represented the inflicted damage in the structure.

In trial 16, the element identified with maximum damage was element 44, which is the cross bracing symmetrical to element 43 on the first floor in the middle bay. The predicted damage for this cross bracing was about 50%. Since the structure is also symmetrical the same level of damage in symmetrical members would produce similar vibration signatures especially if the excitation and measurement location were also symmetrical. This solution can be considered as a local optimum and to prevent this result from being identified by the SDIM, the unsymmetrical placement of excitation and measurement locations may be desired when the fixed representation GA with seeded initial population is used. The trials for the fixed representation GA also show that the reliability of damage detection degrades with increasing number of unknown variables due to the larger search space that needs to be explored and exploited. For this particular problem considering that 20 binary bits were used to encode each damage indicators, the search space has a size of $|\mathcal{S}| = \left(2^{20}\right)^{40} = 6.668 \cdot 10^{240}$, which is extremely large and explains the degraded performance of the fixed representation GA.

Table 8.2. Comparison of results for the braced frame case BRFRM I

Trial	Number of Iterations		Number of Damaged Elements		Damage Indicators	
	GA	Hillclimb	Before Hillclimbing	After Hillclimbing	Before Hillclimbing, Element 43 and Maximum False Predicition	After Hillclimbing
1	200	3673	5	4	43:49.08%, 44:1.05%	43:49.98%, 39:0.004%, 28:0.002%, 44,:0.03%
2	200	4960	4	4	43:46.43%, 44:3.9%	43:49.98%, 6:0.003%, 44:0.026%, 46:0.0004%
3	200	37	2	1	43:50.02%, 36:0.20%	43:50%
4	200	94	Almost All	1	43:49.45%, 27:3.11%	43:50%
5	200	73	5	1	43:50.01%, 25:1.57%	43:50%
6	200	14	1	1	43:50%	43:50%
7	120	93	Almost All	1	43:49.28%, 24:12.4%	43: 50%
8	200	2106	Almost All	1	43:48.54%, 26:3.18%	43:50%
9	200	38	3	1	43:50%, 30:0.68%	43:50%
10	74	4680	Almost All	5	43:46.41%, 4:6.19%	43:49.98%, 6:0.002%, 18:0.001%, 39:0.003%, 44:0.03%
11	169	0	1	1	43:50%	43:50%
12	177	0	1	1	43:50%	43:50%
13	57	99	Almost All	1	43:49.5%, 30:49.3%	43:50%
14	175	0	1	1	43:50%	43:50%
15	200	761	Failed	Failed	Failed	Failed
16	50	92	Failed	Failed	43:0.0%, 44:49.5%	Found 44: 49.73% and Four Others
17	200	7352	All	6	43:24.72%, 44:24.64%	43:49.98%, 18:0.0007%, 26:0.0006%, 37:0.001%, 44:.03%, 46:0.0003%
18	155	2360	All	4	43:49.5%, 6:5.44%	43:49.97%, 28:0.001%, 37:0.001%, 44:0.03%
19	145	0	1	1	43:50%	43:50%
20	78	4702	Almost All	5	43.11.7%, 44:24.65%	43:49.73%, 32:0.002%, 39:0.033%, 44: 0.3%, 46:0.005%
21	200	3	1	1	43:50%	43:50%

Table 8.2. (Continued)

Trial	Number of Iterations		Number of Damaged Elements		Damage Indicators	
	GA	Hillclimb	Before Hillclimbing	After Hillclimbing	Before Hillclimbing, Element 43 and Maximum False Predicition	After Hillclimbing
22	101	3380	About Half	4	43:47.95%, 24:6.15%	43:49.95%, 6:0.018%, 29:0.004%, 44:0.058%
23	200	94	2	2	43:49.86%, 44:0.16%	43:49.9%, 44:0.03%
24	200	25	3	1	43:50%, 30:0.040%	43:50%
25	200	537	Failed	Failed	Failed	Failed

The IRR GA performed consistently better than the fixed representation. The global solution was always found either during the GA run or after hillclimbing. The IRR GA with initial seed, however, provided better results than the IRR GA without initial seed. The global solution was found 4 out of 6 times before the maximum number of generations was reached. Seeding the initial population proved to beneficial for the IRR GA for this particular problem. Also the seeded IRR GA was less sensitive to change in other parameters such as population size, mutation and crossover rate. For the unseeded IRR GA, a higher mutation rate of 0.1 lead to better results than a mutation rate of 0.005. Another factor that was important for the unseeded IRR GA was the population size. A population size of 100 resulted in slower convergence than any of the higher population sizes, but a population size of 200 proved to be sufficient.

Even though differences in the performances of the seeded and unseeded IRR GAs existed in all trials, using IRR GA outperformed the fixed representation GA in every aspect. The IRR GA was able to effectively reduce the search space by adjusting the number of gene instances present in the string. For instance for trial 19 (Table 8.1), the best individual in the initial population had 8 gene instances (damaged elements), which is equivalent to a $\left(2^{20}\right)^{32} = 4.562 \cdot 10^{192}$ times reduction in the search space when compared to the fixed GA. In the final population there was only a single gene instance in

the best individual, which meant that the search space had a size of $2^{20} = 1,048,576$ considerably less than the initial search space or the search space for the fixed representation.

Table D.47 of APPENDIX D shows the results of the 25 initial trials arranged in trial pairs based on the mutation rate. The data suggests that a mutation rate of 0.01 is preferable for this problem. To investigate the effect of the primary crossover rate, Table D.48 of APPENDIX D shows the result of the initial 25 trials arranged in trial pairs based on the primary crossover rate. The primary crossover rates used in the sensitivity analysis have little effect on the GA results. The population size had again little effect on the GA results as shown in Table D.49 of APPENDIX D. Having analyzed the initial 25 trials in detail, the GA parameters in trial 19 (Table 8.1) were selected for use in further studies on braced and unbraced frames. The specific parameters selected are a mutation rate of 0.01, IRR representation, primary crossover rate of 0.9, and a population size of 200. Seeding the initial population provided better results, therefore, seeding will also be used in the following studies.

To validate the repeatability of results, two additional trials with different random seeds using the GA setting given above were performed. Results for the two additional cases showed similar performance when compared to trial 19. The global optimum was found in 180 generations and no false identifications occurred as shown in Table 8.3.

Table 8.3. Results for braced frame study BRFRM I using different random seeds

Trial	Random Seed	Number of GA Generations	Number of Damaged Elements	Damage Indicators
26	21	180	1	43:50%
27	23	180	1	43:50%

8.1.2 A Mixture of Bracing and Joint Damages in Beams and Columns

In order to extend the knowledge gained from the sensitivity analysis, the case study BRFRM II defined in Table 5.3 will be investigated. This problem is considerably more difficult than the previous braced frame study BRFRM I, since four damaged elements are included. Among the damaged elements there is a cross brace with 50% damage (element 43), two damages in the first floor perimeter column at the fixed support and at the joint with 20% damages (elements 37 and 39), and a 10% damage located in the first floor perimeter beam at the joint (element 35, for the location of elements see Figure C.2 of APPENDIX C). The trials for this study involved the use of the best parameters from the sensitivity study, except for the last trial where equal probability crossover was used instead of the adaptive crossover.

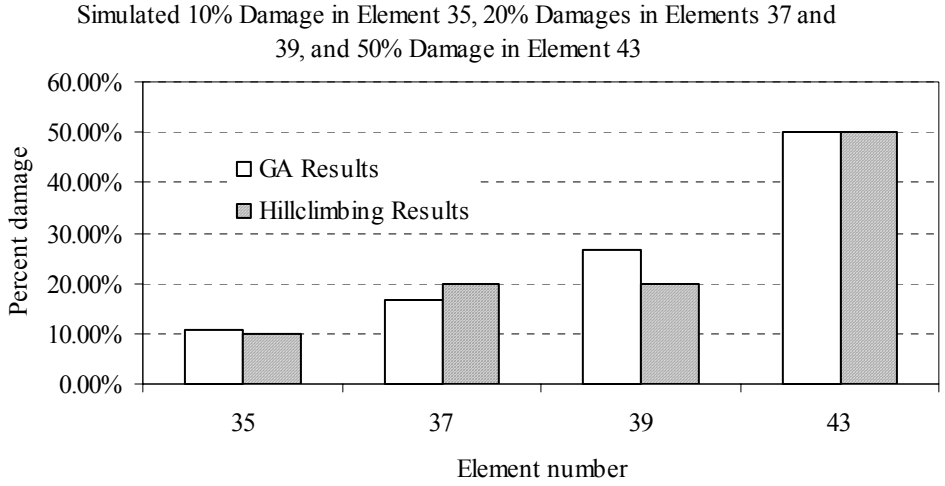

Figure 8.1. Results for trial 28, noise free measurements case study BRFRM II

Results for the BRFRM II problem involving noise free measurements (trial 28) are depicted in Figure 8.1 and summarized in Table D.50 of APPENDIX D. After 200 GA generations, there were four gene instances in the best individual identifying the four correct damaged elements. For two of the elements, the predicted damages were very close to the imposed values: 10.8% for element 35 (joint element on the first floor beam)

instead of 10% and 50.14% for element 43 (cross bracing) instead of 50%. The identified damage indicators for the joint element in the first floor perimeter column were somewhat under- and overestimated (16.48 5 and 26.48% instead of 20%) for elements 37 and 39. After only 299 hillclimbing iterations, the global optimum was found within the precision provided by the binary representation (Figure 8.1).

Case study BRFRM II was repeated with 5% noise included in the measurements. Three trials using the noisy measurements were performed (trials 29, 30 and 31). In Trial 29, the same GA settings from the sensitivity study were used to investigate the effect on noise on the accuracy of damage detection. Two additional trials (30 and 31) investigated the effect of using optimal excitation and sensor locations.

Table 8.4. Pareto optimal excitation and sensor locations for the two-story three-bay braced moment frame problem, BRFRM

Number of sensors	Excitation at Node*	Sensor(s) at Node	Measurement Information	
			Value	Percent
1	5	38	$6.6806 \cdot 10^{13}$	100.0%
2	5	38, 36	$9.3420 \cdot 10^{13}$	139.8%
3	5	38, 36, 35	$1.1236 \cdot 10^{15}$	168.2%
4	5	38, 36, 35, 33	$1.2660 \cdot 10^{15}$	189.5%
5	5	38, 36, 35, 33, 39	$1.3377 \cdot 10^{15}$	200.2%
6	5	38, 36, 35, 33, 39, 5	$1.3982 \cdot 10^{15}$	209.3%
7	5	38, 36, 35, 33, 39, 5, 40	$1.4331 \cdot 10^{15}$	214.5%
8	5	38, 36, 35, 33, 39, 5, 40, 3	$1.4555 \cdot 10^{15}$	217.9%
9	5	38, 36, 35, 33, 39, 5, 40, 38↑	$1.4714 \cdot 10^{15}$	220.2%
10	5	38, 36, 35, 33, 39, 5, 40, 38↑, 32↑	$1.4861 \cdot 10^{15}$	222.4%

* Excitation and measurements are in the horizontal direction except where the node number if followed by "↑" symbol in which case the vertical DOF is used

Based on the experience obtained from the excitation and sensor location optimization trials for the cantilever and two-span continuous beams, the fixed representation GA was used to determine the optimal sensor locations for the braced frame. The GA settings were selected from Table 7.4. The optimum excitation and sensor

locations for the braced frame are summarized in Table 8.4 and the final population showing the Pareto front plotted in the objective space is depicted in Figure 8.2. The results obtained from these trials show that the increase in the measurement information becomes less significant as the number of sensors is increased. The optimal location for the excitation was in the horizontal DOF located at node 5 in the left second floor perimeter column. Unlike the optimum layouts determined for the beam problems, in which the fist sensor was placed at the same location as the excitation, the first sensor is placed symmetrically on the opposite end of the frame in the horizontal direction. Subsequent sensors were located at either side of the frame in the horizontal direction up to a sensor number of 8. The ninth and tenth sensors measured vertical DOFs. For Trials 30 and 31, the optimum sensor locations for two sensors were selected as the base measurement FRFs.

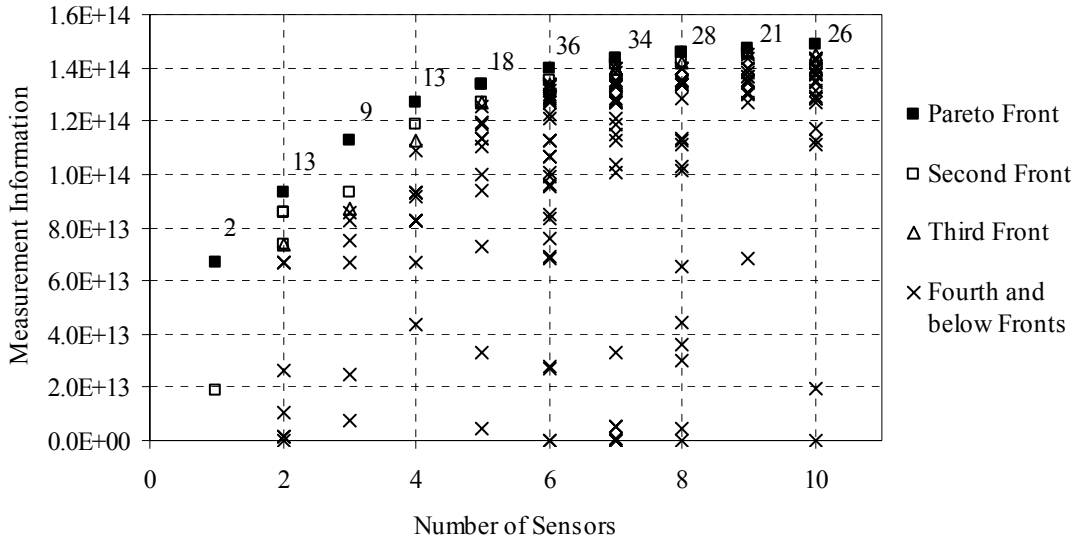

Figure 8.2. Pareto front and individuals in the final population represented in the objective space for the two-story three-bay braced moment frame problem using fixed representation GA, population size is 200

Results obtained for the noisy measurement trials (29, 30 and 31) are depicted in Figure 8.3 and summarized in Table D.50 of APPENDIX D. In Trial 29, a total of eight

elements were reported damaged. The cross bracing with the highest damage, 50%, was identified with 49.8% damage and two other elements that were damaged in the column had damages of 22.99 and 11.94% instead of the imposed 20% after 200 GA generations. The element in the first floor beam was not identified, instead five elements were falsely identified. Element 42 in the second floor perimeter column was falsely reported to have 9.67% damage. The severity of the other four false identifications ranged between 0.95 and 7.845% in elements scattered all around the structure. Hillclimbing did not significantly improve the results.

In Trial 30, the two optimal sensor locations were used that were by coincidence only in the region of the damaged elements. The GA located seven damaged elements and again the cross bracing was correctly identified with 49.33% damage. Element 35 and 39 had 9.1% and 37.94% damage, respectively. The column element at the fixed support was not identified as damaged, however, the column element right next to it was reported to have 11.88% damage. The other three falsely identified elements had damages less than 3%. Hillclimbing only slightly improved the results. Although these results vary significantly from the results obtained in Trial 29, the elements that were falsely identified were not scattered in the structure but instead were confined to regions neighboring the actual damaged elements.

A closer look at the genotypes of the best individuals in consecutive generations revealed that a premature convergence occurred. The zero damage individual quickly spread through the population during early generations, and therefore dominated the overall search. The combination of adaptive crossover with elitism prevented the GA from discovering regions of the search space. Therefore, in Trial 31 the crossover type used was changed to the equal probability crossover.

In Figure 8.3, results for Trial 31 show that all damaged elements were found and that the severity estimates were in good agreement with the inflicted damage scenario. The only falsely identified element spans between the originally damaged elements 37 and 39 in the first floor perimeter column confining the damage in a single structural member. Hillclimbing results were in an even better agreement with the original damage case. The final results were 49.77% damage in element 43, 8.45% in element 35, 20.43%

in element 37 and 19.54% in element 39. The only false reading represented a 0.41% damage. This trial signifies the importance of using a good set of GA parameters by showing that slight changes in the input GA parameters can have significant impact on the obtained results due to the selection pressure imposed during the search.

Table 8.5 shows the change in the average fitness of the initial population for trials using the optimal sensor locations relative to trials using the non-optimal sensor locations. The fitness value increased by 75.2%, which is an indicator of higher sensitivities for damage when optimum sensor locations are used. Studies including four damaged elements showed that the IRR GA was robust and could identify damages in a noisy measurement environment.

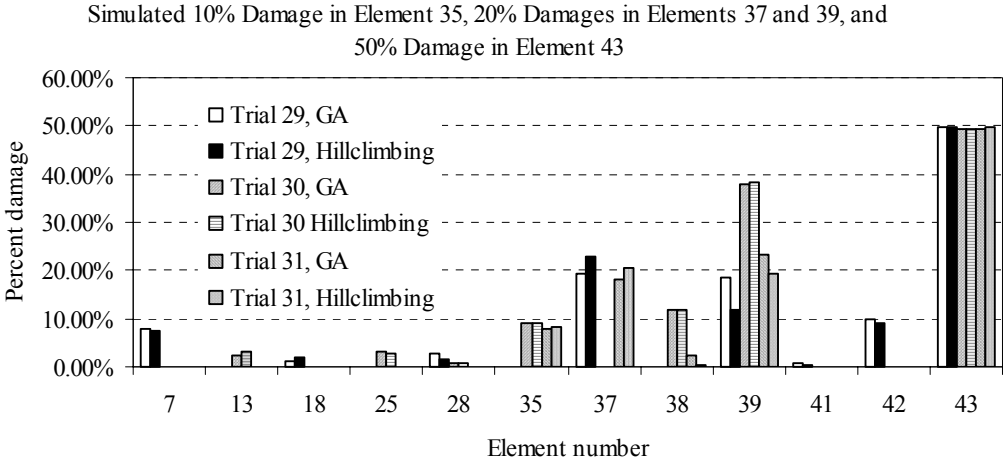

Figure 8.3. Results for trial 29, 30 and 31, 5% measurement noise, case study BRFRM II

Table 8.5. Comparison of individuals' average fitness for trials 29, 30 and 31

Trial	Average Fitness of Initial Population	
	Value	Percent
29	12682.239	100.0%
30	22220.492	175.2%
31	22220.492	175.2%

8.2 Three-story, Three-bay Unbraced Frame

The three-story, three bay unbraced frame case studies investigated provide an additional study of the robustness of the proposed SDIM on an unbraced moment frame with 81 finite elements. This structure is of a larger-scale then structures previously studied. The first two case studies investigated simulated single damage situations with damage either in a first floor beam at mid-span and at a perimeter joint. Trials including several different noise levels were performed to investigate the sensitivity of damage detection for larger-scale problems.

The first damage scenario considered in the second set of case studies introduces multi-damages with different severities in the first floor columns. This configuration simulates damages caused by a possible soft story mechanism in the first floor columns at the joints within the first floor beams. The second damage scenario considered introduces damages in the first floor beams at the joints simulating a damage mechanism that is involved in the strong columns weak beams design concept. The goal of the second set of case studies is to investigate the effect of the number of sensors and their locations on the accuracy of damage detection. Multiple damages with different severities result in increased uniqueness problems that make it increasingly difficult to find the true damaged elements and severities. Therefore, case studies included in this section pose problems that any of the existing SDIMs would have difficulty in solving accurately.

8.2.1 Single Damage Cases for a First Floor Beam

The set of GA parameters used for the two case studies, UBFRM I and II (Table 5.4), for the unbraced frame are summarized in Table 8.6. Input parameters for the fixed representation GA were not provided in the table because during initial trials, GA parameters that would lead to acceptable solutions could not be found. For this reason the performance of the fixed representation GA was not investigated for the unbraced frame. The GA parameters for the IRR GA were selected on the basis of initial trials that used different GA parameters and the experience gained in previous case studies. The number of significant digits for the unbraced frame trials was 6, which required 20 bits to

represent a damage indicator value with a precision of approximately $9.44 \cdot 10^{-7}$ or $9.44 \cdot 10^{-5}$%.

Table 8.6. GA input parameters for three-story three-bay unbraced moment frame

	IRR, Seeded*	IRR, Unseeded
Population Size	200	200
Tournament Size	8	8
Initial Seed	Yes	No
Maximum Generations	300	300
Stop if no Improvement	20	20
Crossover Type	Adaptive	Adaptive
Crossover Sites	6	6
Crossover Rates	Primary: 0.9, Secondary: 1.0	Primary: 0.9, Secondary: 1.0
Mutation Type	Uniform	Uniform
Mutation Rate	0.005	0.005
Elitism	Yes	Yes
Hillclimbing	Yes, Reduced	Yes, Reduced
Coding	Gray	Gray

* For the IRR the number of gene instances (expected number of damaged elements) was 15 and the gene locator (GL) length is 3

Damage detection results for the first unbraced frame case study, UBFRM I (Table 5.4), are summarized in Table D.51 and Table D.52 of APPENDIX D. Only IRR GA solutions are presented, since no acceptable solutions were found using the fixed representation GA. The true damaged element 21 is located on the left perimeter first floor beam at mid-span with a 10% severity (Figure C.4 of APPENDIX C). Noise levels of zero, 5 and 10% were investigated. Solutions obtained using the seeded IRR GA are presented in Figure 8.4 and results for the unseeded IRR GA are depicted in Figure 8.5. For the case of noise free measurements, the seeded IRR GA found the global optimum after 261 generations identifying element 21 with 10% damage. Although the solution provided by the unseeded IRR GA after 300 generations was not the global optimum, it

correctly identified element 21 with 9.71% damage and the global optimum was obtained after a few hillclimbing iterations.

When the noise level increased, the severity of false identifications also increased, although, the true damage element was always identified with the highest damage indicator value. For both IRR GAs, the maximum number of false identifications stayed below 2 and 3% for the 5 and 10% noise levels, respectively. The figures show that the predicted severity for the true damage element was always close to the inflicted 10%. In most trials, hillclimbing did not improve the results significantly.

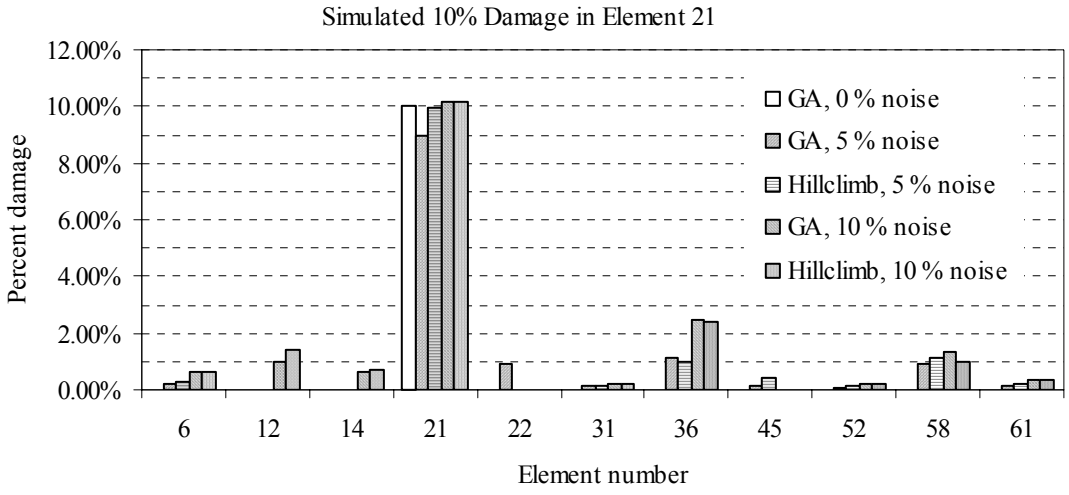

Figure 8.4. Damage detection results for case UBFRM I, implicit redundant representation (IRR), seeded initial population, noise levels of 0, 5 and 10%

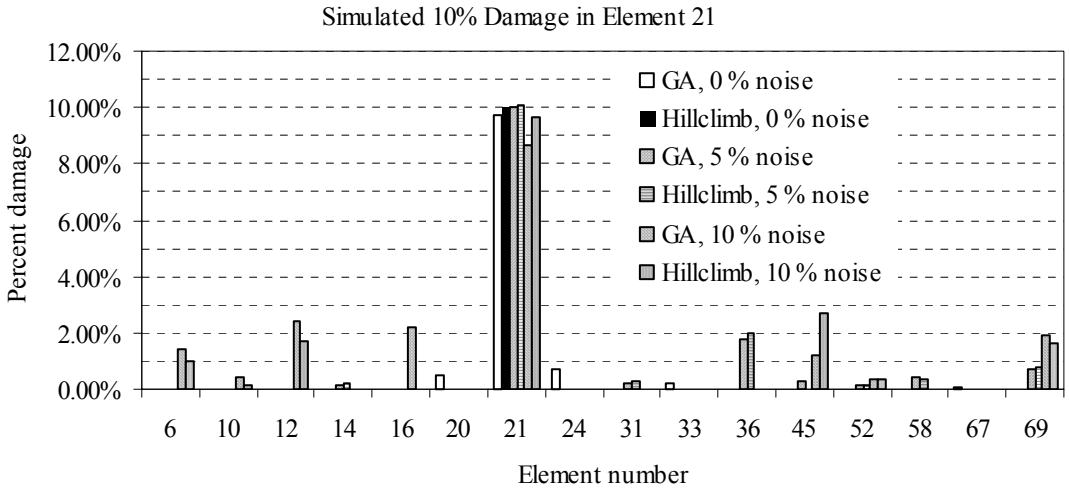

Figure 8.5. Damage detection results for case UBFRM I, implicit redundant representation (IRR), unseeded initial population, noise levels of 0, 5 and 10%

Damage detection results for the second unbraced frame case study, UBFRM II (Table 5.4), are summarized in Table D.53 and Table D.54 of APPENDIX D. The true damaged element 28 is located on the left perimeter first floor beam at the perimeter joint with a 10% severity (Figure C.4 of APPENDIX C). Solutions obtained using the seeded IRR GA are shown in Figure 8.6 and results for the unseeded IRR GA are depicted in Figure 8.7 for noise levels of zero, 5 and 10%, respectively. In the case of noise free measurements, the seeded IRR GA found the global optimum after 141 generations identifying element 28 with 10% damage. For the unseeded IRR GA, hillclimbing took only five iterations to find the global optimum starting from the solution obtained after 300 GA generations.

At a noise level of 5%, the solutions obtained clearly identified the true damaged element with a severity of approximately 8.7% for both the seeded and unseeded IRR GA trials. The severity of false identifications remained below 1.3% for all trials. At a higher noise level of 10%, the predicted damages for the true damage element were underestimated for both trials. The seeded IRR GA found a solution in which the true damage element was identified with approximately 6.1% damage, while the unseeded IRR GA provided a solution identifying element 28 with approximately 7.6% damage.

The largest false identification occurred at element 45 for both the seeded and unseeded IRR GA trials with severities of 2.8/2.5%, respectively. Other falsely identified elements had predicted damages smaller than those of element 45.

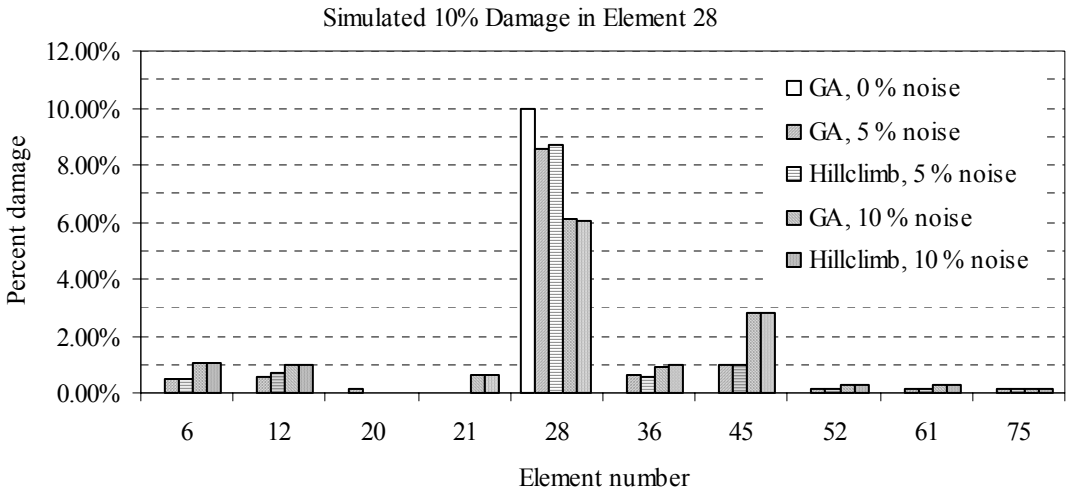

Figure 8.6. Damage detection results for case UBFRM II, implicit redundant representation (IRR), seeded initial population, noise levels of 0, 5 and 10%

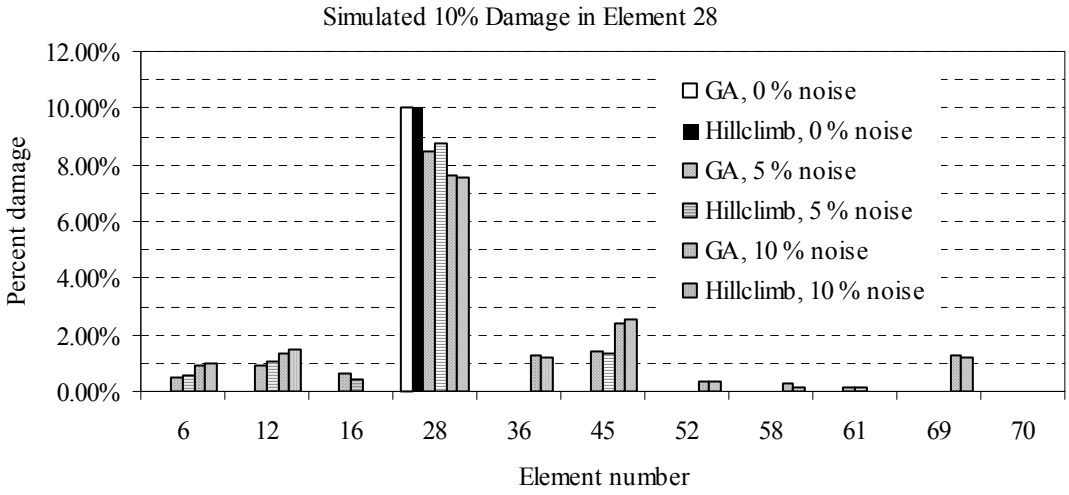

Figure 8.7. Damage detection results for case UBFRM II, implicit redundant representation (IRR), unseeded initial population, noise levels of 0, 5 and 10%

8.2.2 Optimum Excitation and Sensor Locations for the Unbraced Frame

Before damage detection results for case studies UBFRM III and IV can be presented, the optimum sensor layout design problem must be presented. Based on the experience obtained from the excitation and sensor location optimization trials for the cantilever and two-span continuous beams, the fixed representation GA was used to determine the optimal sensor locations for the unbraced frame. The GA settings were similar to those shown in Table 7.4. The optimum excitation and sensor locations for the unbraced frame are summarized in Table 8.7 and the final population obtained from one of the trials is plotted in objective space and is presented in Figure 8.8.

The results obtained showed that the increase in the measurement information became less significant as the number of sensors was increased. The best excitation and sensor locations are all found at vertical DOFs. There could be several reasons for obtaining this particular arrangement. The information measure is based on FRF sensitivities with respect to all finite elements in the model. Since the number of beam elements is 45 and the number of column elements is 35 for the unbraced frame problem it is possible that the beam elements receive more emphasis in the information measure. The columns were also stiffer than the beams, and therefore, responses in the beams excited in the vertical direction may be larger than those caused by horizontal excitations. Nevertheless, placing a sensor at the excitation DOF (interior node on the right, first floor perimeter beam, Figure C.3 of APPENDIX C) was the most beneficial just as it was for the cantilever and two-span continuous beam cases. The results presented in Table 8.7 show that using two sensors increases the information by approximately 90%, but using more than two sensors does not increase FRF sensitivities significantly. Additional sensors were placed on beams in an alternating fashion starting with the right bay then the middle bay. In the optimal sensor configuration two sensors are placed on each beam.

Table 8.7. Pareto optimal excitation and sensor locations for the three-story three-bay unbraced moment frame problem, UBFRM

Number of sensors	Excitation at Node*	Sensor(s) at Node	Measurement Information	
			Value	Percent
1	61	61	$9.8223 \cdot 10^{11}$	100.0 %
2	61	61, 62	$1.8670 \cdot 10^{12}$	190.1 %
3	61	61, 62, 72	$1.8850 \cdot 10^{12}$	191.9 %
4	61	61, 62, 71, 72	$1.9029 \cdot 10^{12}$	193.7 %
5	61	61, 62, 66, 71, 72	$1.9066 \cdot 10^{12}$	194.1 %
6	61	61, 62, 65, 66, 71, 72	$1.9101 \cdot 10^{12}$	194.5 %
7	61	59, 61, 62, 65, 66, 71, 72	$1.9132 \cdot 10^{12}$	194.8 %
8	61	59, 60, 61, 62, 65, 66, 71, 72	$1.9155 \cdot 10^{12}$	195.0 %
9	61	59, 60, 61, 62, 65, 66, 67, 71, 72	$1.9166 \cdot 10^{12}$	195.1 %
10	61	59, 60, 61, 62, 65, 66, 67, 68, 71, 72	$1.9174 \cdot 10^{12}$	195.2 %

* Excitation and measurements are in the vertical direction

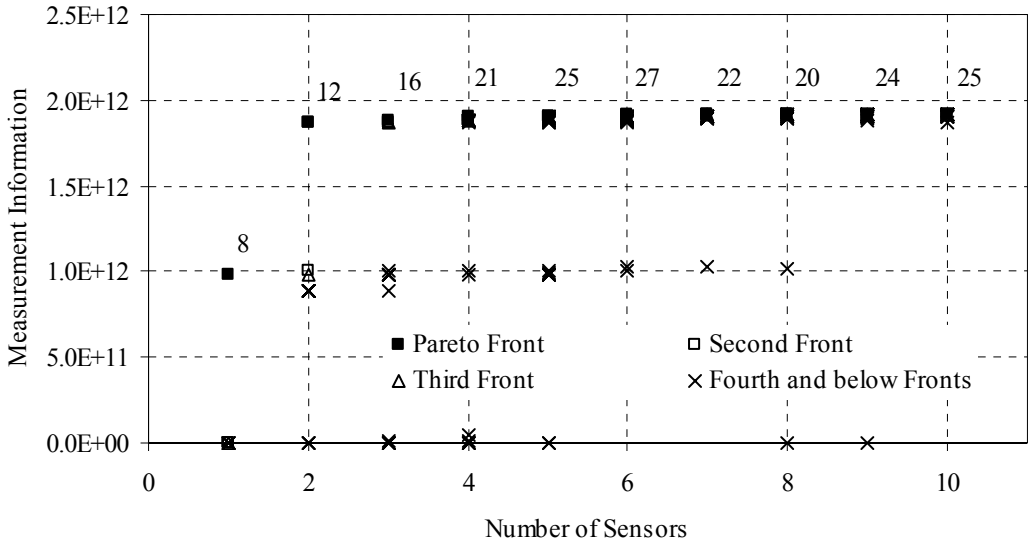

Figure 8.8. Pareto front and individuals in the final population represented in the objective space for the three-story three-bay unbraced moment frame problem using fixed representation GA, population size of 200

8.2.3 Damages Associated with Soft-story Mechanism

In case study UBFRM III, damages in four column elements were introduced (Table 5.4). All damaged elements were located on the first floor columns right where the columns were framed into the first floor beams. The severities of damage for the perimeter columns were 10% (elements 34 and 49), while the damage severities for the interior columns were 5% (elements 3 and 27, Figure C.4 of APPENDIX C). Four trials based on the damage scenarios defined in case study UBFRM III were performed. Most of the GA input parameters were selected from Table 8.6. Some input parameters, however, were altered to enhance convergence and these are listed in Table 8.8. Two trials, 1(a) and 2(a), used the same sensor configuration defined for case study UBFRM III in Table 5.4. Two other trials, 1(b) and 2(b), used 3 optimal sensors found in Table 8.7. From the observations made for the braced frame studies that adaptive crossover can cause premature convergence, two of the trials, 2(a) and 2(b), used the equal probability crossover to reduce selection pressure. All trials assumed that the noise level in measurements was zero and that seeded IRR GA was used to perform the optimization.

Table 8.8. GA input parameters for the soft-story mechanism case study, UBFRM III

Trial	Population Size	Tournament Size	Crossover Type	Crossover Rate(s)	Crossover Sites	Sensor Placement
1(a)	200	6	Adaptive	Primary: 0.9 Secondary: 1.0	6	3 Non-optimal Sensors
1(b)	200	6	Adaptive	Primary: 0.9 Secondary: 1.0	6	3 Optimal Sensors
2(a)	250	3	Equal Probability	0.8	4	3 Non-optimal Sensors
2(b)	250	3	Equal Probability	0.8	4	3 Optimal Sensors

Damage detection results obtained for all four trials are presented in Figure 8.9 and Figure 8.10, and are summarized in Table D.55 and Table D.56 of APPENDIX D. For the high selection pressure trials, 1(a) and 1(b), neither of the solutions contained the

true damaged element 49 as shown in Figure 8.9. Both trials, however, located the true damaged interior column elements, 3 and 27, although with damage severities larger than the imposed 5%. The predicted damage indicators for the interior columns obtained using the optimal sensor configuration were better than those predicted using the non-optimal measurement pattern. One of the true damaged exterior column elements (element 34), however, was also identified by the IRR GA using the non-optimal sensor configuration while the IRR GA using the optimal sensor locations did not identify it. After hillclimbing, the damage indicator for this column element in trial 1(a) was 9.36% instead of the imposed 10%. False identifications occurred in both trials away from the true damage elements. As was expected, premature convergence occurred in both cases due to the high selection pressure combined with the adaptive crossover.

In an attempt to overcome the difficulties associated with premature convergence, the tournament size was reduced and equal probability crossover was selected for trials 2(a) and 2(b) according to Table 8.8. With the new set of input parameters the trials were repeated and the results are presented in Figure 8.10. There were no apparent improvements in the solution obtained in trial 2(a) using the non-optimal sensor configuration. Actually the results obtained were worse than in case 1(a) since in this trial only the two interior column elements were identified. The information provided by the three non-optimal sensors was not sufficient for locating all four true damaged elements. Result obtained, however, for the optimal sensor locations are strikingly better using the new GA input parameters. All four true damage elements were identified after 300 GA generations and only one element was falsely identified with a severity of 0.13%. After hillclimbing, the global optimum was obtained with the correct damage indicators for all true damage elements as shown in Figure 8.10 for trial 2(b). The average increase of the average fitness of the initial population was approximately 120 times between the non-optimal and optimal sensor cases. This increase shows a significantly higher sensitivity of the objective function when optimum sensor locations are used. Finding all damaged elements showed the superiority of using optimal sensor locations over non-optimal sensor configurations.

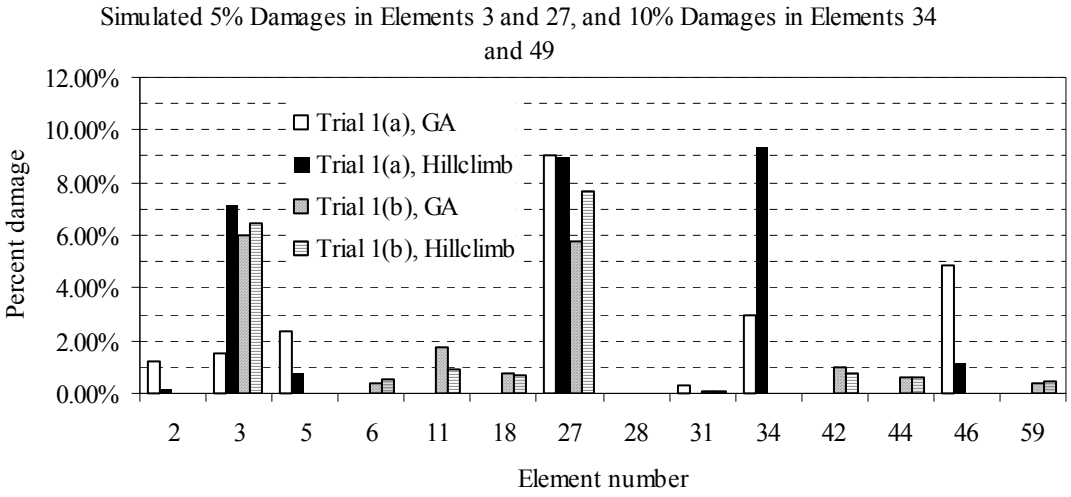

Figure 8.9. Damage detection results for soft-story mechanism case UBFRM III, seeded IRR GA, trials 1(a) and 1(b)

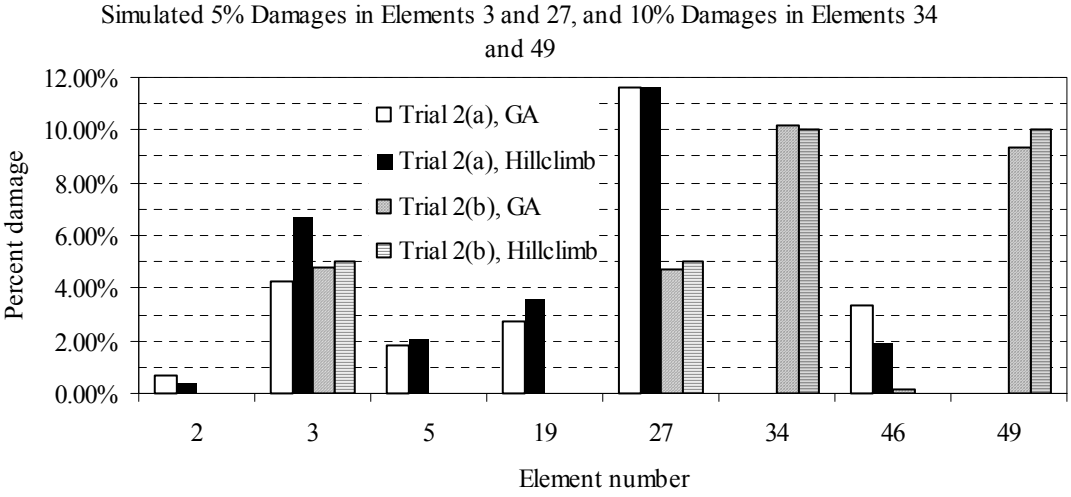

Figure 8.10. Damage detection results for soft-story mechanism case UBFRM III, seeded IRR GA, trials 2(a) and 2(b)

8.2.4 Damages Associated with Strong Column Weak Beam Design Concept

In case study UBFRM IV, which is defined in Table 5.4, six first floor beam elements framing into the joints have nonzero damages (Figure C.4 of APPENDIX C). This case

study was intended to simulate a damage scenario that may occur in frames sized according to the strong column, weak beam design concept. Beam elements at the perimeter joint (element 28 and 18) have 20% damage while beam elements at the interior joints (element 4, 10, 11 and 16) have 10% damages. The GA input parameters used are the same as in trial 2(b) and are given in Table 8.6 and Table 8.8. Only trials using the seeded IRR GA were performed.

The trials performed for case study UBFRM IV are summarized in Table 8.9. In this table, the trial number also designates the number of sensors used for measurements, e.g. in trial 7, 7 optimal sensors are used. The optimal sensor locations are defined in Table 8.7. The trials were intended to reveal the effect of the number of sensors on the accuracy of damage detection for two different noise levels (0 and 5%). The maximum number of generations was also increased from 300 to 400 to allow for a more thorough exploration and exploitation of the search space.

Table 8.9. Trials for case study UBFRM IV

Trial	Measurement Configuration	Noise Level
3	3 Optimal Sensors	0%
4	4 Optimal Sensors	0%
5(a)	5 Optimal Sensors	0%
5(b)	5 Optimal Sensors	5%
6	6 Optimal Sensors	5%
7	7 Optimal Sensors	5%
8	8 Optimal Sensors	5%
9	9 Optimal Sensors	5%
10	10 Optimal Sensors	5%

The first three trials defined by Table 8.9 correspond to noise free measurement cases and results for these trials are depicted in Figure 8.11 and summarized in Table D.57 of APPENDIX D. The number of correctly identified elements was 4, 5 and 6 using 3, 4 or 5 optimum sensors, respectively. Three interior beam elements (4, 10 and 11) and

one the exterior beam element (18) were correctly identified as damaged in all three trials and the accuracy of the severity estimates increased with an increasing number of sensors. By using four sensors instead of three, the additional exterior beam element (28) was also identified with a severity somewhat higher than the imposed 20%. Another improvement in the number and severity of falsely identified elements was observed in Figure 8.11 between the three and four sensor cases. The inclusion of the fifth sensor provided enough information for damage detection to uniquely identify all six damaged elements without any false identification. After hillclimbing, the global optimum was found when five sensors were used. Clearly with increasing number of sensors, the SDIM developed becomes more stable and unique, and therefore more robust. The total number of possible sensor locations for this model equals to 216 if the rotational DOFs are included or 144 if they are not included in the set of possible sensors. Using the IRR GA, only a fraction (5 sensors) out of the total number of potential sensor locations were needed to locate and quantify multiple damages with different severities.

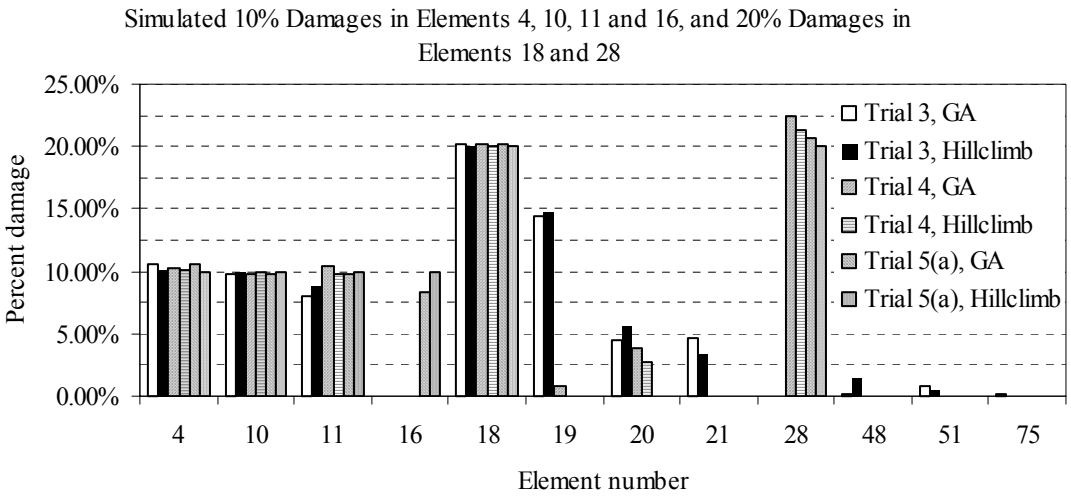

Figure 8.11. Damage detection results for case UBFRM IV, seeded IRR GA, trials 3, 4 and 5(a)

The last five trials shown in Table 8.9 assume that a 5% noise exists in the measurements. The increasing trial numbers, 5(b), 6,…, 10, again correspond to the

number of optimal sensors used for the measurements. The goal of the five trials was to determine the effect that increasing the number of sensors in the measurements has on the performance of the SDIM. Damage detection results obtained for these trials are summarized in Table D.58 and Table D.59 of APPENDIX D. The results of trials 5(b) and 6 are depicted in Figure 8.12. In Trial 5(b), five of the true damaged elements were identified, including all four interior beam elements and one perimeter beam element. The predicted damage severities for the interior beam elements (4, 10, 11 and 16) were mainly higher than the inflicted 10% damage, e.g. for element 16 the damage predicted was approximately 37%. The one correctly identified perimeter beam element 18 had a damage indicator of 20.3% instead of the imposed 20%. As shown in Figure 8.12, hillclimbing did not significantly improve the results obtained after 400 GA generations. There were false identification with damage indicators around 10% for elements 47 and 59, while other falsely identified elements had smaller predicted damages. Including the sixth optimal sensor in Trial 6 did not improve the damage detection accuracy compared to Trial 5(b). On the contrary, only three of the true damaged elements were identified, including two interior and one exterior beam elements.

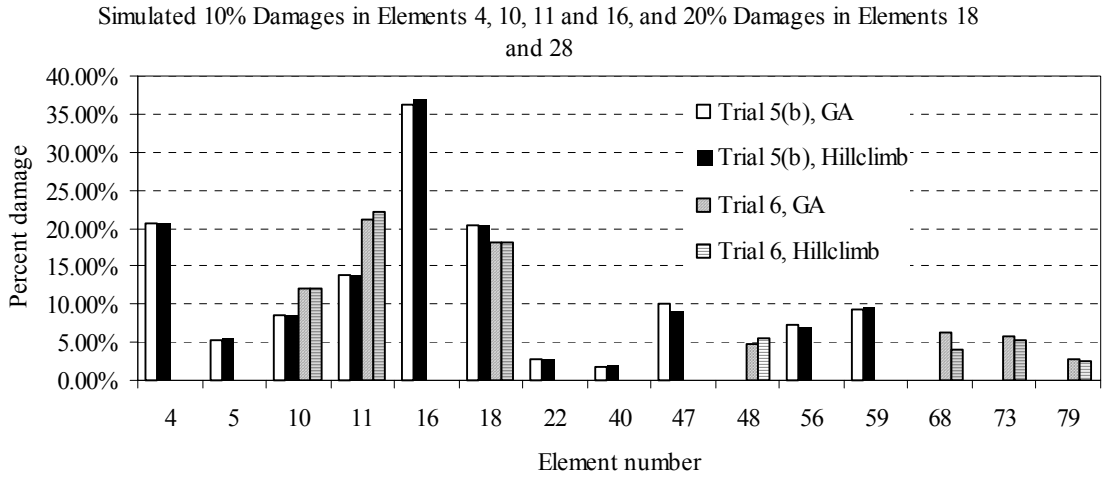

Figure 8.12. Damage detection results for case UBFRM IV, seeded IRR GA, trials 5(b) and 6

In trial 7 (7 sensors), element 28 (the exterior beam element that was not identified in trials 5(b) and 6) was included in the correctly located set of damaged elements, although the total number of correctly identified elements was four (Figure 8.13). The predicted damage severities of the correctly identified elements were closer to the inflicted values than they were in trial 5. Other elements were falsely identified, such as element 55, with considerable damage indicator values. In trial 8, an improvement in damage localization and severity prediction was observed as shown in Figure 8.13. Five out of the six true damage elements were located with reasonable damage indicator values, including all four interior beam elements and one exterior beam element. Element 38 was identified as damaged, which is adjacent to element 28 (exterior true damage element), which in a sense correctly localizes the damage to the proper, first floor exterior joint. Trial 8 overall shows significantly better results than any of the previous trials.

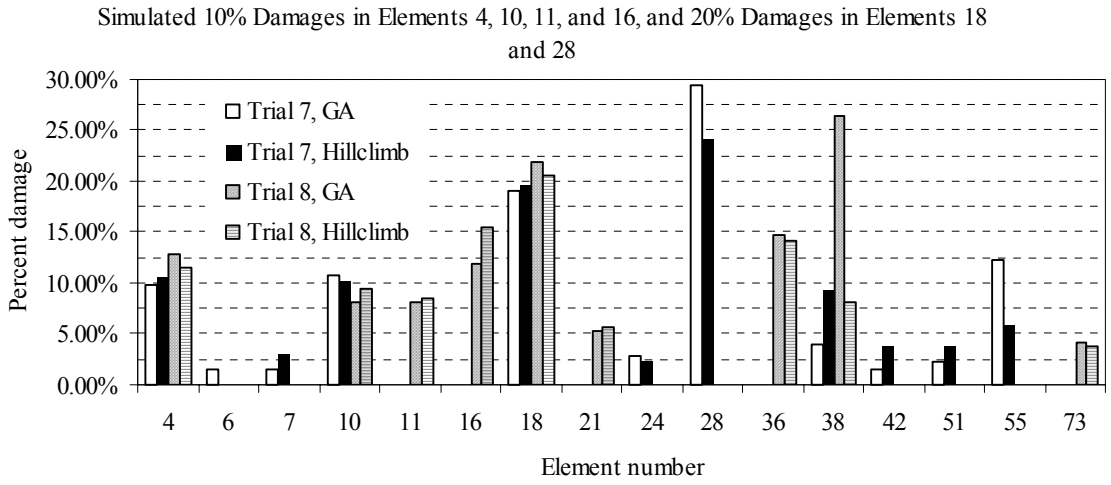

Figure 8.13. Damage detection results for case UBFRM IV, seeded IRR GA, trials 7 and 8

After performing 400 generations in trial 9, all six true damage elements were identified with damage indicator values reasonably close to the inflicted damages as depicted in Figure 8.14. After hillclimbing, however, element 28 was assigned a zero

damage indicator reducing the correctly located elements to five. The information contained in the measurements using nine sensors was not sufficient to uniquely locate all damage elements, which was expected. In the ten-sensor trial 10 only three elements were located correctly. Again element 38 was found to be damaged instead of element 28 at one of the first floor joints.

Based on the trials performed, it is concluded that that increasing the number of sensors may not always facilitate damage detection, although typically both localization and quantification of damages becomes more accurate with increasing number of sensors. Sensor configurations that introduced sensors on the beams where damages were actually located provided more information than sensors residing far from the true damage locations.

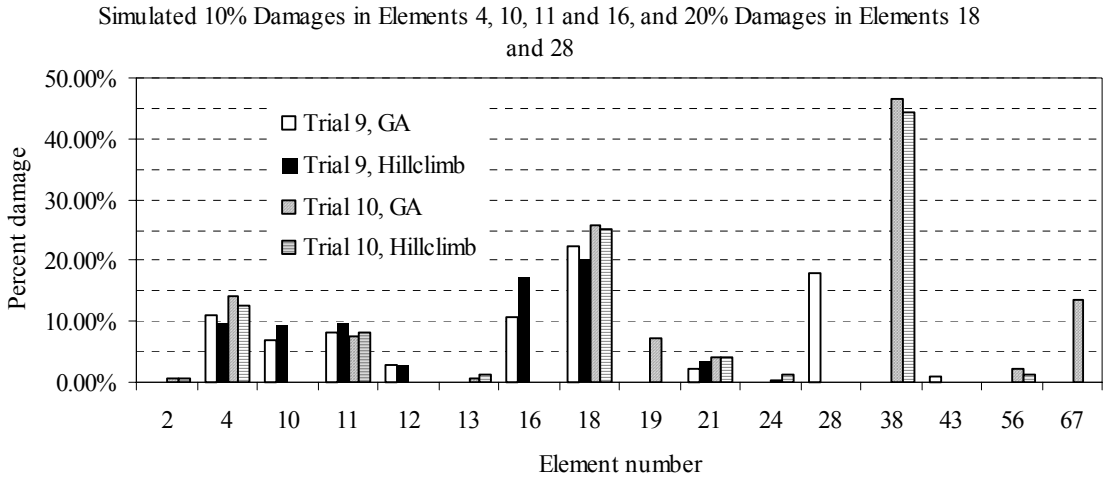

Figure 8.14. Damage detection results for case UBFRM IV, seeded IRR GA, trials 9 and 10

The results of trials investigated for the noisy measurements suggest that there is an optimal sensor configuration that is dependent on the damage scenario. In other words, different damage locations may impose a different set of optimum sensor locations. Intuitively for the damage case UBFRM IV, one could argue that sensors located on the damaged beams may contain the most information regarding damage detection.

To investigate this intuition, another trial called trial 11 was performed using six sensors all located on the first floor beams. Two sensors were placed on each beam and the same excitation location from previous trials was used. The excitation was located at node 61, while sensors were located at nodes 59, 60, 61, 62, 63 and 64 (Figure C.3 of APPENDIX C). Note that four out of these six sensor locations were also defined in the optimum configurations obtained from sensor optimization using 8, 9 and 10 sensors, which are listed in Table 8.7.

Damage detection results obtained for trial 11 are presented in Figure 8.15 and summarized in Table D.60 of APPENDIX D. The intuition of placing the sensors proved to be correct since all six true damage elements were identified. The predicted severity values were close to the inflicted values of 10% for the interior and 20% for the exterior beam elements. After hillclimbing, only one falsely identified location remained at element 3, which is the column element, that frames into the same joint as element 4 and 10. Even the false prediction was confined to the region of one of the correct joint damages. These results are superior to any of the trials previously conducted for noisy measurements suggesting that the damage configuration has significant effect on the optimal sensor placement.

For certain types of civil engineering structures, such as frames, the designer may have a good understanding about possible damage locations before measurements are taken. For instance, joints on lower floors are more likely to be damaged than joints at higher elevations. In addition, if beams are weaker than columns, then the beams have a higher probability of being damaged than columns. The information measure defined in Section 2.5.1 was formulated with respect to all finite elements in the model. This measure, however, could be prioritized to include intuitive knowledge during optimization. The simplest prioritization technique would be to exclude damage information sensitivities for elements that are not likely to be damaged. An additional approach would be to use a weighted sum of the damage sensitivities that accounts for the importance of detecting damage in each element. The improvement of the sensor location optimization proposed in Section 2.5 is not investigated in this research and remains the target of future studies.

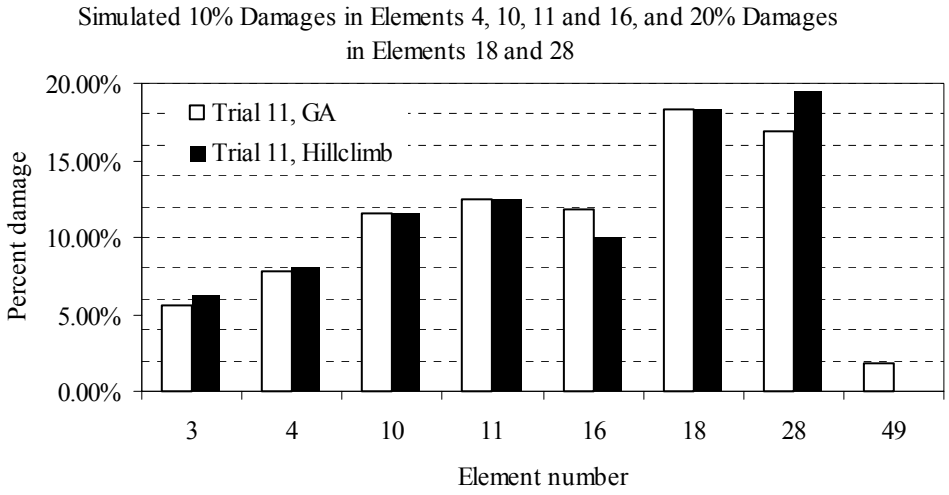

Figure 8.15. Damage detection results for case UBFRM IV, seeded IRR GA, trial 11

9 CASE STUDY RESULTS AND DISCUSSION, BENCHMARK STRUCTURE

Objective evaluation of newly developed SDIMs by comparing their performance with existing methods is crucial in assessing their contribution to the field of damage detection. In Section 1.5 of Section 1 three modal-based SDIMs developed by Kim and Stubbs (2002) were reviewed. The damage index methods use the information contained in mode shape measurements on the damaged structure. Trials in this section are based on the theoretical model of a plate girder structure investigated by Kim and Stubbs (2002). The description of the finite element model and case studies were presented in Section 5.3 of this research dissertation. Results obtained using the damage index methods for the plate girder case studies were summarized in Table 5.6. This section provides an objective comparison of the results obtained by the SDIM developed in this research with the results obtained using the damage index methods. New accuracy measures were developed that account for both the location and severity estimation accuracy of SDIMs.

9.1 Result Obtained for the Benchmark Case Studies

In order to directly compare the results of the damage index methods (A, B and C) obtained by Kim and Stubbs (2002) in their research with the SDIM presented in this research, the damage indicators obtained by the GA and hillclimbing in this research must be postprocessed. In their studies, Kim and Stubbs (2002) used a statistical criterion to select possible damage locations based on the damage index of each element. In general, the identification of anomalous data from a set is called the outlier analysis in statistics (Barnett and Lewis, 1994). This procedure is based on the discordant outlier in a data set, which is different from the rest of the data. The discordancy of a candidate outlier is a measure, which can be compared with some objective threshold, enabling the statistical judgment of the outlier. In damage detection, the judgment is whether or not damage in the given element exists.

The identification of a set of damaged elements can be established using the assumption that damage indices have Gaussian distribution. This assumption enables the assertion that indices more than two standard deviations above the mean can be associated with possible damage locations. Using the notation, β_j, for the damage indices, the normalized index for element j is defined.

$$Z_j = \frac{\beta_j - \bar{\beta}}{\sigma_\beta} - 2 \tag{9.1}$$

where β_j is the damage index of element j, which is the ratio of the Young's moduli of the undamaged and damaged element j, $\bar{\beta}$ is the mean of all damage indices in the model, and σ_β is the standard deviation. Based on the assumption that damaged elements have damage indices that lie more than two standard deviations above the average damage indices, potential damages are associated with non-negative normalized indices, $Z_j \geq 0$. The severity of damage using the damage indices is determined from the expression.

$$\alpha_j = \frac{1}{\beta_j} - 1, \quad \alpha_j \geq -1 \tag{9.2}$$

This definition of damage severity, α_j, is exactly the same as the damage indicator definition, x_j^s, used in the present research except that there is a sign difference between the two. Another interpretation of the statistical damage classification is that a threshold for the damage indicator can be obtained. If the damage indicator of an element is above this threshold then the element is classified as damaged. The severity of damage in this case equals the damage indicator. Otherwise the element is not damaged. The threshold damage indicator is obtained using Eqs. (9.1) and (9.2) with the limit value of $Z_j = 0$.

$$x_{th}^s = 1 - \frac{1}{2\sigma_\beta + \bar{\beta}} \tag{9.3}$$

The set of GA parameters used in the plate girder trials are summarized in Table 9.1. These parameters were selected on the basis of initial trials using different GA parameters and on the experience gained during previous trials. The number of significant digits for the plate girder trials was 6, which required 20 bits to represent a damage indicator with a precision of about $9.44 \cdot 10^{-7}$ or $9.44 \cdot 10^{-5}$%.

Table 9.1. GA parameters for plate girder trials

	Fixed Representation	IRR, Seeded*	IRR, Unseeded
Population Size	200	200	200
Tournament Size	6	4, 6	4, 6
Initial Seed	Yes	Yes	No
Maximum Generations	200	200	200
Stop if no Improvement	20	20	20
Crossover Type	Adaptive	Equal Probability, Adaptive	Equal Probability, Adaptive
Crossover Sites	6	4, 6	4, 6
Crossover Rates	Primary: 0.9, Secondary: 1.0	Primary: 0.8, 0.9, Secondary: 1.0	Primary: 0.8, 0.9, Secondary: 1.0
Mutation Type	Uniform	Uniform	Uniform
Mutation Rate	0.005	0.005	0.005
Elitism	Yes	Yes	Yes
Hillclimbing	Yes, Reduced	Yes, Reduced	Yes, Reduced
Coding	Gray	Gray	Gray

* For the IRR the number of gene instances (expected number of damaged elements) was 15 and the gene locator (GL) length is 3

Results obtained using the fixed representation GA and hillclimbing for noise free measurements are summarized in Table D.61 through Table D.64 of APPENDIX D. The results presented in these tables are the raw data without any statistical postprocessing. After 200 GA generations almost all elements were predicted as damaged in all trials. In most cases, however, the correct damaged elements had larger damage indicator values than the damage indicator values of the elements that were not damaged. The large number of variables (50) defined in the fixed representation caused the GA to converge

slowly to the global optimum. Using the best individual after 200 GA generations, the global optimum identifying the correct damaged elements with exact damage indicators was found after hillclimbing for all trials.

Results for the fixed representation GA and hillclimbing using the statistical postprocessing are summarized in Table 9.2. To demonstrate the statistical selection criteria, the normalized damage indices for case study KSTSP II after 200 GA generations are plotted in Figure 9.1. First the damage indices, β_j, were obtained from the damage indicators, x_j^s, using Eq. (9.2). Then having computed the damage indices, the average (100.32%) and standard deviation (1.124%) of the damage indices were obtained. Using the statistical measures, the normalized damage indices were calculated for each element from Eq. (9.1) and plotted in Figure 9.1. Elements that had nonnegative normalized damage indices were considered as damaged. In Figure 9.1 two of these elements (element 1 and 9) can be identified. In this case, only element 9 was the correct damaged element and element 1 was a false identification. Substituting the mean and standard deviation of the damage indices into Eq. (9.3) determines the damage indicator threshold value, which was 2.51% for this particular example (Table 9.2). The threshold value for the damage indicator indicated that elements that have damage indicator values above the threshold were not considered as damaged. The threshold for case study KSTSP VIII for example was above 20%. This means that any damage below this level would not be detected. The statistical selection procedure assumes that the severity of damages have similar magnitudes otherwise low-level damages will not be detected.

Table 9.2 shows that the fixed representation GA after 200 generations was able to identify the damaged elements in all cases except for case KSTSP X when element 36 instead of element 39 was located based on the statistical criterion. After hillclimbing, the global optimum was found for all cases. Therefore the SDIM showed perfect agreement with the imposed damage scenarios. Based on the perfect agreement, the application of the statistical postprocessing can be omitted for results obtained after hillclimbing.

Table 9.2. Damage detection result for the plate girder case studies after discordancy test for fixed representation GA and reduced hillclimbing, noise free measurements

Damage Case	Fixed Representation after 200 GA Generations			Fixed Representation after Hillclimbing		
	Threshold	Location	Severity	Threshold	Location	Severity
KSTSP I	2.07%	4	5.99%	3.26%	4	10.0%
KSTSP II	2.51%	1, 9	4.22, 6.36%	3.26%	9	10.0%
KSTSP III	2.12%	14	6.18%	3.26%	14	10.0%
KSTSP IV	2.32%	15, 19	5.41, 4.05%	3.25%	19	10.0%
KSTSP V	1.85%	20, 24	3.10, 3.09%	3.26%	24	10.0%
KSTSP VI	0.17%	37, 39, 46	0.19, 0.37, 0.19%	0.30%	39	1.00%
KSTSP VII	2.28%	36, 39	3.13, 6.18%	3.25%	39	10.0%
KSTSP VIII	20.5%	39	45.58%	23.2%	39	50.0%
KSTSP IX	2.99%	9, 34	6.11, 6.19%	4.62%	9, 34	10.0, 10.0%
KSTSP X	2.87%	14, 36	3.67, 6.21%	4.62%	14, 39	10.0, 10.0%

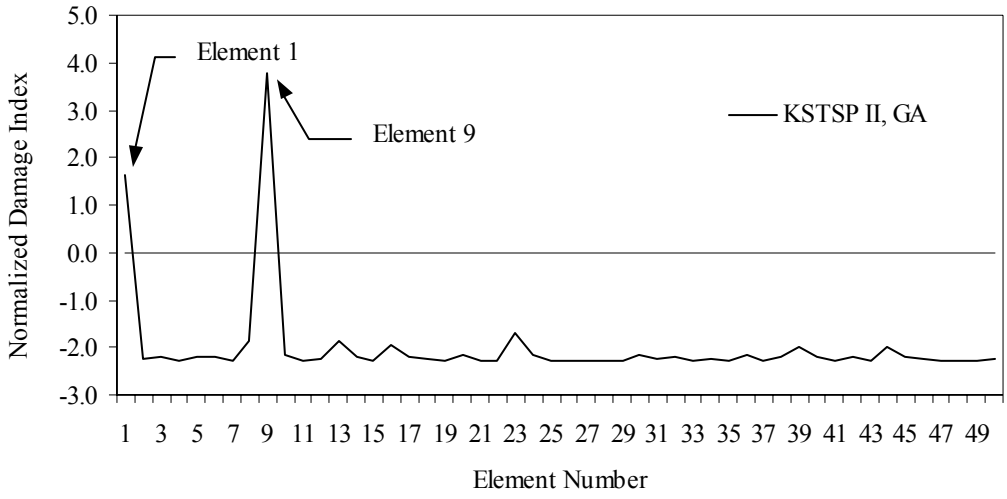

Figure 9.1. Normalized damage indices for case study KSTSP II, fixed representation GA after 200 generations

Table D.65 through Table D.68 of APPENDIX D summarize the damage detection results for the plate girder studies in case of noise free measurements without

statistical postprocessing using the seeded IRR GA and hillclimbing. Similarly, results for the unseeded IRR GA and hillclimbing are summarized in Table D.69 through Table D.72 of APPENDIX D. Both IRR GAs converged to solutions that were very good representations of the imposed damage cases after 200 GA generations. The seeded IRR GA found the global optimum 5 times out of the 10 damage cases. Therefore hillclimbing could not improve these results. Since all IRR GA trials provided a very good solution, only a small number of hillclimbing iterations were necessary to obtain the global optimum in the other cases.

Results obtained after applying the statistical postprocessing are summarized in Table 9.3 and Table 9.4 for the IRR GA with and without initial seeding, respectively. The tables reinforce the superior performance provided by IRR GAs in damage detection over the fixed representation. The global optimum was always found either by the GA or after hillclimbing. In any case the statistical postprocessing could be omitted since no false damage identifications were obtained in the solutions.

Table 9.3. Damage detection result for the plate girder case studies after discordancy test for seeded IRR GA and reduced hillclimbing, noise free measurements

Damage Case	Seeded IRR GA after 200 or less GA Generations			Seeded IRR GA after Hillclimbing		
	Threshold	Location	Severity	Threshold	Location	Severity
KSTSP I	3.26%	4	10.0%	-*	-	-
KSTSP II	3.26%	9	10.0%	3.26%	9	10.0%
KSTSP III	3.26%	14	10.0%	-	-	-
KSTSP IV	3.05%	19	9.33%	3.26%	19	10.0%
KSTSP V	3.26%	24	10.0%	-	-	-
KSTSP VI	0.27%	39	0.89%	0.30%	39	1.00%
KSTSP VII	3.26%	39	10.0%	-	-	-
KSTSP VIII	23.2%	39	50.0%	23.2%	39	50.0%
KSTSP IX	4.62%	9, 34	10.0, 10.0%	-	-	-
KSTSP X	4.62%	14, 39	10.0, 10.0%	4.62%	14, 39	10.0, 10.0%

* Hillclimbing could not improve the results

Table 9.4. Damage detection result for the plate girder case studies after discordancy test for unseeded IRR GA and reduced hillclimbing, noise free measurements

Damage Case	Unseeded IRR GA after 200 or less GA Generations			Unseeded IRR GA after Hillclimbing		
	Threshold	Location	Severity	Threshold	Location	Severity
KSTSP I	3.26%	4	10.0%	-*	-	-
KSTSP II	3.18%	9	9.71%	3.26%	9	10.0%
KSTSP III	3.13%	14	9.48%	3.26%	14	10.0%
KSTSP IV	2.85%	19	8.69%	3.26%	19	10.0%
KSTSP V	3.25%	24	9.98%	3.26%	24	10.0%
KSTSP VI	0.29%	39	0.96%	0.30%	39	1.00%
KSTSP VII	3.09%	39	9.50%	3.25%	39	10.0%
KSTSP VIII	23.2 5	39	50.0%	23.2%	39	50.0%
KSTSP IX	4.31%	9, 34	9.84, 8.69%	4.62%	9, 34	10.0, 10.0%
KSTSP X	4.60%	14, 39	10.0, 9.91%	4.62%	14, 39	10.0, 10.0%

* Hillclimbing could not improve the results

9.2 Accuracy Measures of SDIMs

Although the damage detection error measures defined by Kim and Stubbs (2002) are capable of measuring the accuracy of SDIMs these measures were not adapted in this research. The main reason that these measures were not used were that the measures were not bounded (ranged from zero to infinity) or that they could only account for the location or severity of predicted damages, but not both. In this research, new error measures are introduced that are normalized between zero and unity and that account for both the location and severity of damage predictions.

The proposed error measures are based on geometrical properties of vectors using Euclidean geometry. Consider two vectors, the vector of true damage indicators, $\mathbf{x}^s_{true} \in \mathbb{R}^{n_e}$, and the vector of predicted damage indicators, $\mathbf{x}^s_{pred} \in \mathbb{R}^{n_e}$. The vector difference of the two damage indicator vectors is the damage indicator error vector, $\mathbf{x}^s_{error} \in \mathbb{R}^{n_e}$.

$$\mathbf{x}^s_{error} = \mathbf{x}^s_{true} - \mathbf{x}^s_{pred} \tag{9.4}$$

These vectors are depicted in Figure 9.2. The first measure called the Euclidean normalized error (*ene*) is simply the norm or length of the error vector normalized to the worst possible damage detection result in which all damage indicators have 100% error. The length of the worst damage detection result is $\sqrt{n_e}$ since all entries in the damage indicator error vector are unity.

$$ene = \frac{\sqrt{\langle \mathbf{x}^s_{error}, \mathbf{x}^s_{error} \rangle}}{\sqrt{n_e}} = \frac{\sqrt{\left(\mathbf{x}^s_{error}\right)^T \mathbf{x}^s_{error}}}{\sqrt{n_e}} = \frac{\left\|\mathbf{x}^s_{error}\right\|}{\sqrt{n_e}}, \quad 0 \le ene \le 1 \tag{9.5}$$

where $\langle , \rangle$ is an inner product of vectors (for Euclidean geometry the inner product is equivalent to the dot product of vectors). If this measure is zero then the predicted damage indicators are exactly equal to the true damage indicators and both the locations and severities of damages are correctly identified without any false identification. A unit value for this measure would indicate that all of the predicted damage indicators are in 100% error.

The next geometric measure is called the true projection error (*tpe*), which is also normalized to the worst possible damage detection scenario.

$$tpe = \frac{1}{\sqrt{n_e}} \frac{\left|\left(\mathbf{x}^s_{error}\right)^T \mathbf{x}^s_{true}\right|}{\left\|\mathbf{x}^s_{true}\right\|}, \quad 0 \le tpe \le 1 \tag{9.6}$$

The geometrical interpretation of the true projection error can be seen in Figure 9.2. This measure represents the amount of error that occurred with respect to the true damaged elements (projection of the error vector on the true damage vector). If all the true damages are identified with the correct severities then the measure is zero (no error), regardless of the number and severity of false identifications. A value of unity indicates that all elements were damaged, but none of them was identified.

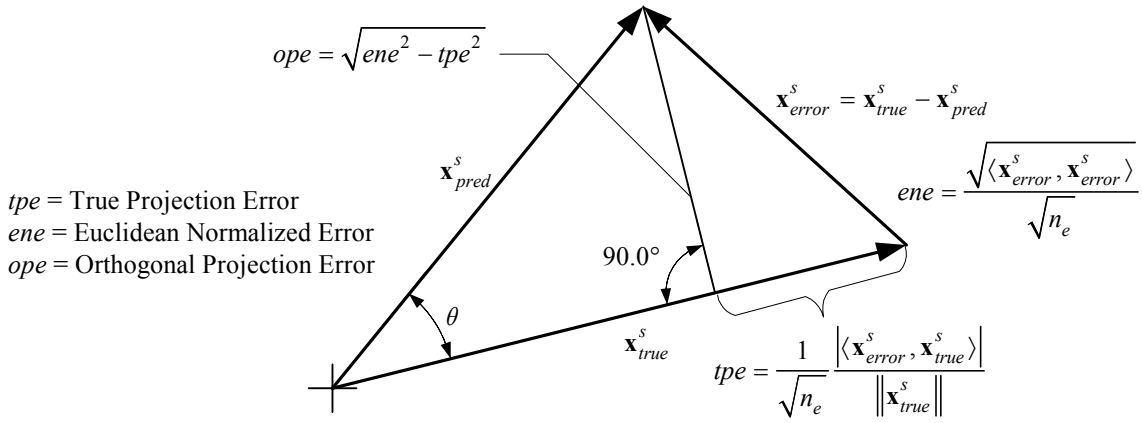

Figure 9.2. Geometrical definition of error measures

Consequently, the error that relates to the falsely identified elements can be obtained from the Pythagorean relationship of *ene* and *tpe* and is called the orthogonal projection error (*ope*) (Figure 9.2).

$$ope = \sqrt{ene^2 - tpe^2}, \quad 0 \le ope \le 1 \tag{9.7}$$

A zero value of this measure indicates that there are no false identifications and all, if any, errors are in the identification of the true damaged elements. This measure with a unit magnitude is interpreted as all of the non-damaged elements are falsely identified with 100% error.

The last geometrical measure defined is the cosine of the angle between the true and predicted damage indicator vectors. This measure is called the trigonometric angle error (*tae*).

$$tae = \cos\theta = \frac{\left(\mathbf{x}^s_{true}\right)^T \mathbf{x}^s_{pred}}{\left\|\mathbf{x}^s_{true}\right\| \left\|\mathbf{x}^s_{pred}\right\|}, \quad 0 \le tae \le 1 \tag{9.8}$$

In general the *tae* is bounded between negative unity, and unity but in this case since all entries of the damage indicator vectors are between zero and unity the angle between the vectors is bounded by zero and 90°. Therefore the *tae* is bounded by zero and

unity. A value of one indicates that only true damaged elements were identified and all predicted severities can be obtained from the true damage values by multiplying them with the same scalar (the true and predicted damage vectors are linearly dependent). When this measure becomes zero than none of the true damages were identified.

Based on the damage detection results provided in Table 5.6, the accuracy measures for the damage index A, B and C algorithms are summarized in Table 9.5 and Table 9.6. In these tables, all of the measures were applied to each individual case study and then the average value of each measure was calculated. The first measure considered was the Euclidean normalized error (*ene*), which clearly shows the superiority of the damage index C algorithm over the other two algorithms. Another way to interpret the geometrical accuracy measures is to multiply them with the normalizing worst possible damage detection results and compare the absolute error values. The average Euclidean absolute errors are 22.43%, 11.14% and 1.16% for the damage index A, B and C procedures, respectively, which can be used as indicators of an overall error. For example, the damage index A method resulted in a 22.34% absolute error. The next two measures, true projection error (*tpe*) and orthogonal projection error (*ope*), express the vector components of *ene* related to the true damaged elements and the non-damaged elements. The *tpe* measures for the damage index A and B methods are similar 9.37% and 11.14%, and are indication of the absolute error in predicting the damage severities for the true damaged elements. The absolute *tpe* measure is only 0.99% for the damage index C method. Similar *ene* and *tpe* values, such as for damage index B and C algorithms, indicate that most of the errors resulted in the vector direction of the true damaged elements. In other words, there were very little or no false damage identifications. Consequently, similar *ene* and *ope* values (damage index A method 22.43% and 18.94%, respectively) state that most errors occurred in the vector direction of non-damaged elements suggesting that false identifications happened frequently.

The trigonometric angle error (*tae*) is an indicator of the linear dependence of the predicted and true damage vectors (note that *tae* is not a normalized value and therefore there is not an average absolute value reported in the tables for this measure). Since the damage index A method frequently identified false damaged elements the average *tae*

value of this procedure is only 0.64. For the other two damage index SDIMs the average *tae* values show an almost perfect correlation of the predicted and true damage vectors (only true damaged elements were predicted as damaged).

The proposed measures well reflect the performance of SDIMs that can be inferred from the results in Table 5.6 intuitively. For instance, damage index A and B methods consistently over and underestimated the true damages, but with about the same error. This is reflected in similar *tpe* values for these two methods. Furthermore, damage index methods B and C only identified true damage locations, which is expressed in almost unit *tae* values and very small *ope* values. The damage index A procedure falsely identified several elements as damaged and therefore its *ope* measure is large compared to the other two methods. It is also clear that the measures can capture both location and severity type errors in an efficient way.

Table 9.5. Damage detection accuracy measures for Damage Index A and B methods, noise free measurement cases

Damage Case	Damage Index A				Damage Index B			
	ene	*tpe*	*ope*	*tae*	*ene*	*tpe*	*ope*	*tae*
KSTSP I	0.04170	0.01259	0.03975	0.55800	0.00877	0.00877	0.00000	1.00000
KSTSP II	0.03597	0.01230	0.03380	0.61617	0.01230	0.01230	0.00000	1.00000
KSTSP III	0.04593	0.01174	0.04441	0.50353	0.01216	0.01216	0.00000	1.00000
KSTSP IV	0.02638	0.01146	0.02376	0.73294	0.01301	0.01301	0.00000	1.00000
KSTSP V	0.02966	0.00806	0.02855	0.61395	0.01344	0.01344	0.00000	1.00000
KSTSP VI	0.02023	0.00141	0.02018	0.00000	0.00127	0.00127	0.00000	1.00000
KSTSP VII	0.04274	0.01202	0.04101	0.53782	0.01202	0.01202	0.00000	1.00000
KSTSP VIII	0.03348	0.03210	0.00950	0.99576	0.04978	0.04978	0.00000	1.00000
KSTSP IX	0.01921	0.01580	0.01092	0.95650	0.01760	0.01760	0.00310	0.99655
KSTSP X	0.02199	0.01510	0.01598	0.91008	0.01720	0.01720	0.00060	1.00000
Average:	0.03173	0.01326	0.02679	0.64247	0.01576	0.01576	0.00002	0.99965
Average Absolute:	22.43%	9.37%	18.94%	-	11.14%	11.14%	0.01%	-

Table 9.6. Damage detection accuracy measures for Damage Index C method, noise free measurement cases

Damage Case	Damage Index C			
	ene	*tpe*	*ope*	*tae*
KSTSP I	0.00269	0.00269	0.00000	1.00000
KSTSP II	0.00099	0.00099	0.00000	1.00000
KSTSP III	0.00085	0.00085	0.00000	1.00000
KSTSP IV	0.00071	0.00071	0.00000	1.00000
KSTSP V	0.00099	0.00099	0.00000	1.00000
KSTSP VI	0.00000	0.00000	0.00000	1.00000
KSTSP VII	0.00057	0.00057	0.00000	1.00000
KSTSP VIII	0.00509	0.00509	0.00000	1.00000
KSTSP IX	0.00323	0.00090	0.00310	0.98708
KSTSP X	0.00134	0.00120	0.00060	0.99960
Average:	0.00164	0.00140	0.00037	0.99867
Average Absolute:	1.16%	0.99%	0.26%	-

Accuracy measures calculated for results obtained for the plate girder problem using the SDIM developed using GAs are reported in Table 9.7 through Table 9.9 for noise free measurements. Since the global optimum was found in all cases after hillclimbing, all measures show 100% accuracy of the methods, i.e. zero values of *ene*, *tpe* and *ope* and unit magnitude of *tae*. As a result all GA procedures combined with hillclimbing perform better than any of the damage index procedures for the case of noise free measurements.

Variations in performance of the different GA representations can be better identified using the accuracy measure values for solutions before hillclimbing. The average absolute value of *ene* for the fixed representation GA was 5.85%, which is better than the corresponding values of damage index A and B methods, but worse than that of damage index C. In general, the prediction of damage severities using the fixed representation GA were more representative of the true damage cases than those obtained using damage index A and B. The similar average value of *ene* and *tpe* (5.02%) also is an

indication that errors primarily occurred in predicting the correct severity of the true damages. The 2.42% average absolute *ope* value shows that the fixed representation GA resulted in some false identifications and in this sense was less effective than damage index B and C methods although the fixed representation performed much better than damage index A. Due to some false damage identifications, the *tae* measure of the fixed representation was on average worse than those of damage index B and C, but still better than that of damage index A. The measures reveal the lack of robustness of fixed representation GAs when the problem domain is relatively large.

Table 9.7. Damage detection accuracy measures for fixed representation GA, noise free measurement cases

Damage Case	Fixed Representation							
	After 200 GA Generations				After Hillclimbing			
	ene	*tpe*	*ope*	*tae*	*ene*	*tpe*	*ope*	*tae*
KSTSP I	0.00567	0.00567	0.00000	1.00000	0.00000	0.00000	0.00000	1.00000
KSTSP II	0.00788	0.00514	0.00597	0.83336	0.00000	0.00000	0.00000	1.00000
KSTSP III	0.00540	0.00540	0.00000	1.00000	0.00000	0.00000	0.00000	1.00000
KSTSP IV	0.01137	0.00842	0.00765	0.59935	0.00000	0.00000	0.00000	1.00000
KSTSP V	0.01156	0.00977	0.00619	0.57712	0.00000	0.00000	0.00000	1.00000
KSTSP VI	0.00097	0.00088	0.00039	0.80772	0.00000	0.00000	0.00000	1.00000
KSTSP VII	0.00698	0.00540	0.00443	0.89220	0.00001	0.00001	0.00000	1.00000
KSTSP VIII	0.00625	0.00625	0.00000	1.00000	0.00000	0.00000	0.00000	1.00000
KSTSP IX	0.00770	0.00770	0.00007	0.99998	0.00000	0.00000	0.00000	1.00000
KSTSP X	0.01890	0.01633	0.00952	0.35995	0.00000	0.00000	0.00000	1.00000
Average:	0.00827	0.00710	0.00342	0.80697	0.00000	0.00000	0.00000	1.00000
Average Absolute:	5.85%	5.02%	2.42%	-	0.00%	0.00%	0.00%	-

Performance measures calculated based on the results obtained using the seeded and unseeded IRR GAs are presented in Table 9.8 and Table 9.9, respectively. The average absolute accuracy measures for the IRR GA with seeded initial population after 200 or fewer generations show the outstanding performance of the SDIM developed. Two

of the measures (*ope*, *tae*) show no errors in damage detection (no false identifications and linearly dependent true and predicted damage vectors) and the other two errors (*ene*, *tpe*) are very small in average absolute value 0.08%. The small measures of *ene* and *tpe* are also an indication of the high precision attainable in damage severity prediction using the IRR GA. Overall, the IRR GA with a seeded initial population performed better than any of the damage index methods in every aspect for the plate girder test cases investigated in this research.

Table 9.8. Damage detection accuracy measures for seeded implicit redundant representation (IRR) GA, noise free measurement cases

Damage Case	Seeded Implicit Redundant Representation							
	After 200 or less GA Generations				After Hillclimbing			
	ene	*tpe*	*ope*	*tae*	*ene*	*tpe*	*ope*	*tae*
KSTSP I	0.00000	0.00000	0.00000	1.00000	-*	-	-	-
KSTSP II	0.00000	0.00000	0.00000	1.00000	0.00000	0.00000	0.00000	1.00000
KSTSP III	0.00000	0.00000	0.00000	1.00000	-	-	-	-
KSTSP IV	0.00095	0.00095	0.00000	1.00000	0.00000	0.00000	0.00000	1.00000
KSTSP V	0.00000	0.00000	0.00000	1.00000	-	-	-	-
KSTSP VI	0.00016	0.00016	0.00000	1.00000	0.00000	0.00000	0.00000	1.00000
KSTSP VII	0.00000	0.00000	0.00000	1.00000	-	-	-	-
KSTSP VIII	0.00000	0.00000	0.00000	1.00000	0.00000	0.00000	0.00000	1.00000
KSTSP IX	0.00000	0.00000	0.00000	1.00000	-	-	-	-
KSTSP X	0.00000	0.00000	0.00000	1.00000	0.00000	0.00000	0.00000	1.00000
Average:	0.00011	0.00011	0.00000	1.00000	0.00000	0.00000	0.00000	1.00000
Average Absolute:	0.08%	0.08%	0.00%	-	0.00%	0.00%	0.00%	-

* Hillclimbing could not improve the results

The performance measures in Table 9.9 calculated based on the results obtained by the unseeded IRR GA after 200 or less generations were slightly worse than those of the IRR GA with initial seed and on average were better than any of the damage index methods investigated. Again errors are confined to severity estimates of the true damaged

elements without any false identification. The linear dependence of the predicted and true damage vectors were not perfect (average *tae* = 0.99981). The lack of perfect linear dependence resulted in a very small average absolute error, *ope* = 0.09%, projected on the non-damaged elements, although most errors were related to the severity estimates for the true damaged elements (*ene* = 0.41%, *tpe* = 0.38%).

Table 9.9. Damage detection accuracy measures for unseeded implicit redundant representation (IRR) GA, noise free measurement cases

Damage Case	Seeded Implicit Redundant Representation							
	After 200 or less GA Generations				After Hillclimbing			
	ene	*tpe*	*ope*	*tae*	*ene*	*tpe*	*ope*	*tae*
KSTSP I	0.00000	0.00000	0.00000	1.00000	-*	-	-	-
KSTSP II	0.00042	0.00042	0.00000	1.00000	0.00000	0.00000	0.00000	1.00000
KSTSP III	0.00074	0.00074	0.00000	1.00000	0.00000	0.00000	0.00000	1.00000
KSTSP IV	0.00185	0.00185	0.00000	1.00000	0.00000	0.00000	0.00000	1.00000
KSTSP V	0.00003	0.00003	0.00000	1.00000	0.00000	0.00000	0.00000	1.00000
KSTSP VI	0.00005	0.00005	0.00000	1.00000	0.00000	0.00000	0.00000	1.00000
KSTSP VII	0.00071	0.00071	0.00000	1.00000	0.00000	0.00000	0.00000	1.00000
KSTSP VIII	0.00003	0.00003	0.00000	1.00000	0.00000	0.00000	0.00000	1.00000
KSTSP IX	0.00186	0.00147	0.00114	0.99811	0.00000	0.00000	0.00000	1.00000
KSTSP X	0.00013	0.00009	0.00009	0.99999	0.00000	0.00000	0.00000	1.00000
Average:	0.00058	0.00054	0.00012	0.99981	0.00000	0.00000	0.00000	1.00000
Average Absolute:	0.41%	0.38%	0.09%	-	0.00%	0.00%	0.00%	-

* Hillclimbing could not improve the results

To investigate the accuracy measures of the proposed SDIM, the plate girder case studies were repeated using the seeded IRR GA and adding 5% Gaussian random noise to the FRF measurements. The damage detection results obtained without statistical postprocessing are summarized in Table D.73 through Table D.76 of APPENDIX D. The results obtained after applying the statistical criterion to identify damaged elements are listed in Table 9.10. From the table it is clear that only true damaged elements were

identified in all cases except for case KSTSP VI, in which the correct damaged element 39 was not identified and instead three non-damaged elements were falsely picked. For this case, the imposed damage at element 39 was 1%, which caused very small changes in FRF measurements that was comparable to changes introduced by the added noise. For this low-severity level damage case, the SDIM failed to locate and quantify the true damage. For the other case studies, however, both the locations and severities of damages were identified with reasonable accuracy as shown in Table 9.10.

Table 9.10. Damage detection result for the plate girder case studies after discordancy test for seeded IRR GA and reduced hillclimbing, 5% measurement noise included

Damage Case	Seeded IRR GA after 200 or less GA Generations			Seeded IRR GA after Hillclimbing		
	Threshold	Location	Severity	Threshold	Location	Severity
KSTSP I	3.00%	4	9.12%	2.99%	4	9.09%
KSTSP II	3.09%	9	9.27%	3.24%	9	9.92%
KSTSP III	2.69%	14	8.12%	2.65%	14	7.99%
KSTSP IV	2.92%	19	8.79%	3.19%	19	9.58%
KSTSP V	3.30%	24	10.0%	3.30%	24	10.0%
KSTSP VI	0.39%	1, 25, 46	0.42, 0.85, 0.60%	0.36%	1, 25, 46	0.39, 0.71, 0.64%
KSTSP VII	2.35%	39	6.25%	2.35%	39	6.22%
KSTSP VIII	22.6%	39	48.9%	22.3%	39	48.6%
KSTSP IX	4.65%	9, 34	10.2, 9.83%	4.64%	9, 34	10.1, 9.82%
KSTSP X	3.66%	14, 39	5.72, 8.60%	3.93%	14, 39	7.94, 8.62%

The accuracy measures calculated for the results obtained using the seeded IRR GA in case of 5% noise in measurements are reported in Table 9.11. The average absolute *ene* of damage detection after 200 generations was 1.57%, which shows that errors in the severity estimation were small. The 1.45% *tpe* indicates that most errors occurred in the severity estimation of the true damaged elements and only a small portion of the total error occurred in non-damaged elements (average absolute *ope* = 0.34%). The linear dependence of the true and predicted damage indicator vectors was 0.9 on average,

which includes the zero *tae* value of case KSTSP VI where the true damage element was not identified. Without this false identification case the average *tae* is very close to unity. Since the severity of false predictions for case KSTSP VI were small (the largest false reading was 0.85% in Table 9.10) the *ene*, *tpe* and *ope* measures were not significantly affected by the results for this case. After hillclimbing, all measures showed improvements and the average absolute error, *ene*, was only 1.28%.

Table 9.11. Damage detection accuracy measures for seeded implicit redundant representation (IRR) GA, 5% measurement noise included

Damage Case	Seeded Implicit Redundant Representation							
	After 200 or less GA Generations				After Hillclimbing			
	ene	*tpe*	*ope*	*tae*	*ene*	*tpe*	*ope*	*tae*
KSTSP I	0.00124	0.00124	0.00000	1.00000	0.00129	0.00129	0.00000	1.00000
KSTSP II	0.00103	0.00103	0.00000	1.00000	0.00012	0.00012	0.00000	1.00000
KSTSP III	0.00266	0.00266	0.00000	1.00000	0.00284	0.00284	0.00000	1.00000
KSTSP IV	0.00171	0.00171	0.00000	1.00000	0.00059	0.00059	0.00000	1.00000
KSTSP V	0.00001	0.00001	0.00000	1.00000	0.00001	0.00001	0.00000	1.00000
KSTSP VI	0.00213	0.00141	0.00159	0.00000	0.00204	0.00141	0.00147	0.00000
KSTSP VII	0.00531	0.00531	0.00000	1.00000	0.00534	0.00534	0.00000	1.00000
KSTSP VIII	0.00149	0.00149	0.00000	1.00000	0.00200	0.00200	0.00000	1.00000
KSTSP IX	0.00032	0.00001	0.00032	0.99987	0.00030	0.00008	0.00029	0.99990
KSTSP X	0.00637	0.00568	0.00288	0.98032	0.00351	0.00344	0.00068	0.99915
Average:	0.00223	0.00206	0.00048	0.89802	0.00180	0.00171	0.00024	0.89990
Average Absolute:	1.57%	1.45%	0.34%	-	1.28%	1.21%	0.17%	-

The measures obtained for the noisy measurement cases using the seeded IRR GA are comparable with the measures obtained for damage index C method without noise (Table 9.6), and much better than those obtained for damage index A and B methods (except the *tae* measure for damage index B due to the failure in identifying the true damaged element for case study KSTSP VI). One of the current limitations of the IRR

GA SDIM is computational time. The average run for the plate girder studies took 6-7 hours.

As a conclusion to this section, the proposed accuracy measures for damage detection are summarized in Table 9.12 for the different SDIMs. In this table the average absolute values are used for comparison. For noise free measurements, it is clear that GAs combined with hillclimbing have the best performance measures. The fixed representation GA, however, is less effective in localizing and quantifying damages than the IRR GA. In this research, the seeded IRR GA SDIM was superior over any of the other SDIMs since it provides high confidence in damage detection when noise in measurements is negligible.

Table 9.12. Comparison of accuracy measures for different types of damage detection algorithms

Damage Detection Algorithm	Average Absolute Damage Detection Accuracy Measures			
	ene	*tpe*	*ope*	*tae*
Damage Index A	22.43%	9.37%	18.94%	0.64247
Damage Index B	11.14%	11.14%	0.01%	0.99965
Damage Index C	1.16%	0.99%	0.26%	0.99867
Fixed Representation GA before Hillclimbing	5.85%	5.02%	2.42%	0.80697
Fixed Representation GA after Hillclimbing	0.00%	0.00%	0.00%	1.00000
Seeded IRR GA before Hillclimbing	0.08%	0.08%	0.00%	1.00000
Seeded IRR GA after Hillclimbing	0.00%	0.00%	0.00%	1.00000
Unseeded IRR GA before Hillclimbing	0.41%	0.38%	0.00012%	0.99981
Unseeded IRR GA after Hillclimbing	0.00%	0.00%	0.00%	1.00000
Seeded IRR GA before Hillclimbing, 5% noise	1.57%	1.45%	0.34%	0.89802
Seeded IRR GA after Hillclimbing, 5% noise	1.28%	1.21%	0.17%	0.89990

Kim and Stubbs (1995) investigated the effect of uncertainties on damage detection using the damage index A method. In their study, three types of uncertainties were investigated; 1. Uncertainties of damage detection model (shear building, Bernoulli or Timoshenko elements, 3-dimensional model); 2. Uncertainty in stiffness parameters of elements; and 3. Uncertainty in mode shape measurements. Their conclusion was that the first type of error has significant influence on the severity estimation of the true damaged elements and on the number of falsely identified elements. Uncertainty in stiffness parameters had relatively small influence on damage detection. The uncertainties in mode shape measurements had the most influence on damage detection especially on identifying true damaged elements and falsely predicting undamaged elements.

Other studies found in literature have identified the current limitations of the damage index B method using experimental data and in noisy environments (Worden et al. 1999, Ho and Ewins 1999). Worden et al. (1999) classified the damage index B method as a level two SDIM, i.e. it gives the location of probable damages. The studies showed that the method could locate damages to nearest sensor, which implies that spatial distribution of sensors have significant influence on the accuracy of damage detection. The numerical studies used by Ho and Ewins (1999) lead to the conclusion that the damage index B method is sensitive to measurements noise, spatial resolution of the mode shapes, and the location of the damage. Estimates for the acceptable noise level for successful damage detection were also presented for the case studies, which limited noise to 0.15% and 0.19% for a 99% and 68% chance of successful damage location, respectively. A spatial distribution density of measurement locations was also established for the case studies. The damage index showed a large drop when 33% of all possible mode shape data were used in the identification process. This again implies that a large number of sensor locations must be available for damage detection in order to apply damage index A, B and C methods. References on the evaluation of the performance of the damage index C method were not found in the literature (Kim and Stubbs 2002).

The proposed SDIM using GAs provides an alternative to the damage index methods by requiring only a few number of measurement locations. In this study for the GAs it was assumed that measurements were taken at two out of the 50 possible sensor

locations, while the damage index procedures assumed that all 50 mode shape measurements are available. Another important observation is that statistical postprocessing of the results is not required by the present algorithm therefore providing the chance to detect damages with dissimilar severities.

10 CONCLUSIONS

This research addressed the problem of structural damage detection using the inherent information contained in vibration signatures for specific type of damages. The SDIM developed adjusts the stiffness properties of the undamaged linear discrete analytical model by minimizing the difference between the measured and analytically computed FRFs. The problem of damage detection is therefore stated as an unconstrained optimization problem using continuous variables representing the stiffness reductions of elements. A non-zero value of a damage indicator for a particular element signals the occurrence of damage and its magnitude expresses the severity of that damage.

To avoid the loss of crucial measurement information, the measured FRFs are directly used in the objective function of optimization. Reduction or expansion of discrete measurement information on a continuous domain may result in the loss of useful information or may lead to undesirable false data signaling unrealistic identification of undamaged elements. Recovery of characteristic properties of a continuous system from noisy, discrete and often limited information results in an ill-posed problem for which a unique solution often does not exist. In optimization terms, the objective has multiple local optima suggesting that traditional local search algorithms may result in solutions that are not representations of the actual damage scenario. To overcome the difficulties associated with uniqueness of solutions GAs have been chosen as the primary tool to solve the optimization problem.

In this research, two types of GAs were considered and were tested on simulated damage cases that included cantilever, two-span continuous beam and planar frame structures. The first implementation investigated uses a fixed representation in which each parameter is encoded to form a chromosome providing a complete solution to the damage detection problem. The fixed representation GA was able to evolve solutions that were representation of the true damage cases as long as the search domain was reasonably small. The use of fixed representation GA was limited by the size of the search domain and in all trials the initial population had to be seeded with a zero damage individual in

order to obtain a solution representing true damage identification. Because the fixed representation GA works with a complete solution of the optimization problem the local hillclimbing algorithm implemented improved the solution obtained by the fixed GA significantly. As the complexity of damage detection increased the fixed representation GA failed to correctly locate damaged elements due to the ill-posed nature of damage detection. The accuracy of damage detection using the fixed representation GA also degraded when noise was included in measurements.

To circumvent the difficulties associated with fixed representation GAs, an implicit redundant representation (IRR) was adapted for damage detection. Consideration of the unstructured nature of damage detection problem, i.e. the number of damaged elements, although not know, is much less than the number of finite elements in the model, makes the IRR gene encoding extremely efficient. In a typical IRR GA the number of damage indicators is not explicitly encoded in the representation but changes as the individuals converge to a steady state population. The IRR GA could determine the number of damaged elements, while minimizing the error between the measured and analytical FRF information. The adaptive characteristics of IRR GA facilitated the efficient reduction of search space without making subjective assumptions about candidate damaged elements. In a noise free environment, the solutions found were global or near-global optimum and the IRR GA was considerably less sensitive to measurement noise compared to the fixed representation GA. As consequence, on average the IRR GA converged faster than the fixed representation GA and its ability to find the true damaged elements was much more stable and unique. Even for large problems, the IRR GA was capable of identifying the true damaged elements due to encoding only a small subset of all possible finite elements. Seeding the initial population with the zero damage individual was not necessary to find the solution for IRR GA, but was advantageous in certain situations.

Objective comparison between the SDIM developed and other modal-based benchmark procedures was presented in Section 9. The proposed FRF-based SDIM performed considerably better than the damage index methods developed by Kim and Stubbs (2002) on the plate girder benchmark case study. The benefit of having a new set

of accuracy measures is that these measures account for both location and severity accuracies based on geometrical considerations. The measures objectively represent the errors of SDIMs in relation to the true damaged elements and false damage identifications. All measures are bounded between zero and unity and provide a clear quantitative and qualitative interpretation of SDIM accuracy.

The FRF-based SDIM developed in this research is distinct from other methods in several aspects. The measured FRF data is used directly in the SDIM without preprocessing the measured information. Damage can be localized and quantified using only a small subset of the possible measurement locations. Unlike other optimization techniques, the IRR GA is able to evolve solutions that adapt the unstructured nature of damage detection. The SDIM developed is robust and is able to locate and quantify multiple damages in relatively large-scale structures. Reduced sensitivity of the proposed SDIM to noise provides high confidence in damage detection for measurements containing noise at a practical level. The SDIM developed requires linear responses of structures after damage has occurred. In time critical situations the applicability of the presented SDIM is limited due to its iterative, and therefore time consuming nature.

This research presents a methodology for optimizing excitation and sensor layouts used for detecting damage in structures by applying multi-objective genetic algorithms. The contradicting objectives of sensor optimization are to reduce the number of sensors required while trying to maximize the amount and quality of information contained in the vibration signatures. The sensor layout design is formulated as a multiobjective combinatorial optimization problem. The solution to the multi objective optimization problem is a set of optimal sensor layout designs, which define tradeoffs between the two objectives. An information measure was designed particularly for the damage detection technique proposed, which quantitatively characterizes each frequency response function measurement on the basis of their sensitivities for damage detection. To solve the multiobjective optimization problem a nondominated sorting genetic algorithm was implemented and a finite element model of the structure was used. In addition, two different gene representations were investigated to determine their impact on obtaining the Pareto front. The fixed representation encoded all design variables representing a

complete solution in a string, while the IRR allowed the number of encoded design variables defining a complete solution to change during optimization. Sensor layout results provided by the fixed and IRR GAs resulted in the same prioritization of sensor locations, although the fixed representation GA converged faster and the distribution of individuals was more uniform in the Pareto front. Damage detection trials were repeated for the case study simulations to determine the effect of using the optimum sensor layout designs evolved on the performance of the damage detection method. The results showed that the quality of the measurement information increased when the optimal sensor locations were used. For all trials, the ability of the damage detection method to uniquely identify damaged elements was enhanced using the optimal sensor layout designs, even in noisy measurement environments. Significant improvement in the robustness of the damage detection method was found when the optimal sensor layout designs were used for detecting damage in larger frame structures having multiple damaged elements.

10.1 Future Recommendations

The SDIM developed in this research updates stiffness parameters of the analytical model iteratively and therefore requires a significant amount of computation time. To enhance convergence speed, alternative procedures for the calculation of FRFs could be considered. Several possibilities to reduce computation time include sub-structuring the finite element model, approximate calculation of FRFs using sensitivities, and advanced modal analysis. Parallel implementation of GAs on multiprocessor systems would also be an alternative since GAs are relatively easy to parallelize due to the use of a set of solutions. Considering advanced biological phenomena (variable population size, niching, competing populations, aging, etc.) in genetic operators could further increase convergence speed. Combination of local search techniques with GAs at various stages of the optimization may also increase convergence speed. Experimental verification of the proposed algorithms is desired in future studies.

Results obtained in Section 8.2.4 indicate that knowledge about the possible damage locations should be exploited in the information measure defined for different sensor locations. One possible improvement is to only include elements that are likely to

be damaged in the definition of the information measure. Alternatively, weights could be used to emphasize the relative importance of particular elements for damage detection. For instance, if the designer is most interested in locating damages in beams of a multi-story frame, then the information measure can be modified to only include beam elements with higher weights assigned to beam elements with lower story number. Taking into consideration the loss of sensors in the sensor optimization problem provides further improvements in selecting the optimal set of sensors. The goal in this case is to ensure that the amount of diagnostic information is sufficient for damage detection even if a certain number of sensors are lost or give false measurements, which may introduce noise bias.

This research shows that GAs, in particular IRR GAs, have the ability to adapt information from the environment to adjust system parameters. The power of GAs combined with artificial intelligence promotes the development of smart structures as outlined in Section 1.1. The application of GAs in smart structures as a damage detection tool currently may be limited due to the time intensive nature of the proposed SDIM. Their ability, however, to optimize unstructured problems makes GAs an attractive tool for optimizing the individual modules and the connections between them in smart structures. For instance, GAs can be used to optimize the number of neurons and layers in neural networks (NN) that may be the primary tool of damage detection.

The robustness and versatility of GAs promotes the development of interactive, highly-sophisticated, engineering systems capable of identifying crucial changes in the environment. In future research, the roles of GAs and their linkage with other soft computing technologies in smart structures must be defined to facilitate the development of intelligent decision-making systems. The widespread use of GAs in engineering will identify new solution techniques, alter the way in which we define the problems, and will broaden the boundaries of smart design technologies.

The objective of this research outlined in Section 1 to develop a robust and efficient SDIM that only requires minimal measurement information to precisely locate and quantify the severity of damage in structures has been met.

REFERENCES

ABAQUS/Standard user's manual - version 6.3. (2002), Electronic online documentation, Available: http://sc.tamu.edu/help/

Abdalla, M.O., Grigoriadis, K.M., and Zimmerman, D.C., (1998). "Enhanced structural damage detection using alternating projection methods." *AIAA Journal*, 36(7), 1305-1311.

Alvin, K.F., and Park, K.C., (1999). "Extraction of substructural flexibility from global frequencies and mode shapes." *AIAA Journal*, 37(11), 1444-1451.

Barnett, V., and Lewis, T., (1994). *Outlier in statistical data, 3rd edition*, New York, John Wiley and Sons.

Bates, J., and Tompkins, T., (1998). *Using visual C++ 6.* Indianapolis, IN, Que.

Béliveau, J-G., and Chater, S., (1982). "System identification of structural dynamic parameters from modal data." *Computational Methods and Experimental Measurements: Proceedings of the International Conference*, Washington, DC, New York, Springer-Verlag, 40-50.

Brown, A.S., Ankireddi, S., and Yang, H.T.Y., (1999). "Actuator and sensor placement for multiobjective control of structures." *Journal of Structural Engineering*, 125(7), 757-765.

Bruant, I., Coffignal, G., Lene, F., and Verge, M., (2001). "A methodology for determination of piezoelectric actuator and sensor location on beam structures." *Journal of Sound and Vibration*, 243(5), 861-882.

Capecchi, D., and Vestroni, F., (1999). "Monitoring of structural systems by using frequency data." *Earthquake Engineering and Structural Dynamics*, 28, 447-461.

Cawley, P., and Adams, R.D., (1979). "The location of defects in structures from measurements of natural frequencies." *Journal of Strain Analysis*, 14(2), 49-57.

Chiang, D-Y., and Lai, W-Y., (1999). "Structural damage detection using the simulated evolution method." *AIAA Journal*, 37(10), 1331-1333.

Chondros, T.G., and Dimarogonas, A.D., (1980). "Identification of cracks in welded joints of complex structures." *Journal of Sound and Vibration*, 69(4), 531-538.

Chou, J-H., and Ghaboussi, J., (2001). "Genetic algorithm in structural damage detection." *Computers and Structures*, 79(14), 1335-1353.

Cobb, R.G., and Liebst, B.S., (1997). "Sensor placement and structural damage identification from minimal sensor information." *AIAA Journal*, 35(2), 369-374.

Coello, C.A.C., (2001). "A short tutorial on evolutionary multiobjective optimization." *First International Conference on Evolutionary Multi-Criterion Optimization*, *EMO 2001*, Berlin, Springer-Verlag, 21-40.

Cook, R.D., Malkus, D.S., Plesha, M.E., and Witt, R.J., (2002). *Concepts and applications of finite element analysis*. New York, Wiley.

Deitel, H.M., and Deitel, P.J., (2001). *C++ How to program.* Upper Saddle River, NJ, Prentice Hall.

De Jong, K.A., (1975). "An analysis of the behavior of a class of genetic adaptive systems." Doctoral Dissertation, University of Michigan, *Dissertation Abstracts International*, 36(10), 5140B, (University Microfilms No. 76-9381).

Doebling, S.W., Hemez, F.M., Peterson, L.D., and Farhat, C., (1997). "Improved damage location accuracy using strain energy-based mode selection criteria." *AIAA Journal*, 35(4), 693-699.

Dunn, S.A., (1998). "The use of genetic algorithms and stochastic hill-climbing in dynamic finite element model identification." *Computers & Structures*, 66(4), 489-497.

Eshelman, L.J., Caruana, R.A., and Schaffer, J.D., (1989). "Biases in the crossover landscape." *Proceedings of the Third International Conference on Genetic Algorithms*, San Mateo, CA, Morgan Kaufmann Publishers, 10-19.

Ewins, D.J., (2000). *Modal testing: Theory, practice and applications*. Baldock, Hertfordshire, England, Research Studies Press Ltd.

Fritzen, C.-P., Jennewein, D., and Kiefer, T., (1998). "Damage detection based on model updating." *Mechanical Systems and Signal Processing*, 12(1), 163-186.

Gatti, P., and Ferrari, V., (1999). *Applied structural and mechanical vibrations*. London, E & FN Spon.

Gawronski, W., (1997). "Actuator and sensor placement for structural testing and control." *Journal of Sound and Vibration*, 208(1), 101-109.

Ghanem, R., and Shinozuka, M., and (1995). "Structural system identification I: Theory." *Journal of Engineering Mechanics*, 121(2), 264-273.

Goldberg, D.E., (1983). "Computer-aided gas pipeline operation using genetic algorithms and rule learning." Doctoral dissertation, University of Michigan, *Dissertation Abstracts International*, 44(10), 3174B. (University Microfilms No. 8402282)

Goldberg, D.E., (1989). *Genetic algorithm in search, optimization, and machine learning*. Reading, MA, Addison-Wesley Pub. Co.

Goldberg, D.E., (1991). "Do not worry, be messy." *Proceedings of the Fourth International Conference on Genetic Algorithms*, San Mateo, CA, Morgan Kaufmann Publishers, 24-30.

Hajela, P., and Soeiro, F.J., (1990). "Structural damage detection based on static and modal analysis." *AIAA Journal*, 28, 1110-1115.

Hamamoto, T., and Kondo, I., (1994). "Global and local damage detection of existing structures." *Structural Safety and Reliability: Proceedings of ICOSSAR '93*, *the 6th International Conference on Structural Safety and Reliability*, Innsbruck, Austria, 9-13 August 1993, Rotterdam, A.A. Balkema, 789-797.

Hanagan, L.M., Kulasekere, E.C., Walgama, K.S., and Premaratne. K., (2000). "Optimal placement of actuators and sensors for floor vibration control." *Journal of Structural Engineering*, 126(12), 1380-1387.

Hao, H., and Xia, Y., (2002). "Vibration-based damage detection of structures by genetic algorithm." *Journal of Computing in Civil Engineering*, 16(3), 222-229.

Hart, G.C., and Yao, J.T.P., (1977). "System identification in structural dynamics." *Journal of the Engineering Mechanics Division*, *Proceedings of the American Society of Civil Engineers*, 103(EM6), 1089-1103.

Haykin, S.S., (1999). *Neural networks: A comprehensive foundation*. Upper Saddle River, NJ, Prentice Hall.

Heylen, W., and Avitabile, P., (1998). "Correlation considerations – Part 5." *Proceedings of the 16th International Modal Analysis Conference*, February 2-5, Santa Barbara, California, Bethel, CT, Society for Experimental Mechanics, 207-214.

Ho, Y.K., and Ewins, D.J., (1999). "Numerical evaluation of the damage index." *Structural Health Monitoring 2000: Proceedings of the 2nd International Workshop on Structural Health Monitoring*, Stanford University, Stanford, CA, September 8-10, 1999, Lancaster, PA: Technomic Pub., 995-1011.

Holland, J.H., (1975). *Adaptation in natural and artificial systems*. Ann Arbor, MI, The University of Michigan Press.

Hoshiya, M., and Saito, E., (1984). "Structural identification by extended Kalman filter." *Journal of Engineering Mechanics*, 110(12), 1757-1771.

InstallShield for Microsoft Visual C++ 6 user's guide. (1997). Schaumburg, IL, InstallShield Software Corporation.

Jones, K., and Turcotte, J., (2002). "Finite element model updating using antiresonant frequencies." *Journal of Sound and Vibration*, 252(4), 717-727.

Kabe, A.M., (1985). "Stiffness matrix adjustment using mode data." *AIAA Journal*, 23(9), 1431-1436.

Kim, H.M., and Bartkowicz, T.J., (2001). "An experimental study for damage detection using a hexagonal truss." *Computers and Structures*, 79, 173-182.

Kim, J.T., and Stubbs, N., (1995). "Model-uncertainty impact and damage-detection accuracy in plate girder." *Journal of Structural Engineering*, 121, 1409-1417.

Kim, J.T., and Stubbs, N., (2002). "Improved damage detection identification method based on modal information." *Journal of Sound and Vibration*, 252(2), 223-238.

Kobayashi, T., Kan, S., Yamaya, H., and Kitamura, E., (1997). "System identification of the Hualien LSST model structure." *Earthquake Engineering and Structural Dynamics*, 26, 1157-1167.

Krawczuk, M., (2002). "Application of spectral beam finite element with a crack and iterative search technique for damage detection." *Finite Elements in Analysis and Design*, 38, 537-548.

Law, S.S., Shi, Z.Y., and Zhang, L.M., (1998). "Structural damage detection from incomplete and noisy modal test data." *Journal of Engineering Mechanics*, 124(11), 1280-1288.

Law, S.S., Chan, T.H.T., and Wu, D., (2001). "Efficient numerical model for the damage detection of large scale structure." *Engineering Structures*, 23, 436-451.

Lee, U., and Shin, J., (2002). "A frequency response function-based structural damage identification method." *Computers & Structures*, 80, 117-132.

Lieven, N.A., and Ewins, D.J., (1988). "Spatial correlation of mode shapes, the co-ordinate modal assurance criterion (COMAC)." *Proceedings of the 6th International Modal Analysis Conference*, February 1-4, Kissimmee, Florida, Bethel, CT, Society for Experimental Mechanics, 690-695.

Liu, S-C., and Yao, J.T.P., (1978). "Structural identification concept." *Journal of the Structural Division*, ASCE, 104(ST12), 1845-1858.

Lutes, L.D., and Sarkani, S., (1997). *Stochastic analysis of structural and mechanical vibrations*. Upper Saddle River, NJ, Prentice Hall.

Mares, C., and Surace, C., (1996). "An application of genetic algorithms to identify damage in elastic structures." *Journal of Sound and Vibration*, 195(2), 195-215.

Marwala, T., and Heyns, P.S., (1998). "Multiple-criterion method for determining structural damage." *AIAA Journal*, 36(8), 1494-1501.

Marwala, T., (2000). "Damage identification using committee of neural networks." *Journal of Engineering Meachanics*, 126(1), 43-50.

MATLAB user's guide. (1999a). Natick, MA, The Mathworks Inc.

MATLAB C/C++ math library 2.1 user's guide. (1999b). Natick, MA, The Mathworks Inc.

McConnell, K.G., (1995). *Vibration testing. Theory and practice*. New York, Wiley Interscience.

Michalewicz, Z., (1996). *Genetic algorithms + data structures = evolution programs*. New York, Springer-Verlag.

Michalewicz, Z., and Fogel, D.B., (2000). *How to solve it: modern heuristics*. New York, Springer-Verlag.

Moslem, K., and Nafaspour, R., (2002). "Structural damage detection by genetic algorithms." *AIAA Journal*, 40(7), 1395-1401.

Mottershead, J.E., and Friswell, M.I., (1993). "Model updating in structural dynamics: a survey." *Journal of Sound and Vibration*, 167(2), 347-375.

MSDN Library Visual Studio 6.0. (1998). Electronic resource CD-ROM 1 and 2, Redmond, WA, Microsoft Corporation.

Natke, H.G., (1988). "Updating computational models in the frequency domain based on measured data: a survey." *Probabilistic Engineering Mechanics*, 3(1), 28-34.

Padula, S.L., and Kinacid, R.K., (1999). "Optimization strategies for sensor and actuator placement." *Technical Memorandum, NASA/TM-1999-209126*, National Aeronautics and Space Administration, Langley Research Center, Hampton, VA.

Palacz, M., and Krawczuk, M., (2002). "Vibration parameters for damage detection in structures." *Journal of Sound and Vibration*, 249(5), 999-1010.

Pandey, A.K., and Biswas, M., (1994). "Damage detection in structures using changes in flexibility." *Journal of Sound and Vibration*, 169(1), 3-17.

Pareto, V., (1896). *Cours D'Economie Politique*, Volume I and II., Lausanne, Switzerland, F. Rouge,.

Park, K.C., Reich, G.W., and Alvin, K.F., (1997). "Structural damage detection using localized flexibilities." *Structural health monitoring: current status and perspectives: Proceedings of the International Workshop on Structural Health Monitoring:* Stanford University, Stanford, CA, September 18-20 1997, Lancaster, PA: Technomic Pub., 125-139.

Park, K.C., and Reich, G.W., (1999). "Model-based health monitoring of structural systems: progress, potential and challenges." *Structural Health Monitoring 2000: Proceedings of the 2nd International Workshop on Structural Health Monitoring,* Stanford University, Stanford, CA, September 8-10, 1999, Lancaster, PA: Technomic Pub., 82-95.

Pascual, R., Golinval, J.C., and Razeto, M., (1997). "A frequency domain correlation technique for model correlation and updating." *Proceedings of the 15th International Modal Analysis Conference*, February 3-6, Orlando, Florida, Bethel, CT: Society for Experimental Mechanics, 587-592.

Pothisiri, T., and Hjelmstad, K.D., (2002). "Strategy for finding a near-optimal measurement set for parameter estimation from modal response." *Journal of Sound and Vibration*, 257(1), 89-106.

Quek, S.T., Wang, W., and Koh, C.G., (1999). "Sytem identification of linear MDOF structures under ambient excitation." *Earthquake Engineering and Structural Dynamics*, 28, 61-77.

Raich, A.M., and Ghaboussi, J., (1997a). "Implicit redundant representation in genetic algorithms." *Evolutionary Computation*, 5(3), 277-302.

Raich, A.M., and Ghaboussi, J., (1997b). "Autogenesis and redundancy in genetic algorithm representation." *Proceedings of the International Conference on Artificial Neural Networks in Engineering*, ANNIE' 97, St. Louis, Missouri, 377-382.

Reich, G.W., and Park, K.C., (2000). "Use of substructural transmission zeros for structural health monitoring." *AIAA Journal*, 38(6), 1040-1046.

Reich, G.W., and Park, K.C., (2001). "A theory for strain-based structural system identification." *Journal of Applied Mechanics*, 68, 521-527.

Ren, Y., and Beards, C.F., (1995). "Identification of joint properties of a structure using FRF data." *Journal of Sound and Vibration*, 186(4), 567-587.

Reynier, M., and Kandil, H.A., (1999). "Sensors location for updating problems." *Mechanical Systems and Signal Processing*, 13(2), 297-314.

Rytter, A., (1993). "Vibration based inspection of civil engineering structures." Doctoral dissertation, Department of Building Technology and Structural Engineering, University of Aalborg, Denmark.

Sawyer, J.P., and Rao, S.S., (2000). "Structural damage detection and identification using fuzzy logic." *AIAA Journal*, 38(12), 2328-2335.

Shi, Z.Y., Law, S.S., and Zhang, L.M., (2000). "Optimum sensor placement for structural damage detection." *Journal of Engineering Mechanics*, 126(11), 1173-1179.

Shih, Y.-T., and Lee, A.C., (1998). "Sensor and actuator placement for modal identification." *Mechanical Systems and Signal Processing*, 12(5), 641-659.

Shinozuka, M., and Ghanem, R., (1995). "Structural system identification II: Experimental verification." *Journal of Engineering Mechanics*, 121(2), 265-273.

Springer, W.T., Lawrence, K.L., and Lawley, T.J., (1988). "Damage assessment based on the structural frequency-response function." *Experimental Mechanics*, 28(1), 34-37.

Srinivas, N., and Deb, K., (1994a). "Multiobjective optimization using nondominated sorting in genetic algorithms." *Evolutionary Computation*, 2(3), 221-248.

Srinivas, N., and Patnaik, L.M., (1994b). "Adaptive probabilities of crossover and mutation in genetic algorithms." *IEEE Transactions on Systems, Man, and Cybernetics*, 24(4), 17-26.

Stubbs, N., and Kim, J.T., (1996). "Damage localization in structures without baseline modal parameters." *AIAA Journal*, 34, 1644-1649.

Takewaki, I., and Nakamura, M., (2000). "Stiffness-damping simultaneous identification using limited earthquake records." *Earthquake Engineering and Structural Dynamics*, 29, 1219-1238.

Thyagarajan, S.K., Schulz, M.J., and Pai, P.F., (1998). "Detecting structural damage using frequency response functions." *Journal of Sound and Vibration*, 210(1), 162-170.

Waldron, K., Ghoshal, A., Schulz, M.J., Sundaresan, M.J., Ferguson, F., Pai, P.F., and Chung, J.H., (2002). "Damage detection using finite element and laser operational deflection shapes." *Finite Elements in Analysis and Design*, 38, 193-226.

Wang, Z., Lin, R.M., and Lim, M.K., (1997). "Structural damage detection using measured FRF data." *Computer Methods in Applied Mechanics and Engineering*, 147, 187-197.

Weaver W.Jr., and Johnston, P.R., (1984). *Finite elements for structural analysis*. Engelwood Cliffs, NJ, Prentice-Hall.

Worden, K., Manson, G., Wardle, R., Staszewski, W., and Allman, D., (1999). "Experimental validation of two structural health monitoring methods." *Structural Health Monitoring 2000: Proceedings of the 2nd International Workshop on Structural Health Monitoring*, Stanford University, Stanford, CA, September 8-10, 1999, Lancaster, PA: Technomic Pub., 784-799.

Worden, K., Manson, G., and Fieller, N.R.J., (2000). "Damage detection using outlier analysis." *Journal of Sound and Vibration*, 229(3), 647-667.

Worden, K., and Burrows, A.P., (2001). "Optimal sensor placement for fault detection." *Engineering Structures*, 23, 885-901.

Xu, Y.G., Liu, G.r., and Wu, Z.P., (2002). "Damage detection for composite plates using lamb waves and projection genetic algorithm." *AIAA Journal*, 40(9), 1860-1866.

Yun, C-B., and Bahng, E.Y., (2000). "Substructural identification using neural networks." *Computers and Structures*, 77, 41-52.

Yun, C-B., Yi, J-H., Bahng, E.Y., (2001). "Joint damage assessment of framed structures using a neural networks technique." *Engineering Structures*, 23, 425-435.

Zang, C., Grafe, H., and Imregun, M., (2001). "Frequency domain criteria for correlating and updating dynamic finite element models." *Mechanical Systems and Signal Processing*, 15(1), 139-155.

APPENDIX A

A plane frame member can deform both axially and in bending. To obtain a frame element, the assumption that the axial forces can be uncoupled from bending forces is made. After uncoupling the equilibrium equations, a bar and a beam element can be derived from the virtual work principle. Figure A.1 shows a 2-DOF plane-bar element and a 4-DOF plane-beam element.

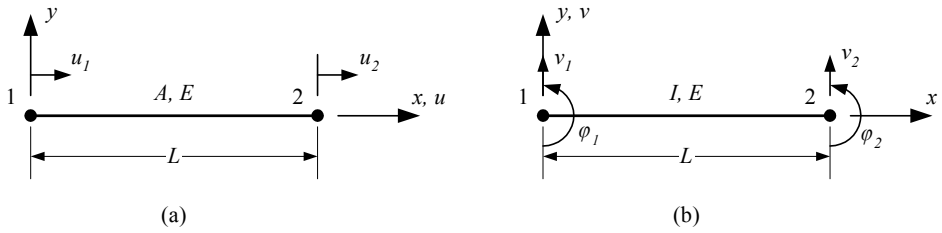

Figure A.1. One dimensional finite elements, (a) Bar element, (b) Beam element

From the constant state of strains requirement for any finite element it is established that for a bar element the interpolation functions must be at least first order polynomials. Therefore, linear interpolation functions are appropriate to approximate the displacement field for bar elements.

$$u = \mathbf{N}\begin{Bmatrix} u_1 \\ u_2 \end{Bmatrix}, \quad \text{where} \quad \mathbf{N} = \begin{bmatrix} \dfrac{L-x}{L} & \dfrac{x}{L} \end{bmatrix}$$
$$\mathbf{B} = \frac{d}{dx}\mathbf{N} = \begin{bmatrix} -\dfrac{1}{L} & \dfrac{1}{L} \end{bmatrix} \tag{A.1}$$

If the material is linear elastic, has a modulus of elasticity, E and mass density, ρ, and the cross-sectional area of the element is constant, A, along the longitudinal axis, then the integrals for the element stiffness and consistent mass matrices can be stated:

$$\mathbf{k} = \int_0^L \mathbf{B}^T AE\mathbf{B}dx = \frac{AE}{L}\begin{bmatrix} 1 & -1 \\ -1 & 1 \end{bmatrix} \tag{A.2}$$

$$\mathbf{m} = \int_0^L \mathbf{N}^T \rho A\mathbf{N}dx = \frac{\rho AL}{6}\begin{bmatrix} 2 & 1 \\ 1 & 2 \end{bmatrix} \tag{A.3}$$

For the beam element, the constant state of strain requirement imposes cubic interpolation functions for the displacement fields.

$$v = \mathbf{N}\begin{Bmatrix} v_1 \\ \varphi_1 \\ v_2 \\ \varphi_2 \end{Bmatrix} \qquad \mathbf{N} = \begin{bmatrix} 1-\dfrac{3x^2}{L^2}+\dfrac{2x^3}{L^3} & x-\dfrac{2x^2}{L}+\dfrac{x^3}{L^2} & \dfrac{3x^2}{L^2}-\dfrac{2x^3}{L^3} & -\dfrac{x^2}{L}+\dfrac{x^3}{L^2} \end{bmatrix}$$

$$\mathbf{B} = \frac{d^2}{dx^2}\mathbf{N} = \begin{bmatrix} -\dfrac{6}{L^2}+\dfrac{12x}{L^3} & -\dfrac{4}{L}+\dfrac{6x}{L^2} & \dfrac{6}{L^2}-\dfrac{12x}{L^3} & -\dfrac{2}{L}+\dfrac{6x}{L^2} \end{bmatrix} \tag{A.4}$$

Assuming a linear elastic material and constant cross-section with a second moment of inertia, I, the element stiffness and consistent mass matrices can be stated.

$$\mathbf{k} = \int_0^L \mathbf{B}^T EI\mathbf{B}dx = \frac{EI}{L^3}\begin{bmatrix} 12 & 6L & -12 & 6L \\ 6L & 4L^2 & -6L & 2L^2 \\ -12 & -6L & 12 & -6L \\ 6L & 2L^2 & -6L & 4L^2 \end{bmatrix} \tag{A.5}$$

$$\mathbf{m} = \int_0^L \mathbf{N}^T \rho A\mathbf{N}dx = \frac{\rho AL}{420}\begin{bmatrix} 156 & 22L & 54 & -13L \\ 22L & 4L^2 & 13L & -3L^2 \\ 54 & 13L & 156 & -22L \\ -13L & -3L^2 & -22L & 4L^2 \end{bmatrix} \tag{A.6}$$

A general two-dimensional, frame element is depicted in Figure A.2, with arbitrary orientation with respect to the global coordinate system. The element stiffness and consistent mass matrices are obtained by the combination of a bar and a beam element. In the development of the frame element, the effect of rotational inertia is neglected, which is a reasonable assumption for slender beams.

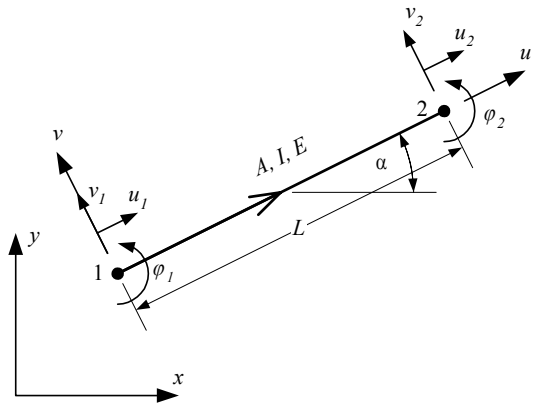

Figure A.2. Arbitrarily oriented two-dimensional frame element with 6 DOF

$$\mathbf{k} = \begin{bmatrix} X & 0 & 0 & -X & 0 & 0 \\ 0 & Y_1 & Y_2 & 0 & -Y_1 & Y_2 \\ 0 & Y_2 & Y_3 & 0 & -Y_2 & Y_4 \\ -X & 0 & 0 & X & 0 & 0 \\ 0 & -Y_1 & -Y_2 & 0 & Y_1 & Y_2 \\ 0 & Y_2 & Y_4 & 0 & -Y_2 & Y_3 \end{bmatrix}$$

$$X = \frac{AE}{L}, \quad Y_1 = \frac{12EI}{\left(1+\phi_y\right)L^3}, \quad Y_2 = \frac{6EI}{\left(1+\phi_y\right)L^2} \tag{A.7}$$

$$Y_3 = \frac{\left(4+\phi_y\right)EI}{\left(1+\varphi_y\right)L}, \quad Y_4 = \frac{\left(2-\phi_y\right)EI}{\left(1+\phi_y\right)L}, \quad \phi_y = \frac{12EIk_y}{AGL^2}$$

$$\mathbf{m} = \frac{\rho AL}{420}\begin{bmatrix} 140 & 0 & 0 & 70 & 0 & 0 \\ 0 & 156 & 22L & 0 & 54 & -13L \\ 0 & 22L & 4L^2 & 0 & 13L & -3L^2 \\ 70 & 0 & 0 & 140 & 0 & 0 \\ 0 & 54 & 13L & 0 & 156 & -22L \\ 0 & -13L & -3L^2 & 0 & -22L & 4L^2 \end{bmatrix} \tag{A.8}$$

The stiffness matrix appearing in Eq. (A.7) is a modified version of the original Bernoulli beam element stiffness matrix, which accounts for transverse shear deformation. For slender beams, the value of ϕy approaches zero resulting in the engineering beam theory. Since the distribution of shear stresses across the cross section is not uniform, a so-called shear factor ky also appears in the expression. For a rectangular cross section the parabolic variation of shear stresses gives a ky of 1.2. For other cross sections, the shear factor changes, although it is usually between 1.2 for rectangular cross section and 2.0 for I shapes.

In Eqs. (A.7) and (A.8), the element stiffness and consistent mass matrices are formulated in the local coordinate system of the element (u, v) as shown in Figure A.2. The relationship between the global and local coordinate axes is established by the introduction of the rotation matrix Tr.

$$\begin{Bmatrix} x \\ y \\ \varphi \end{Bmatrix} = \mathbf{T}_r \begin{Bmatrix} u \\ v \\ \varphi \end{Bmatrix} = \begin{bmatrix} \cos\alpha & -\sin\alpha & 0 \\ \sin\alpha & \cos\alpha & 0 \\ 0 & 0 & 1 \end{bmatrix} \begin{Bmatrix} u \\ v \\ \varphi \end{Bmatrix} \tag{A.9}$$

The element rotation matrix $\mathbf{T}_r^e$ for a 2-node element can be constructed from the rotation matrix of the global and local coordinate axes. The element stiffness and consistent mass matrices in the global coordinate system are obtained from Eq. (A.10).

$$\mathbf{T}_r^e = \begin{bmatrix} \mathbf{T}_r & 0 \\ 0 & \mathbf{T}_r \end{bmatrix}, \quad \mathbf{k}^g = \mathbf{T}_r^{eT}\mathbf{k}\mathbf{T}_r^e, \quad \mathbf{m}^g = \mathbf{T}_r^{eT}\mathbf{m}\mathbf{T}_r^e \tag{A.10}$$

APPENDIX B

Table B.1. Cards that can be used in the text input file (*.inp) for the *ModalFEM* utility program

Card	Usage	Explanation
*Node	*NODE Node #, X-coor, Y-coor	Defines finite element nodes. The first input is the node number followed by the x and y coordinates of the node. The iput line can be repeated as many as necessary to define all nodes in the model.
*Element	*ELEMENT, TYPE = B23 Elem. #, 1st node #, 2nd node #	Defines finite elements. The "TYPE =" option determines the finite element type (B23 = Bernoulli frame element). The input parameters are the element number followed by the first and second node numbers enclosing that element.
*Material	*MATERIAL, NAME = STEEL	Defines a material. The option "NAME =" is used to uniquely identify this material definition. This card does not have any input parameters but it is followed by other cards defining the material behavior.
*Elastic	*ELASTIC Young's Modulus, Poisson's ratio	Preceded by the "*Material" card and defines a linear elastic material. Input parameters are the Young's modulus and Poisson's ratio.
*Density	*Density ρ	Preceded by the "*Material" card and defines the mass density of the material. The only input parameter is the mass density ρ.
*Elset	*ELSET, ELSET = NAME Elem. #, Elem. #, Elem. # *ELSET, ELSET = A, GENERATE 1st Elem. #, Last Elem. #, Increment	Groups selected elements that share some common characteristics. The "ELSET =" option is used to uniquely identify this group of elements. Input parameters are the element numbers. Using "GENERATE" option, element numbers are generated between the first and last element with increment given in the input line.
*Beam General Section	*BEAM GENERAL SECTION, ELSET = ELS_NAME, MATERIAL = MAT_NAME Moment of Inertia, Area	Sectional properties of frame finite element. The option "ELSET =" identifies the element set for which these properties are applied. The option "MATERIAL =" identifies the material used for these set of elements. The input line contains the moment of inertia and the area of the frame element.
*Nset	*NSET, NSET = NAME Node #, Node #, Node #	Defines a set of nodes that share some common characteristics. The input line contains the node numbers in this set and can be repeated as many times as necessary to list all nodes.
*Boundary	*BOUNDARY Nset, DOF	Defines the boundary conditions. The first input identifies the set of nodes for which this boundary condition is applied. The second input parameter identifies the degree of freedom in the local coordinate system that is restrained (1 – horizontal, 2 – vertical, 3 – rotational)
*Step	*STEP	Identifies the beginning of a finite element step
*End Step	*END STEP	Identifies the end of a finite element step
*Frequency	*FREQUENCY Number of modes	Performs mode shape and eigenvalue extraction. The input parameter identifies the number of modes to be extracted.

Table B.1. (Continued)

Card	Usage	Explanation
*Node Print	*NODE PRINT Output *NODE PRINT, NSET = NAME Output	Output request associated with nodal finite element results. If the option "NSET =" is omitted then information for all nodes are output. Using "NSET =" a subset of nodes can be defined. The input line can be U (natural frequencies and mode shapes) provided that the *FREQUENCY card is used in the current step. In a *MODAL DYNAMIC step the input line can be U (displacement), V (velocity), A (acceleration), FRFI1, FRFI2, FRFI3 (accelerance in 1, 2 or 3 DOF).
*Modal Dynamic	*MODAL DYNAMIC Δt, T_{total}	Defines a response analysis or a frequency response function calculation analysis using modal decomposition. The input line contains the time interval Δt and the total time for the analysis. For the frequency response function analysis the time data are converted into the frequency domain.
*Modal Damping	*MODAL DAMPING Start mode, Last mode, damping	Defines the modal damping ratio for different modes. The first input parameter identifies the starting mode, the second input parameter the end mode and the third input parameter the damping ratio for each mode between the starting and ending modes.
*Base Motion	*BASE MOTION, DOF = #, INPUT = file.ext, SCALE = #	Defines a base motion within a step. The option "DOF =" identifies the degree of freedom for which the base motion is defined. The option "INPUT =" identifies the input file containing acceleration information of the base motion. The option "SCALE =" multiplies (scales) the input data with the provided scale number.
*Cload	*CLOAD, INPUT = file.txt Nset, DOF, scale	Defines a load applied at a node or nodes. The option "INPUT =" identifies the input file containing load data. This parameter is omitted for frequency response function calculations. The first parameter in the input line identifies the node set for which this load is applied. The second parameter identifies the degree of freedom in which the load acts. The third parameter scales the input data (omitted for FRF calculations).
*Noise	*NOISE level, # of measurements	Introduces noise into simulated measurement (frequency response function) data. The first parameter defines the noise level and the second parameter identifies the number of simulated measurements. If the second parameter is more than 1 then the average of the generated frequency response functions are taken.

```
*NODE
1,  0.,   0.
2,  30.,  0.
3,  60.,  0.
4,  90.,  0.
5,  120., 0.
6,  150., 0.
7,  180., 0.
8,  210., 0.
9,  240., 0.
10, 270., 0.
11, 300., 0.
*ELEMENT,TYPE=B23
1, 1, 2
2, 2, 3
3, 3, 4
4, 4, 5
5, 5, 6
6, 6, 7
7, 7, 8
8, 8, 9
9, 9, 10
10, 10, 11
*MATERIAL,NAME=STEEL
*ELASTIC
30.E6, 0.3
*DENSITY
0.000728
*ELSET, ELSET=EALL, GENERATE
1, 10, 1
*BEAM GENERAL SECTION,ELSET=EALL,MATERIAL=STEEL
19.1, 533.0
*NSET,NSET=FIXED
1
*BOUNDARY
FIXED, 1
FIXED, 2
FIXED, 3
*NSET,NSET=MEAS
11
*NSET,NSET=EXC
11
*STEP
*FREQUENCY
12
*NODE PRINT
U
*END STEP
*STEP
*MODAL DYNAMIC
0.001, 0.4
*MODAL DAMPING
1, 3, 0.02
4, 6, 0.035
7, 10, 0.05
*CLOAD, INPUT=dummy.txt
EXC, 2, 100.0
*NOISE
0.0, 0
*NODE PRINT, NSET=MEAS
FRFI2
*END STEP
```

Figure B.1. Sample input file of a cantilever beam for the *ModalFEM* utility program

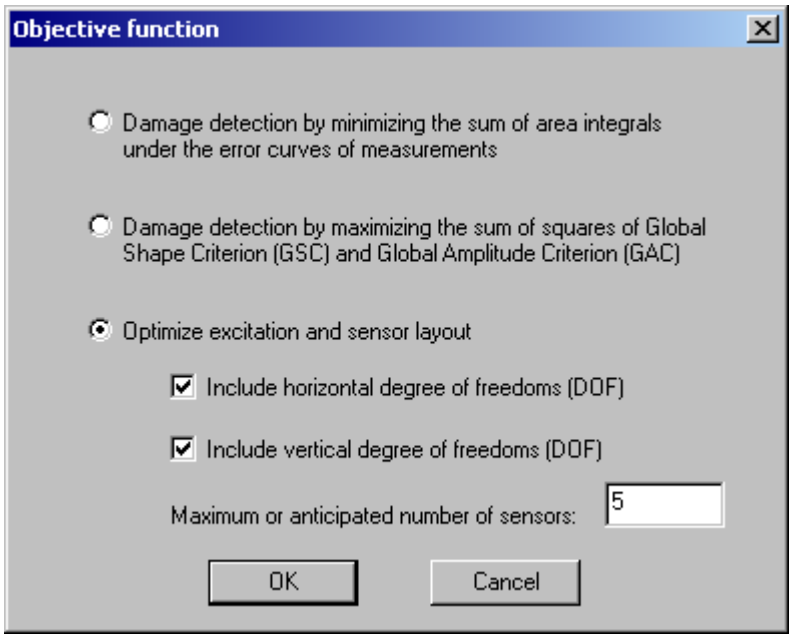

Figure B.2. Objective function dialog box

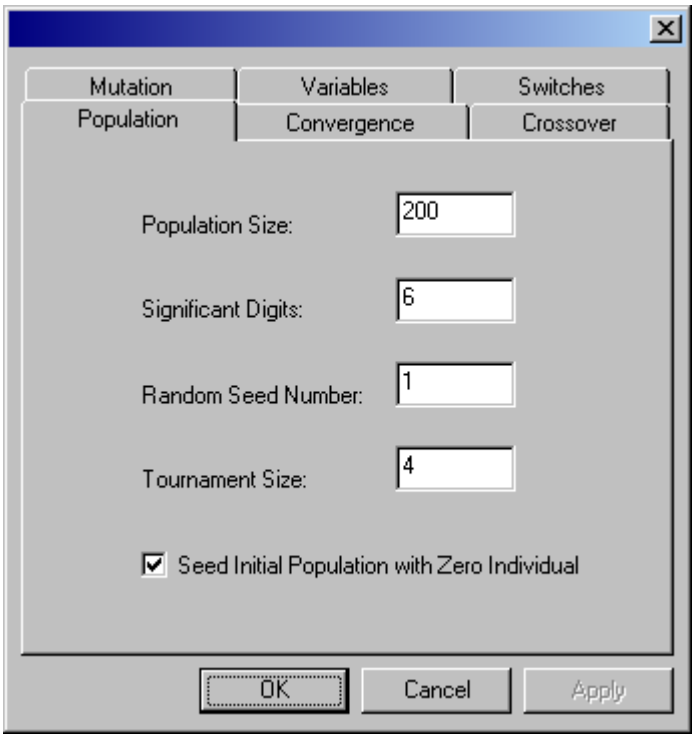

Figure B.3. Genetic algorithm property sheet in *GaDamDet* program

Figure B.4. Additional property pages on the genetic algorithm property sheet

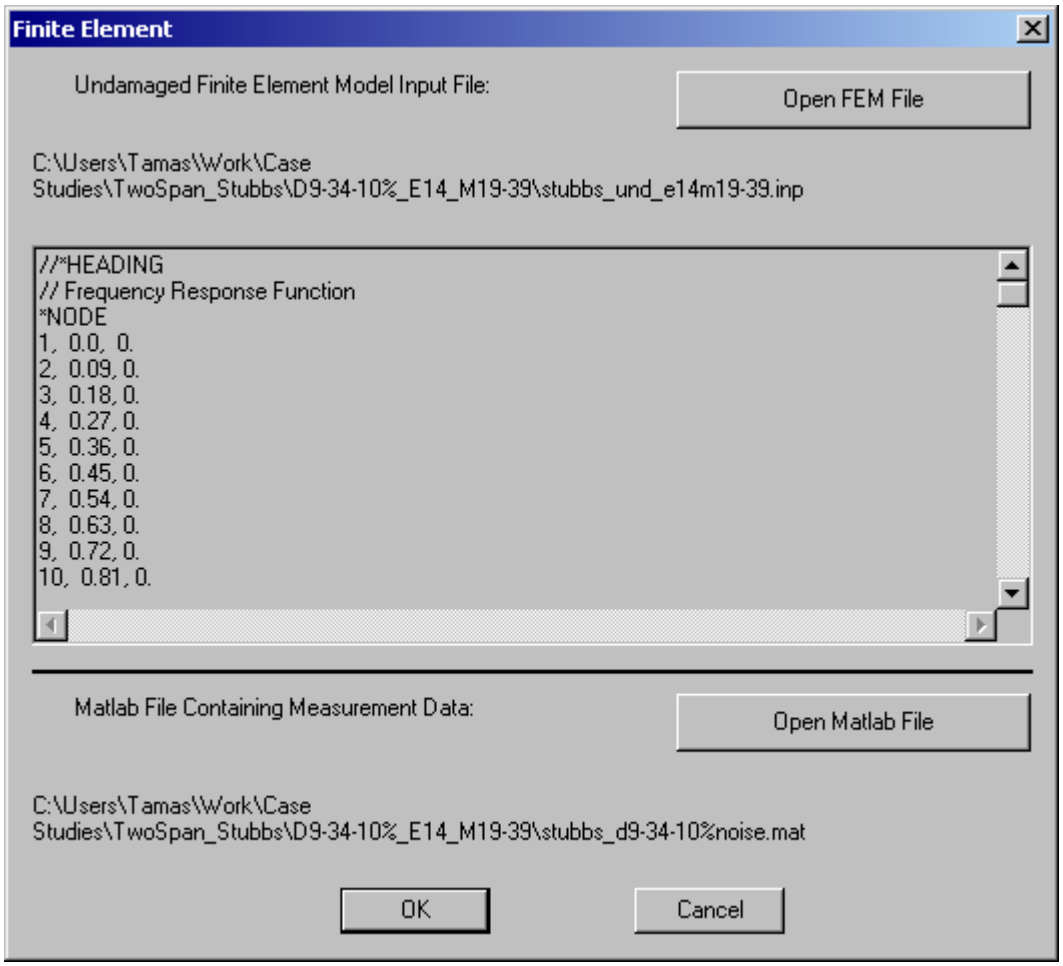

Figure B.5. Finite element input and MATLAB measurement data file dialog

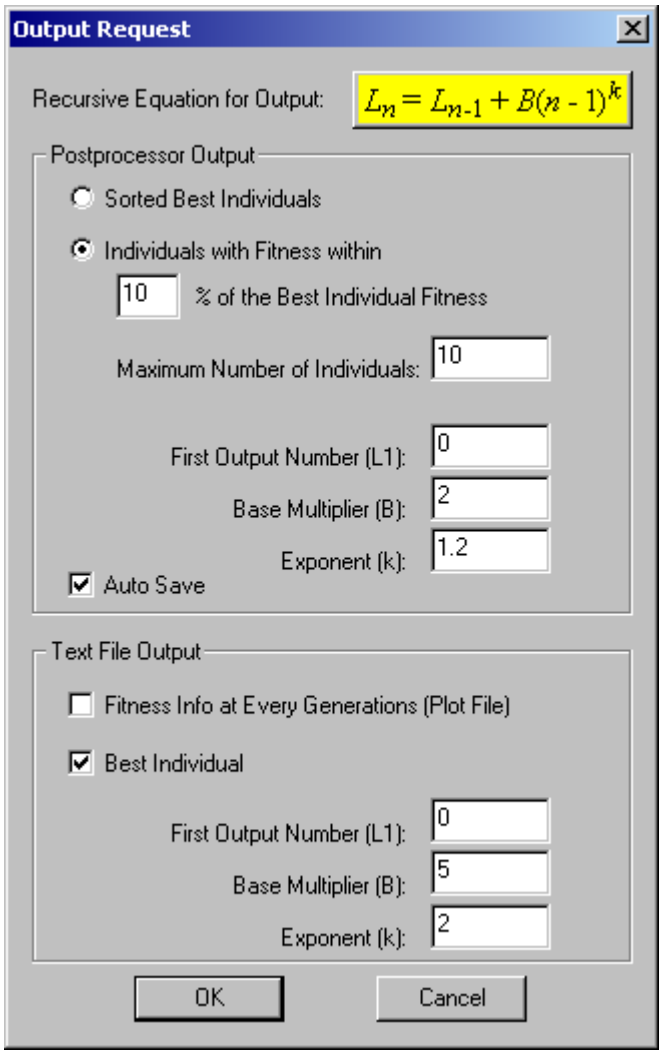

Figure B.6. Preprocessor dialog box for output request control

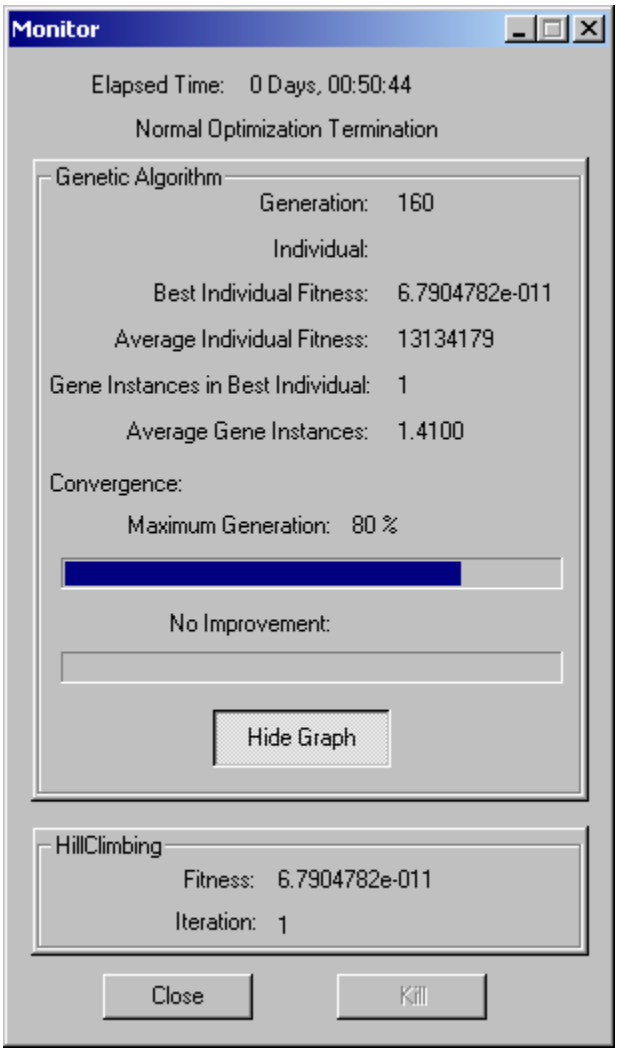

Figure B.7. Dialog to monitor progress of the GA and hillclimber at run-time

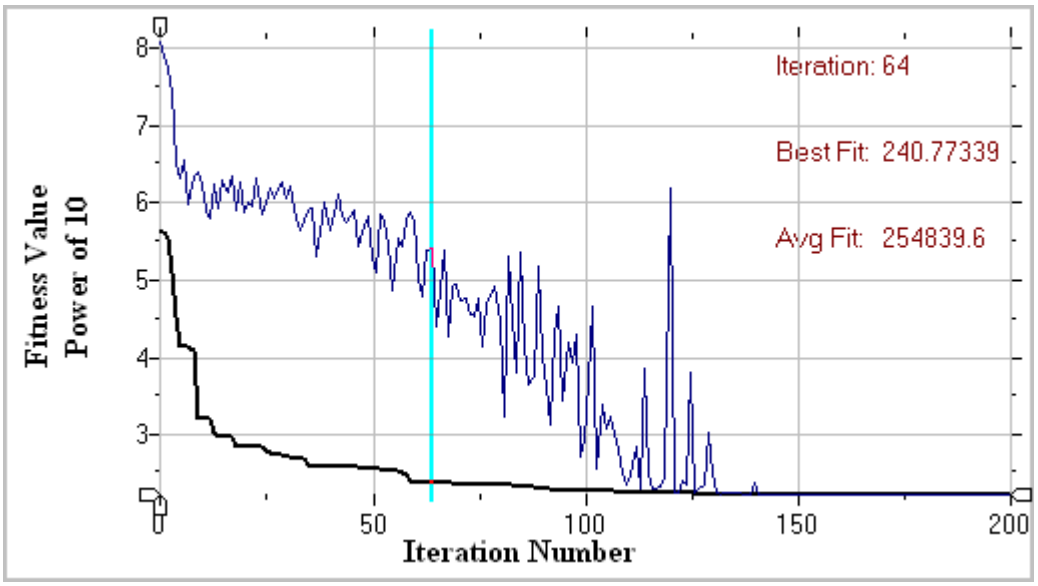

Figure B.8. Monitor graph of a fixed GA run

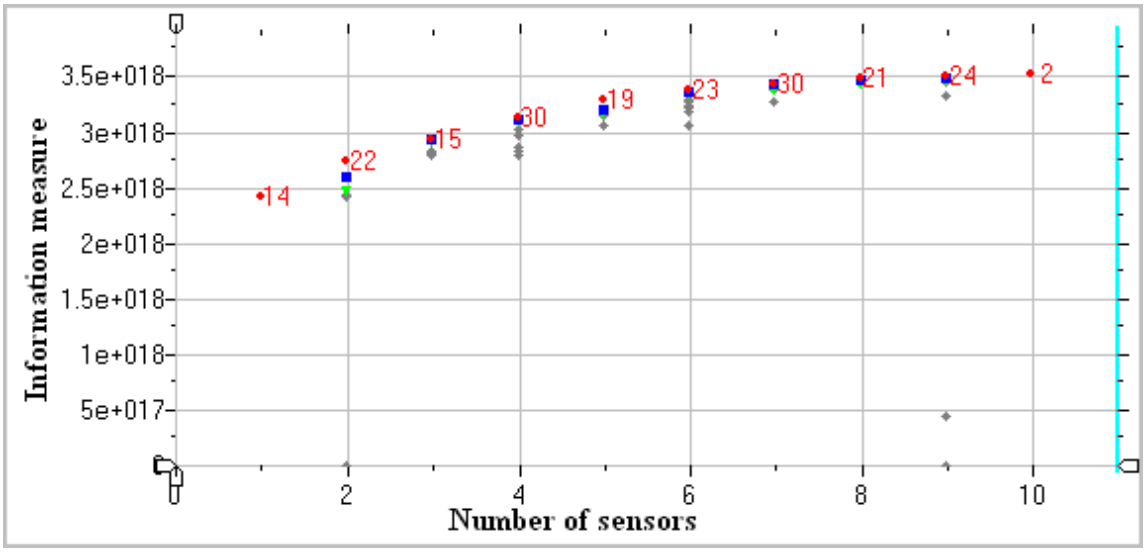

Figure B.9. Monitor graph of an excitation/sensor layout design problem

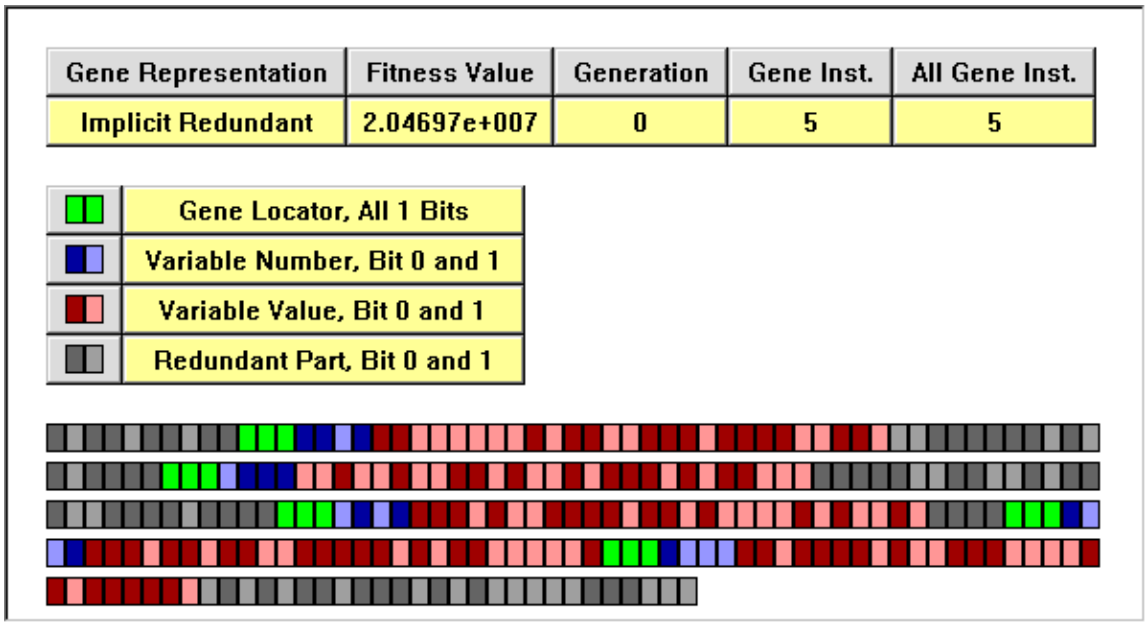

Figure B.10. Individual plot of an IRR string

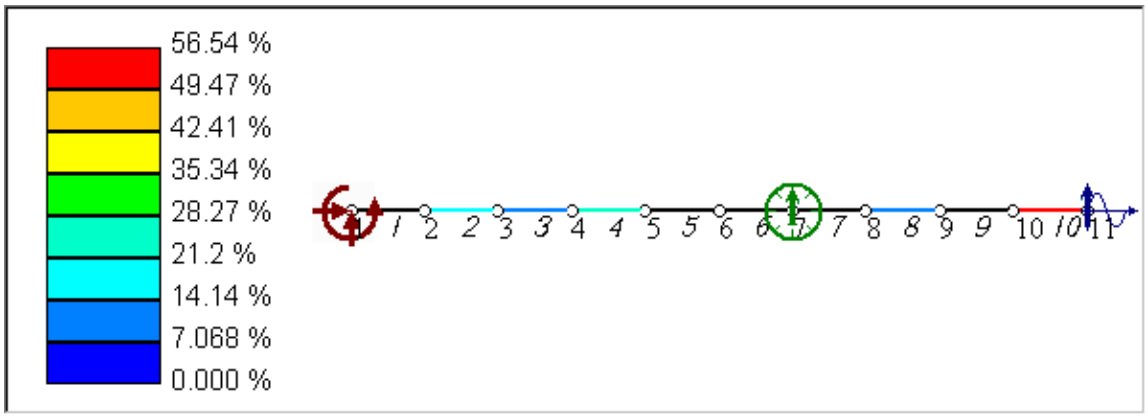

Figure B.11. Structure plot of a cantilever beam

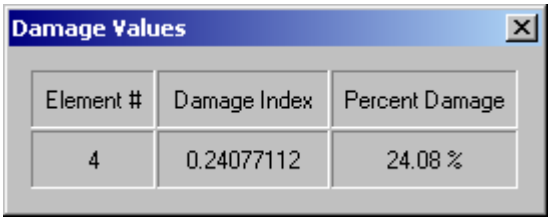

Figure B.12. Damage indicator dialog

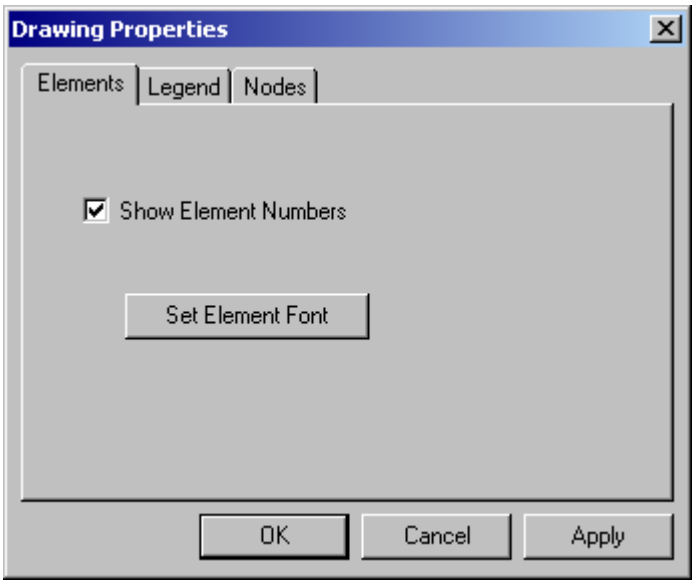

Figure B.13. Drawing properties property sheet and property page to set element display configuration

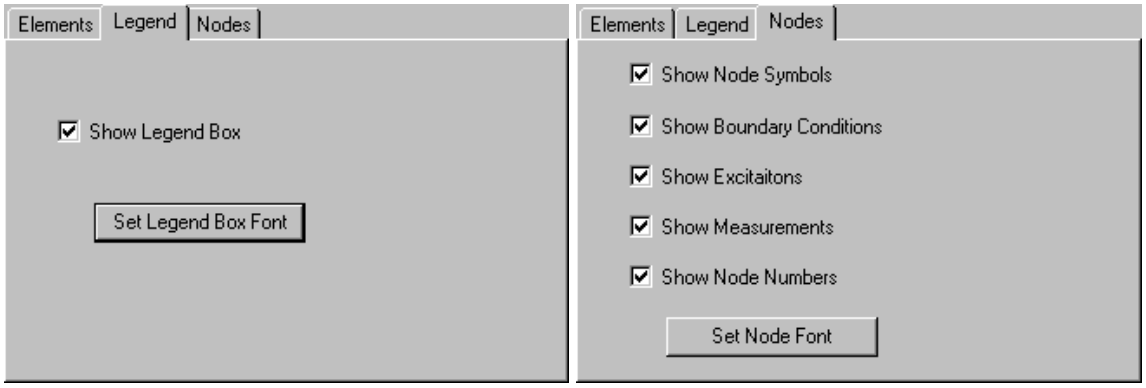

Figure B.14. Property pages for legend and finite element nodes display settings

APPENDIX

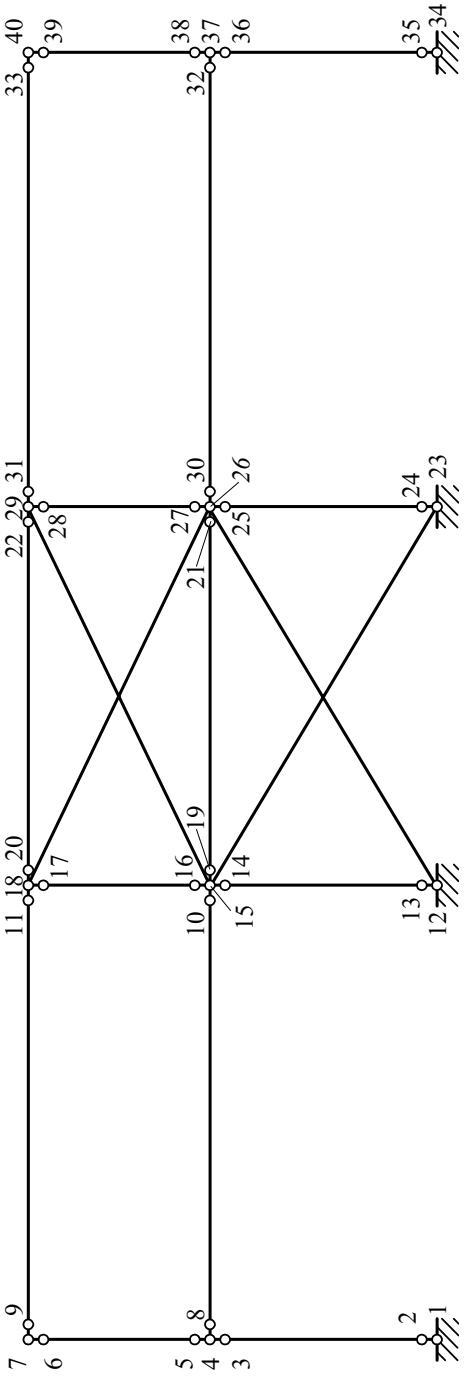

Figure C.1. Finite element mesh and node numbering for braced two-story three bay moment frame

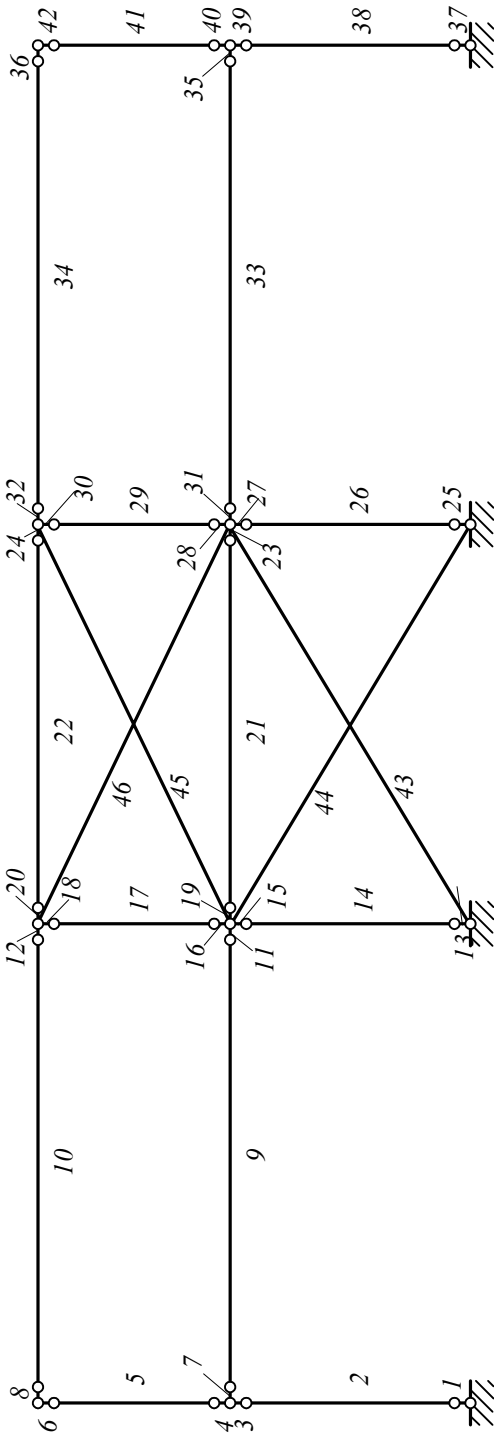

Figure C.2. Finite element mesh and element numbering for braced two-story three bay moment frame

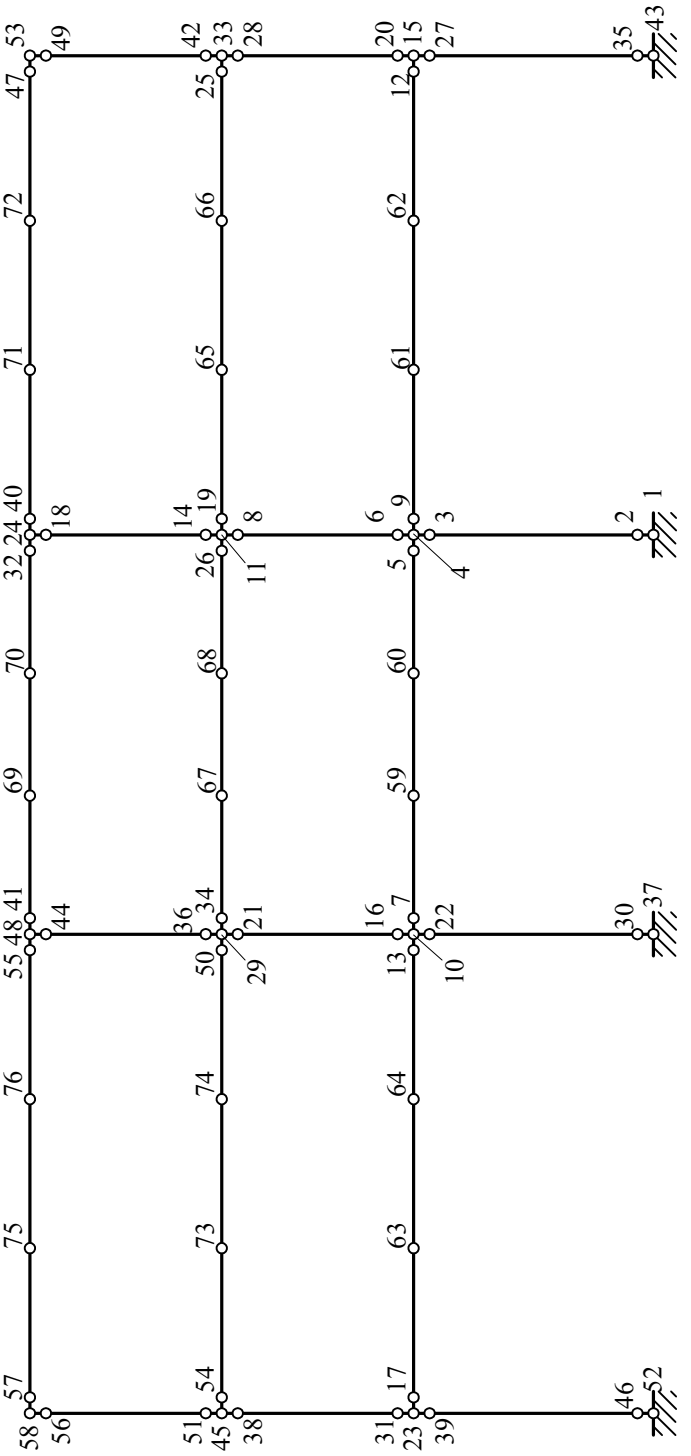

Figure C.3. Finite element mesh and node numbering for unbraced three-story three-bay moment frame

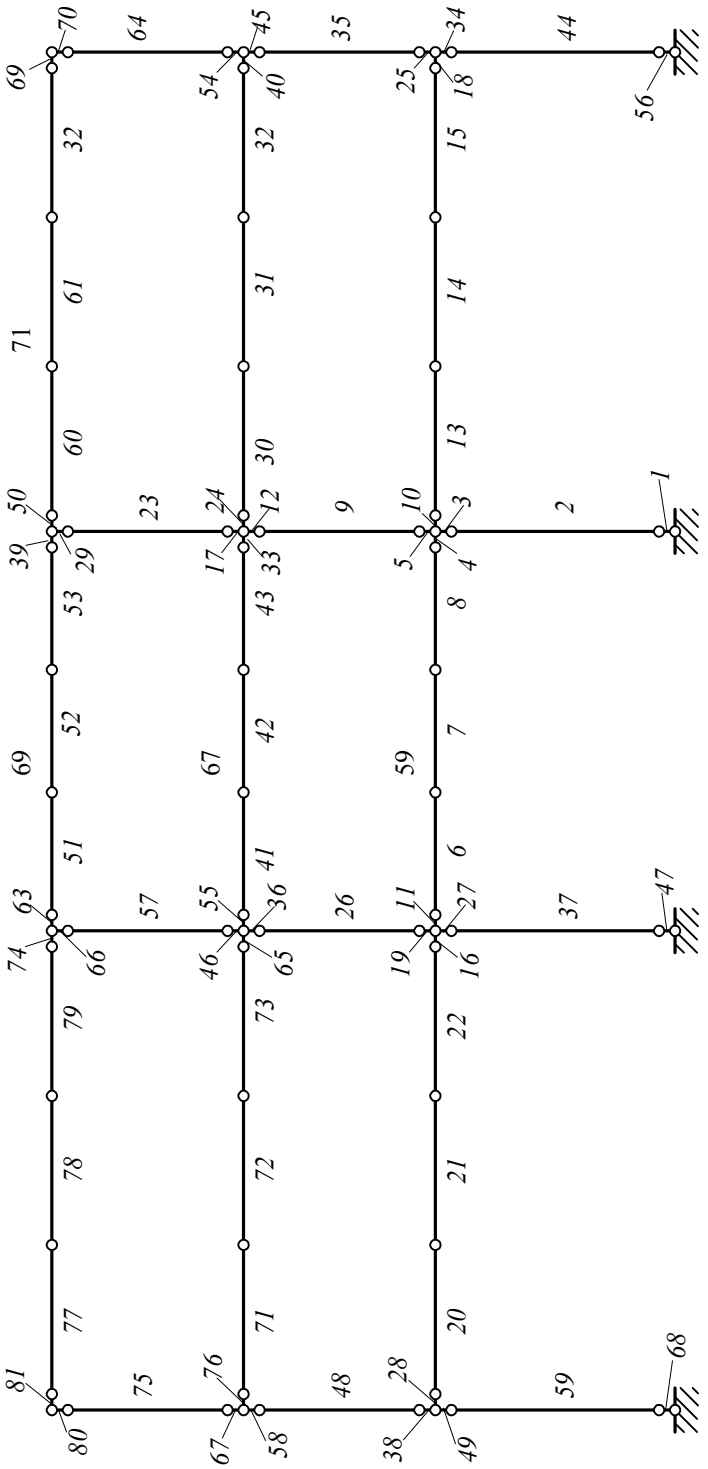

Figure C.4. Finite element mesh and element numbering for unbraced three-story three-bay moment frame

APPENDIX D

Table D.1. Damage detection results for case CANT I, fixed representation, seeded initial population, noise levels of 0, 5 and 10%

Element	Fixed Representation, Seeded Initial Population					
	Damage Indicator, 0% noise		Damage Indicator, 5% noise		Damage Indicator, 10% noise	
	200 GA Generations	1492 Hillclimbing Iterations	200 GA Generations	522 Hillclimbing Iterations	200 GA Generations	466 Hillclimbing Iterations
1	0.00001%	0.00000%	0.00005%	0.00000%	0.00014%	0.00000%
2	9.46989%	9.99997%	7.63769%	9.24123%	6.96041%	8.46504%
3	0.02455%	0.00000%	0.00000%	0.00000%	0.00009%	0.00000%
4	0.31257%	0.00000%	0.14112%	0.27812%	0.19965%	0.56216%
5	0.03763%	0.00001%	0.38844%	0.00000%	0.00000%	0.00000%
6	0.00682%	0.00000%	0.00081%	0.05283%	0.58128%	0.10285%
7	0.00009%	0.00000%	0.00009%	0.00000%	0.00000%	0.00000%
9	0.12951%	0.00002%	1.45024%	0.34569%	1.78881%	0.69349%
10	0.20794%	0.00000%	0.00009%	0.00000%	0.00000%	0.00000%

Table D.2. Damage detection results for case CANT I, fixed representation, seeded initial population, noise levels of 20 and 50%

Element	Fixed Representation, Seeded Initial Population			
	Damage Indicator 20% noise		Damage Indicator 50% noise	
	200 GA Generations	970 Hillclimbing Iterations	200 GA Generations	1194 Hillclimbing Iterations
1	0.00000%	0.00000%	0.00009%	0.00000%
2	6.96085%	7.84201%	3.45751%	3.98700%
3	0.00000%	0.00000%	0.00019%	0.00000%
4	1.12390%	0.81451%	3.22744%	2.23694%
6	0.11226%	0.00000%	1.54729%	0.00000%
8	0.14190%	0.44460%	0.65491%	1.02702%
9	1.31235%	0.85530%	1.50497%	2.34162%
10	0.00000%	0.00000%	0.00042%	0.00000%

Table D.3. Damage detection results for case CANT I, implicit redundant representation (IRR), seeded initial population, noise levels of 0, 5 and 10%

Element	IRR, Seeded Initial Population					
	Damage Indicator 0% noise		Damage Indicator 5% noise		Damage Indicator 10% noise	
	200 GA Generations	1233 Hillclimbing Iterations	200 GA Generations	1130 Hillclimbing Iterations	200 GA Generations	181 Hillclimbing Iterations
2	9.99907%	9.99993%	9.65594%	9.49064%	9.54556%	9.51973%
4	0.00074%	0.00006%	0.13786%	0.19211%	0.26858%	0.30362%
5	0.00045%	0.00004%	0.00000%	0.00000%	0.00000%	0.00000%
8	0.00000%	0.00000%	0.17231%	0.11397%	0.41130%	0.39419%
9	0.00000%	0.00000%	0.09862%	0.20390%	0.00000%	0.00000%

Table D.4. Damage detection results for case CANT I, implicit redundant representation (IRR), seeded initial population, noise levels of 20 and 50%

Element	IRR, Seeded Initial Population			
	Damage Indicator 20% noise		Damage Indicator 50% noise	
	200 GA Generations	193 Hillclimbing Iterations	200 GA Generations	1146 Hillclimbing Iterations
2	9.05524%	9.01000%	4.38611%	3.98869%
4	0.57470%	0.63063%	2.08773%	2.23636%
8	0.82232%	0.79622%	1.16577%	1.02758%
9	0.00000%	0.00000%	2.13629%	2.34069%

Table D.5. Damage detection results for case CANT I, implicit redundant representation (IRR), unseeded initial population, noise levels of 0, 5 and 10%

Element	IRR, Unseeded Initial Population					
	Damage Indicator 0% noise		Damage Indicator 5% noise		Damage Indicator 10% noise	
	130 GA Generations	0 Hillclimbing Iterations	200 GA Generations	199 Hillclimbing Iterations	200 GA Generations	583 Hillclimbing Iterations
2	10.00000%	-	9.72164%	9.76354%	9.02287%	9.39894%
4	0.00000%	-	0.19184%	0.14888%	0.00000%	0.00000%
8	0.00000%	-	0.18339%	0.19603%	0.39144%	0.45845%
9	0.00000%	-	0.00000%	0.00000%	0.57560%	0.27398%

Table D.6. Damage detection results for case CANT I, implicit redundant representation (IRR), unseeded initial population, noise levels of 20 and 50%

Element	IRR, Unseeded Initial Population			
	Damage Indicator 20% noise		Damage Indicator 50% noise	
	200 GA Generations	228 Hillclimbing Iterations	200 GA Generations	156 Hillclimbing Iterations
2	9.25336%	9.01001%	7.33490%	7.32853%
4	0.27789%	0.63062%	1.71190%	1.72483%
8	0.98131%	0.79622%	2.03632%	2.03191%

Table D.7. Damage detection results for case CANT I, fixed representation, seeded initial population, objective function is the sum of GSC and GAC squares, noise levels of 0, 5 and 10%

Element	Fixed Representation Seeded Initial Population					
	Damage Indicator 0% noise		Damage Indicator 5% noise		Damage Indicator 10% noise	
	200 GA Generations	145 Hillclimbing Iterations	200 GA Generations	313 Hillclimbing Iterations	200 GA Generations	213 Hillclimbing Iterations
1	0.00000%	0.00000%	0.00153%	0.00000%	0.00000%	0.00000%
2	9.87712%	9.99998%	8.48057%	8.66573%	7.20235%	7.44847%
3	0.00003%	0.00000%	0.19412%	0.00000%	0.05152%	0.00000%
4	0.00164%	0.00000%	0.09728%	0.08292%	0.27197%	0.23736%
5	0.09669%	0.00001%	0.01874%	0.07984%	0.00015%	0.00000%
6	0.00095%	0.00000%	1.20898%	1.03130%	2.41714%	2.22387%
7	0.00604%	0.00000%	0.00000%	0.00000%	0.00000%	0.00000%
8	0.00116%	0.00000%	0.82021%	1.04380%	2.07844%	2.22831%
9	0.02592%	0.00000%	0.38899%	0.27622%	0.41165%	0.26918%
10	0.01218%	0.00000%	0.00000%	0.00000%	0.00076%	0.00000%

Table D.8. Damage detection results for case CANT I, fixed representation, seeded initial population, objective function is the sum of GSC and GAC squares, noise levels of 20 and 50%

Element	Fixed Representation Seeded Initial Population			
	Damage Indicator 20% noise		Damage Indicator 50% noise	
	200 GA Generations	159 Hillclimbing Iterations	200 GA Generations	61 Hillclimbing Iterations
2	4.47063%	4.54827%	0.00000%	0.00000%
4	0.77549%	0.74391%	0.00000%	0.00000%
6	4.85824%	4.77670%	5.60742%	5.48590%
8	4.63897%	4.68195%	12.22920%	12.32950%

Table D.9. Damage detection results for case CANT I, implicit redundant representation (IRR), seeded initial population, objective function is the sum of GSC and GAC squares, noise levels of 0, 5 and 10%

Element	IRR, Seeded Initial Population					
	Damage Indicator 0% noise		Damage Indicator 5% noise		Damage Indicator 10% noise	
	115 GA Generations	0 Hillclimbing Iterations	200 GA Generations	79 Hillclimbing Iterations	200 GA Generations	122 Hillclimbing Iterations
2	9.99998%	-	8.88843%	8.87897%	7.59546%	7.58479%
5	0.00001%	-	0.00000%	0.00000%	0.00000%	0.00000%
6	0.00000%	-	1.06034%	1.07454%	2.18710%	2.19911%
8	0.00000%	-	1.20567%	1.19902%	2.33847%	2.32807%
9	0.00000%	-	0.00000%	0.00000%	0.27747%	0.28495%

Table D.10. Damage detection results for case CANT I, implicit redundant representation (IRR), seeded initial population, objective function is the sum of GSC and GAC squares, noise levels of 20 and 50%

Element	IRR, Seeded Initial Population			
	Damage Indicator 20% noise		Damage Indicator 50% noise	
	200 GA Generations	95 Hillclimbing Iterations	100 GA Generations	0 Hillclimbing Iterations
2	4.55385%	4.54833%	0.00000%	-
4	0.74182%	0.74388%	0.00000%	-
6	4.76893%	4.77661%	5.48587%	-
8	4.68574%	4.68200%	12.32960%	-

Table D.11. Damage detection results for case CANT I, implicit redundant representation (IRR), unseeded initial population, objective function is the sum of GSC and GAC squares, noise levels of 0, 5 and 10%

Element	IRR, Unseeded Initial Population					
	Damage Indicator 0% noise		Damage Indicator 5% noise		Damage Indicator 10% noise	
	170 GA Generations	0 Hillclimbing Iterations	200 GA Generations	108 Hillclimbing Iterations	200 GA Generations	108 Hillclimbing Iterations
2	10.00000%	-	8.78771%	8.78275%	7.59490%	7.58477%
6	0.00000%	-	1.04798%	1.05489%	2.18922%	2.19912%
8	0.00000%	-	1.10679%	1.10064%	2.32900%	2.32808%
9	0.00000%	-	0.24410%	0.24747%	0.28046%	0.28495%

Table D.12. Damage detection results for case CANT I, implicit redundant representation (IRR), unseeded initial population, objective function is the sum of GSC and GAC squares, noise levels of 20 and 50%

Element	IRR, Unseeded Initial Population			
	Damage Indicator 20% noise		Damage Indicator 50% noise	
	200 GA Generations	89 Hillclimbing Iterations	130 GA Generations	0 Hillclimbing Iterations
2	5.04175%	5.02909%	0.00000%	-
6	4.66383%	4.67692%	5.48589%	-
8	5.01702%	5.01090%	12.32950%	-

Table D.13. Damage detection results for case CANT II, fixed and implicit redundant representations (IRR), noise free measurements

Element	Damage Indicator, 0% noise					
	Fixed Representation, Seeded Initial Population		IRR, Seeded Initial Population		IRR, Unseeded Initial Population	
	200 GA Generations	1502 Hillclimbing Iterations	200 GA Generations	306 Hillclimbing Iterations	130 GA Generations	0 Hillclimbing Iterations
2	9.46167%	9.99997%	9.99960%	10.00000%	10.00000%	-
3	0.01854%	0.00000%	0.00000%	0.00000%	0.00000%	-
4	0.31496%	0.00000%	0.00000%	0.00000%	0.00000%	-
5	0.05051%	0.00001%	0.00000%	0.00000%	0.00000%	-
6	0.00670%	0.00000%	0.00040%	0.00000%	0.00000%	-
8	0.00005%	0.00000%	0.00000%	0.00000%	0.00000%	-
9	0.13331%	0.00002%	0.00000%	0.00000%	0.00000%	-
10	0.20785%	0.00000%	0.00074%	0.00001%	0.00000%	-

Table D.14. Damage detection results for case CANT III, fixed and implicit redundant representations (IRR), noise free measurements

Element	Damage Indicator, 0% noise					
	Fixed Representation Seeded Initial Population		IRR, Seeded Initial Population		IRR, Unseeded Initial Population	
	200 GA Generations	2459 Hillclimbing Iterations	129 GA Generations	0 Hillclimbing Iterations	200 GA Generations	1145 Hillclimbing Iterations
1	0.25380%	0.00000%	0.00000%	-	0.00000%	0.00000%
2	0.00256%	0.00000%	0.00000%	-	0.00000%	0.00000%
3	0.02340%	0.00000%	0.00000%	-	0.10732%	0.00001%
4	0.72149%	0.00003%	0.00000%	-	0.09482%	0.00000%
5	0.00203%	0.00000%	0.00000%	-	0.00000%	0.00000%

Table D.14. (Continued)

Element	Damage Indicator, 0% noise					
	Fixed Representation Seeded Initial Population		IRR, Seeded Initial Population		IRR, Unseeded Initial Population	
	200 GA Generations	2459 Hillclimbing Iterations	129 GA Generations	0 Hillclimbing Iterations	200 GA Generations	1145 Hillclimbing Iterations
6	9.06363%	9.99998%	10.00000%	-	9.85362%	9.99999%
7	0.58333%	0.00002%	0.00000%	-	0.19715%	0.00001%
8	0.18839%	0.00000%	0.00000%	-	0.00000%	0.00000%
9	0.28378%	0.00001%	0.00000%	-	0.00000%	0.00000%
10	0.40565%	0.00000%	0.00000%	-	0.00000%	0.00000%

Table D.15. Damage detection results for case CANT IV, fixed and implicit redundant representations (IRR), noise free measurements

Element	Damage Indicator 0% noise					
	Fixed Representation Seeded Initial Population		IRR, Seeded Initial Population		IRR, Unseeded Initial Population	
	200 GA Generations	23700 Hillclimbing Iterations	200 GA Generations	20000 Hillclimbing Iterations	200 GA Generations	3566 Hillclimbing Iterations
1	0.02588%	0.00000%	0.00000%	0.00000%	0.00000%	0.00000%
2	0.01208%	0.00000%	0.00000%	0.00000%	0.00000%	0.00000%
3	0.25412%	0.01243%	0.04117%	0.01121%	7.84827%	0.72110%
4	0.03805%	0.00000%	0.00000%	0.00000%	3.10735%	0.30362%
5	0.03983%	0.04437%	0.12433%	0.04225%	1.50064%	9.18526%
6	9.68912%	9.95258%	9.85895%	9.95550%	0.00000%	0.00000%
7	0.00774%	0.00000%	0.00000%	0.00000%	0.00000%	0.00000%
8	0.00001%	0.00000%	0.00000%	0.00000%	0.00000%	0.00000%
9	0.01526%	0.00000%	0.00312%	0.00000%	0.00000%	0.00000%
10	0.07970%	0.00118%	0.00000%	0.00000%	0.00000%	0.00000%

Table D.16. Damage detection results for case CANT OPT, fixed representation, seeded initial population, noise levels of 0, 10 and 20%

Element	Fixed Representation Seeded Initial Population					
	Damage Indicator 0% noise		Damage Indicator 10% noise		Damage Indicator 20% noise	
	200 GA Generations	1281 Hillclimbing Iterations	200 GA Generations	170 Hillclimbing Iterations	200 GA Generations	113 Hillclimbing Iterations
1	0.00021%	0.00000%	0.00076%	0.00000%	0.00005%	0.00000%
2	4.19312%	9.99997%	8.50479%	9.59081%	8.50781%	9.16841%
3	0.00000%	0.00000%	0.00607%	0.00000%	0.00085%	0.00000%
4	3.09683%	0.00002%	0.53225%	0.00000%	0.35027%	0.00000%
5	1.93397%	0.00001%	0.00001%	0.00000%	0.00614%	0.00000%
6	0.00001%	0.00000%	0.87164%	0.00000%	0.41728%	0.00000%
7	0.00151%	0.00000%	0.00000%	0.00000%	0.00077%	0.00000%
8	0.00151%	0.00000%	0.13409%	0.56156%	0.88805%	1.13376%
9	1.25684%	0.00000%	0.12451%	0.00000%	0.00405%	0.00000%
10	0.02426%	0.00000%	0.00000%	0.00000%	0.00012%	0.00000%

Table D.17. Damage detection results for case CANT OPT, implicit redundant representation (IRR), seeded initial population, noise levels of 0, 10 and 20%

Element	IRR, Seeded Initial Population					
	Damage Indicator 0% noise		Damage Indicator 10% noise		Damage Indicator 20% noise	
	101 GA Generations	0 Hillclimbing Iterations	170 GA Generations	0 Hillclimbing Iterations	91 GA Generations	0 Hillclimbing Iterations
2	10.00000%	-	9.59081%	-	9.16840%	10.00000%
8	0.00000%	-	0.56156%	-	1.13376%	0.00000%

Table D.18. Damage detection results for case CANT OPT, implicit redundant representation (IRR), unseeded initial population, noise levels of 0, 10 and 20%

Element	IRR, Unseeded Initial Population					
	Damage Indicator 0% noise		Damage Indicator 10% noise		Damage Indicator 20% noise	
	200 GA Generations	71 Hillclimbing Iterations	170 GA Generations	32 Hillclimbing Iterations	141 GA Generations	0 Hillclimbing Iterations
2	9.99945%	10.00000%	9.59281%	9.59082%	9.16841%	-
6	0.00018%	0.00000%	0.00000%	0.00000%	0.00000%	-
8	0.00000%	0.00000%	0.56146%	0.56156%	1.13376%	-
10	0.00072%	0.00000%	0.00000%	0.00000%	0.00000%	-

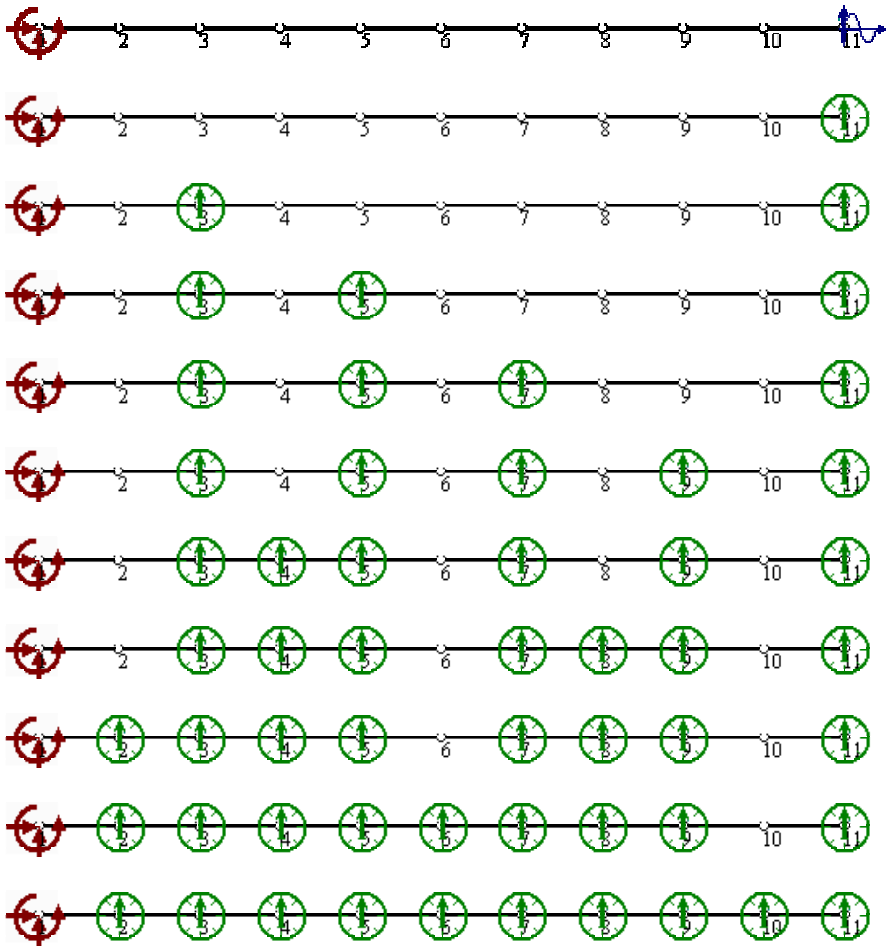

Figure D.1. Optimum excitation and sensor layout designs in the Pareto front for the cantilever problem

Table D.19. Damage detection results for case TWSP IA, fixed and implicit redundant representations (IRR), noise free measurements

Element	Damage Indicator 0% noise					
	Fixed Representation Seeded Initial Population		IRR, Seeded Initial Population		IRR, Unseeded Initial Population	
	200 GA Generations	315 Hillclimbing Iterations	200 GA Generations	215 Hillclimbing Iterations	200 GA Generations	40 Hillclimbing Iterations
1	0.19959%	0.00000%	0.00000%	0.00000%	0.00000%	0.00000%
5	1.54990%	0.00009%	0.03824%	0.00009%	0.00000%	0.00000%
6	7.54093%	9.99975%	9.90637%	9.99975%	9.99795%	9.99965%
7	0.01209%	0.00000%	0.00000%	0.00000%	0.00000%	0.00000%
10	9.45904%	9.99965%	9.93253%	9.99965%	9.99852%	9.99965%
11	1.58842%	0.00047%	0.11462%	0.00047%	0.00330%	0.00066%

Table D.19. (Continued)

Element	Damage Indicator 0% noise					
	Fixed Representation Seeded Initial Population		IRR, Seeded Initial Population		IRR, Unseeded Initial Population	
	200 GA Generations	315 Hillclimbing Iterations	200 GA Generations	215 Hillclimbing Iterations	200 GA Generations	40 Hillclimbing Iterations
13	0.00151%	0.00000%	0.00000%	0.00000%	0.00000%	0.00000%
14	0.00651%	0.00000%	0.00000%	0.00000%	0.00000%	0.00000%
15	0.00349%	0.00000%	0.00000%	0.00000%	0.00000%	0.00000%
18	0.00727%	0.00009%	0.01539%	0.00009%	0.00000%	0.00000%
19	0.00019%	0.00000%	0.00000%	0.00000%	0.00000%	0.00000%

Table D.20. Damage detection results for case TWSP IB, fixed and implicit redundant representations (IRR), noise free measurements

Element	Damage Indicator 0% noise					
	Fixed Representation Seeded Initial Population		IRR, Seeded Initial Population		IRR, Unseeded Initial Population	
	200 GA Generations	923 Hillclimbing Iterations	200 GA Generations	156 Hillclimbing Iterations	200 GA Generations	195 Hillclimbing Iterations
1	0.00019%	0.00000%	0.00000%	0.00000%	0.00000%	0.00000%
4	0.00000%	0.00000%	0.00000%	0.00000%	0.00028%	0.00000%
5	0.25039%	0.00028%	0.00000%	0.00000%	0.00000%	0.00000%
6	6.93498%	9.99937%	9.99625%	9.99937%	9.99295%	9.99937%
7	0.00000%	0.00000%	0.00000%	0.00000%	0.00057%	0.00000%
10	0.77259%	9.99899%	9.99323%	9.99852%	9.98913%	9.99876%
11	9.86738%	0.00123%	0.00935%	0.00189%	0.01766%	0.00161%
12	0.61039%	0.00000%	0.00000%	0.00000%	0.00000%	0.00000%
13	0.48982%	0.00000%	0.00000%	0.00000%	0.00000%	0.00000%
14	0.00151%	0.00019%	0.00000%	0.00000%	0.00000%	0.00000%
15	1.09860%	0.00028%	0.00189%	0.00057%	0.00208%	0.00066%
16	0.00321%	0.00000%	0.00000%	0.00000%	0.00000%	0.00000%
18	0.00000%	0.00000%	0.00076%	0.00009%	0.00000%	0.00000%
19	0.37841%	0.00000%	0.00000%	0.00000%	0.00000%	0.00000%
20	0.15229%	0.00000%	0.00000%	0.00000%	0.00000%	0.00000%

Table D.21. Damage detection results for case TWSP II, fixed and implicit redundant representations (IRR), noise free measurements

Element	Damage Indicator 0% noise					
	Fixed Representation Seeded Initial Population		IRR, Seeded Initial Population		IRR, Unseeded Initial Population	
	200 GA Generations	2333 Hillclimbing Iterations	200 GA Generations	971 Hillclimbing Iterations	200 GA Generations	1615 Hillclimbing Iterations
1	0.01671%	0.00000%	0.00000%	0.00000%	0.00000%	0.00000%
2	0.00028%	0.00000%	0.00000%	0.00000%	0.00000%	0.00000%
3	0.00472%	0.00000%	0.00000%	0.00000%	0.00000%	0.00000%
4	0.00047%	0.00000%	0.00000%	0.00000%	0.00000%	0.00000%
5	0.31742%	0.00113%	0.00000%	0.00000%	0.01086%	0.00142%
6	10.04600%	9.99928%	10.03570%	10.00190%	10.07440%	9.99909%
7	0.00566%	0.00000%	0.00000%	0.00000%	0.00000%	0.00000%
8	0.00670%	0.00000%	0.00000%	0.00000%	0.00000%	0.00000%
9	0.03314%	0.00000%	0.00000%	0.00000%	0.00000%	0.00000%
10	0.02908%	0.00104%	0.00000%	0.00000%	0.05328%	0.00126%
11	0.26285%	0.00000%	0.00000%	0.00000%	0.00000%	0.00000%
12	0.00227%	0.00000%	0.00000%	0.00000%	0.00000%	0.00000%
13	0.00604%	0.00000%	0.00000%	0.00000%	0.00000%	0.00000%
14	0.01312%	0.00000%	0.00000%	0.00000%	0.00000%	0.00000%
15	8.16142%	9.99824%	9.86502%	9.99323%	9.66996%	9.99777%
16	1.20812%	0.00161%	0.08979%	0.00576%	0.28579%	0.00208%
17	0.01076%	0.00000%	0.00000%	0.00000%	0.00000%	0.00000%
18	0.01794%	0.00000%	0.00000%	0.00000%	0.00000%	0.00000%
19	0.39087%	0.00000%	0.00000%	0.00000%	0.00000%	0.00000%
20	0.02077%	0.00000%	0.09602%	0.00085%	0.00000%	0.00000%

Table D.22. Damage detection results for case TWSP IIIA, fixed representation, seeded initial population, noise levels of 0, 5 and 10%

Element	Fixed Representation Seeded Initial Population					
	Damage Indicator 0% noise		Damage Indicator 5% noise		Damage Indicator 10% noise	
	200 GA Generations	341 Hillclimbing Iterations	200 GA Generations	176 Hillclimbing Iterations	200 GA Generations	740 Hillclimbing Iterations
1	0.39220%	0.00000%	0.19921%	0.00000%	0.01057%	0.00000%
2	0.00009%	0.00000%	0.00028%	0.00000%	0.00019%	0.00000%
3	0.00736%	0.00000%	0.00066%	0.00000%	0.00349%	0.00000%
4	0.00009%	0.00000%	0.01067%	0.00000%	0.00142%	0.00000%
5	0.17098%	0.00009%	0.12652%	0.00000%	0.05013%	0.00000%

Table D.22. (Continued)

Element	Fixed Representation Seeded Initial Population					
	Damage Indicator 0% noise		Damage Indicator 5% noise		Damage Indicator 10% noise	
	200 GA Generations	341 Hillclimbing Iterations	200 GA Generations	176 Hillclimbing Iterations	200 GA Generations	740 Hillclimbing Iterations
6	4.18914%	4.99969%	4.67094%	5.47232%	5.55871%	5.73356%
7	0.00576%	0.00000%	0.00312%	0.00000%	0.00293%	0.00000%
8	0.00651%	0.00000%	0.00566%	0.00000%	0.00019%	0.00000%
9	0.00670%	0.00000%	0.00094%	0.00000%	0.00019%	0.00000%
10	8.81599%	9.99965%	10.05580%	9.74379%	9.31846%	9.21923%
11	1.48400%	0.00047%	0.00019%	0.00000%	0.40768%	0.42297%
12	0.02559%	0.00000%	0.00066%	0.00000%	0.00264%	0.00000%
13	0.02700%	0.00000%	0.01209%	0.00000%	0.00245%	0.00000%
14	0.08677%	0.00000%	0.00009%	0.00000%	0.00142%	0.00000%
15	0.04532%	0.00000%	0.28560%	0.35840%	0.84944%	0.86814%
16	0.01350%	0.00000%	0.05098%	0.12491%	0.09101%	0.15559%
17	0.04589%	0.00000%	0.00293%	0.00000%	0.00094%	0.00000%
18	0.04268%	0.00009%	0.00019%	0.00000%	0.00019%	0.00000%
19	0.08072%	0.00000%	0.03229%	0.00000%	0.00000%	0.00000%
20	0.14200%	0.00000%	0.00699%	0.00000%	0.01218%	0.00000%

Table D.23. Damage detection results for case TWSP IIIA, fixed representation, seeded initial population, noise levels of 20 and 30%

Element	Fixed Representation Seeded Initial Population			
	Damage Indicator 20% noise		Damage Indicator 30% noise	
	200 GA Generations	1717 Hillclimbing Iterations	200 GA Generations	2552 Hillclimbing Iterations
1	0.00066%	0.00000%	0.01360%	0.00000%
2	0.00425%	0.00000%	0.00085%	0.00000%
3	0.00538%	0.00000%	0.01690%	0.00000%
4	0.00651%	0.00000%	0.00028%	0.00000%
5	0.21215%	0.00000%	0.20252%	0.00000%
6	6.19393%	6.22537%	6.97171%	6.51144%
7	0.00906%	0.00000%	0.00094%	0.00000%
8	0.00264%	0.00000%	0.00009%	0.00000%
9	0.00368%	0.00000%	0.00217%	0.00000%
10	7.89762%	8.27113%	8.72998%	7.12928%
11	1.38071%	1.16478%	0.25265%	2.20655%

Table D.23. (Continued)

Element	Fixed Representation Seeded Initial Population			
	Damage Indicator 20% noise		Damage Indicator 30% noise	
	200 GA Generations	1717 Hillclimbing Iterations	200 GA Generations	2552 Hillclimbing Iterations
12	0.00161%	0.00000%	0.00651%	0.00000%
13	0.00680%	0.00000%	0.00132%	0.00000%
14	0.00161%	0.00000%	0.00264%	0.00000%
15	2.23714%	1.78612%	1.31415%	2.77180%
16	0.06798%	0.21073%	0.86927%	0.16456%
17	0.00151%	0.00000%	0.01218%	0.00000%
18	0.00869%	0.00000%	0.00264%	0.00000%
19	0.00009%	0.00000%	0.01020%	0.00000%
20	0.02077%	0.00000%	0.00576%	0.00000%

Table D.24. Damage detection results for case TWSP IIIA, implicit redundant representation (IRR), seeded initial population, noise levels of 0, 5 and 10%

Element	IRR, Seeded Initial Population					
	Damage Indicator 0% noise		Damage Indicator 5% noise		Damage Indicator 10% noise	
	200 GA Generations	240 Hillclimbing Iterations	200 GA Generations	1598 Hillclimbing Iterations	200 GA Generations	70 Hillclimbing Iterations
1	0.01416%	0.00000%	0.00000%	0.00000%	0.00000%	0.00000%
6	4.93057%	4.99931%	4.54404%	5.38376%	5.88916%	5.90889%
10	9.96661%	9.99918%	7.73212%	9.56346%	9.53306%	9.50927%
11	0.07902%	0.00132%	2.63670%	0.26955%	0.00000%	0.00000%
13	0.00529%	0.00019%	0.00000%	0.00000%	0.00000%	0.00000%
15	0.00000%	0.00000%	1.19424%	0.50719%	0.69522%	0.68927%
16	0.00000%	0.00000%	0.00000%	0.00000%	0.20403%	0.24312%

Table D.25. Damage detection results for case TWSP IIIA, implicit redundant representation (IRR), seeded initial population, noise levels of 20 and 30%

Element	IRR, Seeded Initial Population			
	Damage Indicator 20% noise		Damage Indicator 30% noise	
	200 GA Generations	2162 Hillclimbing Iterations	200 GA Generations	1899 Hillclimbing Iterations
6	5.82467%	6.22508%	5.12195%	6.48972%
10	7.15298%	8.27065%	4.58143%	6.97086%
11	2.54020%	1.16544%	5.25073%	2.40916%
15	2.31772%	1.78645%	3.96755%	2.91635%
16	0.00236%	0.21054%	0.00000%	0.00000%
20	0.00038%	0.00000%	0.00000%	0.00000%

Table D.26. Damage detection results for case TWSP IIIA, implicit redundant representation (IRR), unseeded initial population, noise levels of 0, 5 and 10%

Element	IRR, Unseeded Initial Population					
	Damage Indicator 0% noise		Damage Indicator 5% noise		Damage Indicator 10% noise	
	200 GA Generations	71 Hillclimbing Iterations	200 GA Generations	1588 Hillclimbing Iterations	200 GA Generations	1406 Hillclimbing Iterations
1	0.01614%	0.00019%	0.00000%	0.00000%	0.00000%	0.00000%
6	4.99006%	4.99987%	4.59389%	5.38367%	5.33235%	5.71199%
10	10.00170%	10.00000%	8.07668%	9.56341%	8.42307%	9.10436%
11	0.00000%	0.00000%	2.24790%	0.26965%	1.48135%	0.59131%
15	0.00000%	0.00000%	0.99865%	0.50722%	1.29838%	1.00003%
16	0.00238%	0.00000%	0.00000%	0.00000%	0.00000%	0.00000%

Table D.27. Damage detection results for case TWSP IIIA, implicit redundant representation (IRR), unseeded initial population, noise levels of 20 and 30%

Element	IRR, Unseeded Initial Population			
	Damage Indicator 20% noise		Damage Indicator 30% noise	
	200 GA Generations	116 Hillclimbing Iterations	200 GA Generations	58 Hillclimbing Iterations
6	6.72793%	6.68129%	7.34559%	7.33095%
10	9.08422%	9.10253%	8.77194%	8.77251%
15	1.30678%	1.27695%	1.77007%	1.78149%
16	0.42916%	0.46107%	0.65240%	0.65712%

Table D.28. Damage detection results for case TWSP IIIB, fixed and implicit redundant representations (IRR), noise free measurements

Element	Damage Indicator 0% noise					
	Fixed Representation Seeded Initial Population		IRR, Seeded Initial Population		IRR, Unseeded Initial Population	
	200 GA Generations	981 Hillclimbing Iterations	200 GA Generations	1131 Hillclimbing Iterations	180 GA Generations	40 Hillclimbing Iterations
1	0.33007%	0.00000%	0.00000%	0.00000%	0.00000%	-
2	0.00935%	0.00000%	0.00000%	0.00000%	0.00000%	-
3	0.05193%	0.00000%	0.00000%	0.00000%	0.00000%	-
5	0.46074%	0.00047%	0.23464%	0.00050%	0.00000%	-
6	3.86530%	4.99780%	3.95821%	4.99770%	5.00008%	-
7	0.07846%	0.00000%	0.00000%	0.00000%	0.00000%	-
8	0.00066%	0.00000%	0.00000%	0.00000%	0.00000%	-
9	0.00028%	0.00000%	0.00000%	0.00000%	0.00000%	-
10	9.91090%	9.99843%	9.33800%	9.99843%	9.99994%	-
11	0.21706%	0.00208%	0.90033%	0.00208%	0.00000%	-
12	0.00104%	0.00000%	0.00000%	0.00000%	0.00000%	-
13	0.00604%	0.00000%	0.00000%	0.00000%	0.00000%	-
14	0.00519%	0.00000%	0.00000%	0.00000%	0.00000%	-
15	0.39909%	0.00189%	0.85482%	0.00198%	0.00000%	-
16	0.01350%	0.00000%	0.00000%	0.00000%	0.00000%	-
17	0.00463%	0.00000%	0.00000%	0.00000%	0.00000%	-
18	0.00387%	0.00000%	0.00000%	0.00000%	0.00000%	-
19	0.00019%	0.00000%	0.00000%	0.00000%	0.00000%	-
20	0.00179%	0.00000%	0.00000%	0.00000%	0.00000%	-

Table D.29. Damage detection results for case TWSP IIIB, fixed representation, seeded initial population, objective function is the sum of GSC and GAC squares, noise levels of 0, 5 and 10%

Element	Fixed Representation Seeded Initial Population					
	Damage Indicator 0% noise		Damage Indicator 5% noise		Damage Indicator 10% noise	
	200 GA Generations	1525 Hillclimbing Iterations	200 GA Generations	664 Hillclimbing Iterations	200 GA Generations	633 Hillclimbing Iterations
1	0.04079%	0.00000%	0.00935%	0.00000%	0.00038%	0.00000%
2	0.04853%	0.00000%	0.00019%	0.00000%	0.00302%	0.00000%
3	0.00000%	0.00000%	0.00217%	0.00000%	0.00009%	0.00000%
4	0.00104%	0.00000%	0.06571%	0.00000%	0.00123%	0.00000%
5	0.47660%	0.00019%	0.58395%	0.00000%	0.00009%	0.00000%
6	2.31871%	4.99884%	3.40758%	5.57297%	5.89718%	6.04031%

Table D.29. (Continued)

Element	Fixed Representation Seeded Initial Population					
	Damage Indicator 0% noise		Damage Indicator 5% noise		Damage Indicator 10% noise	
	200 GA Generations	1525 Hillclimbing Iterations	200 GA Generations	664 Hillclimbing Iterations	200 GA Generations	633 Hillclimbing Iterations
7	0.00463%	0.00000%	0.00057%	0.00000%	0.00208%	0.00000%
8	0.01001%	0.00000%	0.00887%	0.00000%	0.04910%	0.00000%
9	0.01180%	0.00000%	0.26049%	0.15050%	0.00661%	0.42581%
10	5.81108%	9.99795%	6.86115%	9.37095%	6.95915%	8.60337%
11	5.05671%	0.00255%	3.41504%	0.00000%	1.46700%	0.00000%
12	1.20113%	0.00066%	1.05819%	0.37718%	1.35342%	0.82178%
13	0.53353%	0.00028%	0.16947%	0.00000%	0.59528%	0.00000%
14	0.10150%	0.00000%	0.05637%	0.00000%	0.00529%	0.00000%
15	0.33904%	0.00028%	1.16016%	0.25520%	0.20214%	0.00000%
16	0.00718%	0.00000%	0.00151%	0.06212%	0.51352%	0.40957%
17	0.00085%	0.00000%	0.04947%	0.00000%	0.02417%	0.00000%
18	0.05325%	0.00000%	0.78713%	1.06433%	1.44784%	2.33438%
19	0.00113%	0.00000%	0.04371%	0.02398%	0.06005%	0.00000%
20	0.05693%	0.00000%	0.09592%	0.00000%	0.38672%	0.00000%

Table D.30. Damage detection results for case TWSP IIIB, fixed representation, seeded initial population, objective function is the sum of GSC and GAC squares, noise levels of 20 and 30%

Element	Fixed Representation Seeded Initial Population			
	Damage Indicator 20% noise		Damage Indicator 30% noise	
	200 GA Generations	1171 Hillclimbing Iterations	200 GA Generations	548 Hillclimbing Iterations
1	0.00378%	0.00000%	0.00623%	0.00000%
2	0.00113%	0.00000%	0.00633%	0.00000%
3	0.00104%	0.00000%	0.10187%	0.00000%
4	0.01671%	0.00000%	0.00453%	0.00000%
5	0.41703%	0.00000%	0.09696%	0.00000%
6	3.47802%	5.92636%	3.67081%	4.48843%
7	0.02256%	0.00000%	0.00076%	0.00000%
8	0.03031%	0.00000%	0.00935%	0.00000%
9	3.53958%	2.05718%	5.22798%	5.02470%
10	7.07924%	7.14127%	3.40551%	5.46156%
11	0.68403%	0.00000%	0.40362%	0.00000%
12	1.29611%	1.57898%	3.62068%	2.38763%

Table D.30. (Continued)

Element	Fixed Representation Seeded Initial Population			
	Damage Indicator 20% noise		Damage Indicator 30% noise	
	200 GA Generations	1171 Hillclimbing Iterations	200 GA Generations	548 Hillclimbing Iterations
13	1.02241%	0.00000%	0.03078%	0.00000%
14	0.00019%	0.00000%	0.00321%	0.00000%
15	1.37703%	0.00000%	0.43053%	0.00000%
16	0.33914%	0.90071%	2.06596%	1.63242%
17	0.01945%	0.00000%	0.01142%	0.00000%
18	2.43682%	4.62014%	6.17835%	6.62814%
19	0.57111%	0.00991%	0.00038%	0.00000%
20	0.00085%	0.00000%	0.00227%	0.00000%

Table D.31. Damage detection results for case TWSP IIIB, implicit redundant representation (IRR), seeded initial population, objective function is the sum of GSC and GAC squares, noise levels of 0, 5 and 10%

Element	IRR, Seeded Initial Population					
	Damage Indicator 0% noise		Damage Indicator 5% noise		Damage Indicator 10% noise	
	200 GA Generations	1301 Hillclimbing Iterations	200 GA Generations	407 Hillclimbing Iterations	200 GA Generations	255 Hillclimbing Iterations
5	0.00000%	0.00000%	0.78798%	0.00000%	0.00000%	0.00000%
6	3.57479%	4.99893%	3.54817%	5.72337%	5.91304%	6.45186%
10	7.07755%	9.99777%	6.46546%	9.28598%	7.18055%	8.47015%
11	3.53353%	0.00283%	3.44636%	0.00000%	1.47359%	0.00000%
12	1.02175%	0.00076%	1.43197%	0.42449%	1.39563%	0.89618%
13	0.21762%	0.00028%	0.02596%	0.00000%	0.00000%	0.00000%
15	0.42080%	0.00028%	0.86880%	0.23405%	0.62304%	0.34461%
18	0.00000%	0.00000%	0.75899%	1.18999%	2.36601%	2.43607%
20	0.00000%	0.00000%	0.27040%	0.00000%	0.00000%	0.00000%

Table D.32. Damage detection results for case TWSP IIIB, implicit redundant representation (IRR), seeded initial population, objective function is the sum of GSC and GAC squares, noise levels of 20 and 30%

Element	IRR, Seeded Initial Population			
	Damage Indicator 20% noise		Damage Indicator 30% noise	
	200 GA Generations	831 Hillclimbing Iterations	200 GA Generations	660 Hillclimbing Iterations
6	3.43100%	5.84762%	7.95418%	4.48796%
9	4.21312%	2.12573%	1.90792%	5.02508%
10	8.85677%	7.19292%	3.12538%	5.46165%
12	0.49020%	1.51761%	3.79322%	2.38758%
15	1.35880%	0.77873%	0.00000%	0.00000%
16	0.00000%	0.00000%	1.75629%	1.63242%
18	4.46681%	4.81737%	6.72066%	6.62814%
20	0.27739%	0.00000%	0.00000%	0.00000%

Table D.33. Damage detection results for case TWSP IIIB, implicit redundant representation (IRR), unseeded initial population, objective function is the sum of GSC and GAC squares, noise levels of 0, 5 and 10%

Element	IRR, Unseeded Initial Population					
	Damage Indicator 0% noise		Damage Indicator 5% noise		Damage Indicator 10% noise	
	200 GA Generations	3 Hillclimbing Iterations	200 GA Generations	83 Hillclimbing Iterations	200 GA Generations	302 Hillclimbing Iterations
5	0.00000%	0.00000%	0.55638%	0.00000%	0.00000%	0.00000%
6	4.99997%	4.99997%	5.15141%	5.69976%	5.40463%	6.45186%
10	9.99994%	10.00000%	9.66751%	9.84425%	6.23434%	8.47015%
11	0.00000%	0.00000%	0.00000%	0.00000%	2.40538%	0.00000%
12	0.00000%	0.00000%	0.00000%	0.00000%	1.84088%	0.89618%
15	0.00000%	0.00000%	0.00000%	0.00000%	0.85983%	0.34461%
16	0.00000%	0.00000%	0.14540%	0.11009%	0.00000%	0.00000%
18	0.00000%	0.00000%	1.37726%	1.26066%	2.38225%	2.43607%

Table D.34. Damage detection results for case TWSP IIIB, implicit redundant representation (IRR), unseeded initial population, objective function is the sum of GSC and GAC squares, noise levels of 20 and 30%

Element	IRR, Unseeded Initial Population			
	Damage Indicator 20% noise		Damage Indicator 30% noise	
	200 GA Generations	123 Hillclimbing Iterations	200 GA Generations	272 Hillclimbing Iterations
6	7.93662%	7.93633%	0.00000%	0.00000%
9	0.00000%	0.00000%	8.60629%	8.45514%
10	6.37020%	6.39484%	8.27660%	6.91223%
12	2.06493%	2.05020%	0.51635%	1.50222%
16	0.72066%	0.71434%	1.62633%	2.00209%
18	4.82068%	4.82540%	6.68412%	6.25926%

Table D.35. Damage detection results for case TWSP OPT, fixed representation, seeded initial population, noise levels of 0, 5 and 10%

Element	Fixed Representation Seeded Initial Population					
	Damage Indicator 0% noise		Damage Indicator 5% noise		Damage Indicator 10% noise	
	200 GA Generations	577 Hillclimbing Iterations	200 GA Generations	186 Hillclimbing Iterations	200 GA Generations	208 Hillclimbing Iterations
1	1.11635%	0.00000%	0.02691%	0.00000%	0.03021%	0.00000%
2	0.04673%	0.00000%	0.01879%	0.00000%	0.00179%	0.00000%
3	0.00349%	0.00000%	0.00425%	0.00000%	0.05061%	0.00000%
4	0.03002%	0.00000%	0.00566%	0.00000%	0.03361%	0.00000%
5	0.51588%	0.00000%	0.04768%	0.00000%	0.00538%	0.00000%
6	3.93328%	4.99921%	4.69171%	4.94965%	4.62987%	4.89819%
7	0.02946%	0.00000%	0.04296%	0.00000%	0.01275%	0.00000%
8	0.01964%	0.00000%	0.00444%	0.00000%	0.00897%	0.00000%
9	0.00161%	0.00028%	0.00028%	0.00000%	0.00151%	0.00000%
10	9.18354%	9.99871%	9.66798%	9.92875%	9.45007%	9.85775%
11	0.17080%	0.00170%	0.17552%	0.00000%	0.51021%	0.00000%
12	0.01917%	0.00000%	0.02266%	0.00000%	0.00009%	0.00000%
13	0.02323%	0.00000%	0.00548%	0.00000%	0.00264%	0.00000%
14	0.00009%	0.00000%	0.06373%	0.00680%	0.03928%	0.01567%
15	0.29344%	0.00019%	0.00906%	0.00000%	0.01275%	0.00000%
16	0.03333%	0.00019%	0.00963%	0.00000%	0.11481%	0.00000%
17	0.02493%	0.00000%	0.02266%	0.11301%	0.09961%	0.22065%
18	0.01803%	0.00000%	0.01435%	0.00000%	0.00972%	0.00000%

Table D.35. (Continued)

Element	Fixed Representation Seeded Initial Population					
	Damage Indicator 0% noise		Damage Indicator 5% noise		Damage Indicator 10% noise	
	200 GA Generations	577 Hillclimbing Iterations	200 GA Generations	186 Hillclimbing Iterations	200 GA Generations	208 Hillclimbing Iterations
19	0.00595%	0.00000%	0.02832%	0.00000%	0.00312%	0.00000%
20	0.05306%	0.00000%	0.02615%	0.00000%	0.05316%	0.00000%

Table D.36. Damage detection results for case TWSP OPT, fixed representation, seeded initial population, noise levels of 20 and 30%

Element	Fixed Representation Seeded Initial Population			
	Damage Indicator 20% noise		Damage Indicator 30% noise	
	200 GA Generations	262 Hillclimbing Iterations	200 GA Generations	301 Hillclimbing Iterations
1	0.01728%	0.00000%	0.01803%	0.00000%
2	0.00236%	0.00000%	0.00170%	0.00000%
3	0.00028%	0.00000%	0.00142%	0.00000%
4	0.00991%	0.00000%	0.00359%	0.00000%
5	0.01086%	0.00000%	0.00236%	0.00000%
6	4.07707%	4.79141%	3.65429%	4.67972%
7	0.02313%	0.00000%	0.00312%	0.00000%
8	0.00170%	0.00000%	0.00142%	0.00000%
9	0.00217%	0.00000%	0.00746%	0.00000%
10	8.49602%	9.71603%	7.26420%	9.57423%
11	1.80057%	0.00000%	3.17448%	0.00000%
12	0.01124%	0.00000%	0.00019%	0.00000%
13	0.00349%	0.00000%	0.00604%	0.00000%
14	0.14521%	0.04135%	0.38625%	0.07742%
15	0.00482%	0.00000%	0.00000%	0.00000%
16	0.29910%	0.00000%	0.48689%	0.00000%
17	0.32620%	0.41825%	0.09460%	0.59367%
18	0.00085%	0.00000%	0.00009%	0.00000%
19	0.00132%	0.00000%	0.01057%	0.00000%
20	0.02351%	0.00000%	0.00330%	0.00000%

Table D.37. Damage detection results for case TWSP OPT, implicit redundant representation (IRR), seeded initial population, noise levels of 0, 5 and 10%

Element	IRR, Seeded Initial Population					
	Damage Indicator 0% noise		Damage Indicator 5% noise		Damage Indicator 10% noise	
	200 GA Generations	508 Hillclimbing Iterations	200 GA Generations	12 Hillclimbing Iterations	184 GA Generations	31 Hillclimbing Iterations
1	1.91986%	0.00033%	0.00000%	0.00000%	0.00000%	0.00000%
2	0.32620%	0.00000%	0.00000%	0.00000%	0.00000%	0.00000%
6	2.87188%	4.99950%	4.94360%	4.94304%	4.80392%	4.88540%
10	8.69932%	9.99912%	10.00390%	10.00330%	10.02410%	10.00650%
11	1.59805%	0.00113%	0.00000%	0.00000%	0.00000%	0.00000%
15	0.38342%	0.00028%	0.00000%	0.00000%	0.00000%	0.00000%

Table D.38. Damage detection results for case TWSP OPT, implicit redundant representation (IRR), seeded initial population, noise levels of 20 and 30%

Element	IRR, Seeded Initial Population			
	Damage Indicator 20% noise		Damage Indicator 30% noise	
	200 GA Generations	133 Hillclimbing Iterations	200 GA Generations	27 Hillclimbing Iterations
6	3.96321%	4.79528%	4.68170%	4.68699%
10	8.46515%	9.72736%	9.60864%	9.59608%
11	1.94219%	0.00000%	0.00000%	0.00000%
16	0.28834%	0.00000%	0.00000%	0.00000%
17	0.05174%	0.46556%	0.66864%	0.68186%

Table D.39. Damage detection results for case TWSP OPT, implicit redundant representation (IRR), unseeded initial population, noise levels of 0, 5 and 10%

Element	IRR, Unseeded Initial Population					
	Damage Indicator 0% noise		Damage Indicator 5% noise		Damage Indicator 10% noise	
	200 GA Generations	189 Hillclimbing Iterations	180 GA Generations	0 Hillclimbing Iterations	180 GA Generations	0 Hillclimbing Iterations
5	0.22395%	0.00019%	0.00000%	-	0.00000%	-
6	4.74736%	4.99983%	4.95031%	-	4.89965%	-
7	0.09035%	0.00009%	0.00000%	-	0.00000%	-
10	9.88617%	9.99984%	9.93051%	-	9.86190%	-
15	0.02370%	0.00009%	0.00000%	-	0.00000%	-
17	0.00000%	0.00000%	0.12085%	-	0.23868%	-

Table D.40. Damage detection results for case TWSP OPT, implicit redundant representation (IRR), unseeded initial population, noise levels of 20 and 30%

Element	IRR, Unseeded Initial Population			
	Damage Indicator 20% noise		Damage Indicator 30% noise	
	115 GA Generations	0 Hillclimbing Iterations	200 GA Generations	57 Hillclimbing Iterations
6	4.76110%	-	4.68028%	4.67981%
10	9.68972%	-	9.57489%	9.57441%
14	0.35698%	-	0.07402%	0.07666%
17	0.00000%	-	0.59868%	0.59452%

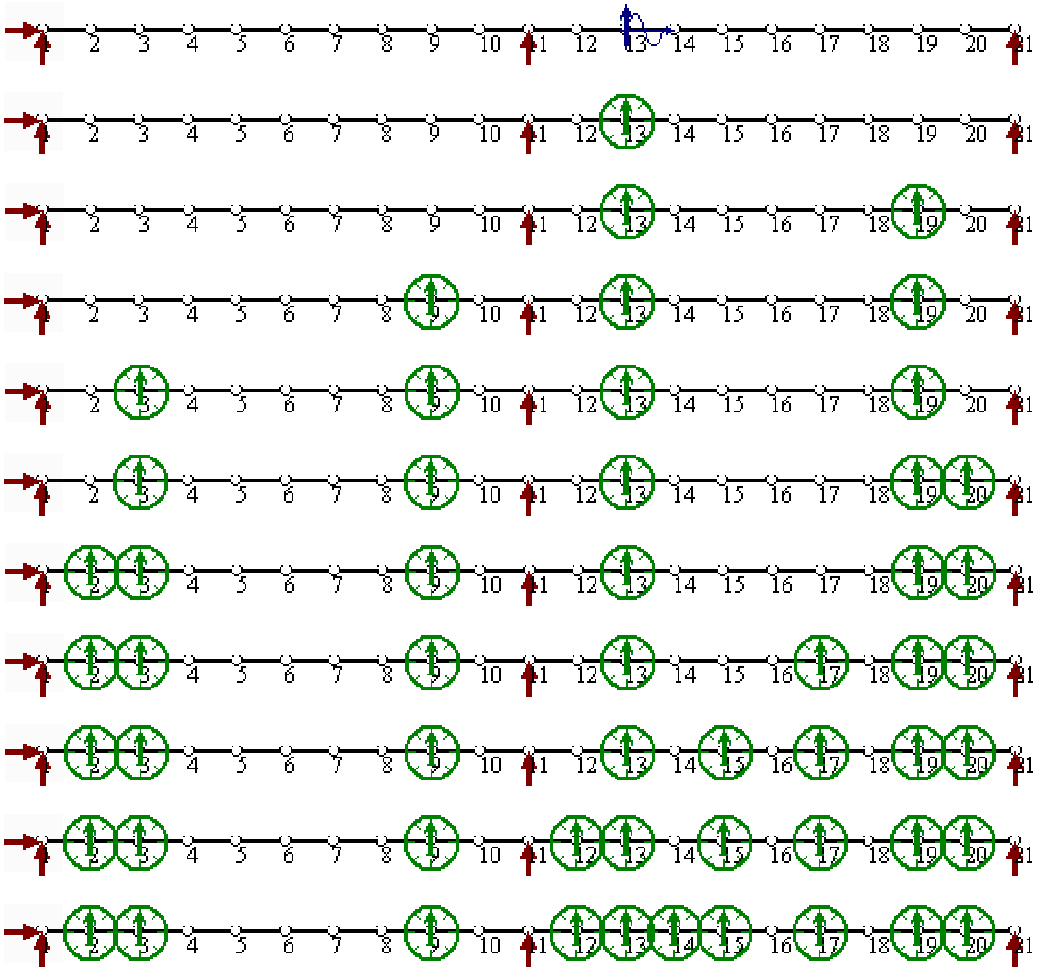

Figure D.2. Optimum excitation and sensor layout designs in the Pareto front for the two-span continuous beam problem

Table D.41. Damage detection results of trials 1, 2, 3 and 5 for the braced frame problem BRFRM I

Element	Damage Indicators							
	Trial 1		Trial 2		Trial 3		Trial 5	
	GA	Hillclimb	GA	Hillclimb	GA	Hillclimb	GA	Hillclimb
2	0.00161%	0.00000%	0.00000%	0.00000%	0.00000%	0.00000%	0.00000%	0.00000%
4	0.00000%	0.00000%	0.00000%	0.00000%	0.00000%	0.00000%	0.72812%	0.00000%
6	0.00000%	0.00000%	0.54685%	0.00349%	0.00000%	0.00000%	0.00000%	0.00000%
18	0.00000%	0.00000%	0.00000%	0.00000%	0.00000%	0.00000%	0.15701%	0.00000%
25	0.00000%	0.00000%	0.00000%	0.00000%	0.00000%	0.00000%	1.56963%	0.00000%
28	0.06902%	0.00179%	0.00000%	0.00000%	0.00000%	0.00000%	0.00000%	0.00000%
30	0.00000%	0.00000%	0.00000%	0.00000%	0.00000%	0.00000%	0.45734%	0.00000%
36	0.00000%	0.00000%	0.00000%	0.00000%	0.19775%	0.00000%	0.00000%	0.00000%
39	0.11830%	0.00378%	0.00000%	0.00000%	0.00000%	0.00000%	0.00000%	0.00000%
43	49.07550%	49.97520%	46.42820%	49.97720%	50.01890%	50.00000%	50.00550%	50.00000%
44	1.04502%	0.02809%	3.98965%	0.02578%	0.00000%	0.00000%	0.00000%	0.00000%
46	0.00000%	0.00000%	0.07997%	0.00038%	0.00000%	0.00000%	0.00000%	0.00000%

Table D.42. Damage detection results of trials 4, 7, 8 and 10 for the braced frame problem BRFRM I

Element	Damage Indicators							
	Trial 4		Trial 7		Trial 8		Trial 10	
	GA	Hillclimb	GA	Hillclimb	GA	Hillclimb	GA	Hillclimb
1	0.00132%	0.00000%	0.00585%	0.00000%	0.32922%	Corrupted	0.08988%	0.00000%
2	0.00142%	0.00000%	0.00264%	0.00000%	0.23556%	Corrupted	0.01199%	0.00000%
3	0.00472%	0.00000%	0.38634%	0.00000%	2.74593%	Corrupted	0.38370%	0.00000%
4	0.40485%	0.00000%	0.19270%	0.00000%	0.42552%	Corrupted	6.18751%	0.00000%
5	0.00000%	0.00000%	0.59207%	0.00000%	0.08459%	Corrupted	0.00529%	0.00000%
6	0.00566%	0.00000%	0.01199%	0.00000%	1.64384%	Corrupted	0.01813%	0.00189%
7	0.00066%	0.00000%	0.33838%	0.00000%	0.04220%	Corrupted	0.00038%	0.00000%
8	0.09366%	0.00000%	0.04825%	0.00000%	0.01048%	Corrupted	0.19327%	0.00000%
9	0.00000%	0.00000%	0.00000%	0.00000%	0.00009%	Corrupted	0.00264%	0.00000%
10	0.00000%	0.00000%	0.00227%	0.00000%	0.02861%	Corrupted	0.00453%	0.00000%
11	0.87002%	0.00000%	2.70703%	0.00000%	0.28985%	Corrupted	0.02341%	0.00000%
12	0.00000%	0.00000%	0.00000%	0.00000%	0.30137%	Corrupted	0.09659%	0.00000%
13	0.00028%	0.00000%	0.00585%	0.00000%	0.02115%	Corrupted	0.41080%	0.00000%
14	0.58461%	0.00000%	0.04825%	0.00000%	0.04862%	Corrupted	0.00066%	0.00000%

Table D.42. (Continued)

Element	Damage Indicators							
	Trial 4		Trial 7		Trial 8		Trial 10	
	GA	Hillclimb	GA	Hillclimb	GA	Hillclimb	GA	Hillclimb
15	0.19912%	0.00000%	0.19279%	0.00000%	3.16655%	Corrupted	0.38521%	0.00000%
16	0.01813%	0.00000%	0.77042%	0.00000%	2.99802%	Corrupted	0.00000%	0.00000%
17	0.01124%	0.00000%	3.09338%	0.00000%	0.00642%	Corrupted	1.73561%	0.00000%
18	0.21413%	0.00000%	1.52327%	0.00000%	0.01473%	Corrupted	0.00123%	0.00104%
19	0.00179%	0.00000%	2.47128%	0.00000%	0.62955%	Corrupted	0.02408%	0.00000%
20	0.00009%	0.00000%	0.67676%	0.00000%	0.01209%	Corrupted	0.77334%	0.00000%
21	0.00000%	0.00000%	6.18751%	0.00000%	0.01218%	Corrupted	0.00000%	0.00000%
22	0.01813%	0.00000%	0.19176%	0.00000%	0.09253%	Corrupted	0.02379%	0.00000%
23	0.09347%	0.00000%	0.02417%	0.00000%	0.00000%	Corrupted	0.00000%	0.00000%
24	0.18845%	0.00000%	12.37500%	0.00000%	0.76825%	Corrupted	0.19034%	0.00000%
25	0.00038%	0.00000%	5.49253%	0.00000%	0.58914%	Corrupted	0.04825%	0.00000%
26	0.00066%	0.00000%	0.00000%	0.00000%	3.17665%	Corrupted	0.18128%	0.00000%
27	3.11245%	0.00000%	2.93665%	0.00000%	1.37504%	Corrupted	2.99981%	0.00000%
28	0.02341%	0.00000%	0.00869%	0.00000%	0.37388%	Corrupted	0.00000%	0.00000%
29	0.00283%	0.00000%	1.54716%	0.00000%	0.10839%	Corrupted	0.00000%	0.00000%
30	0.02219%	0.00000%	1.50448%	0.00000%	3.14134%	Corrupted	0.00000%	0.00000%
31	0.29287%	0.00000%	0.77334%	0.00000%	1.65526%	Corrupted	0.04825%	0.00000%
32	0.13303%	0.00000%	0.00000%	0.00000%	0.03588%	Corrupted	0.00293%	0.00000%
33	0.19024%	0.00000%	1.54678%	0.00000%	0.00255%	Corrupted	0.02417%	0.00000%
34	0.01511%	0.00000%	0.02408%	0.00000%	0.01199%	Corrupted	0.00009%	0.00000%
35	0.16976%	0.00000%	0.29004%	0.00000%	0.03635%	Corrupted	0.38663%	0.00000%
36	0.00142%	0.00000%	0.38634%	0.00000%	3.28107%	Corrupted	0.00000%	0.00000%
37	0.00000%	0.00000%	0.00538%	0.00000%	0.65958%	Corrupted	0.00604%	0.00000%
38	0.00916%	0.00000%	0.02275%	0.00000%	1.16459%	Corrupted	0.68847%	0.00000%
39	0.01095%	0.00000%	0.37445%	0.00000%	0.07544%	Corrupted	0.02408%	0.00274%
40	0.08308%	0.00000%	0.00585%	0.00000%	0.00076%	Corrupted	0.00293%	0.00000%
41	3.09375%	0.00000%	11.79190%	0.00000%	2.12809%	Corrupted	0.09659%	0.00000%
42	1.54386%	0.00000%	0.00000%	0.00000%	2.71789%	Corrupted	1.54083%	0.00000%
43	49.45160%	50.00000%	49.28260%	50.00000%	48.54280%	Corrupted	46.40630%	49.97560%
44	0.19298%	0.00000%	0.00000%	0.00000%	0.59981%	Corrupted	3.09366%	0.02766%
45	0.04239%	0.00000%	0.00585%	0.00000%	0.37152%	Corrupted	1.59220%	0.00000%
46	0.00000%	0.00000%	0.00595%	0.00000%	0.15087%	Corrupted	0.04825%	0.00000%

Table D.43. Damage detection results of trials 6, 9, 11 and 12 for the braced frame problem BRFRM I

Element	Damage Indicators							
	Trial 6		Trial 9		Trial 11		Trial 12	
	GA	Hillclimb	GA	Hillclimb	GA	Hillclimb	GA	Hillclimb
30	0.00000%	0.00000%	0.68054%	0.00000%	0.00000%	-	0.00000%	-
31	0.00000%	0.00000%	0.27677%	0.00000%	0.00000%	-	0.00000%	-
43	50.00260%	50.00000%	49.99660%	50.00000%	50.00000%	-	50.00000%	-

Table D.44. Damage detection results of trials 13, 15, 16 and 17 for the braced frame problem BRFRM I

Element	Damage Indicators							
	Trial 13		Trial 15		Trial 16		Trial 17	
	GA	Hillclimb	GA	Hillclimb	GA	Hillclimb	GA	Hillclimb
1	0.00009%	0.00000%	54.41260%	54.12450%	0.00000%	0.00000%	0.00227%	0.00000%
2	0.00293%	0.00000%	80.85270%	7.45813%	0.00000%	0.00000%	0.01161%	0.00000%
3	0.00066%	0.00000%	70.57250%	77.05070%	0.00000%	0.00000%	0.38615%	0.00000%
4	0.00000%	0.00000%	29.61760%	43.15640%	0.00000%	0.00000%	0.02398%	0.00000%
5	0.77334%	0.00000%	0.34895%	1.03714%	0.00142%	0.00000%	0.20072%	0.00000%
6	0.74927%	0.00000%	86.90370%	96.14170%	0.00000%	0.00000%	0.04749%	0.00000%
7	0.00906%	0.00000%	57.73530%	59.40040%	0.00000%	0.00000%	0.00066%	0.00000%
8	12.37200%	0.00000%	21.66080%	15.84760%	0.02408%	0.00000%	0.19317%	0.00000%
9	0.38521%	0.00000%	1.88809%	0.00000%	0.00066%	0.00000%	0.26766%	0.00000%
10	0.40787%	0.00000%	4.31405%	5.20862%	0.00000%	0.00000%	0.02445%	0.00000%
11	3.09366%	0.00000%	48.77350%	72.95930%	0.00000%	0.00000%	0.77334%	0.00000%
12	0.04825%	0.00000%	9.52296%	11.27340%	0.00000%	0.00000%	0.16910%	0.00000%
13	0.04825%	0.00000%	89.58850%	90.20570%	0.00595%	0.00000%	0.02426%	0.00000%
14	0.00009%	0.00000%	78.41260%	64.29120%	0.00000%	0.00000%	0.03852%	0.00000%
15	0.00000%	0.00000%	65.05840%	76.82010%	0.01199%	0.00000%	0.11622%	0.00000%
16	3.14200%	0.00000%	4.85976%	0.00000%	0.00000%	0.00000%	2.32041%	0.00000%
17	0.00529%	0.00000%	96.65170%	95.41500%	0.00000%	0.00000%	0.14785%	0.00000%
18	1.54083%	0.00000%	18.90890%	0.00000%	0.00000%	0.00000%	0.02408%	0.00066%
19	0.33980%	0.00000%	53.23130%	88.56880%	0.04825%	0.00000%	0.03635%	0.00000%
20	0.00000%	0.00000%	36.19300%	42.71410%	0.00000%	0.00000%	0.13435%	0.00000%
21	0.00057%	0.00000%	75.96550%	85.88320%	0.00000%	0.00000%	0.07327%	0.00000%
22	0.00000%	0.00000%	0.99352%	0.00000%	3.04541%	0.00000%	0.00028%	0.00000%
23	0.08459%	0.00000%	57.00420%	36.96350%	0.00000%	0.00000%	0.00019%	0.00000%

Table D.44. (Continued)

Element	Damage Indicators							
	Trial 13		Trial 15		Trial 16		Trial 17	
	GA	Hillclimb	GA	Hillclimb	GA	Hillclimb	GA	Hillclimb
24	0.00000%	0.00000%	1.01589%	29.11130%	0.00000%	0.00000%	3.09064%	0.00000%
25	4.64063%	0.00000%	28.58440%	0.00000%	0.09659%	0.24330%	0.34008%	0.00000%
26	0.00000%	0.00000%	30.46230%	0.00000%	0.00000%	0.00000%	0.01265%	0.00057%
27	10.85860%	0.00000%	59.46320%	84.14710%	0.00000%	0.00000%	4.25391%	0.00000%
28	1.74014%	0.00000%	47.77320%	49.00120%	0.02408%	2.93051%	0.09545%	0.00000%
29	0.00000%	0.00000%	73.75180%	54.02320%	0.00293%	0.00000%	1.24504%	0.00000%
30	49.30660%	0.00000%	60.34000%	47.78830%	0.19327%	0.00000%	0.00019%	0.00000%
31	10.84010%	0.00000%	86.05240%	81.03160%	0.00000%	0.00000%	0.77353%	0.00000%
32	0.58036%	0.00000%	2.36082%	1.66008%	0.00595%	0.10008%	0.00293%	0.00000%
33	0.00595%	0.00000%	65.81550%	41.09830%	0.00000%	0.00000%	0.16324%	0.00000%
34	0.02408%	0.00000%	9.43902%	5.28633%	0.00000%	0.00000%	0.00000%	0.00000%
35	0.00595%	0.00000%	1.34993%	6.24972%	0.00000%	0.00000%	0.00293%	0.00000%
36	0.00000%	0.00000%	63.03360%	47.59390%	0.00000%	0.00000%	0.01199%	0.00000%
37	5.60733%	0.00000%	86.33660%	86.28590%	0.00000%	0.00000%	2.70854%	0.00123%
38	0.02408%	0.00000%	66.47860%	91.83910%	0.00000%	0.00000%	0.81725%	0.00000%
39	0.09659%	0.00000%	25.50810%	0.00000%	18.56250%	6.51720%	7.43688%	0.00000%
40	6.18741%	0.00000%	56.37880%	46.73180%	0.00000%	0.00000%	0.38653%	0.00000%
41	0.04230%	0.00000%	57.71420%	49.26250%	0.00264%	0.00000%	0.05429%	0.00000%
42	1.54074%	0.00000%	69.12020%	0.00000%	0.00000%	0.00000%	1.45586%	0.00000%
43	49.50000%	50.00000%	6.14719%	0.00000%	0.00000%	0.00000%	24.72280%	49.97670%
44	0.00066%	0.00000%	0.12274%	0.00000%	49.49700%	49.72710%	24.63510%	0.02625%
45	0.00000%	0.00000%	0.31997%	0.00000%	0.00000%	0.00000%	0.07515%	0.00000%
46	0.29297%	0.00000%	4.18555%	0.00000%	0.00000%	0.00000%	0.41127%	0.00028%

Table D.45. Damage detection results of trials 14, 19, 21, 23, 24 for the braced frame problem BRFRM I

Element	Damage Indicators							
	Trial 14	Trial 19	Trial 21		Trial 23		Trial 24	
	GA	GA	GA	Hillclimb	GA	Hillclimb	GA	Hillclimb
6	0.00000%	0.00000%	0.00000%	0.00000%	0.00000%	Corrupted	0.00444%	0.00000%
30	0.00000%	0.00000%	0.00009%	0.00000%	0.00000%	Corrupted	0.04044%	0.00000%
43	50.00000%	50.00000%	50.00000%	50.00000%	49.86010%	Corrupted	49.99950%	50.00000%
44	0.00000%	0.00000%	0.00000%	0.00000%	0.15852%	Corrupted	0.00000%	0.00000%

Table D.46. Damage detection results of trials 18, 20, 22, and 25 for the braced frame problem BRFRM I

Element	Damage Indicators							
	Trial 18		Trial 20		Trial 22		Trial 25	
	GA	Hillclimb	GA	Hillclimb	GA	Hillclimb	GA	Hillclimb
1	1.20840%	0.00000%	0.38663%	0.00000%	0.00000%	0.00000%	86.51860%	94.28540%
2	0.04825%	0.00000%	0.04825%	0.00000%	0.00113%	0.00000%	91.97620%	90.19280%
3	0.69489%	0.00000%	24.36470%	0.00000%	0.02408%	0.00000%	39.30120%	52.84360%
4	0.01057%	0.00000%	0.04560%	0.00000%	0.00000%	0.00000%	9.65306%	23.85630%
5	0.19043%	0.00000%	9.28126%	0.00000%	0.74955%	0.00000%	0.40201%	4.46068%
6	5.43522%	0.00000%	0.38030%	0.00000%	0.00585%	0.01784%	14.86390%	0.00000%
7	0.00000%	0.00000%	9.28721%	0.00000%	0.00000%	0.00000%	55.56570%	24.52340%
8	0.01832%	0.00000%	0.01133%	0.00000%	0.00009%	0.00000%	69.90200%	59.31170%
9	0.03918%	0.00000%	0.17514%	0.00000%	0.00000%	0.00000%	1.45841%	0.00000%
10	0.01199%	0.00000%	0.00000%	0.00000%	0.08601%	0.00000%	0.12302%	0.00000%
11	0.38955%	0.00000%	1.53489%	0.00000%	3.11783%	0.00000%	81.88700%	59.27040%
12	0.14502%	0.00000%	3.04532%	0.00000%	0.38653%	0.00000%	29.50190%	9.90552%
13	0.15069%	0.00000%	0.00000%	0.00000%	0.04230%	0.00000%	67.19970%	65.48070%
14	0.04532%	0.00000%	0.00000%	0.00000%	0.00142%	0.00000%	21.00750%	23.16670%
15	0.01511%	0.00000%	0.39871%	0.00000%	0.02408%	0.00000%	1.04469%	0.00000%
16	0.68743%	0.00000%	1.54669%	0.00000%	0.04806%	0.00000%	62.67410%	58.29140%
17	0.04371%	0.00000%	0.00142%	0.00000%	0.02351%	0.00000%	13.53970%	14.01600%
18	0.02332%	0.00000%	0.77334%	0.00000%	0.74927%	0.00000%	9.62256%	0.00000%
19	0.00132%	0.00000%	0.02323%	0.00000%	1.54678%	0.00000%	61.32670%	67.35020%
20	0.01133%	0.00000%	0.00066%	0.00000%	0.00066%	0.00000%	7.85514%	15.16820%
21	0.02408%	0.00000%	0.01813%	0.00000%	0.00028%	0.00000%	45.88990%	32.04900%
22	0.62700%	0.00000%	0.01209%	0.00000%	0.14502%	0.00000%	1.73721%	0.00000%
23	0.19327%	0.00000%	0.09630%	0.00000%	0.76740%	0.00000%	55.33450%	45.64440%
24	0.24765%	0.00000%	0.07251%	0.00000%	6.15116%	0.00000%	61.92440%	60.12340%
25	2.82845%	0.00000%	11.60160%	0.00000%	0.00000%	0.00000%	33.37780%	16.04830%
26	1.37533%	0.00000%	18.56540%	0.00000%	1.54688%	0.00000%	24.59650%	44.01560%
27	0.05108%	0.00000%	11.98970%	0.00000%	0.00000%	0.00000%	91.77840%	92.07220%
28	0.00453%	0.00123%	3.04551%	0.00000%	0.01057%	0.00000%	36.86410%	31.21650%
29	0.19213%	0.00000%	1.45029%	0.00000%	0.00009%	0.00359%	84.85330%	80.03480%
30	0.05108%	0.00000%	1.54688%	0.00000%	0.19279%	0.00000%	57.22560%	57.22560%
31	0.77259%	0.00000%	0.77334%	0.00000%	0.00293%	0.00000%	85.23010%	86.39190%
32	0.01171%	0.00000%	0.00066%	0.00179%	0.09659%	0.00000%	16.60150%	22.48760%

Table D.46. (Continued)

Element	Damage Indicators							
	Trial 18		Trial 20		Trial 22		Trial 25	
	GA	Hillclimb	GA	Hillclimb	GA	Hillclimb	GA	Hillclimb
33	0.00264%	0.00000%	1.16082%	0.00000%	0.00000%	0.00000%	31.52170%	27.21440%
34	0.00066%	0.00000%	0.02408%	0.00000%	0.00000%	0.00000%	2.41180%	2.79153%
35	0.33838%	0.00000%	0.00142%	0.00000%	0.00000%	0.00000%	27.61530%	40.50390%
36	0.01813%	0.00000%	2.90899%	0.00000%	2.90020%	0.00000%	15.61750%	0.00000%
37	0.00283%	0.00123%	0.00000%	0.00000%	0.00000%	0.00000%	36.06120%	33.71710%
38	0.00000%	0.00000%	0.00604%	0.00000%	0.00000%	0.00000%	90.45890%	90.24560%
39	0.74917%	0.00000%	0.37605%	0.03333%	3.81885%	0.00000%	75.05040%	81.38550%
40	0.35915%	0.00000%	0.09649%	0.00000%	0.07242%	0.00000%	35.66120%	35.66120%
41	0.77325%	0.00000%	0.00009%	0.00000%	0.04862%	0.00000%	58.06210%	55.02630%
42	1.53621%	0.00000%	0.19327%	0.00000%	0.00000%	0.00000%	11.92840%	0.00000%
43	49.50000%	49.97480%	11.69810%	49.73350%	47.95320%	49.94900%	3.69290%	3.53570%
44	0.13303%	0.02861%	24.65330%	0.30118%	2.70703%	0.05778%	7.08793%	7.53234%
45	0.00000%	0.00000%	0.38209%	0.00000%	0.04825%	0.00000%	0.64268%	0.00000%
46	0.00585%	0.00000%	0.72510%	0.00491%	3.11783%	0.00000%	0.80205%	0.00000%

Table D.47. Results of 25 initial trials arranged in trial pairs by mutation rate

Trial	Population Size	Primary Crossover Rate	Mutation Rate	Fixed or IRR	Initial Seed	Generation Number	Hillclimbing Iterations	Elements located before hill-climbing	Elements located after hill-climbing
4	100	0.7	0.005	Fixed	yes	200	94	Almost All	1
7	100	0.7	0.01	Fixed	yes	120	93	Almost All	1
8	200	0.7	0.005	Fixed	yes	200	2106	Almost All	1
22	200	0.7	0.01	Fixed	yes	101	3380	About Half	5
18	300	0.7	0.005	Fixed	yes	155	2360	Almost All	4
16	300	0.7	0.01	Fixed	yes	50	92	Failed	Failed
10	100	0.9	0.005	Fixed	yes	74	4680	Almost All	5
15	100	0.9	0.01	Fixed	no	200	761	Failed	Failed
25	200	0.9	0.005	Fixed	no	200	537	Failed	Failed
20	200	0.9	0.01	Fixed	yes	78	4702	Almost All	5
17	300	0.9	0.005	Fixed	yes	200	7352	Almost All	6
13	300	0.9	0.01	Fixed	yes	57	99	Almost All	1

Table D.47. (Continued)

Trial	Population Size	Primary Crossover Rate	Mutation Rate	Fixed or IRR	Initial Seed	Generation Number	Hillclimbing Iterations	Elements located before hill-climbing	Elements located after hill-climbing
1	100	0.7	0.005	IRR	no	200	3673	5	4
9	100	0.7	0.01	IRR	no	200	38	3	1
24	200	0.7	0.005	IRR	no	200	25	3	1
6	200	0.7	0.01	IRR	no	200	14	1	1
2	300	0.7	0.005	IRR	no	200	4960	4	4
3	300	0.7	0.01	IRR	no	200	37	2	1
11	100	0.9	0.005	IRR	yes	169	0	1	1
23	100	0.9	0.01	IRR	yes	200	94	2	2
21	200	0.9	0.005	IRR	yes	200	3	1	1
19	200	0.9	0.01	IRR	yes	145	0	1	1
12	300	0.9	0.005	IRR	yes	177	0	1	1
5	300	0.9	0.01	IRR	no	200	73	5	1
14	300	0.9	0.01	IRR	yes	175	0	1	1

Table D.48. Results of 25 initial trials arranged in trial pairs by primary crossover rate

Trial	Population Size	Primary Crossover Rate	Mutation Rate	Fixed or IRR	Initial Seed	Number Generations	Hill-climbing Operations	Elements located before climbing	Elements located after climbing
4	100	0.7	0.005	Fixed	yes	200	94	Almost All	1
10	100	0.9	0.005	Fixed	yes	74	4680	Almost All	5
8	200	0.7	0.005	Fixed	yes	200	2106	Almost All	1
25	200	0.9	0.005	Fixed	no	200	537	Failed	Failed
18	300	0.7	0.005	Fixed	yes	155	2360	Almost All	4
17	300	0.9	0.005	Fixed	yes	200	7352	Almost All	6
1	100	0.7	0.005	IRR	no	200	3673	5	4
11	100	0.9	0.005	IRR	yes	169	0	1	1
24	200	0.7	0.005	IRR	no	200	25	3	1
21	200	0.9	0.005	IRR	yes	200	3	1	1
2	300	0.7	0.005	IRR	no	200	4960	4	4
12	300	0.9	0.005	IRR	yes	177	0	1	1
7	100	0.7	0.01	Fixed	yes	120	93	Almost All	1
15	100	0.9	0.01	Fixed	no	200	761	Failed	Failed

Table D.48. (Continued)

Trial	Population Size	Primary Crossover Rate	Mutation Rate	Fixed or IRR	Initial Seed	Number Generations	Hill-climbing Operations	Elements located before climbing	Elements located after climbing
22	200	0.7	0.01	Fixed	yes	101	3380	About Half	5
20	200	0.9	0.01	Fixed	yes	78	4702	Almost All	5
16	300	0.7	0.01	Fixed	yes	50	92	Failed	Failed
13	300	0.9	0.01	Fixed	yes	57	99	Almost All	1
9	100	0.7	0.01	IRR	no	200	38	3	1
23	100	0.9	0.01	IRR	yes	200	94	2	2
6	200	0.7	0.01	IRR	no	200	14	1	1
19	200	0.9	0.01	IRR	yes	145	0	1	1
3	300	0.7	0.01	IRR	no	200	37	2	1
5	300	0.9	0.01	IRR	no	200	73	5	1
14	300	0.9	0.01	IRR	yes	175	0	1	1

Table D.49. Results of 25 preliminary trials arranged by population size

Trial	Population Size	Primary Crossover Rate	Mutation Rate	Fixed or IRR	Initial Seed	Number Generations	Hill-climbing Operations	Elements located before climbing	Elements located after climbing
4	100	0.7	0.005	Fixed	yes	200	94	Almost All	1
1	100	0.7	0.005	IRR	no	200	3673	5	4
7	100	0.7	0.01	Fixed	yes	120	93	Almost All	1
9	100	0.7	0.01	IRR	no	200	38	3	1
10	100	0.9	0.005	Fixed	yes	74	4680	Almost All	5
11	100	0.9	0.005	IRR	yes	169	0	1	1
15	100	0.9	0.01	Fixed	no	200	761	Failed	Failed
23	100	0.9	0.01	IRR	yes	200	94	2	2
8	200	0.7	0.005	Fixed	yes	200	2106	Almost All	1
24	200	0.7	0.005	IRR	no	200	25	3	1
22	200	0.7	0.01	Fixed	yes	101	3380	About Half	5
6	200	0.7	0.01	IRR	no	200	14	1	1
25	200	0.9	0.005	Fixed	no	200	537	Failed	Failed
21	200	0.9	0.005	IRR	yes	200	3	1	1
20	200	0.9	0.01	Fixed	yes	78	4702	Almost All	5
19	200	0.9	0.01	IRR	yes	145	0	1	1

Table D.49. (Continued)

Trial	Population Size	Primary Crossover Rate	Mutation Rate	Fixed or IRR	Initial Seed	Number Generations	Hill-climbing Operations	Elements located before climbing	Elements located after climbing
18	300	0.7	0.005	Fixed	yes	155	2360	Almost All	4
2	300	0.7	0.005	IRR	no	200	4960	4	4
16	300	0.7	0.01	Fixed	yes	50	92	Failed	Failed
3	300	0.7	0.01	IRR	no	200	37	2	1
17	300	0.9	0.005	Fixed	yes	200	7352	Almost All	6
12	300	0.9	0.005	IRR	yes	177	0	1	1
13	300	0.9	0.01	Fixed	yes	57	99	Almost All	1
5	300	0.9	0.01	IRR	no	200	73	5	1
14	300	0.9	0.01	IRR	yes	175	0	1	1

Table D.50. Damage detection results of trials 28, 29, 30, and 31 for the braced frame problem BRFRM II including 5% measurement noise

Element	Damage Indicators							
	Trial 28		Trial 29		Trial 30		Trial 31	
	GA	Hillclimb	GA	Hillclimb	GA	Hillclimb	GA	Hillclimb
7	0.00000%	0.00000%	7.83550%	7.46549%	0.00000%	0.00000%	0.00000%	0.00000%
13	0.00000%	0.00000%	0.00000%	0.00000%	2.52925%	3.04390%	0.00000%	0.00000%
18	0.00000%	0.00000%	1.29687%	2.04444%	0.00000%	0.00000%	0.00000%	0.00000%
25	0.00000%	0.00000%	0.00000%	0.00000%	3.10102%	2.69816%	0.00000%	0.00000%
28	0.00000%	0.00000%	2.72648%	1.54943%	0.65703%	0.66571%	0.00000%	0.00000%
35	10.80300%	10.00000%	0.00000%	0.00000%	9.09281%	9.05155%	8.05284%	8.44711%
37	16.54160%	19.99960%	19.36170%	22.99270%	0.00000%	0.00000%	18.23220%	20.42830%
38	0.00000%	0.00000%	0.00000%	0.00000%	11.88210%	11.76250%	2.19541%	0.41098%
39	26.48200%	20.00080%	18.35700%	11.94120%	37.93530%	38.18210%	23.22010%	19.53880%
41	0.00000%	0.00000%	0.95226%	0.50011%	0.00000%	0.00000%	0.00000%	0.00000%
42	0.00000%	0.00000%	9.67421%	9.07402%	0.00000%	0.00000%	0.00000%	0.00000%
43	50.14190%	50.00000%	49.80030%	49.55560%	49.32840%	49.34110%	49.45930%	49.76620%

Table D.51. Damage detection results for case UBFRM I, implicit redundant representation (IRR), seeded initial population, noise levels of 0, 5 and 10%

Element	IRR, Seeded Initial Population					
	Damage Indicator 0 % noise		Damage Indicator 5 % noise		Damage Indicator 10 % noise	
	261 GA Generations	0 Hillclimbing Iterations	300 GA Generations	332 Hillclimbing Iterations	300 GA Generations	231 Hillclimbing Iterations
6	0.00000%	-	0.23566%	0.26823%	0.61907%	0.65316%
12	0.00000%	-	0.00000%	0.00000%	1.02194%	1.39279%
14	0.00005%	-	0.00000%	0.00000%	0.62738%	0.68308%
21	10.00000%	-	8.99736%	9.94867%	10.19170%	10.18320%
22	0.00000%	-	0.88900%	0.00000%	0.00000%	0.00000%
31	0.00000%	-	0.12293%	0.11103%	0.23056%	0.21555%
36	0.00000%	-	1.15062%	0.96935%	2.48733%	2.42464%
45	0.00000%	-	0.14870%	0.40900%	0.00000%	0.00000%
52	0.00000%	-	0.10329%	0.10650%	0.20894%	0.19742%
58	0.00000%	-	0.93857%	1.12589%	1.36088%	1.01023%
61	0.00000%	-	0.15729%	0.17929%	0.33399%	0.32842%

Table D.52. Damage detection results for case UBFRM I, implicit redundant representation (IRR), unseeded initial population, noise levels of 0, 5 and 10%

Element	IRR, Unseeded Initial Population					
	Damage Indicator 0 % noise		Damage Indicator 5 % noise		Damage Indicator 10 % noise	
	300 GA Generations	179 Hillclimbing Iterations	300 GA Generations	181 Hillclimbing Iterations	300 GA Generations	164 Hillclimbing Iterations
6	0.00000%	0.00000%	0.00000%	0.00000%	1.43396%	0.98077%
10	0.00000%	0.00000%	0.00000%	0.00000%	0.43666%	0.11877%
12	0.00000%	0.00000%	0.00000%	0.00000%	2.44491%	1.70631%
14	0.00000%	0.00000%	0.14285%	0.24312%	0.00000%	0.00000%
16	0.00000%	0.00000%	0.00000%	0.00000%	2.22080%	0.00000%
20	0.48387%	0.00047%	0.00000%	0.00000%	0.00000%	0.00000%
21	9.71037%	9.99965%	10.04130%	10.11320%	8.66209%	9.64334%
24	0.73369%	0.00000%	0.00000%	0.00000%	0.00000%	0.00000%
31	0.00000%	0.00000%	0.23802%	0.26653%	0.00000%	0.00000%
33	0.21998%	0.00000%	0.00000%	0.00000%	0.00000%	0.00000%
36	0.00000%	0.00000%	1.80028%	1.99449%	0.00000%	0.00000%
45	0.00000%	0.00000%	0.25256%	0.00000%	1.20878%	2.66521%
52	0.00000%	0.00000%	0.14342%	0.14105%	0.36293%	0.34414%
58	0.00000%	0.00000%	0.45432%	0.37643%	0.00000%	0.00000%
67	0.08724%	0.00028%	0.00000%	0.00000%	0.00000%	0.00000%
69	0.00000%	0.00000%	0.74096%	0.75295%	1.89262%	1.65451%

Table D.53. Damage detection results for case UBFRM II, implicit redundant representation (IRR), seeded initial population, noise levels of 0, 5 and 10%

Element	IRR, Seeded Initial Population					
	Damage Indicator 0 % noise		Damage Indicator 5 % noise		Damage Indicator 10 % noise	
	141 GA Generations	0 Hillclimbing Iterations	300 GA Generations	82 Hillclimbing Iterations	300 GA Generations	89 Hillclimbing Iterations
6	0.00000%	-	0.46036%	0.47301%	1.02722%	1.02600%
12	0.00000%	-	0.57687%	0.70046%	0.99050%	0.98606%
20	0.00000%	-	0.10584%	0.00000%	0.00000%	0.00000%
21	0.00000%	-	0.00000%	0.00000%	0.62955%	0.63701%
28	10.00000%	-	8.57570%	8.70779%	6.08054%	6.05967%
36	0.00000%	-	0.60963%	0.56696%	0.94046%	0.95131%
45	0.00000%	-	0.99097%	0.96397%	2.77407%	2.77699%
52	0.00000%	-	0.15031%	0.14181%	0.29429%	0.29495%
61	0.00000%	-	0.13463%	0.13180%	0.29391%	0.29382%
75	0.00000%	-	0.11849%	0.11481%	0.17212%	0.16928%

Table D.54. Damage detection results for case UBFRM II, implicit redundant representation (IRR), unseeded initial population, noise levels of 0, 5 and 10%

Element	IRR, Unseeded Initial Population					
	Damage Indicator 0 % noise		Damage Indicator 5 % noise		Damage Indicator 10 % noise	
	300 GA Generations	5 Hillclimbing Iterations	300 GA Generations	179 Hillclimbing Iterations	300 GA Generations	55 Hillclimbing Iterations
6	0.00000%	0.00000%	0.50096%	0.53627%	0.94197%	0.97010%
12	0.00000%	0.00000%	0.91430%	1.04110%	1.32642%	1.45728%
16	0.00000%	0.00000%	0.61431%	0.41557%	0.00000%	0.00000%
28	9.99994%	10.00000%	8.48006%	8.74640%	7.59635%	7.52242%
36	0.00000%	0.00000%	0.00000%	0.00000%	1.29828%	1.22927%
45	0.00000%	0.00000%	1.38703%	1.30914%	2.41407%	2.50895%
52	0.00000%	0.00000%	0.00000%	0.00000%	0.37341%	0.37737%
58	0.00000%	0.00000%	0.00000%	0.00000%	0.29193%	0.16862%
61	0.00000%	0.00000%	0.14096%	0.16050%	0.00000%	0.00000%
69	0.00000%	0.00000%	0.00000%	0.00000%	1.27969%	1.22313%
70	0.00047%	0.00000%	0.00000%	0.00000%	0.00000%	0.00000%

Table D.55. Damage detection results of trials 1(a) and 1(b) for the unbraced frame problem UBFRM III

Element	Damage Indicator, 0% noise			
	Trial 1(a)		Trial 1(b)	
	300 GA Generations	2026 Hillclimbing Iterations	300 GA Generations	327 Hillclimbing Iterations
2	1.20585%	0.12840%	0.00000%	0.00000%
3	1.53243%	7.14826%	5.98876%	6.43251%
5	2.38031%	0.76725%	0.00000%	0.00000%
6	0.00000%	0.00000%	0.37378%	0.50729%
11	0.00000%	0.00000%	1.73655%	0.89146%
18	0.00000%	0.00000%	0.73737%	0.71377%
27	9.02615%	8.95553%	5.78285%	7.67547%
28	0.00000%	0.00000%	0.00264%	0.00000%
31	0.28107%	0.00000%	0.06005%	0.05759%
34	2.99405%	9.36208%	0.00000%	0.00000%
42	0.00000%	0.00000%	0.96954%	0.76315%
44	0.00000%	0.00000%	0.59830%	0.57187%
46	4.88082%	1.11862%	0.00000%	0.00000%
59	0.00000%	0.00000%	0.34782%	0.46924%

Table D.56. Damage detection results of trials 2(a) and 2(b) for the unbraced frame problem UBFRM III

Element	Damage Indicator, 0% noise			
	Trial 2(a)		Trial 2(b)	
	300 GA Generations	1150 Hillclimbing Iterations	300 GA Generations	159 Hillclimbing Iterations
2	0.68497%	0.37482%	0.00000%	0.00000%
3	4.26533%	6.70310%	4.82105%	4.99959%
5	1.84716%	2.03759%	0.00000%	0.00000%
19	2.74409%	3.56823%	0.00000%	0.00000%
27	11.64880%	11.61440%	4.72485%	4.99950%
34	0.00000%	0.00000%	10.14160%	10.00030%
46	3.36491%	1.90952%	0.12576%	0.00000%
49	0.00000%	0.00000%	9.34404%	9.99984%

Table D.57. Damage detection results of trials 3, 4 and 5(a) for the unbraced frame problem UBFRM IV

Element	Damage Indicators, 0% noise					
	Trial 3		Trial 4		Trial 5(a)	
	255 GA Generations	490 Hillclimbing Iterations	330 GA Generations	258 Hillclimbing Iterations	400 GA Generations	293 Hillclimbing Iterations
4	10.61320%	10.14140%	10.25360%	10.04200%	10.49980%	10.00120%
10	9.81932%	9.99276%	9.72236%	9.99541%	9.81828%	9.99918%
11	8.08428%	8.80135%	10.45030%	9.83330%	9.77098%	9.99975%
16	0.00000%	0.00000%	0.00000%	0.00000%	8.32900%	9.99862%
18	20.18990%	20.00060%	20.18140%	20.00090%	20.14120%	20.00070%
19	14.44860%	14.72690%	0.81810%	0.00000%	0.00000%	0.00000%
20	4.48400%	5.60856%	3.83651%	2.72620%	0.00000%	0.00000%
21	4.71465%	3.37690%	0.00000%	0.00000%	0.00000%	0.00000%
28	0.00000%	0.00000%	22.48590%	21.39320%	20.74540%	20.00080%
48	0.23018%	1.37646%	0.00000%	0.00000%	0.00000%	0.00000%
51	0.86776%	0.48821%	0.00000%	0.00000%	0.00000%	0.00000%
75	0.17127%	0.00000%	0.00000%	0.00000%	0.00000%	0.00000%

Table D.58. Damage detection results of trials 5(b), 6 and 7 for the unbraced frame problem UBFRM IV

Element	Damage Indicators, 5% noise					
	Trial 5(b)		Trial 6		Trial 7	
	400 GA Generations	211 Hillclimbing Iterations	400 GA Generations	424 Hillclimbing Iterations	379 GA Generations	758 Hillclimbing Iterations
4	20.59410%	20.55670%	0.00000%	0.00000%	9.86323%	10.48130%
5	5.37290%	5.49913%	0.00000%	0.00000%	0.00000%	0.00000%
6	0.00000%	0.00000%	0.00000%	0.00000%	1.59286%	0.00000%
7	0.00000%	0.00000%	0.00000%	0.00000%	1.44425%	3.06203%
10	8.53784%	8.63179%	12.08830%	11.99440%	10.80200%	10.09610%
11	13.91800%	13.91800%	21.14400%	22.11360%	0.00000%	0.00000%
16	36.33210%	36.98790%	0.00000%	0.00000%	0.00000%	0.00000%
18	20.34630%	20.31970%	18.05740%	18.11920%	19.09350%	19.67370%
22	2.79238%	2.79248%	0.00000%	0.00000%	0.00000%	0.00000%
24	0.00000%	0.00000%	0.00000%	0.00000%	2.85064%	2.22071%
28	0.00000%	0.00000%	0.00000%	0.00000%	29.50820%	24.22880%
38	0.00000%	0.00000%	0.00000%	0.00000%	4.02264%	9.20540%
40	1.78782%	2.00516%	0.00000%	0.00000%	0.00000%	0.00000%
42	0.00000%	0.00000%	0.00000%	0.00000%	1.50411%	3.69234%

Table D.58. (Continued)

Element	Damage Indicators, 5% noise					
	Trial 5(b)		Trial 6		Trial 7	
	400 GA Generations	211 Hillclimbing Iterations	400 GA Generations	424 Hillclimbing Iterations	379 GA Generations	758 Hillclimbing Iterations
47	10.16050%	8.94363%	0.00000%	0.00000%	0.00000%	0.00000%
48	0.00000%	0.00000%	4.81935%	5.65766%	0.00000%	0.00000%
51	0.00000%	0.00000%	0.00000%	0.00000%	2.23761%	3.72972%
55	0.00000%	0.00000%	0.00000%	0.00000%	12.32780%	5.87197%
56	7.23474%	7.08472%	0.00000%	0.00000%	0.00000%	0.00000%
59	9.41523%	9.66439%	0.00000%	0.00000%	0.00000%	0.00000%
68	0.00000%	0.00000%	6.19364%	3.96283%	0.00000%	0.00000%
73	0.00000%	0.00000%	5.81769%	5.31748%	0.00000%	0.00000%
79	0.00000%	0.00000%	2.65501%	2.50461%	0.00000%	0.00000%

Table D.59. Damage detection results of trials 8, 9 and 10 for the unbraced frame problem UBFRM IV

Element	Damage Indicators, 5% noise					
	Trial 8		Trial 9		Trial 10	
	400 GA Generations	624 Hillclimbing Iterations	400 GA Generations	502 Hillclimbing Iterations	400 GA Generations	308 Hillclimbing Iterations
2	0.00000%	0.00000%	0.00000%	0.00000%	0.62502%	0.75767%
4	12.79700%	11.44210%	11.02550%	9.72642%	14.25630%	12.54260%
10	8.04637%	9.49629%	6.88296%	9.58792%	0.00000%	0.00000%
11	8.12157%	8.50961%	8.23751%	9.72104%	7.43481%	8.04132%
12	0.00000%	0.00000%	2.73583%	2.90370%	0.00000%	0.00000%
13	0.00000%	0.00000%	0.00000%	0.00000%	0.78005%	1.32859%
16	11.83270%	15.47480%	10.75810%	17.15590%	0.00000%	0.00000%
18	21.82430%	20.64470%	22.35360%	20.19610%	25.89780%	25.08900%
19	0.00000%	0.00000%	0.00000%	0.00000%	7.13400%	0.00000%
21	5.21929%	5.57712%	2.06351%	3.52135%	4.15581%	4.03732%
24	0.00000%	0.00000%	0.00000%	0.00000%	0.27446%	1.29092%
28	0.00000%	0.00000%	17.97740%	0.00000%	0.00000%	0.00000%
36	14.80750%	14.06480%	0.00000%	0.00000%	0.00000%	0.00000%
38	26.34010%	8.03358%	0.00000%	0.00000%	46.59810%	44.25530%
43	0.00000%	0.00000%	0.87342%	0.00000%	0.00000%	0.00000%
56	0.00000%	0.00000%	0.00000%	0.00000%	2.26055%	1.10983%
67	0.00000%	0.00000%	0.00000%	0.00000%	13.38410%	0.00000%
73	4.23125%	3.78609%	0.00000%	0.00000%	0.00000%	0.00000%

Table D.60. Damage detection results of trial 11 for the unbraced frame problem UBFRM IV

Element	Trial 11, Damage Indicators, 5% noise	
	400 GA Generations	302 Hillclimbing Iterations
3	5.60157%	6.29816%
4	7.75978%	8.00988%
10	11.56650%	11.50770%
11	12.52250%	12.45570%
16	11.81700%	9.95164%
18	18.35340%	18.37000%
28	16.87670%	19.43840%
49	1.78225%	0.00000%

Table D.61. Plate girder damage detection results for cases KSTSP I, II and III, fixed representation, seeded initial population, noise free measurements

Element	Damage Indicators, Fixed Representation Seeded Initial Population, 0% noise					
	KSTSP I		KSTSP II		KSTSP III	
	200 GA Generations	119 Hillclimbing Iterations	200 GA Generations	285 Hillclimbing Iterations	200 GA Generations	187 Hillclimbing Iterations
1	0.33262%	0.00000%	4.22049%	0.00047%	0.00000%	0.00000%
2	0.09130%	0.00000%	0.03635%	0.00000%	0.36255%	0.00000%
3	0.38899%	0.00000%	0.10083%	0.00000%	0.00000%	0.00000%
4	5.99075%	10.00000%	0.00642%	0.00000%	1.54952%	0.00000%
5	0.39909%	0.00000%	0.11830%	0.00000%	0.01057%	0.00000%
6	0.00415%	0.00000%	0.09064%	0.00000%	0.00066%	0.00000%
7	1.37721%	0.00000%	0.00755%	0.00000%	0.01133%	0.00000%
8	0.04900%	0.00000%	0.46150%	0.00000%	0.09668%	0.00000%
9	0.00009%	0.00000%	6.36330%	9.99975%	0.00009%	0.00000%
10	0.02530%	0.00000%	0.14445%	0.00000%	0.68242%	0.00000%
11	0.11084%	0.00000%	0.00529%	0.00000%	0.02379%	0.00000%
12	0.04164%	0.00000%	0.04815%	0.00000%	0.00142%	0.00000%
13	0.09300%	0.00000%	0.47094%	0.00000%	0.00028%	0.00000%
14	0.00944%	0.00000%	0.08384%	0.00000%	6.18146%	9.99994%
15	0.04796%	0.00000%	0.00264%	0.00000%	0.43525%	0.00009%
16	0.00038%	0.00000%	0.38691%	0.00009%	0.02408%	0.00000%
17	0.00283%	0.00000%	0.09828%	0.00000%	0.01199%	0.00000%
18	0.02181%	0.00000%	0.05429%	0.00000%	0.72529%	0.00000%
19	0.01124%	0.00000%	0.00038%	0.00000%	0.19034%	0.00009%

Table D.61. (Continued)

Element	Damage Indicators, Fixed Representation Seeded Initial Population, 0% noise					
	KSTSP I		KSTSP II		KSTSP III	
	200 GA Generations	119 Hillclimbing Iterations	200 GA Generations	285 Hillclimbing Iterations	200 GA Generations	187 Hillclimbing Iterations
20	0.04721%	0.00000%	0.15097%	0.00000%	0.77948%	0.00000%
21	0.77363%	0.00000%	0.02011%	0.00000%	0.00453%	0.00000%
22	0.42420%	0.00000%	0.00000%	0.00000%	0.00000%	0.00000%
23	0.03559%	0.00000%	0.67534%	0.00009%	0.10612%	0.00000%
24	0.05721%	0.00000%	0.16919%	0.00000%	0.00000%	0.00000%
25	0.00906%	0.00000%	0.00283%	0.00000%	0.00085%	0.00000%
26	0.00000%	0.00000%	0.00283%	0.00000%	0.00670%	0.00000%
27	0.16910%	0.00000%	0.00255%	0.00000%	0.00000%	0.00000%
28	0.02842%	0.00000%	0.01180%	0.00000%	0.04843%	0.00000%
29	0.12746%	0.00000%	0.00142%	0.00000%	0.07742%	0.00000%
30	0.19336%	0.00000%	0.15210%	0.00000%	0.01133%	0.00000%
31	0.04825%	0.00000%	0.04683%	0.00000%	0.00000%	0.00000%
32	0.12378%	0.00000%	0.10839%	0.00000%	0.07478%	0.00000%
33	0.00283%	0.00000%	0.00651%	0.00000%	0.01841%	0.00000%
34	0.04296%	0.00000%	0.07553%	0.00000%	0.19902%	0.00000%
35	0.00633%	0.00000%	0.02115%	0.00000%	0.00302%	0.00000%
36	0.00161%	0.00000%	0.16881%	0.00000%	0.39607%	0.00000%
37	0.33196%	0.00000%	0.01237%	0.00000%	0.00142%	0.00000%
38	0.10839%	0.00000%	0.09810%	0.00000%	0.04598%	0.00000%
39	0.38710%	0.00000%	0.34707%	0.00000%	0.00028%	0.00000%
40	0.02747%	0.00000%	0.11906%	0.00000%	0.00217%	0.00000%
41	0.48604%	0.00000%	0.01180%	0.00000%	0.01209%	0.00000%
42	0.67902%	0.00000%	0.11840%	0.00000%	0.02124%	0.00000%
43	0.10480%	0.00000%	0.02747%	0.00000%	0.00000%	0.00000%
44	0.19147%	0.00000%	0.31487%	0.00000%	0.10640%	0.00000%
45	0.02530%	0.00000%	0.09696%	0.00000%	0.00066%	0.00000%
46	0.33970%	0.00000%	0.07393%	0.00000%	0.00000%	0.00000%
47	0.02398%	0.00000%	0.01643%	0.00000%	0.00028%	0.00000%
48	0.11330%	0.00000%	0.00066%	0.00000%	0.00151%	0.00000%
49	0.00293%	0.00000%	0.00312%	0.00000%	0.00000%	0.00000%
50	0.16834%	0.00000%	0.03767%	0.00000%	0.00000%	0.00000%

Table D.62. Plate girder damage detection results for cases KSTSP IV, V and VI, fixed representation, seeded initial population, noise free measurements

Element	Damage Indicators, Fixed Representation Seeded Initial Population, 0% noise					
	KSTSP IV		KSTSP V		KSTSP VI	
	200 GA Generations	656 Hillclimbing Iterations	200 GA Generations	286 Hillclimbing Iterations	109 GA Generations	608 Hillclimbing Iterations
1	0.28409%	0.00000%	0.38700%	0.00000%	0.00000%	0.00000%
2	0.37747%	0.00000%	0.00312%	0.00000%	0.00009%	0.00000%
3	0.00595%	0.00000%	0.01482%	0.00000%	0.00000%	0.00000%
4	0.00000%	0.00000%	0.01057%	0.00000%	0.02408%	0.00000%
5	0.10877%	0.00000%	0.00000%	0.00000%	0.00000%	0.00000%
6	0.00066%	0.00000%	0.00444%	0.00000%	0.00000%	0.00000%
7	0.00066%	0.00000%	0.01190%	0.00000%	0.00009%	0.00000%
8	0.00066%	0.00000%	0.18128%	0.00009%	0.00066%	0.00000%
9	0.00066%	0.00000%	0.36397%	0.00000%	0.00009%	0.00009%
10	0.00113%	0.00000%	0.02341%	0.00000%	0.00566%	0.00000%
11	0.00000%	0.00000%	0.00566%	0.00000%	0.00132%	0.00000%
12	0.05117%	0.00000%	0.02341%	0.00000%	0.00633%	0.00000%
13	0.00076%	0.00000%	0.00132%	0.00000%	0.00000%	0.00000%
14	0.04966%	0.00000%	0.03616%	0.00000%	0.00009%	0.00000%
15	5.40793%	0.00113%	0.00019%	0.00000%	0.00000%	0.00000%
16	0.08913%	0.00047%	0.01879%	0.00000%	0.00000%	0.00000%
17	0.77042%	0.00000%	0.09640%	0.00000%	0.00000%	0.00000%
18	1.63761%	0.00085%	0.00028%	0.00000%	0.00453%	0.00000%
19	4.04913%	9.99843%	0.01171%	0.00000%	0.07251%	0.00000%
20	0.37530%	0.00028%	3.09517%	0.00038%	0.00000%	0.00000%
21	0.01133%	0.00000%	0.00312%	0.00000%	0.00000%	0.00000%
22	0.01275%	0.00000%	0.02087%	0.00000%	0.00028%	0.00000%
23	0.10933%	0.00000%	1.26552%	0.00000%	0.00000%	0.00000%
24	0.00736%	0.00000%	3.09309%	9.99946%	0.01199%	0.00000%
25	0.00000%	0.00000%	0.54260%	0.00000%	0.00595%	0.00019%
26	0.38445%	0.00000%	0.01237%	0.00000%	0.00142%	0.00000%
27	0.00161%	0.00000%	1.49863%	0.00038%	0.00009%	0.00000%
28	0.19402%	0.00000%	0.00000%	0.00000%	0.09668%	0.00000%
29	0.10867%	0.00000%	0.00009%	0.00000%	0.00000%	0.00000%
30	0.24236%	0.00000%	0.10763%	0.00000%	0.01209%	0.00028%
31	0.12321%	0.00000%	0.07175%	0.00000%	0.00000%	0.00000%
32	0.10046%	0.00000%	0.01822%	0.00000%	0.00000%	0.00000%
33	0.19327%	0.00000%	0.00066%	0.00000%	0.02408%	0.00028%
34	0.00595%	0.00000%	0.02039%	0.00000%	0.00293%	0.00000%

Table D.62. (Continued)

Element	Damage Indicators, Fixed Representation Seeded Initial Population, 0% noise					
	KSTSP IV		KSTSP V		KSTSP VI	
	200 GA Generations	656 Hillclimbing Iterations	200 GA Generations	286 Hillclimbing Iterations	109 GA Generations	608 Hillclimbing Iterations
35	0.10301%	0.00000%	0.00085%	0.00000%	0.09659%	0.00000%
36	0.00170%	0.00000%	0.00746%	0.00000%	0.00000%	0.00000%
37	0.09555%	0.00000%	0.01237%	0.00000%	0.19345%	0.00000%
38	0.01322%	0.00000%	0.01171%	0.00000%	0.00028%	0.00170%
39	0.19506%	0.00000%	0.07572%	0.00000%	0.37463%	0.99720%
40	0.07666%	0.00000%	0.05146%	0.00000%	0.15701%	0.00094%
41	0.39588%	0.00000%	0.09677%	0.00000%	0.01199%	0.00000%
42	0.79534%	0.00000%	0.38058%	0.00000%	0.00000%	0.00000%
43	0.56167%	0.00000%	0.04230%	0.00000%	0.00000%	0.00000%
44	0.19364%	0.00000%	3.09479%	0.00000%	0.00000%	0.00000%
45	0.04230%	0.00000%	0.07251%	0.00000%	0.00000%	0.00000%
46	0.00283%	0.00000%	0.00142%	0.00000%	0.19327%	0.00000%
47	0.07260%	0.00000%	0.00019%	0.00000%	0.01199%	0.00000%
48	0.31402%	0.00000%	0.00897%	0.00000%	0.00000%	0.00000%
49	0.42515%	0.00000%	0.00444%	0.00000%	0.00000%	0.00000%
50	0.07544%	0.00000%	0.18364%	0.00000%	0.09054%	0.00000%

Table D.63. Plate girder damage detection results for cases KSTSP VII and VIII, fixed representation, seeded initial population, noise free measurements

Element	Damage Indicators, Fixed Representation Seeded Initial Population, 0% noise			
	KSTSP VII		KSTSP VIII	
	200 GA Generations	1370 Hillclimbing Iterations	200 GA Generations	1173 Hillclimbing Iterations
1	0.09507%	0.00000%	0.42854%	0.00000%
2	0.01218%	0.00000%	0.16910%	0.00000%
3	0.00293%	0.00000%	0.00368%	0.00000%
4	0.01209%	0.00000%	0.38719%	0.00000%
5	0.01057%	0.00000%	0.03852%	0.00000%
6	0.00009%	0.00000%	0.02115%	0.00000%
7	0.04758%	0.00000%	0.00076%	0.00000%
8	0.01199%	0.00000%	0.00557%	0.00000%
9	0.00566%	0.00000%	0.14172%	0.00019%

Table D.63. (Continued)

Element	Damage Indicators, Fixed Representation Seeded Initial Population, 0% noise			
	KSTSP VII		KSTSP VIII	
	200 GA Generations	1370 Hillclimbing Iterations	200 GA Generations	1173 Hillclimbing Iterations
10	0.00009%	0.00000%	0.02172%	0.00000%
11	0.04683%	0.00000%	0.02341%	0.00000%
12	0.02530%	0.00000%	0.42439%	0.00000%
13	0.00434%	0.00000%	0.26710%	0.00000%
14	0.00831%	0.00000%	0.38766%	0.00000%
15	0.00066%	0.00000%	0.15522%	0.00000%
16	0.00000%	0.00000%	0.10801%	0.00000%
17	0.00151%	0.00000%	0.04211%	0.00000%
18	0.00066%	0.00000%	0.10744%	0.00000%
19	0.00009%	0.00000%	0.02256%	0.00000%
20	0.01057%	0.00000%	0.07393%	0.00000%
21	0.19648%	0.00000%	0.09073%	0.00000%
22	0.02143%	0.00000%	0.24123%	0.00000%
23	0.00293%	0.00000%	0.03635%	0.00000%
24	0.05174%	0.00000%	0.80507%	0.00000%
25	0.33838%	0.00038%	0.13039%	0.00028%
26	0.01171%	0.00000%	0.09432%	0.00000%
27	0.09394%	0.00000%	0.01256%	0.00000%
28	0.03918%	0.00000%	0.03314%	0.00000%
29	0.00142%	0.00076%	0.00736%	0.00142%
30	0.32639%	0.00019%	0.07279%	0.00000%
31	0.08526%	0.00000%	3.28371%	0.00000%
32	0.00529%	0.00151%	0.29967%	0.00170%
33	0.00161%	0.00000%	0.05278%	0.00000%
34	0.00000%	0.00000%	0.06939%	0.00000%
35	0.00113%	0.00000%	0.54345%	0.00000%
36	3.12925%	0.00000%	0.04551%	0.00000%
37	0.00453%	0.00000%	0.41070%	0.00000%
38	0.76268%	0.00293%	3.80705%	0.00397%
39	6.18184%	9.99474%	45.58140%	49.99770%
40	0.09630%	0.00236%	3.89882%	0.00359%
41	0.00595%	0.00000%	0.06109%	0.00000%
42	0.02691%	0.00000%	1.31651%	0.00000%
43	0.09696%	0.00019%	1.20689%	0.00000%

Table D.63. (Continued)

Element	Damage Indicators, Fixed Representation Seeded Initial Population, 0% noise			
	KSTSP VII		KSTSP VIII	
	200 GA Generations	1370 Hillclimbing Iterations	200 GA Generations	1173 Hillclimbing Iterations
44	0.09139%	0.00000%	0.12085%	0.00000%
45	0.77372%	0.00000%	0.63814%	0.00000%
46	0.02294%	0.00000%	0.08724%	0.00000%
47	0.01199%	0.00000%	0.81281%	0.00000%
48	0.29004%	0.00000%	0.01293%	0.00000%
49	0.39880%	0.00000%	0.00472%	0.00000%
50	0.07534%	0.00000%	0.04164%	0.00000%

Table D.64. Plate girder damage detection results for cases KSTSP IX and X, fixed representation, seeded initial population, noise free measurements

Element	Damage Indicators, Fixed Representation Seeded Initial Population, 0% noise			
	KSTSP IX		KSTSP X	
	200 GA Generations	425 Hillclimbing Iterations	200 GA Generations	1582 Hillclimbing Iterations
1	0.39909%	0.00000%	0.08308%	0.00000%
2	0.65259%	0.00000%	0.00028%	0.00000%
3	0.05117%	0.00000%	0.00085%	0.00000%
4	0.00302%	0.00000%	0.03890%	0.00000%
5	0.19336%	0.00000%	0.00151%	0.00000%
6	0.00623%	0.00000%	0.00142%	0.00000%
7	0.00670%	0.00000%	0.00897%	0.00000%
8	0.24161%	0.00009%	0.00293%	0.00000%
9	6.11490%	9.99984%	0.10310%	0.00000%
10	0.00670%	0.00000%	2.27764%	0.00000%
11	0.00085%	0.00000%	0.06637%	0.00000%
12	0.02332%	0.00000%	0.09158%	0.00000%
13	1.46096%	0.00000%	2.75537%	0.00028%
14	0.01171%	0.00000%	3.67393%	9.99946%
15	0.08875%	0.00009%	0.77268%	0.00038%
16	0.09555%	0.00000%	0.00028%	0.00000%
17	0.19327%	0.00000%	0.00217%	0.00000%
18	0.00142%	0.00000%	0.04843%	0.00000%

Table D.64. (Continued)

Element	Damage Indicators, Fixed Representation Seeded Initial Population, 0% noise			
	KSTSP IX		KSTSP X	
	200 GA Generations	425 Hillclimbing Iterations	200 GA Generations	1582 Hillclimbing Iterations
19	0.00028%	0.00000%	0.01199%	0.00000%
20	1.64497%	0.00000%	0.06307%	0.00000%
21	0.00123%	0.00000%	0.00066%	0.00000%
22	0.00482%	0.00000%	0.84274%	0.00000%
23	0.00000%	0.00000%	0.09668%	0.00000%
24	0.00274%	0.00000%	0.00019%	0.00000%
25	0.26653%	0.00000%	0.38587%	0.00000%
26	0.16910%	0.00000%	0.02417%	0.00009%
27	0.00151%	0.00000%	0.08223%	0.00000%
28	0.00142%	0.00000%	0.02228%	0.00019%
29	0.01199%	0.00000%	0.19506%	0.00000%
30	0.40419%	0.00000%	1.01419%	0.00019%
31	0.01218%	0.00000%	0.00151%	0.00000%
32	0.09196%	0.00000%	0.02408%	0.00038%
33	0.79676%	0.00047%	0.01190%	0.00019%
34	6.18581%	9.99937%	0.38398%	0.00000%
35	0.72973%	0.00038%	0.07846%	0.00000%
36	0.01662%	0.00000%	6.21215%	0.00000%
37	0.59160%	0.00000%	0.94112%	0.00000%
38	0.02493%	0.00000%	1.54612%	0.00198%
39	0.09130%	0.00000%	2.02914%	9.99720%
40	0.04522%	0.00000%	0.16617%	0.00123%
41	0.02436%	0.00000%	0.11528%	0.00000%
42	1.04837%	0.00000%	0.00293%	0.00000%
43	0.19185%	0.00000%	0.19327%	0.00000%
44	0.00104%	0.00000%	0.04135%	0.00000%
45	0.09064%	0.00000%	0.78316%	0.00000%
46	0.00000%	0.00000%	0.20847%	0.00000%
47	0.02332%	0.00000%	0.19176%	0.00000%
48	0.01199%	0.00000%	1.58729%	0.00000%
49	0.00113%	0.00000%	0.43534%	0.00000%
50	0.19374%	0.00038%	0.18581%	0.00000%

Table D.65. Plate girder damage detection results for cases KSTSP I, II and III, implicit redundant representation (IRR), seeded initial population, noise free measurements

Element	Damage Indicators, IRR Seeded Initial Population, 0% noise					
	KSTSP I		KSTSP II		KSTSP III	
	143 GA Generations	0 Hillclimbing Iterations	200 GA Generations	18 Hillclimbing Iterations	123 GA Generations	0 Hillclimbing Iterations
4	10.00000%	-	0.00000%	0.00000%	0.00000%	-
9	0.00000%	-	9.99937%	10.00000%	0.00000%	-
14	0.00000%	-	0.00000%	0.00000%	9.99994%	-
17	0.00000%	-	0.01718%	0.00000%	0.00000%	-

Table D.66. Plate girder damage detection results for cases KSTSP IV, V and VI, implicit redundant representation (IRR), seeded initial population, noise free measurements

Element	Damage Indicators, IRR Seeded Initial Population, 0% noise					
	KSTSP IV		KSTSP V		KSTSP VI	
	200 GA Generations	266 Hillclimbing Iterations	144 GA Generations	0 Hillclimbing Iterations	200 GA Generations	705 Hillclimbing Iterations
15	0.81187%	0.00047%	0.00000%	-	0.00000%	0.00000%
18	0.30973%	0.00024%	0.00000%	-	0.00000%	0.00000%
19	9.32941%	9.99956%	0.00000%	-	0.00000%	0.00000%
24	0.00000%	0.00000%	10.00000%	-	0.00000%	0.00000%
29	0.00000%	0.00000%	0.00000%	-	0.01614%	0.00028%
32	0.00000%	0.00000%	0.00000%	-	0.02700%	0.00076%
33	0.00000%	0.00000%	0.00000%	-	0.00302%	0.00009%
38	0.00000%	0.00000%	0.00000%	-	0.05778%	0.00113%
39	0.00000%	0.00000%	0.00000%	-	0.88579%	0.99748%
40	0.00000%	0.00000%	0.00000%	-	0.04343%	0.00104%
50	0.30647%	0.00000%	0.00000%	-	0.00000%	0.00000%

Table D.67. Plate girder damage detection results for cases KSTSP VII and VIII, implicit redundant representation (IRR), seeded initial population, noise free measurements

Element	Damage Indicators, IRR Seeded Initial Population, 0% noise			
	KSTSP VII		KSTSP VIII	
	176 GA Generations	0 Hillclimbing Iterations	200 GA Generations	6 Hillclimbing Iterations
32	0.00000%	-	0.00024%	0.00014%
38	0.00000%	-	0.00057%	0.00047%
39	10.00000%	-	49.99990%	49.99990%

Table D.68. Plate girder damage detection results for cases KSTSP IX and X, implicit redundant representation (IRR), seeded initial population, noise free measurements

Element	Damage Indicators, IRR Seeded Initial Population, 0% noise			
	KSTSP IX		KSTSP IX	
	157 GA Generations	0 Hillclimbing Iterations	200 GA Generations	17 Hillclimbing Iterations
9	10.00000%	-	0.00000%	0.00000%
14	0.00000%	-	9.99998%	9.99998%
29	0.00000%	-	0.00184%	0.00005%
34	9.99998%	-	0.00000%	0.00000%
39	0.00000%	-	9.99909%	9.99994%

Table D.69. Plate girder damage detection results for cases KSTSP I, II and III, implicit redundant representation (IRR), unseeded initial population, noise free measurements

Element	IRR Unseeded Initial Population, 0% noise					
	KSTSP I		KSTSP II		KSTSP III	
	143 GA Generations	0 Hillclimbing Iterations	200 GA Generations	339 Hillclimbing Iterations	123 GA Generations	62 Hillclimbing Iterations
1	0.00000%	-	0.88858%	0.00090%	1.15201%	0.00000%
4	9.99998%	-	0.00000%	0.00000%	0.00000%	0.00000%
9	0.00000%	-	9.70603%	9.99965%	0.00000%	0.00000%
14	0.00000%	-	0.00000%	0.00000%	9.47811%	10.00000%
16	0.00000%	-	0.07166%	0.00009%	0.00000%	0.00000%
18	0.00000%	-	0.00000%	0.00000%	0.46258%	0.00000%
23	0.00000%	-	0.05533%	0.00009%	0.00000%	0.00000%
32	0.00000%	-	0.00000%	0.00000%	0.58804%	0.00000%
33	0.00000%	-	0.00000%	0.00000%	0.37010%	0.00000%
43	0.00000%	-	0.07204%	0.00009%	0.00000%	0.00000%

Table D.70. Plate girder damage detection results for cases KSTSP IV, V and VI, implicit redundant representation (IRR), unseeded initial population, noise free measurements

Element	IRR Unseeded Initial Population, 0% noise					
	KSTSP IV		KSTSP V		KSTSP VI	
	200 GA Generations	321 Hillclimbing Iterations	200 GA Generations	30 Hillclimbing Iterations	200 GA Generations	122 Hillclimbing Iterations
13	0.03824%	0.00000%	0.00000%	0.00000%	0.00000%	0.00000%
15	1.05172%	0.00052%	0.00000%	0.00000%	0.00000%	0.00000%
18	0.66309%	0.00031%	0.00000%	0.00000%	0.00000%	0.00000%
19	8.69240%	9.99946%	0.00000%	0.00000%	0.00000%	0.00000%
24	0.00000%	0.00000%	9.97869%	10.00000%	0.00000%	0.00000%
26	0.04173%	0.00009%	0.00000%	0.00000%	0.00000%	0.00000%
27	0.00000%	0.00000%	0.01992%	0.00000%	0.00000%	0.00000%
32	0.00000%	0.00000%	0.00000%	0.00000%	0.02030%	0.00009%
39	0.00000%	0.00000%	0.00000%	0.00000%	0.96198%	0.99984%
41	0.27050%	0.00000%	0.00000%	0.00000%	0.00000%	0.00000%
42	0.00000%	0.00000%	0.00189%	0.00000%	0.00000%	0.00000%
46	0.00000%	0.00000%	0.00000%	0.00000%	0.02710%	0.00009%
50	0.00000%	0.00000%	0.00000%	0.00000%	0.01445%	0.00000%

Table D.71. Plate girder damage detection results for cases KSTSP VII and VIII, implicit redundant representation (IRR), unseeded initial population, noise free measurements

Element	IRR Unseeded Initial Population, 0% noise			
	KSTSP VII		KSTSP VIII	
	176 GA Generations	604 Hillclimbing Iterations	200 GA Generations	46 Hillclimbing Iterations
29	0.00000%	0.00000%	0.06694%	0.00019%
32	0.14644%	0.00057%	0.00000%	0.00000%
38	0.34513%	0.00118%	0.00000%	0.00000%
39	9.49737%	9.99824%	49.98120%	49.99990%
40	0.23674%	0.00090%	0.00000%	0.00000%

Table D.72. Plate girder damage detection results for cases KSTSP IX and X, implicit redundant representation (IRR), unseeded initial population, noise free measurements

Element	IRR Unseeded Initial Population, 0% noise			
	KSTSP IX		KSTSP X	
	109 GA Generations	303 Hillclimbing Iterations	109 GA Generations	90 Hillclimbing Iterations
9	9.83688%	9.99994%	0.00000%	0.00000%
14	0.00000%	0.00000%	10.00250%	9.99998%
29	0.00000%	0.00000%	0.09389%	0.00005%
33	1.16091%	0.00038%	0.00000%	0.00000%
34	8.69495%	9.99956%	0.00000%	0.00000%
35	0.74323%	0.00028%	0.00000%	0.00000%
39	0.00000%	0.00000%	9.90769%	9.99994%
50	0.00000%	0.00000%	0.30109%	0.00009%

Table D.73. Plate girder damage detection results for cases KSTSP I, II and III, implicit redundant representation (IRR), seeded initial population, 5% noise in measurements

Element	Damage Indicators, IRR Seeded Initial Population, 5% noise					
	KSTSP I		KSTSP II		KSTSP III	
	200 GA Generations	342 Hillclimbing Iterations	200 GA Generations	77 Hillclimbing Iterations	200 GA Generations	310 Hillclimbing Iterations
1	0.00000%	0.00000%	1.79292%	0.01463%	0.00000%	0.00000%
4	9.12293%	9.08526%	0.00000%	0.00000%	0.00000%	0.00000%
6	0.14190%	0.12604%	0.00000%	0.00000%	0.66505%	0.53797%
7	0.00000%	0.00000%	0.00000%	0.00000%	0.39512%	0.54656%
8	0.00000%	0.00000%	0.18439%	0.11311%	0.00000%	0.00000%
9	0.00000%	0.00000%	9.27220%	9.91666%	0.00000%	0.00000%
12	0.61133%	0.65986%	0.00000%	0.00000%	0.00000%	0.00000%
14	0.00000%	0.00000%	0.00000%	0.00000%	8.12129%	7.99072%
15	0.00000%	0.00000%	0.00000%	0.00000%	0.50294%	0.84047%
16	0.00000%	0.00000%	0.12043%	0.00000%	0.00000%	0.00000%
19	0.00000%	0.00000%	0.00000%	0.00000%	1.07575%	0.99550%
24	0.00000%	0.00000%	0.01690%	0.01690%	0.00000%	0.00000%
26	0.40315%	0.40589%	0.68969%	0.64343%	0.00000%	0.00000%
34	0.52268%	0.57630%	0.00000%	0.00000%	0.49624%	0.32375%
46	0.53316%	0.55893%	0.00000%	0.00000%	0.52995%	0.62190%
50	0.38233%	0.26545%	0.00000%	0.00000%	0.00000%	0.00000%

Table D.74. Plate girder damage detection results for cases KSTSP IV, V and VI, implicit redundant representation (IRR), seeded initial population, 5% noise in measurements

Element	Damage Indicators, IRR Seeded Initial Population, 5 % noise					
	KSTSP IV		KSTSP V		KSTSP VI	
	200 GA Generations	177 Hillclimbing Iterations	200 GA Generations	51 Hillclimbing Iterations	200 GA Generations	200 Hillclimbing Iterations
1	0.00000%	0.00000%	0.00000%	0.00000%	0.42090%	0.39371%
8	0.00000%	0.00000%	0.13473%	0.13416%	0.00000%	0.00000%
15	1.03940%	0.22244%	0.00000%	0.00000%	0.00000%	0.00000%
16	0.22867%	0.12954%	0.00000%	0.00000%	0.00000%	0.00000%
18	0.19034%	0.00000%	0.00000%	0.00000%	0.00000%	0.00000%
19	8.79135%	9.58036%	0.00000%	0.00000%	0.00000%	0.00000%
24	0.00000%	0.00000%	10.00640%	10.00720%	0.33885%	0.25756%
25	0.00000%	0.00000%	0.40041%	0.40286%	0.84812%	0.71377%
26	0.99153%	0.94083%	0.38124%	0.37860%	0.05415%	0.17075%
33	0.20606%	0.00000%	0.00000%	0.00000%	0.00000%	0.00000%
40	0.00000%	0.00000%	0.01548%	0.01426%	0.33341%	0.31651%
46	0.00000%	0.00000%	0.00000%	0.00000%	0.60415%	0.64353%
49	0.14068%	0.00000%	0.00000%	0.00000%	0.00000%	0.00000%
50	0.77297%	1.64478%	0.94291%	0.94282%	0.00000%	0.00000%

Table D.75. Plate girder damage detection results for cases KSTSP VII and VIII, implicit redundant representation (IRR), seeded initial population, 5% noise in measurements

Element	Damage Indicators, IRR Seeded Initial Population, 5 % noise			
	KSTSP VII		KSTSP VIII	
	200 GA Generations	63 Hillclimbing Iterations	200 GA Generations	3387 Hillclimbing Iterations
1	1.53441%	1.71210%	1.01353%	1.99912%
20	0.00000%	0.00000%	0.10235%	0.01709%
25	0.75479%	0.74129%	0.68988%	0.69413%
30	1.83805%	1.83805%	1.37117%	1.96522%
32	1.35342%	1.37023%	0.00000%	0.00000%
33	0.00000%	0.00000%	0.91808%	1.45879%
34	0.43733%	0.45744%	0.00000%	0.00000%
39	6.24524%	6.22485%	48.94410%	48.58800%
40	2.34033%	2.31720%	0.83169%	1.90848%
46	0.09649%	0.10773%	1.19868%	1.03978%

Table D.76. Plate girder damage detection results for cases KSTSP IX and X, implicit redundant representation (IRR), seeded initial population, 5% noise in measurements

Element	Damage Indicators, IRR Seeded Initial Population, 5 % noise			
	KSTSP IX		KSTSP X	
	200 GA Generations	76 Hillclimbing Iterations	200 GA Generations	860 Hillclimbing Iterations
7	0.00000%	0.00000%	1.05097%	0.63309%
8	0.02370%	0.08535%	0.00000%	0.00000%
9	10.15210%	10.10220%	0.00000%	0.00000%
13	0.00000%	0.00000%	0.77542%	0.25010%
14	0.00000%	0.00000%	5.71676%	7.93841%
15	0.00000%	0.00000%	3.51333%	1.76828%
18	0.00000%	0.00000%	0.82626%	0.66142%
20	0.10121%	0.10423%	0.67846%	0.36227%
25	0.70074%	0.73454%	0.00000%	0.00000%
34	9.83301%	9.81517%	0.00000%	0.00000%
39	0.00000%	0.00000%	8.59945%	8.62041%
43	0.14653%	0.07147%	0.00000%	0.00000%
46	0.00000%	0.00000%	2.10345%	1.97580%
50	0.96359%	1.18074%	0.00000%	0.00000%

VITA

Tamás Róbert Liszkai was born in Miskolc, Hungary on September 8, 1974, the son of Kálmán Liszkai and Irén Krompák. He attended a 5-year integrated program at the University of Miskolc where he received his Master of Science degree in mechanical engineering in 1997 and continued his Ph.D. studies at the same university from 1997 to 1999.

In 1999 Mr. Liszkai received a Fulbright Scholarship and worked as a visiting researcher at Texas A&M University under the guidance of Dr. Gary T. Fry and Dr. Harry L. Jones, professors in the Civil Engineering Department. Having completed his Fulbright program, he started his Ph.D. studies in civil engineering at Texas A&M University in August 2000. From June 2001 to May 2003, he worked as a research assistant in the Civil Engineering Department at Texas A&M University. His research interests include structural mechanics and dynamics, nondestructive damage detection, traditional and heuristic optimization algorithms and the finite element method.

Contact address:
Stadion u. 55. 1/3.
Miskolc,
Hungary, H-3534